X-ray spectroscopy of merging galaxy clusters

Urdampilleta Aldema, I.

X-ray spectroscopy of merging galaxy clusters

Proefschrift

ter verkrijging van
de graad van Doctor aan de Universiteit Leiden
op gezag van de Rector Magnificus prof. mr. C. J. J. M. Stolker,
volgens besluit van het College voor Promoties
te verdedigen op woensdag 13 november 2019,
klokke 15:00 uur

door

Igone Urdampilleta Aldama

geboren te San Sebastián (Gipuzkoa), Spain

in 1981

Promotiecommissie:

Promotor:	Prof. dr. J. S. Kaastra	
Copromotor:	Dr. J. de Plaa	SRON
Overige leden:	Prof. dr. H. Röttgering	
	Prof. dr. J. Schaye	
	Prof. dr. H. Hoekstra	
	Prof. dr. M. Arnaud	CEA Saclay
	Dr. A. Simionescu	SRON
	Dr. J. Vink	University of Amsterdam

The research reported in this thesis was carried out at the Netherlands Institute for Space Research (SRON) and at the Leiden Observatory, with support from a NWO Top Grant.

A David y Shiva,
por estar siempre a mi lado

"El que avance en dirección de sus sueños,
conocerá un éxito inesperado en la vida ordinaria."

- Henry David Thoreau, *El club de los poetas muertos*

"If one advances confidently in the direction of his dreams,
he will meet with a success unexpected in common hours."

- Henry David Thoreau, *Dead Poets Society*

Contents

"Only in the darkness
can you see the stars."

- Martin Luther King Jr.

1 Introduction

1.1 Galaxy clusters

Galaxy clusters are the largest virialized objects in the Universe, which lay at the nodes of the cosmic web. Clusters contain between a hundred to a thousand of galaxies, who include only $\sim$5% of the total mass, $\sim 10^{14}$–10^{15} $M_{\odot}$. These galaxies are embedded in hot (10^{7}–10^{8} K or 1–10 keV) ionized gas, known as the intracluster medium (ICM), which has a significant contribution to the baryonic component and constitutes $\sim$15% of the mass budget. The rest of the mass, $\sim$80%, is dominated by dark matter (e.g. Blumenthal et al. 1984; Sanderson et al. 2003; Vikhlinin et al. 2006). The ICM is a low density plasma ($\sim 10^{-4}$–10^{-3} cm^{-3}) observed in X-rays by measuring its thermal plasma emission (Mitchell et al. 1976; Serlemitsos et al. 1977; Forman & Jones 1982).

Galaxy clusters can be observed not only using X-rays, but also other wavelengths such as optical, infrared, radio and using techniques such as the Sunyaev-Zel'dovich effect or gravitational lensing, see Fig. 1.1. Each of them provides a distinct kind of information about the cluster. Optical light, for example, shows the individual galaxies of the clusters and their overdensities at a similar redshift. X-rays are emitted by the diffuse hot plasma in the ICM, and radio emission traces cosmic rays, magnetic fields and discrete radio sources found in clusters. Moreover, gravitational lensing uses the observed distortions of the galaxies orientation behind the clusters to model the distribution of dark matter and to obtain the cluster masses. Finally, observing the Sunyaev-Zel'dovich effect (distortions of the cosmic microwave background) the density perturbations of the hot plasma can be detected.

Using these techniques the dynamical state of the clusters can be determined as well. They can be either dynamically relaxed or cool-core (CC) clusters, dynamically disturbed or non-cool-core (NCC) clusters and extremely disturbed systems known as merging galaxy clusters.

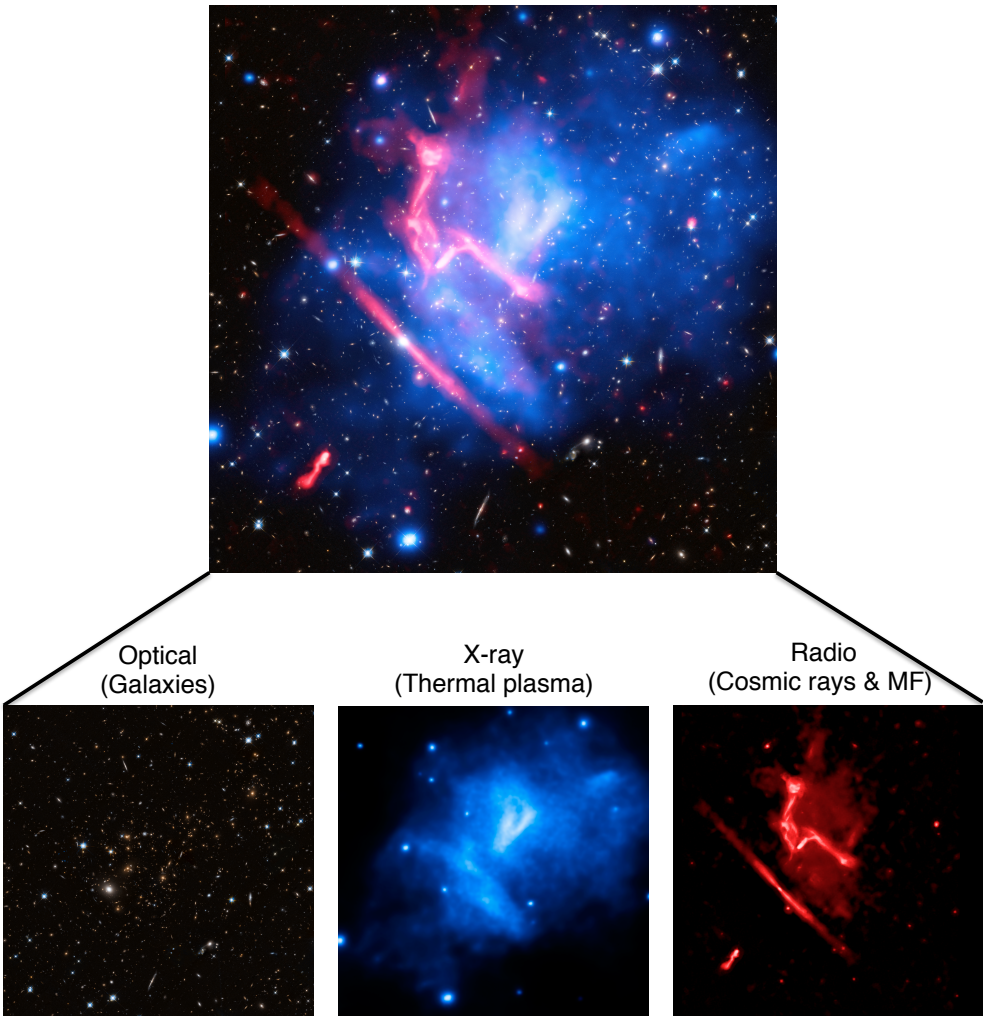

Figure 1.1: The galaxy cluster MACS J0717.5+3745. *Top panel*: Composite image (optical, X-ray and radio) of MACS J0717.5+3745. *Bottom panel*: The *left* panel presents an optical view of the cluster observed with the Hubble Space Telescope (red, green, and blue). In the *middle* panel, the X-ray emission from the thermal ICM is shown in blue using *Chandra* in the 0.5–2.0 keV band (van Weeren et al. 2017). The *right* panel displays the radio emission in red, data from the Jansky Very Large Array (JVLA). (Credit: X-ray: NASA/CXC/SAO/van Weeren et al.; Optical: NASA/STScI; Radio: NRAO/AUI/NSF).

In the CC clusters the central density is high enough to cause a radiative cooling flow on short cosmic timescales. Without any heating mechanism, the temperature in the central region could drop further and form stars (for a review, see Fabian 1994). However, the amount of cool gas found is less than expected (Peterson et al. 2001; Tamura et al. 2001; Kaastra et al. 2001). This suggests that a central source of heating, for example the feedback of an active galactic nucleus (AGN) in the core of the brightest cluster galaxy (BCG), can balance the radiative losses. The CC clusters also show a relatively high central metallicity peak anti-correlated with a low-entropy regime, which will be described in Section 1.3. On the contrary, the NCC clusters show a moderate central abundance peak and higher-entropy profiles.

1.2 Merging Galaxy Clusters

Galaxy clusters are not static entities, they grow hierarchically by the accretion of galaxy filaments (WHIM, warm-hot intergalactic medium) and merging of the surrounding galaxy groups and subclusters. Cluster mergers are the most energetic ($\sim 10^{64}$ erg) events in the Universe since the Big Bang. During these energetic processes (see Fig. 1.2 for a simulation of the Abell 3376 merging process[1]), the ICM of the corresponding (sub)clusters collides and becomes turbulent. Large amounts of thermal (X-ray) and non-thermal (radio) energy are released, giving rise to large scale structures known as shock fronts, cold fronts and turbulence (Markevitch & Vikhlinin 2007). Merger shocks violently compress and heat the X-ray emitting ICM and increase its entropy. In an idealized bimodal merger, "equatorial" shocks form first in the collision region and propagate outwards parallel to the merging axis (see *(c)* panel of Fig. 1.2). After the core passage phase, two shocks move perpendicular to the merging axis, from the center along the hot ICM up to the periphery of the cluster (see *(e)* and *(f)* panels of Fig. 1.2). In some cases, the merger can be violent enough to provoke the core disruption of one (sub)cluster (see *(f)* panel of Fig. 1.2). Cold fronts are also found in mergers and they delimit the boundaries of a cool and dense gas cloud moving through hotter and higher-entropy gas (Vikhlinin et al. 2001). Both, shocks and cold fronts provide a valuable tool to study the physical processes in the ICM at large scales. They can improve the understanding of the dynamical stage of the merger, the gas bulk velocities and their direction of motion.

1.2.1 Shock detection in X-rays

The X-ray shocks produced in a merging cluster show sharp discontinuities between denser and hotter gas in the downstream (post-shock) and more tenuous and cooler gas in the upstream (pre-shock) region. Therefore, temperature and density discontinuities at the same location should be detected to prove the presence of the shocks (see Fig. 1.3). The projected temperatures can be directly inferred from a spectral fit to the spectrum obtained from a selected region in an X-ray observation (see Section 1.4). A proper selection of the post and pre-shock regions is decisive to detect the correct temperature jump value, be-

[1] https://www.youtube.com/watch?v=XYyYIOwdVcw

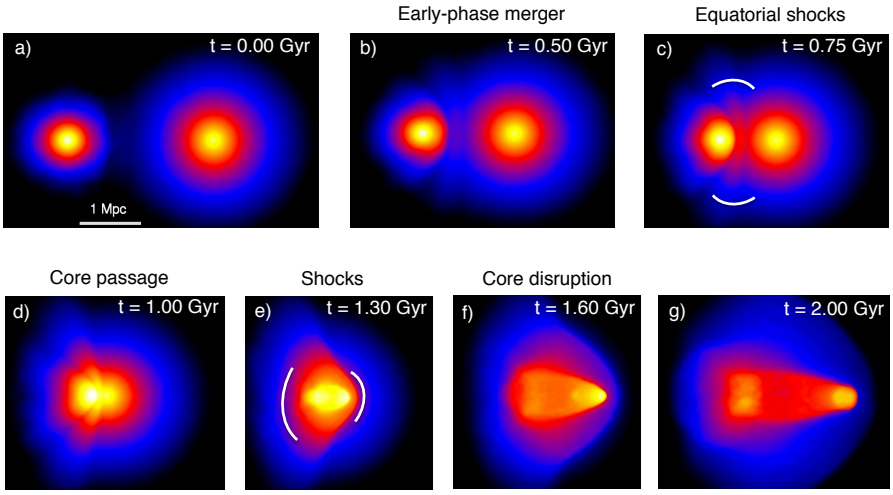

Figure 1.2: Simulation of the merging process of Abell 3376 based on Machado & Lima Neto (2013). *(a)*: Initial scenario with a mass ratio ∼1:6, impact parameter b < 150 kpc and a 1 Mpc separation. *(b)*: Beginning of the collision between the subclusters. *(c)*: Large scale-structures between subclusters and equatorial shocks appear. *(d)*: Beginning of the core passage. *(e)*: Symmetrical shock waves with respect to the center are visible. *(f)*: The core disruption of the most massive cluster has taken place. *(g)*: Late phase of the merging.

cause the post-shock region tends to include a two-temperature structure (mixing of both regions). Meanwhile, the projected density distribution can be derived from the surface brightness (SB) profile assuming spherical symmetry. The SB is frequently described by a broken power-law density profile (Owers et al. 2009; Eckert et al. 2016b):

$$\begin{cases} n_2(r) = n_0 \left(\frac{r}{r_{\rm sh}}\right)^{-\alpha_2} & r \leq r_{\rm sh} \\ \\ n_1(r) = \frac{1}{C} n_0 \left(\frac{r}{r_{\rm sh}}\right)^{-\alpha_1} & r > r_{\rm sh} \end{cases} \tag{1.1}$$

where n_0 is the model density normalization, n is the electron density, C is the compression factor, α_1 and α_2 are the power-law indices, r is the radius from the center, $r_{\rm sh}$ is the shock putative distance and the indices 2 and 1 corresponds to post-shock and pre-shock regions, respectively.

Furthermore, the X-ray shocks can be characterized by the Mach number ($\mathcal{M}_X$) and the shock propagation speeds ($v_{\rm shock} = \mathcal{M}_X \cdot c_{\rm s}$), relative to the pre-shock ICM. $c_{\rm s}$ is the sound speed at the pre-shock regions $c_{\rm s} = \sqrt{\gamma k T_1 / \mu m_p}$ with $\mu = 0.6$. This Mach number is relatively low $\leq$ 3–4 (e.g. Gabici & Blasi 2003; Ryu et al. 2003) and can be assessed from the Rankine-Hugoniot jump condition (Landau & Lifshitz 1959) assuming that all of the dissipated shock energy is thermalized and the ratio of specific heats (the adiabatic

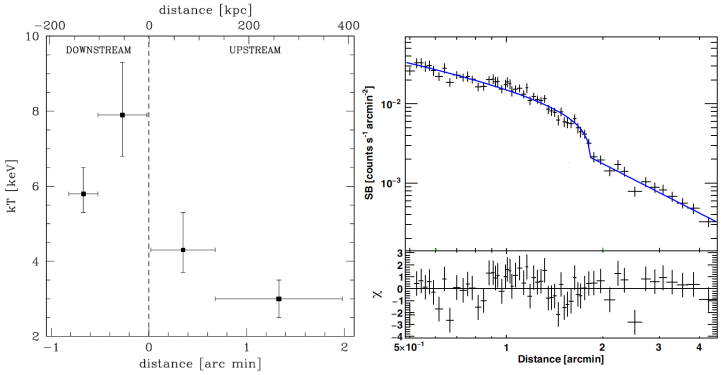

Figure 1.3: *Left panel*: ICM temperature profile across the shock of Abell 115 using *Chandra* observations. The vertical dashed line indicates the tentative shock position derived by the surface brightness discontinuity. *Right panel*: X-ray surface brightness profile in the 0.5-2 keV energy range of Abell 115. Both figures are adopted from Botteon et al. (2016a).

index) is γ = 5/3:

$$\frac{T_2}{T_1} = \frac{5\mathcal{M}_X^4 + 14\mathcal{M}_X^2 - 3}{16\mathcal{M}_X^2}, \tag{1.2}$$

$$\frac{n_2}{n_1} = C = \frac{4\mathcal{M}_X^2}{\mathcal{M}_X^2 + 3}, \tag{1.3}$$

where T is the temperature.

1.2.2 Particle acceleration by shocks

Shocks are thought to (re)accelerate electrons from the thermal distribution up to relativistic energies creating the non-thermal cosmic ray (CR) component of the ICM, by the first-order Fermi diffusive shock acceleration mechanism (hereafter DSA, Drury 1983; Bell 1987; Blandford & Eichler 1987). In the presence of a magnetic field these accelerated electrons can produce extended synchrotron radio emission, inverse Compton (IC) and gamma-ray emission (for a review, see van Weeren et al. 2019). DSA assumes a stationary and continuous injection, which accelerates relativistic CR electrons following a power-law spectrum (for a review, see Feretti et al. 2012):

$$n(E)dE \sim E^{-p}dE, \tag{1.4}$$

with p = 1-2α, where p is the power-law index and α is the radio spectral index for $S_\nu \propto \nu^\alpha$. Diffuse cluster radio sources have usually a step spectral index $\alpha \lesssim$ -1.

The Mach number can be also inferred from the radio observations assuming the simple DSA theory as:

$$\mathcal{M}_R^2 = \frac{2\alpha - 3}{2\alpha + 1}. \tag{1.5}$$

This method and the Rankine-Hugoniot jump condition are a priori independent. Therefore for the same source, if the assumptions are correct, the Mach number derived from these two different wavelength bands should agree with each other.

Recent studies have suggested that the acceleration efficiency of the DSA is low for shocks with $\mathcal{M}$ < 10 and might not be sufficient to produce the observed radio spectral indices (Kang et al. 2012; Pinzke et al. 2013). Nowadays alternative scenarios for the CR acceleration have been proposed as the electron re-acceleration by turbulence (Fujita et al. 2015; Kang 2017), the re-acceleration of pre-existing cosmic ray electrons (Markevitch et al. 2005; Kang et al. 2012; Fujita et al. 2015; Fujita et al. 2016; Kang 2017) or shock drift acceleration (Guo et al. 2014a,b, 2017). They are based on distinct acceleration mechanisms, such as second order Fermi acceleration (Fermi-II), where particles scatter from magnetic inhomogeneities, adiabatic compression or secondary models, where CRe are produced by secondary process.

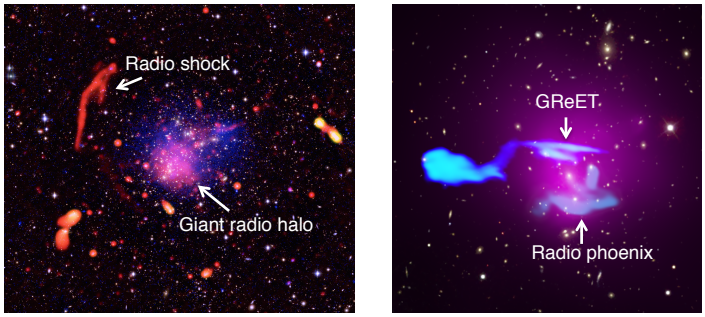

Figure 1.4: *Left panel*: Radio shock and giant radio halo in Abell 2744. The radio features emission in red, data from the Jansky Very Large Array (JVLA), X-ray data from *Chandra* (blue), optical data from *Subaru* and the VLT (red, green and blue). Credit: X-ray: NASA/CXC/ITA/INAF/Merten et al. (2011); Radio: NRAO/AUI/NSF/B. Saxton; Optical: NAOJ/Subaru & ESO/VLT. *Right panel*: GReET and radio phoenix in Abell 1033. Radio emission in blue are data from LOFAR, X-rays from *Chandra* in purple and SDSS optical data. Credit: X-ray: NASA/CXC/Leiden Univ./De Gasperin et al. (2017); Optical: SDSS; Radio: LOFAR/ASTRON, NCRA/TIFR/GMRT.

van Weeren et al. (2019) present a new classification of diffuse radio sources, which includes cluster radio shocks, revived AGN fossil plasma sources, phoenices and GReETs (Gently re-energized tails), and radio halos. The first two ones are thought to trace X-ray shocks:

- **Cluster radio shocks (radio relics)**: Extended diffuse radio sources form by the X-ray shocks (re)acceleration of energetic particles, in the presence of a magnetic field (for a review, see Ferrari et al. 2008; Brunetti & Jones 2014; van Weeren et al. 2019). They are Mpc-size elongated, filamentary and polarized radio structures located usually in the cluster outskirts. The spectral index varies between -1.5 < α < -1.1 and can steepen across the radio shock towards the cluster center. In most of the cases they are associated to a DSA mechanism, although, as mentioned before, there are other

alternatives proposed lately. Only 2–8 % of clusters show radio shocks (Kale et al. 2015) and most of them are generally in or near the plane of the sky, which indicates a clear selection bias. Some of the radio shocks have associated X-ray shocks, usually found at the same location (see Table 1 of van Weeren et al. 2019). In some clusters two radio shocks appear diametrically with respect the center and are known as double shocks (i.e. double radio relics), such as Abell 3667 (Röttgering et al. 1997). Nowadays, a dozen of these systems have been discovered. The first radio shock detected was in the Coma cluster (Jaffe & Rudnick 1979; Ballarati et al. 1981). Afterwards, many others have been identified in the last years (for an extended list see Table 2 of van Weeren et al. 2019).

- **Revived AGN fossil plasma sources, phoenices, and GReETs**: These sources originate from the re-energisation of AGN fossil radio plasma in the ICM and are characterized by ultra-deep radio spectra. They are only visible in low-frequency radio observations.

  –*Revived AGN fossil plasma sources and radio phoenices*: They form by shock compression of old radio plasma. Phoenices (Kempner & David 2004) have irregular morphology, although the most common one is elongated and filamentary. The spectral index is α < -1.5. Compared with radio shocks they are located at smaller distances from the cluster center, they have smaller size ($\leq$ 300-400 kpc), lower polarization and radio power. The re-acceleration of the seed population in the ICM is thought to be the CR acceleration mechanism (Markevitch et al. 2005; Kang et al. 2012). Some of these sources have been found in e.g. Abell 1931 (Brüggen et al. 2018) and Abell 1914 (Mandal et al. 2019).

  –*GReETs*: Gently re-energized radio galaxy tails (De Gasperin et al. 2017), which present unexpected spectral flattening. It seems that the radiative losses of the CR are balanced with the particle re-energization, giving as a result the synchrotron spectrum flattening. Fermi-II processes are proposed for the particle re-acceleration mechanism. GReETs have been found in Abell 1033 (De Gasperin et al. 2017), Abell 1314 (Wilber et al. 2019) and ZwCl0634.1+4750 (Cuciti et al. 2018).

- **Radio halos**: Cluster-wide extended radio sources, which follow the ICM mass in the cluster center, do not present optical counterparts and there is no X-ray shock associated. The particle (re)acceleration is generated by means of the turbulence in the ICM via Fermi-II processes and/or secondary electrons. They include giant radio halos, mini-halos and "intermediate" halos, a possible transition or interface between the two previous categories (for a review, see Brunetti et al. 2001; Feretti et al. 2012; van Weeren et al. 2019).

  –*Giant radio halos*: Mpc-size radio sources found in massive dynamically disturbed clusters, usually as a consequence of a merger (Giovannini et al. 1999; Buote 2001; Cassano et al. 2010). They are found generally unpolarized. The typical spectral index varies between -1.4 < α < -1.1 (Giovannini et al. 2009). Different studies have shown that 60–80% with $M > 8 \times 10^{14}$ $M_{\odot}$ (20–30% below this mass) host giant radio halos. Nowadays, there are about 65 radio halos confirmed, e. g. Coma cluster (Large et al. 1959; Willson 1970), MACS J0717.5+3745 (Bonafede et al. 2009; van Weeren et al. 2009) or Abell 665 (Moffet & Birkinshaw 1989; Feretti et al. 2004b; Vacca et al. 2010).

–*Mini-halos*: They are found in the centers of relaxed CC clusters, often surrounded by cold fronts (Mazzotta & Giacintucci 2008). Their typical size is 100–500 kpc, similar to the extension of the central cooling regions around the BCG (for a review, see Gitti et al. 2015). The spectral index is similar to giant radio halos. Giacintucci et al. (2017) found that 80% of the CC clusters host mini-halos, while no evidence of them is found in NCC clusters. The Perseus cluster (Miley & Perola 1975; Pedlar et al. 1990) hosts a mini-halo as some other clusters such as e.g. Phoenix cluster (van Weeren et al. 2014) or RXJ1347.5-1145 (Gitti et al. 2007).

1.2.3 Comparison between X-ray and radio components of ICM shocks

As mentioned before, in some merging clusters both X-rays and radio emission are associated with the same shock. In 2010 Finoguenov et al. (2010) found the first evidence of X-ray and radio emission from the same shock in Abell 3667. Since then the number of discoveries have been increasing in the last decade (Macario et al. 2011; Ogrean & Brüggen 2013c; Bourdin et al. 2013; Eckert et al. 2016b; Sarazin et al. 2016; Akamatsu & Kawahara 2013a; Akamatsu et al. 2015, 2017; Botteon et al. 2016a,b; Urdampilleta et al. 2018; Di Gennaro et al. 2019).

The study of the radial distribution of these thermal and non-thermal components allows to determine the physical association between X-ray and radio emission from shocks as well as the thermodynamical properties and the dynamical state of the merging system. The comparison of Mach numbers derived from X-ray ($\mathcal{M}_X$) and radio ($\mathcal{M}_R$) observations can also reveal important information about the underlying assumptions, such as the particle acceleration mechanism. In the last years, discrepancies between both values have been found for most of the merging systems. The Mach number tends to be $\mathcal{M}_R > \mathcal{M}_X$ in most of the cases (see Table 2.10 and Fig. 2.16 in **Chapter 2**), except for the western shock of A3376 (see possible explanation in Section 2.4.4 of **Chapter 2**). It seems that $\mathcal{M}_X$ is somehow underestimated due to possible projection effects and/or the complexity of shock surface (Rajpurohit et al. 2018). Furthermore, recent radio observations have contributed to reduce the discrepancy. The low-frequency observations of LOFAR, for example, allow to determine with higher accuracy the injected spectral index (Hoang et al. 2017), therefore the $\mathcal{M}_R$. Akamatsu et al. (2017) discuss possible causes of this discrepancy (see their Section 4.3. for more details): (i) projection effects, (ii) Ion-electron non-equilibrium after shock heating, (iii) clumpiness and inhomogeneities in the ICM, (iv) a non-uniform Mach number or (v) pre-existing low-energy relativistic electrons and/or re-accelerated electrons, among others. A conclusive explanation of the Mach number difference is still far from being determined, but future X-ray observatories, such as *XRISM* and *Athena* will definitely shed further light on this issue (see Section 1.6).

1.3 Metal Enrichment in Galaxy Clusters

The hot plasma, ICM, is also known to be a rich archive of the past chemical history of the galaxy cluster. From the study of this enriched diffuse gas, crucial information over the galaxy cluster formation and evolution can be derived, such as merging and star-formation histories or stellar evolution. The heavy elements present in the ICM originate mainly from core-collapse (SNcc) and type Ia (SNIa) supernovae, which continuously release their nucleosynthesis products since the epoch of major star formation ($z \sim 2$–3) (Hopkins & Beacom 2006; Madau & Dickinson 2014). SNcc evolve from massive short-living stars and produce mainly oxygen (O) and other α-elements such as neon (Ne), magnesium (Mg), silicon (Si) and sulfur (S). On the other hand, SNIa emerge from the explosion of white dwarf stars in binary systems and contribute to increase the heavier metals such as argon (Ar), calcium (Ca), manganese (Mn), iron (Fe) and nickel (Ni). Finally, the bulk of carbon (C) and nitrogen (N) are mostly expelled by low-mass stars on the asymptotic giant branch (AGB). Recent studies (Ezer et al. 2017; Mernier et al. 2017; Mao et al. 2019) address that the ICM is enriched with a similar relative contribution of SNcc and SNIa products in all the cluster extension from the core to the most virialised regions. Once SN explosions or AGB stars release the metals, different physical and dynamical processes drive their distribution and mixing along the ICM, such as galactic winds (Kapferer et al. 2006, 2007; Baumgartner & Breitschwerdt 2009); ram-pressure stripping (Schindler et al. 2005; Kapferer et al. 2007), active galactic nucleus (AGN) outflows (Simionescu et al. 2008, 2009; Kapferer et al. 2009) or gas sloshing (Simionescu et al. 2010; Ghizzardi et al. 2014), among other processes. Detailed reviews on the observation of metals in the ICM include, e.g., Werner et al. (2008); Böhringer & Werner (2010); de Plaa (2013) and Mernier et al. (2018b).

In the last years, the spatial distribution of Fe in galaxy clusters has been extensively studied using the different X-ray observatories such as *ASCA*, *BeppoSAX*, *XMM-Newton*, *Chandra* or *Suzaku* (De Grandi & Molendi 2001; De Grandi et al. 2004; Baldi et al. 2007; Leccardi & Molendi 2008; Maughan et al. 2008; Matsushita 2011; Mernier et al. 2016, 2017; Mantz et al. 2017; Simionescu et al. 2017; Simionescu et al. 2019; Liu et al. 2018; Lovisari & Reiprich 2019). Most of the studies have been mainly devoted to the cool-core clusters except for the work by De Grandi et al. (2004) and Lovisari & Reiprich (2019), where an extended analysis for non-cool-core cluster is described. Previous analyses concluded that the radial distribution of Fe is centrally peaked for CC clusters, with a pronounced gradient up to $0.3 r_{500}$ and flattening for larger radii till a uniform value of $\sim$0.2–0.3 $Z_{\odot}$. The behavior of NCC clusters is clearly different (see Fig. 1.5). They show a flat distribution in the core, followed by a shallower gradient than the CC clusters, but with the same universal distribution for outer radii. The averaged Fe distribution of the recent study by Urdampilleta et al. (2019) (see **Chapter 4**) of six merging clusters show a good agreement with the radial distribution by Lovisari & Reiprich (2019) for NCC clusters. Moreover, X-ray observational studies (Ettori et al. 2015; McDonald et al. 2016; Mantz et al. 2017) and simulations (Biffi et al. 2017; Vogelsberger et al. 2018) suggest that the Fe abundance distribution and ICM metallicity remain nearly invariant within r_{500} between $z \sim 2$ and $z = 0$.

Nowadays, two possible scenarios for the metal enrichment in galaxy clusters are under debate:

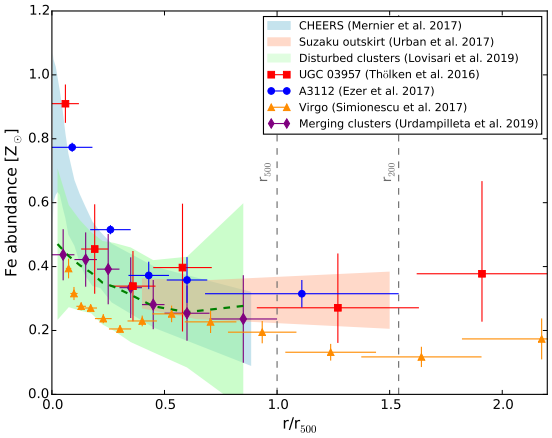

Figure 1.5: Measured radial Fe abundance profile in cool-core and non-cool-core clusters compiled from recent works. The blue, red and green shaded areas show respectively the CHEERS sample (Mernier et al. 2017), the 10 cluster outskirts sample (Urban et al. 2017) and disturbed clusters sample (Lovisari & Reiprich 2019). The CHEERS and *Suzaku* samples are stacked following the Mernier et al. (2017) method. The red squares, the blue circles, the orange triangles and purple diamonds show respectively the UGC 03957 group (Thölken et al. 2016a), the Abell 3112 cluster (Ezer et al. 2017), the Virgo cluster (Simionescu et al. 2017) and the merging clusters sample Urdampilleta et al. (2019). All the abundances are rescaled with respect to the proto-solar values of Lodders et al. (2009).

– Pre-enrichment scenario: Suggests that most of the metal enrichment of the ICM took place in the early stages of cluster formation (i.e. at $z > 2$–3; for recent reviews, see Mernier et al. 2018b; Biffi et al. 2018b). As a result, a uniform Fe abundance in the cluster outskirt is expected with a value around 0.2–0.3 $Z_{\odot}$.

– Late enrichment scenario: Proposes that the bulk of Fe was added at relatively recent times by merging or accretion processes, and mixed efficiently in the entire cluster volume. In this scenario, the Fe abundance at large radii in such dynamically disturbed systems would present notable gradients, with values higher than 0.2–0.3 $Z_{\odot}$.

As explained above, the CC and NCC profiles present similarities in the outskirts of the galaxy clusters, following a uniform radial distribution around 0.2–0.3 $Z_{\odot}$ (Fujita et al. 2008; Werner et al. 2013; Urban et al. 2017; Ezer et al. 2017; Simionescu et al. 2017). The simulations of Biffi et al. (2017) , Biffi et al. (2018a) and Vogelsberger et al. (2018) are able to reproduce the observables of the pre-enrichment scenario including in the physical processes of the stellar and AGN feedback. This means that the Fe distribution in cluster outskirts is independent of the dynamical state of the cluster, which together with the Fe abundance uniformity (0.2–0.3 $Z_{\odot}$) found, establish relevant additional evidence in favour of the pre-enrichment scenario.

1.4 Why X-ray spectroscopy

Many astrophysical sources in our Universe, in addition to galaxy clusters, contain X-ray emitting plasma, such as the coronae of cool stars, the winds of hotter stars, the hot component of the interstellar medium and the Warm-hot intergalactic medium (WHIM). Most of these plasmas are in collisional ionization equilibrium (CIE), where no external radiation field effects are present. Concretely, the ICM is mostly (excluding resonant scattering) an optical thin plasma which is in CIE and confined by the cluster gravitational potential well. Its spectrum contains two main components: one, the X-ray continuum emission mainly by bremsstrahlung, and further, the spectral emission lines. The continuum level can provide the temperature of the ICM and the equivalent width of the emission lines is proportional to the abundance of the metals that produce them (see Fig. 1.6). Apart from the temperature and abundances, X-ray spectra allow to obtain other physical properties such as densities, velocity field and ionization state as well. Therefore, X-ray spectroscopy is a crucial tool to infer the thermodynamical and chemical properties of the ICM.

One of the most significant contributions of X-ray spectroscopy to cluster science is the discovery of the "cooling flow problem". Following the classical cooling flow model the spectra of the cluster center should contain ions emitting at very low temperatures. On the contrary, no evidence of such emission lines was found by different X-ray observatories. Currently, as introduced in Section 1.1, it is thought that the cluster central cooling is balanced by (the) AGN feedback. In the case of merger shocks science, X-ray spectroscopy is decisive to determine the temperature and density of the post-shock and pre-shock regions, and therefore their discontinuities in the presence of the shock. Because shocks often occur at cluster outskirts, where the surface brightness is low, the shock detection can be challenging. Moreover, X-ray spectroscopy is also useful to determine the chemical enrichment in the ICM. The analysis of the emission lines associated with the metal production can reveal valuable information about the enrichment history.

Figure 1.6: *Left panel*: Ilustration of the *Suzaku* satellite. Credit: JAXA. *Middle panel*: Ilustration of the *XMM-Newton* satellite. Credit: ESA. *Right panel*: EPIC instrument (*XMM-Newton* satellite) spectra of the core region of the Abell 4059 cluster (Mernier et al. 2015).

Nowadays there are three methods to measure the X-ray spectra: CCDs, gratings and micro-calorimeters. CCDs are used for imaging observations with moderate field-of-view (FOV) and low/medium spectral resolution. The recent generation of X-ray satellites are

provided with this kind of detectors: the EPIC instrument in *XMM-Newton*, the ACIS instrument in *Chandra* and the XIS instrument in *Suzaku*. Gratings have higher spectral resolution but limited imaging capabilities. They are mainly devoted to point sources. *XMM-Newton* hosts the RGS instrument and *Chandra* the LETG and HETG spectrometers. Microcalorimeters are a recent development, that offer unprecedented high-resolution spectroscopy capabilities. The X-ray spectrometer of *Hitomi*, the Resolve instrument aboard *XRISM* and X-IFU aboard *Athena* are good examples of this kind of detectors.

1.5 Plasma codes for X-ray spectroscopy

Every spectrum containing spectral lines need spectral plasma codes to model and fit it. Atomic data are clearly needed for the interpretation of line fluxes, ratios and ionization states of the emitting plasma. Driven by the future high-resolution spectroscopy requirements (∼6-7 eV or ∼2.5 eV) of new X-ray satellites (i. e. *XRISM* or *Athena*), updates and improvements of the plasma codes are required. Some of the plasma codes for X-ray plasma spectra modeling, fitting and analysis available nowadays (for a review, see Kaastra et al. 2008) are SPEX[2] (Kaastra et al. 1996) , see more details in Section 1.5.1, AtomDB[3], with latest version v3.0.9 included in XSPEC (Arnaud 1996), and CHIANTI[4] (Landi et al. 2006), the latest version v9.0 (Del Zanna et al. 2015) . There also codes focusing on photoionised plasmas such as XSTAR[5] (Kallman & McCray 1982), current version 2.39, and Cloudy[6], with the latest version v17.01 (Ferland et al. 2017).

1.5.1 SPEX

The first work on X-ray spectra modelling at SRON started in the late 1960s and the first code was initially written by Mewe (1972). After some updates (Mewe et al. 1985, 1986), this plasma code became a reference for many years. The code was later updated first as the MEKA (following its main contributors: Rolf Mewe and Jelle Kaastra), and then as MEKAL code in 1995. It was incorporated into the XSPEC fitting package (Arnaud 1996). In 1991 the MEKAL code evolved into the SPEX package and around 1996 the second version v2.0 was developed (Kaastra et al. 1996), driven by the preparation for the *Chandra* and *XMM-Newton* satellites launched in 1999. In 2016 high-resolution spectroscopy observations were expected from the *Hitomi* satellite and most of the plasma codes were considerably updated for the occasion (Hitomi Collaboration et al. 2018a). For this same reason, in January 2016, SPEX v3.0 (Kaastra et al. 2017b) was released. This version aimed to follow the original strategy of Mewe (1972), which is minimizing the number of mathematical operations and data storage to achieve simple and fast, but accurate calculations. A comparison of the Fe abundance for the CHEERS sample using SPEX v2.0 vs. v3.0 can be seen in Mernier et al. (2018a). Currently the latest version is 3.05.00, see the description

[2] https://www.sron.nl/astrophysics-spex
[3] http://www.atomdb.org/
[4] http://www.chiantidatabase.org/
[5] https://heasarc.gsfc.nasa.gov/lheasoft/xstar/xstar.html
[6] https://www.nublado.org/

in the SPEX Manual[7] from December 2018. One of the new updates in SPEX v3.0 was the new atomic database prepared mainly by Ton Raassen, which includes thousands of lines and transitions from hydrogen to zinc, obtained from the literature or calculation made with FAC (Flexible Atomic Code, Gu 2002), and is part of the SPEXACT (SPEX Atomic Code and Tables). The other updates were related to the following radiative processes (Kaastra et al. 2008, 2017c):

- **Radiative recombination (RR)** is the reverse process of photoionization. A free electron is captured by an ion while emitting a photon, it is also known as free-bound continuum emission. The update of RR data for SPEX v3.0 include the parameterization of the most recent calculations done by Mao & Kaastra (2016) and Mao et al. (2017).
- **Collisional ionization (CI)** occurs during the interaction of a free electron with an atom or ion. The free electron transfers a part of its energy to one of the bound electrons and this is able to escape from the ion (Direct Ionization, DI). Another intermediate ionization process can happen called Excitation-Autoionization (EA). If the free electron has insufficient energy to ionize the ion directly, the collision can bring one of the bound electrons in a higher shell by excitation. The ion will return to its ground level by a radiationless autoionization transition, which causes the liberation of the previously excited electron (see Fig. 1.7). The inner-shell ionization data for CI and EA have been updated in SPEX v3.0 including the new laboratory measurements and theoretical calculations of the CI cross-sections (Urdampilleta et al. 2017, see **Chapter 5**).

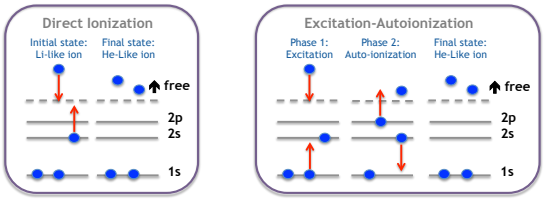

Figure 1.7: Direct Ionization and Excitation-Autoionization of Li-like ion.

- **Charge exchange (CX)** occurs when an ion collides with a neutral atom, and catches an electron from the atom. The captured electron often relaxes down to the ground via line emission. A new CX model has been incorporated in SPEX v3.0 (Gu et al. 2016).
- **The Photoionization** process is similar to CI but with a photon instead of free electron causing the ionization. It takes place during the interaction of a photon with an atom or ion, the photon transfers a part of its energy to one of the bound electrons, which is able to escape from the ion. Updates in the PION model of SPEX that models a photoionized plasma and a comparison with other photoionization codes are described in Mehdipour et al. (2016).

[7] https://www.sron.nl/astrophysics-spex/manual

1.6 Future prospects

Since the 80s, different X-ray observatories (*Einstein*, *EXOSAT*, *ROSAT*, *ASCA*, *BeppoSAX*, *XMM-Newton*, *Chandra*, *Suzaku* and *Astrosat*) have allowed to extensively analyze the gas density, temperature and abundance distribution in galaxy clusters. However, the key improvement came with upgraded spectroscopic and imaging capabilities of the most recent X-ray satellites such as *XMM-Newton*, *Chandra* and *Suzaku*. The first two were launched in 1999 and they are still operative, while *Suzaku* finished its operational lifetime in 2015. *Chandra* has a high angular resolution (i.e. $1''$ at $z < 0.05$ corresponds to < 1 kpc, Markevitch & Vikhlinin 2007), which can provide detailed images of the ICM substructures such as shocks or cold fronts produced as a consequence of gas sloshing, subcluster accretion or merging, among other processes. *XMM-Newton*, in spite of having a moderate angular resolution, is not sufficient to visualized these features, but it can determine the ICM temperature and measure abundances with higher statistical accuracy due to its larger effective area and spectral resolution. On the other hand, the strength of the *Suzaku* satellite was its low instrumental background and stable detectors, which allowed to observe the low surface brightness regions, e. g. cluster outskirts, where usually X-ray shocks are located.

In the last few decades, our understanding of the astrophysics and evolution of galaxy clusters has considerably improved thanks to the previously mentioned X-ray observatories. Nevertheless, some fundamental questions, related to the science topic of this thesis, remain still open such as: (i) how do hot diffuse baryons accrete and dynamically evolve in the dark matter halos? and (ii) what drives the chemical and thermodynamic evolution of galaxy clusters? (Ettori et al. 2013; Guainazzi & Tashiro 2018). The next generation of X-ray missions will address all these open questions. We have already glimpsed the power of micro-calorimeter detectors through the *Hitomi* satellite (Section 1.6.1). In Section 1.6.2 and 1.6.3, the highlights of these exciting missions, *XRISM* and *Athena*, are described respectively.

1.6.1 Hitomi

Hitomi, the Japanese satellite, was successfully launched on 17th February 2016. Unfortunately, during the commissioning phase, one month after the launch, the satellite broke away as a result of several failures in the attitude and orbital control subsystem. On 28th April 2016 JAXA declared the mission officially finalized. *Hitomi* was provided with two soft X-ray telescopes, a soft X-ray imager (SXI) and a soft X-ray spectrometer (SXS), a micro-calorimeter instrument, in addition to two gamma-ray detectors. SXS had a FOV of $3' \times 3'$, with a high energy resolution of $\sim$5 eV in the 0.4–12 keV band, allowing to do high-resolution spectroscopy at an unprecedented level (see the spectrum of the Perseus galaxy cluster in Fig. 1.8).

Before the satellite failure, *Hitomi* was able to observe the Perseus galaxy cluster. The high-resolution of the SXS instrument allowed to measure the detailed structure of spatially resolved emission lines, the velocities of gas motions, metallicities and the multi-temperature structure of the gas in the core of the Perseus cluster (Hitomi Collaboration

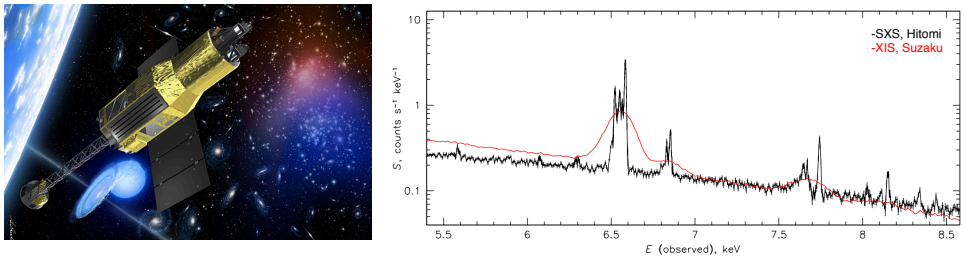

Figure 1.8: *Left panel*: Ilustration of the *Hitomi* satellite. Credit: JAXA. *Right panel*: SXS (*Hitomi*) spectrum of the full field overlaid with a CCD (*Suzaku*) spectrum of the same region of Perseus galaxy cluster. Credit: Hitomi Collaboration et al. (2016).

et al. 2018b,c,d; Simionescu et al. 2019). This observation, accomplished with the gate valve closed (not fully operative), revealed a very high resolution spectrum using the micro-calorimeters. This showed the first realistic proof of the high potential of this kind of detectors, which open a new window on the merging galaxy clusters and the ICM chemical enrichment studies.

1.6.2 XRISM

Based on the extraordinary performance and results obtained from the Perseus cluster, the only available cluster observation, by the *Hitomi* satellite, JAXA and NAXA decided to propose a recovery mission expected to be launched in early 2022. It has been recently renamed as *XRISM* (X-Ray Imaging and Spectroscopy Mision) (Tashiro et al. 2018). There will be two instruments on board XRISM: a soft X-ray micro-calorimeter (Resolve) with an energy resolution of $\leq$ 7 eV in the 0.3–12 keV range and a FOV of $3' \times 3'$, and an array of CCD detectors (Extent) with an energy resolution of $\sim$170 eV @ 6 keV and a larger FOV > $30' \times 30'$. Both instruments have similar characteristics to the SXS and SXI instruments of *Hitomi*. The main advantages of *XRISM* are the high spectral resolution provided by the micro-calorimeter and the low instrumental background level, seven times lower than *Suzaku*. The high resolution will allow to measure with higher accuracy the metal abundances in galaxy clusters such as O, Ne and Mg, to fully resolve all the Ni and Fe lines and to disentangle rare elements as Na or Al. The low background makes *XRISM* one of the most suitable satellite to observe low-count-rate regions at cluster peripheries and to look for accretion and merger X-ray shocks.

1.6.3 Athena

Athena is the second L-mission of the ESA "Cosmic Vision" program to be launched around 2030. *Athena* aims to address the science topics of the "Hot and Energetic Universe" (Nandra et al. 2013). The instruments on board are the X-ray Integral Field Unit (X-IFU, Barret et al. 2018), a cryogenic imaging spectrometer with a 2.5 eV energy resolution in the 0.2–12 keV band and a FOV of $5' \times 5'$, and the Wide Field Imager (WFI, Meidinger et al. 2018), a

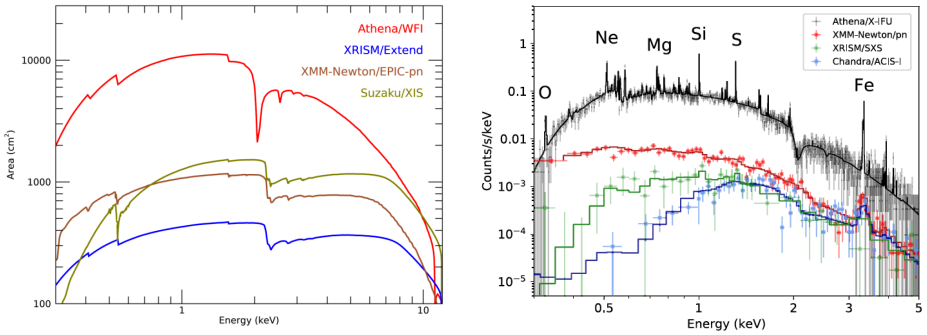

Figure 1.9: *Left panel*: Effective area comparison of CCD detectors. Credit: Mateo Guainazzi, ESA. *Right panel*: Simulated 250 ks spectrum of the core of a galaxy cluster (kT = 3 keV, z = 1) for the *Athena* X-IFU instrument, *XMM-Newton* pn, *XRISM* SXS and Chandra ACIS-I. Credit: Mernier et al. (2018b).

DEPFET detector with a wide FOV (40′×40′) and moderate energy resolution (≤150 eV @ 6 keV). The revolutionary capabilities of *Athena* are focused on its effective area, which is considerably larger than previous satellites (see left panel of Fig. 1.9) and the high spectral resolution of 2.5 eV over a broad energy band. The combination of these performances will enable a definitive understanding of merger X-ray shock physical properties and their role in the evolution of large-scale cosmic structure. For example, *Athena* will allow to obtain an accurate temperature structure map of the post and pre-shock regions, rising possible substructures and reconstructing the original temperature structure. Moreover, the measurement of the ion temperature via the thermal broadening of the emission line will be possible, similar to the diagnostic of the non-Maxwellian tails of the electron distribution (Kaastra et al. 2009). Finally, more accurate temperature and density discontinuities characterization will be obtained in shock regions, providing a better comparison with radio observations, and therefore better understanding of the particle acceleration mechanism.

The chemical enrichment science will benefit from the high spectral and spatial resolution to provide unprecedented accurate abundance measurements, not only the better characterized elements but also the new ones such as Cr, Mn, N or Na (see right panel Fig. 1.9). This will provide better constrains for the metal production mechanisms via SN and AGBs. Moreover, detailed metal distribution maps will be derived, as well as the metal radial distribution for radii larger than r_{500}. For the first time the abundances at the cluster outskirts and beyond will be estimated, which will shed light on the cluster enrichment scenario.

1.7 Thesis outline

This thesis focuses on the X-ray spectral analysis of merging galaxy clusters and the plasma code development for future high-resolution X-ray spectroscopy observations. This work deepens in two different aspects of these merging clusters still under debate: one, the study of the thermal (X-ray shocks) component and its correlation with the non-thermal

(radio shocks/relics) component, and two, their metal enrichment history. The first one is crucial to understand how the shocks propagate and heat the ICM as well as to determine the physical association between these two components. The second one aims to contribute to a better knowledge of the metals origin, evolution and distribution in merging clusters, which can reveal important information on the dynamical history of the mergers.

Chapter 2

In Chapter 2, we investigate the spatial distribution of X-ray shock structures of the merging galaxy cluster Abell 3376 and study their relation with the radio shocks (relics). We analyze *Suzaku* observations, which cover the entire double radio relic region (Mpc-size) in the cluster outskirts. We determine the radial temperature profiles in four different directions: west, east, north and south. All of them except the south show evidence of a deviation from the universal temperature profile of relaxed clusters, suggesting a possible presence of X-ray shocks. However, we find a clear temperature jump and density discontinuity derived from the surface brightness using *XMM-Newton* observations, only in the west and east. We confirm that one X-ray shock is located at the western radio relic and another one probably associated to the 'notch' of the eastern relic. Moreover, we detect a cold front at the east using a *Chandra* observation. The Mach numbers derived from radio observations are consistent with the Mach number derived from X-rays in the eastern shock, but slightly lower for the western one, probably due to the radio ageing effects. Finally, we estimate that the merger is taking place close to the plane of the sky and the dynamical age is ∼0.6 Gyr after core passage, indicating that Abell 3376 is a young merger, still evolving.

Chapter 3

In Chapter 3, we show the spectral analysis of the multi-merging galaxy cluster Abell 3365 observed with *XMM-Newton* satellite. In our study we find two strong X-ray shocks with a $\mathcal{M} > 3$, co-located with a western radio relic and eastern radio relic candidate, based on the temperature discontinuity. We also observe a cold front at the west of the X-ray emission peak, which delimit a very high abundance gas (∼0.6 $Z_{\odot}$), displaced from the central potential well due to dynamical internal force of the cold front. In addition we determine the radial temperature, abundance and pseudo-entropy distribution along the merging axis of the disturbed intra-cluster medium. Finally, we calculate the shock acceleration efficiency at the eastern radio relic, which suggest that the DSA scenario is a possible acceleration mechanism for shocks with $\mathcal{M} \gtrsim 3$.

Chapter 4

In Chapter 4, we present an iron abundance study for merging galaxy clusters using *XMM-Newton* observations. For the first time the temperature, abundance and pseudo-entropy distribution along the merging axis of six well known merging clusters (CIZA J2242.8+5301, 1RXS J0603.3+4214, Abell 3376, Abell 3667, Abell 665 and Abell 2256) are obtained up to r_{500}. The averaged Fe distribution shows a good agreement with NCC or disturbed clusters distribution. It has a moderate central peak, lower than CC or relaxed clusters, and flattens

for large radii towards a similar uniform distribution with a value $\sim$0.2–0.3 $Z_\odot$. Moreover, we find a mild correlation between abundance and psuedo-entropy in the central regions, while no evidence of the correlation is found in the cluster outskirts. This finding together with the abundance uniformity at large radii is valuable additional evidence in favour of the pre-enrichment scenario, which is found to be independent of the dynamical state of the cluster.

Chapter 5

In Chapter 5, we review the new laboratory measurements and theoretical calculations of single ionization cross sections available for ions from H to Zn. As a result of this work, we include in total 45 new data sets for different ions, while the rest of the ions are interpolated or extrapolated. We obtain not only the total cross sections, but all the inner shells cross-sections of the Direct Ionization (DI) and Excitation-Autoionization (EA) processes. We model and fit these processes using an extension of Younger's and Mewe's formula for DI and EA, respectively. The integration of these models over a Maxwellian velocity distribution allow us to derive the subshell ionization rate coefficients, which have been incorporated into the new version of SPEX v3.0.

"Take your passion
And make it happen
Pictures come alive
You can dance right through your life"

- Irene Cara, *Flashdance*

2

X-ray study of the double radio relic Abell 3376 with Suzaku

I. Urdampilleta & H. Akamatsu & F. Mernier & J. S. Kaastra & J. de Plaa & T. Ohashi & Y. Ishisaki & H. Kawahara

Astronomy & Astrophysics, Volume 618, A74 (2018)

Abstract

We present an X-ray spectral analysis of the nearby double radio relic merging cluster Abell 3376 (z = 0.046), observed with the *Suzaku* XIS instrument. These deep (∼360 ks) observations cover the entire double relic region in the outskirts of the cluster. These diffuse radio structures are amongst the largest and arc-shaped relics observed in combination with large-scale X-ray shocks in a merging cluster. We confirm the presence of a stronger shock ($\mathcal{M}_{\rm W}$ = 2.8 ± 0.4) in the western direction at $r \sim 26'$, derived from a temperature and surface brightness discontinuity across the radio relic. In the east, we detect a weaker shock ($\mathcal{M}_{\rm E}$ = 1.5 ± 0.1) at $r \sim 8'$, possibly associated with the 'notch' of the eastern relic, and a cold front at $r \sim 3'$. Based on the shock speed calculated from the Mach numbers, we estimate that the dynamical age of the shock front is ∼0.6 Gyr after core passage, indicating that Abell 3376 is still an evolving merging cluster and that the merger is taking place close to the plane of the sky. These results are consistent with simulations and optical and weak lensing studies from the literature.

2.1 Introduction

Galaxy clusters form hierarchically by the accretion and merging of the surrounding galaxy groups and subclusters. During these energetic processes, the intracluster medium (ICM) becomes turbulent and produces cold fronts, the interface between the infalling cool dense gas core of the subcluster and the hot cluster atmosphere, and shock waves, which propagate into the intracluster medium of the subclusters (Markevitch & Vikhlinin 2007). Part of the kinetic energy involved in the merger is converted into thermal energy by driving these large-scale shocks and turbulence, and the other part is transformed into non-thermal energy. Shocks are thought to (re)accelerate electrons from the thermal distribution up to relativistic energies by the first-order Fermi diffusive shock acceleration mechanism (hereafter DSA, Bell 1987; Blandford & Eichler 1987). The accelerated electrons, in the presence of a magnetic field, may produce radio relics via synchrotron radio emission (Ferrari et al. 2008; Feretti et al. 2012; Brunetti & Jones 2014). They are generally Mpc-scale sized, elongated and steep-spectrum radio structures (Brüggen et al. 2012b; Brunetti & Jones 2014), which appear to be associated with the shock fronts at the outskirts of merging clusters (Finoguenov et al. 2010; Ogrean & Brüggen 2013c).

Discoveries of shocks coinciding with radio relics are increasing (Markevitch et al. 2005; Finoguenov et al. 2010; Macario et al. 2011; Ogrean & Brüggen 2013c; Bourdin et al. 2013; Eckert et al. 2016b; Sarazin et al. 2016; Akamatsu & Kawahara 2013a; Akamatsu et al. 2015, 2017). However, not all merging clusters present the same spatial distribution of the X-ray and radio components (Ogrean et al. 2014; Shimwell et al. 2016). The study of the radial distribution of these thermal and non-thermal components allows us to estimate the dynamical stage of the cluster as well as to understand how the shock propagates and heats the ICM. It can also determine the physical association between radio relics and shocks. The lack of connection between radio relics and shocks in several merging clusters, together with the low efficiency of DSA for $\mathcal{M} \sim 2$–3 of these shocks, seems to suggest that in some cases the DSA assumption is not enough for the electron acceleration from the thermal pool (Vink & Yamazaki 2014; Vazza & Brüggen 2014; Skillman et al. 2013; Pinzke et al. 2013). For this reason, alternative mechanisms have recently been proposed, such as for example, the re-acceleration of pre-existing cosmic ray electrons (Markevitch et al. 2005; Kang et al. 2012; Fujita et al. 2015; Fujita et al. 2016; Kang 2017) and shock drift acceleration (Guo et al. 2014a,b, 2017). However, it is not clear what type of mechanism is involved and whether all relics need additional mechanisms or not. Some merging clusters present different results, as for example 'El Gordo' (Botteon et al. 2016b) is consistent with the DSA mechanism. However, A3667 South (Storm et al. 2018), CIZA J2242.8+5301 (Hoang et al. 2017) and A3411-3412 (van Weeren et al. 2017) challenge the direct shock acceleration of electrons from the thermal pool. Therefore, it is not possible to provide a definitive explanation for these discrepancies.

In this paper, we analyze the spatial distribution of thermal and non-thermal components in Abell 3376, (hereafter A3376), based on *Suzaku* observations (Mitsuda et al. 2007). We have also used *XMM-Newton* and *Chandra* observations to support and confirm the results obtained with *Suzaku*. A3376 is a nearby (z = 0.046, Struble & Rood 1999), bright and moderately massive ($M_{200} \sim 4$–5×10^{14} $M_{\odot}$, Durret et al. 2013; Monteiro-Oliveira et al. 2017)

merging galaxy cluster. This merging system has two giant (∼Mpc) arc-shaped radio relics in the cluster outskirts, discovered by Bagchi et al. (2006). The radio observations (Bagchi et al. 2006; Kale et al. 2012; George et al. 2015), see Fig. 2.1, reveal complex radio structures at the western and eastern directions. In the west, A3376 shows a lowly polarized wide (∼300 kpc) relic with a non-aligned magnetic field (Kale et al. 2012). In the east, the relic is divided in three parts: the northern faint relic with steep spectral index; an elongated and polarized bright relic; and an additional 'notch' with a ∼500 kpc extension toward the center ($\alpha \sim$ –1.5) (Kale et al. 2012; Paul et al. 2011). Radio spectral index studies, assuming diffusive shock acceleration, with an estimated $\mathcal{M} \sim$ 2–3, which is consistent with the previous X-ray study by Akamatsu et al. (2012) of the western relic. A3376 includes two brightest cluster galaxies (BCG), coincident with two overdensities in projected galaxy distribution. BCG1 (ESO 307-13, $\mathrm{RA} = 6^{\mathrm{h}}00^{\mathrm{m}}41^{\mathrm{s}}10$, $\mathrm{Dec.} = -40^{\circ}02'40''00$) belongs to the west subcluster, while BCG2 (2MASX J06020973-3956597, $\mathrm{RA} = 6^{\mathrm{h}}02^{\mathrm{m}}09^{\mathrm{s}}70$, $\mathrm{Dec.} = -39^{\circ}57'05''00$) is located close to the X-ray peak emission at the east subcluster. The N-body hydrodynamical simulations of Machado & Lima Neto (2013) reproduce a bimodal merger system, with a mass ratio of 3–6:1, formed by one compact and dense subcluster, which crossed at high velocity and disrupted the core of the second massive subcluster ∼0.5–0.6 Gyr ago. This merger scenario was later corroborated by the optical analysis of Durret et al. (2013) and the weak lensing study of Monteiro-Oliveira et al. (2017).

For this study, we used the values of protosolar abundances ($Z_{\odot}$) reported by Lodders et al. (2009). The abundance of all metals are coupled to Fe. We used a Galactic absorption column of $N_{\mathrm{H,total}}$ = 5.6 × 10^{20} cm^{-2} (Willingale et al. 2013) for all the fits. We assumed cosmological parameters H_0 = 70 km/s/Mpc, Ω_{M} = 0.27 and Ω_{Λ}= 0.73, respectively, which give 54 kpc per 1 arcmin at z = 0.046. The virial radius is adopted as r_{200}, the radius where the mean interior density is 200 times the critical density at the redshift of the source. For our cosmology and redshift we used the approximation of Henry et al. (2009):

$$r_{200} = 2.77 h_{70}^{-1} (\langle kT \rangle / 10\ \mathrm{keV})^{1/2} / E(z)\ \mathrm{Mpc}, \tag{2.1}$$

where $E(z)$=$(\Omega_{\mathrm{M}}(1+z)^3 + 1 - \Omega_{\mathrm{M}})^{1/2}$, r_{200} is 1.76 Mpc (∼32.6′) with $\langle kT \rangle$ = 4.2 keV as calculated by Reiprich et al. (2013). All errors are given at 1σ (68 %) confidence level unless otherwise stated and all the spectral analysis made use of the modified Cash statistics (Cash 1979; Kaastra 2017a).

2.2 Observations and data reduction

Table 2.1 and Fig. 2.1 summarize the observations used for the present analysis. As shown in Fig. 2.1 six different *Suzaku* pointings have been used together with two additional *XMM-Newton* observations. Three of the *Suzaku* pointings are located in the central and western region (hereafter named as C, W1 and W2), which were obtained in 2005 and 2006, respectively. The other three observations (2013) cover the north (N), east (E), and south (S) of the outer eastern region. The combined observations cover the complete relic structures of A3376 as the western relic (W1 and W2), center (C) and eastern relic (N, E, and S). The total effective exposure time of the *Suzaku* data after screening and filtering of the cosmic-ray cut-off rigidity (COR2, Tawa et al. 2008) is ∼360 ks.

Table 2.1: Observations and exposure times.

Observatory	Name	Sequence ID	Pos. (J2000) (RA, Dec.)	Observation date	Exp.[a] (ks)	Exp.[b] (ks)
Suzaku	C	100043010	(90.56,-39.94)	2005-10-06	110.4	76.8
	W1	800011010	(90.05,-39.98)	2005-11-07	119.4	99.4
	W2	800011020	(90.04,-39.98)	2006-10-26	56.8	44.1
	N[c]	808029010	(90.64,-39.70)	2013-09-18	51.4	33.9
	E[c]	808028010	(90.81,-39.95)	2013-09-14	71.7	51.4
	S[c]	808030010	(90.61,-40.18)	2013-10-15	61.3	44.5
	Q0551 -3637	703036020	(88.19,-36.63)	2008-05-14	18.8	15.3
XMM-Newton	XMM-E	0151900101	(90.54,-39.96)	2003-04-01	47.2	33.1
	XMM-W	0504140101	(90.21,-40.03)	2007-08-24	46.1	40.8
Chandra	Chandra	3202	(90.54,-39.96)	2002-03-16	44.3	–

[a] *Suzaku* data screening without COR2, *XMM-Newton* and *Chandra* total exposure time
[b] *Suzaku* data screening with COR2 > 8 GV; *XMM-Newton* data screening
[c] Additional processing for XIS1

All observations have been performed with the normal 3x3 or 5x5 clocking mode of the X-ray imaging spectrometer (hereafter XIS, Koyama et al. 2007). This instrument had four active detectors: XIS0, XIS2 and XIS3 (front-side illuminated, FI) and XIS1 (back-side illuminated, BI). On November 9, 2006 the XIS2 detector suffered a micrometeorite strike[1] and was no longer operative. The XIS0 detector had a similar accident in 2010 and a part of the segment A was damaged[2]. In the same year the amount of charge injection for XIS1 was increased from 2 to 6 keV, which leads to an increase in the non-X-ray background (NXB) level of XIS1. For that reason an additional screening has been applied to minimize the NXB level following the process described in the *Suzaku* Data Reduction Guide [3].

We used HEAsoft version 6.20 and CALDB 2016-01-28 for all *Suzaku* analysis presented here. We have applied standard data screening with the elevation angle > 10° above the Earth and cut-off rigidity (COR2) > 8 GV to increase the signal to noise. The energy range of 1.7-1.9 keV was ignored in the spectral fitting owing to the residual uncertainties present in the Si-K edge.

For the point sources identification and exclusion, we used *XMM-Newton* observations (ID: 0151900101 and 0504140101, see Table 2.1). We applied the data reduction software SAS v14.0.0 for the *XMM-Newton* EPIC instrument with the task named $edetect\_chain$. We used visual inspection for the point sources identification beyond the *XMM-Newton* observations in the east. We derived the surface brightness (SB) profiles from the *XMM-Newton* and *Chandra* (ID: 3202, see Table 2.1) observations. We used CIAO 4.8 with CALDB 4.7.6

[1] http://www.astro.isas.ac.jp/suzaku/doc/suzakumemo/suzakumemo-degr 2007-08.pdf
[2] http://www.astro.isas.ac.jp/suzaku/doc/suzakumemo/suzakumemo- 2010-07v4.pdf
[3] https://heasarc.gsfc.nasa.gov/docs/suzaku/analysis/abc/node8.html

for the data reduction of *Chandra* observations. Moreover, the *Suzaku* offset observation of Q0551-3637, located at ∼4 degrees distance from A3376, was analyzed to estimate the sky background components as described in the following section.

2.3 Spectral analysis and results

2.3.1 Spectral analysis approach

In our spectral analysis of A3376, we have assumed that the observed spectra include the following components: optically thin thermal plasma emission from the ICM, the cosmic X-ray background (CXB), the local hot bubble (LHB), the Milky Way halo (MWH) and non X-ray background (NXB). We first generated the non X-ray background spectra using *xisnxbgen* (Tawa et al. 2008). Secondly, we identified the point sources present in our data using the two observations of *XMM-Newton* (see Table 2.1) and extracted them with a radius of 1–3′ from the *Suzaku* observations. We have estimated the sky background emission consisting of CXB, LHB, and MWH from the Q0551-3637 observation at 3.8° from A3376 (see Section 2.3.2). We assumed that the sky background component is uniformly distributed along the A3376 extension. We generated the redistribution matrix file (RMF) using *xisrmfgen* and the ancillary response file (ARF) with *xisimarfgen* (Ishisaki et al. 2007) considering a uniform input image (r = 20′).

A proper estimation of the background components is crucial, specially in the outskirts of galaxy clusters, where usually the X-ray emission of the ICM is low and the spectrum can be background dominated. The X-ray shock fronts and radio relics are usually located at these outer regions.

We performed a temperature deprojection assuming spherical symmetry to check the projection effect on the temperature profiles. We applied the method described in Blanton et al. (2003) for the post-shock regions, which are affected by projection of the emission of the outer and cooler regions. The results of the deprojection fits are consistent within 1σ uncertainties with the projected temperatures. For this reason, we used the projected fits in this work.

In our spectral analysis, we used SPEX[4] (Kaastra et al. 1996) version 3.03.00 with SPEX-ACT version 2.07.00. We carried out the spectral fitting in different annular regions as detailed in the sections below. The spectra of the XIS FI and BI detectors were fitted simultaneously and binned using the method of optimal binning (Kaastra & Bleeker 2016). For all the spectral fits, the NXB component is subtracted using the *trafo* tool in SPEX. The free parameters considered in this study are the temperature *kT*, the normalization *Norm* and the metal abundance Z for the inner regions $r \leq 9'$ of the ICM component. For the outer regions (r > 10′) we fixed the abundance to 0.3 $Z_{\odot}$ as explained by Fujita et al. (2008) and Urban et al. (2017).

[4]https://www.sron.nl/astrophysics-spex

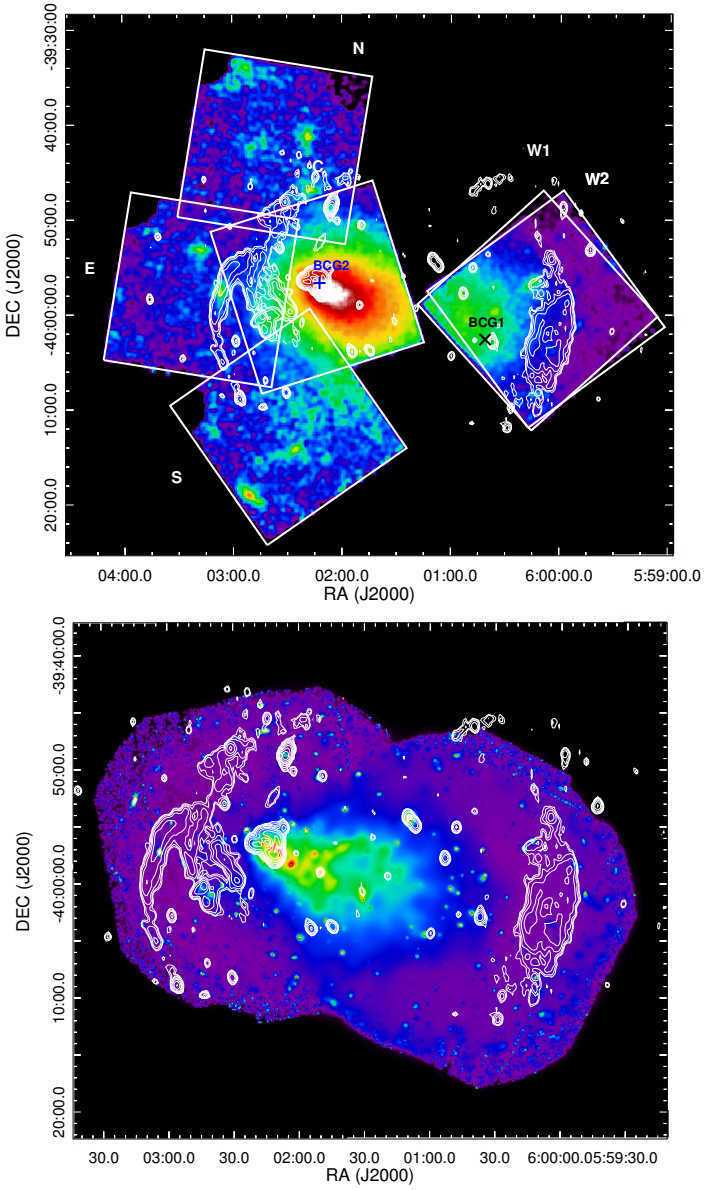

Figure 2.1: *Left*: *Suzaku* smoothed image in the 0.5–10 keV band of A3376 (pixel = 8″ and Gausssian 2-D smooth σ = 16″). The white boxes represent the *Suzaku* XIS FOVs for the C, W1, W2, N, E and S observations listed in Table 2.1. BCG1 is shown as a black cross and BCG2 as a blue cross. *Right*: *XMM-Newton* image in the 0.5–10 keV band of A3376. The white contours correspond to VLA radio observations kindly provided by Dr. R. Kale.

2.3.2 Estimation of the background spectra

The NXB component was obtained as the weighted sum of the XIS Night Earth observations and it was compiled for the same detector area and COR2 condition (COR2 > 8 GV) during 150 days before and after the observation date. In this way the long-term variation of the XIS detector background due to radiation damage can be constrained. The systematic errors corresponding to the NXB intensity are considered to be $\pm$ 3% (Tawa et al. 2008). For the most recent observations (E, N, and S), where a new spectral analysis approach was proposed for XIS1[5] because of the charge injection increase to 6 keV, we detected an excess of source counts in the high energy band (> 10 keV). We managed to compensate for this excess by increasing the NXB level by 13%. In this way the source level (ICM) follows the spectral shape of the CXB at high energies (see Fig. 2.2).

As mentioned in Sect. 2.2, the point source identification in the *Suzaku* FOV was realized using two *XMM-Newton* observations. The SAS task named $edetect\_chain$ was applied in four different bands (0.3–2.0 keV, 2.0–4.5 keV, 4.5–7.5 keV, and 7.5–12 keV) using EPIC pn and MOS data. We used a simulated maximum likelihood value of ten. After this, we combined the detections in these four bands and estimated the flux of each source in a circle with a radius of 0.6′. We established the minimum of flux detection of the extracted sources as $S_c = 10^{-17}$ W m^{-2} in the energy band 2–10 keV. Although this limit is lower than the level reported by Kushino et al. (2002) $S_c = 2 \times 10^{-16}$ W m^{-2}, we obtained an acceptable

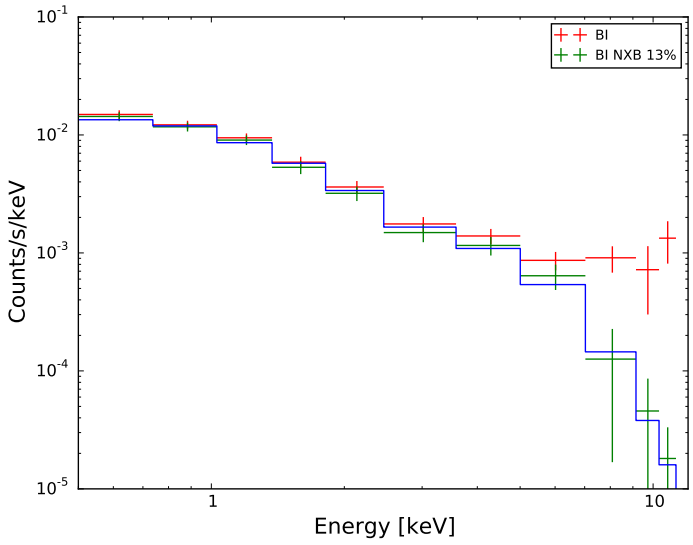

Figure 2.2: Correction of the XIS1 excess in the outer region of the E observation of A3376. The best-fit ICM spectrum is shown as a blue line. The *Suzaku* XIS BI spectra are shown without (red) and with (green) a 13% increase in the NXB level, respectively.

[5]https://heasarc.gsfc.nasa.gov/docs/suzaku/analysis/abc/node8.html

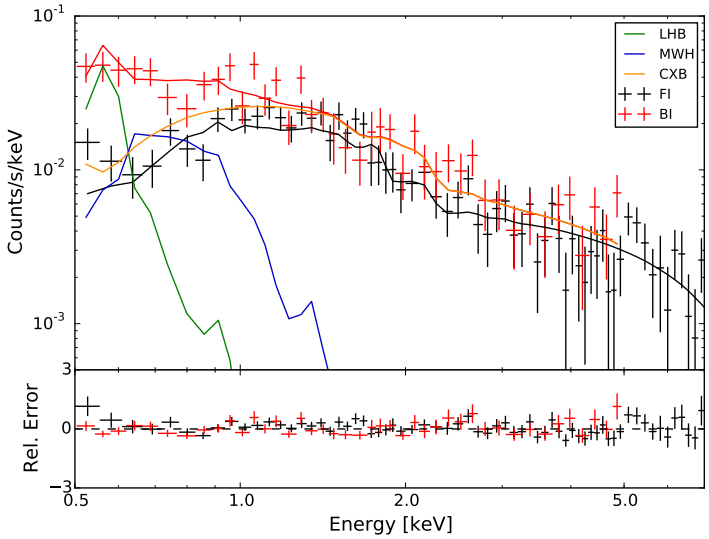

Figure 2.3: Q0551-3637 spectrum used for the sky background estimation. The *Suzaku* XIS FI, BI, the LHB, MWH and CXB components are shown in black, red, green, blue, and orange, respectively. The LHB, MWH, and CXB have been represented relative to the BI spectrum.

Table 2.2: Background components derived from the Q0551-3637 observation.

	LHB	MWH	CXB
Norm[a]	108 ± 21	2.9 ± 0.5	4.9 ± 0.4
kT (keV)	0.08 (fixed)	0.27 (fixed)	–
Γ	–	–	1.41 (fixed)
C-stat/d.o.f.		130/103	

[a] For LHB and MWH norm in units of 10^{71} m^{-3} scaled by 400π
For CXB norm in units of 10^{51} phs^{-1}keV^{-1}

$\log N - \log S$ distribution contained within the Kushino et al. (2002) limits (see their Fig. 20). We excluded in the *Suzaku* observations the identified point sources with a radius of 1 arcmin in order to account for the point spread function (PSF) of XIS (Serlemitsos et al. 2007). As a result, our CXB intensity after the point sources extraction for the 2–10 keV band was estimated as 5.98×10^{-11} W m^{-2} sr^{-1}. This value is within $\pm 10\%$ agreement with Cappelluti et al. (2017), Akamatsu et al. (2012) and Kushino et al. (2002).

As a sanity check, we compared the sky background level of ROSAT observations for the outermost region of A3376 (r = 30′-60′) and the offset pointing Q0551-3637 (r = 3′-

20′) using the HEASARC X-ray Background Tool[6] in the band R45 (0.4–1.2 keV). This band contains most of the emission of the sky background. The R45 intensities in the units of 10^{-6} counts/s/arcmin^2 are 125.3 ± 5.0 for the A3376 outer ring and 114.4 ± 18.5 for Q0551-3637. Both values are in good agreement.

We used the same S_c = 10^{-17} W m^{-2} for extracting the point sources in the offset *Suzaku* observation of Q0551-3637. We also excluded a circle of 3′ centered around the quasar with the same name, which is the brightest source of this region. Thereafter, we fitted the resultant spectra using N_H = 3.2 × 10^{20} cm^{-2} (Willingale et al. 2013), considering the emission of three sky background components at redshift zero and metal abundance of one. For the FI and BI detectors we used the energy ranges of 0.5–7.0 keV and 0.5–5.0 keV, respectively. The two Galactic components are modeled with: LHB (fixed *kT* = 0.08 keV), unabsorbed cie model (collisional ionization equilibrium in SPEX) and MWH (fixed *kT* = 0.27 keV), absorbed cie. The third component is the CXB modeled as an absorbed $powerlaw$ with fixed Γ = 1.41. The complete sky background model is:

$$cie_{\rm LHB} + abs * (cie_{\rm MWH} + powerlaw_{\rm CXB}). \tag{2.2}$$

Best-fit parameters are listed in Table 2.2, and the sky background components are shown in Fig. 2.3. For the calculation of the systematic uncertainties of the CXB fluctuation due to unresolved point sources ($\sigma/I_{\rm CXB}$) we have used Equation (3) proposed by Hoshino et al. (2010) in each spatial region of Fig. 2.4 and Fig. 2.7 as

$$\frac{\sigma}{I_{\rm CXB}} = \frac{\sigma_{\rm Ginga}}{I_{\rm CXB}} \left(\frac{\Omega_{\rm e}}{\Omega_{\rm e,Ginga}}\right)^{-0.5} \left(\frac{S_{\rm c}}{S_{\rm c,Ginga}}\right)^{0.25}, \tag{2.3}$$

where ($\sigma_{\rm Ginga}/I_{\rm CXB}$) = 5, $\Omega_{\rm e,Ginga}$ = 1.2 deg^2, $S_{\rm c,Ginga}$ = 6 × 10^{-15} W m^{-2}, S_c = 10^{-17} W m^{-2} and Ω_e is the effective solid angle of the detector. This way, we have included the effect of systematic uncertainties related to the NXB intensity (±3%, Tawa et al. 2008) and the CXB fluctuation, which varies between 8 to 27%. The contributions of these systematic uncertainties are shown in Fig. 2.5 and Fig. 2.8.

2.3.3 Spectral analysis along the western region

For the spectral analysis of the western region, we have analyzed several annular regions centered on the X-ray emission peak centroid ($\rm RA = 6^h02^m07^s66$, $\rm Dec. = -39°57'42''74$) once the point sources (see green circles in Fig. 2.4) have been excluded. The regions are a circle in the center with r = 2′ and annuli between 2′–4′, 4′–6′, 6′–9′, 13′–15′, 15′–17′, 17′–19′, 19′–21′, 21′–24′, 24′–27′, and 27′–31′. For all of them, the FI (used energy range 0.5–10 keV) and BI (0.5–7.0 keV) spectra have been fitted simultaneously. We analyzed the NXB subtracted spectra with the normalization *Norm*, temperature *kT* and metal abundance Z for the inner region $r \leq 9'$ as free parameters. The sky background components have been fixed to the values presented in Table 2.2.

The best-fit parameters are summarized in Table 2.3. In general, we obtained a good fit for all regions (C-stat/d.o.f. < 1.2). The resulting radial temperature profile is shown in Fig. 2.5. It includes in gray and blue the systematic uncertainties due to the CXB fluctuation

[6] https://heasarc.gsfc.nasa.gov/cgi-bin/Tools/xraybg/xraybg.pl

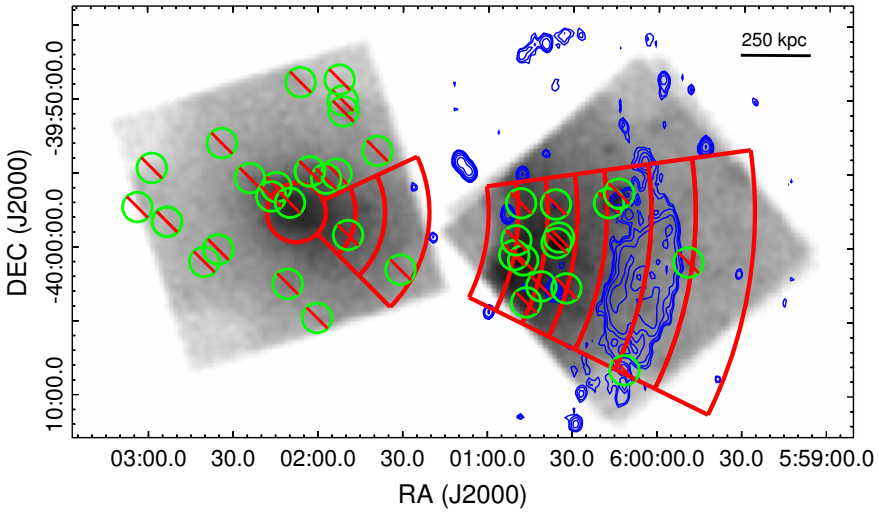

Figure 2.4: A3376 central and western observations in the band 0.5–10 keV. The blue contours represent VLA radio observations. The green circles represent the extracted points sources with r=1′. The red annular regions are used for the spectral analysis detailed in Table 2.3.

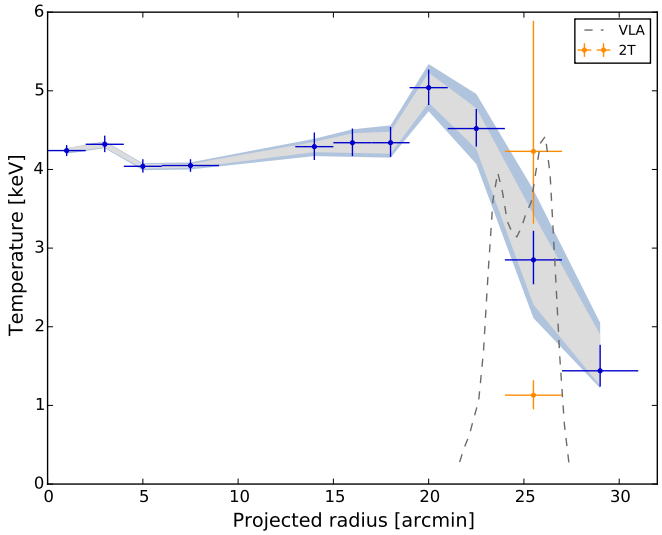

Figure 2.5: Radial temperature profile for the western region. The gray and blue area represent the CXB and NXB systematic uncertainties. The orange points show the 2T model temperatures at the western radio relic. The dashed gray line is the VLA radio radial profile.

Table 2.3: Best-fit parameters for the central and western regions shown in Fig. 2.4.

	Radius (′)	*kT* (keV)	*Norm* (10^{73} m^{-3})	Z ($Z_\odot$)	C-stat /d.o.f.
Center	1.0 ± 1.0	4.27 ± 0.07	7.92 ± 0.11	0.53 ± 0.04	803/793
	3.0 ± 1.0	4.32 ± 0.11	7.32 ± 0.16	0.51 ± 0.06	590/598
	5.0 ± 1.0	4.04 ± 0.09	6.32 ± 0.15	0.41 ± 0.05	634/606
	7.5 ± 1.5	4.05 ± 0.08	5.52 ± 0.09	0.39 ± 0.04	606/583
West	14.0 ± 1.0	4.29 ± 0.18	2.68 ± 0.08	0.3 (fixed)	327/337
	16.0 ± 1.0	4.34 ± 0.18	1.90 ± 0.06	0.3 (fixed)	415/415
	18.0 ± 1.0	4.34 ± 0.19	1.41 ± 0.04	0.3 (fixed)	451/448
	20.0 ± 1.0	5.04 ± 0.23	0.90 ± 0.02	0.3 (fixed)	690/656
	22.5 ± 1.5	4.52 ± 0.24	0.42 ± 0.01	0.3 (fixed)	796/752
	25.5 ± 1.5	2.85 ± 0.34	0.15 ± 0.01	0.3 (fixed)	670/576
	29.0 ± 2.0	1.44 ± 0.27	0.03 ± 0.01	0.3 (fixed)	329/244

Table 2.4: Best-fit parameters for the pre- and post-shock regions at the western relic shown in Fig. 2.6.

	kT (keV)	*Norm* (10^{71} m^{-3})	C-stat/d.o.f.
Post	4.22 ± 0.26	27.7 ± 1.0	680/654
Pre	1.27 ± 0.29	2.3 ± 0.8	638/516

and NXB, respectively, as mentioned above. The radial profile shows an average temperature of ∼4 keV in the central region of the cluster as found earlier by De Grandi & Molendi (2002), Kawano et al. (2009) and Akamatsu et al. (2012). At r = 20′ the temperature increases slightly to ∼5 keV and drops smoothly to ∼1.4 keV beyond the western radio relic. Although there is a temperature decrease, there is not a clear discontinuity in the temperature at the radio relic. One possible explanation is that the annular region at r = 24′–27′ contains gas from the pre and post relic region, which have two different temperatures. In order to investigate this aspect we included a second cie model in this region. As a result, we obtained two distinct temperatures: kT_1 = 4.2 ± 1.3 keV and kT_2 = 1.1 ± 0.2 keV (see orange points in Fig. 2.5) which are consistent with adjacent regions indicating the presence of multi-temperature structure within the extraction region. Therefore, this could be a preliminary indication of a temperature jump in the radio relic area and the possible presence of a shock front.

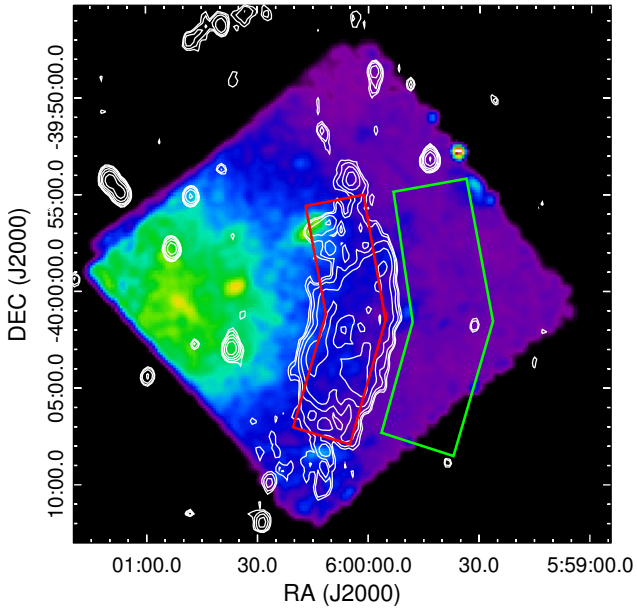

Figure 2.6: A3376 W1 and W2 NXB subtracted images in the band 0.5-10 keV. The white contours correspond to VLA radio observations. The green and red polygonal regions are the pre and post-shock regions of the western radio relic, respectively.

As a next step, we defined two additional regions in order to obtain the temperature upstream and downstream of the possible X-ray shock (Fig. 2.6). We introduced a separation of ∼1′ between pre and post-shock region to avoid a possible photon leakage from the brighter region due to limited PSF of XRT (Akamatsu et al. 2015, 2017). The pre-shock region is located beyond the radio relic edge (the green polygonal region in Fig. 2.6) and the post-shock region is inside the radio relic edge (the red polygonal region in Fig. 2.6). The resulting best-fit parameters for these pre and post-shock regions are shown in Table 2.4 and the spectrum of the post-shock region is shown in Fig. 2.9. In this new analysis, the temperature shows a significant drop from $kT_{\rm post}$ = 4.22 ± 0.26 keV to $kT_{\rm pre}$ = 1.27 ± 0.29 keV. These ICM temperatures of the pre and post-shock regions agree with previous *Suzaku* results ($kT_{\rm post}$ = $4.68^{+0.42}_{-0.24}$ to $kT_{\rm pre}$ = 1.34 ± 0.42 keV, Akamatsu et al. 2012). We discuss the shock properties related to the western radio relic in Sect. 2.4.3.

2.3.4 Spectral analysis along the eastern region

In the spectral analysis of the eastern region we have studied three different directions: N, E, and S, corresponding to the observations with the same names (see Table 2.1). We used annular regions, with the same centroid as the western region ($\mathrm{RA} = 6^{\mathrm{h}}02^{\mathrm{m}}07^{\mathrm{s}}66$, $\mathrm{Dec.} = -39°57'42''74$), between 2′–4′, 4′–6′, 6′–9′, 9′–12′, 12′–16′ and 16′–20′. Figure 2.7 shows green regions for N, blue regions for E and red regions for S. We fit the FI (0.7–7.0 keV) and BI (0.7–5.0 keV) spectra simultaneously. We applied the same criteria for the background components and the ICM definition as explained above for the western regions. The best-fit parameters for east, north, and south are summarized in Table 2.5, 2.6, and 2.7, respectively. In general we obtained a good fit with C-stat/d.o.f. < 1.1 for E and S, and C-stat/d.o.f. < 1.25 for N. Figure 2.8 shows the radial temperature profile for the three directions. In general, the statistical errors in our data are larger than or of the same order of magnitude as the systematic errors.

The radial temperature profile in the E direction shows a slight increase of the temperature at the center followed by a temperature gradient until ∼1 keV in the cluster outer region. Motivated by a surface brightness discontinuity found at $r \sim 8'$ explained in Sec. 2.4.2, we then analyzed a pre-shock (green annular) and post-shock (red annular) region (see Fig. 2.10). The best-fit parameters show a decrease from kT_{post} = 4.71 keV to kT_{pre} = 3.31 keV (Table 2.8). The spectrum of the post-shock region is shown in Fig. 2.9. These ICM temperatures are consistent with the ones estimated in the eastern annular regions at r = 6–9′ and r = 9–12′.

For the N direction, we divided the annular regions in two ($\mathrm{N_a}$: 350-22.5° and $\mathrm{N_b}$: 22.5-55°) sections to investigate possible azimuthal differences. After the spectral analysis we could not find any significant difference between both sides. Therefore, we have analyzed the full annular regions as shown in Fig. 2.7. The temperature increases up to ∼5 keV at r = 7.5′ and decreases till ∼1 keV in the cluster outskirts. We investigated pre and post-shock regions at r = 8′, similar to the case of the eastern direction to analyze the extent of the eastern shock, and there are no signs of a temperature drop.

In the S direction, we obtain a radial temperature profile with a central temperature of ∼4 keV and a smooth decrease down to the cluster peripheries. It follows the predicted trend for relaxed galaxy clusters as described by Reiprich et al. (2013). We discuss this behavior in more detail in Sect. 2.4.1.

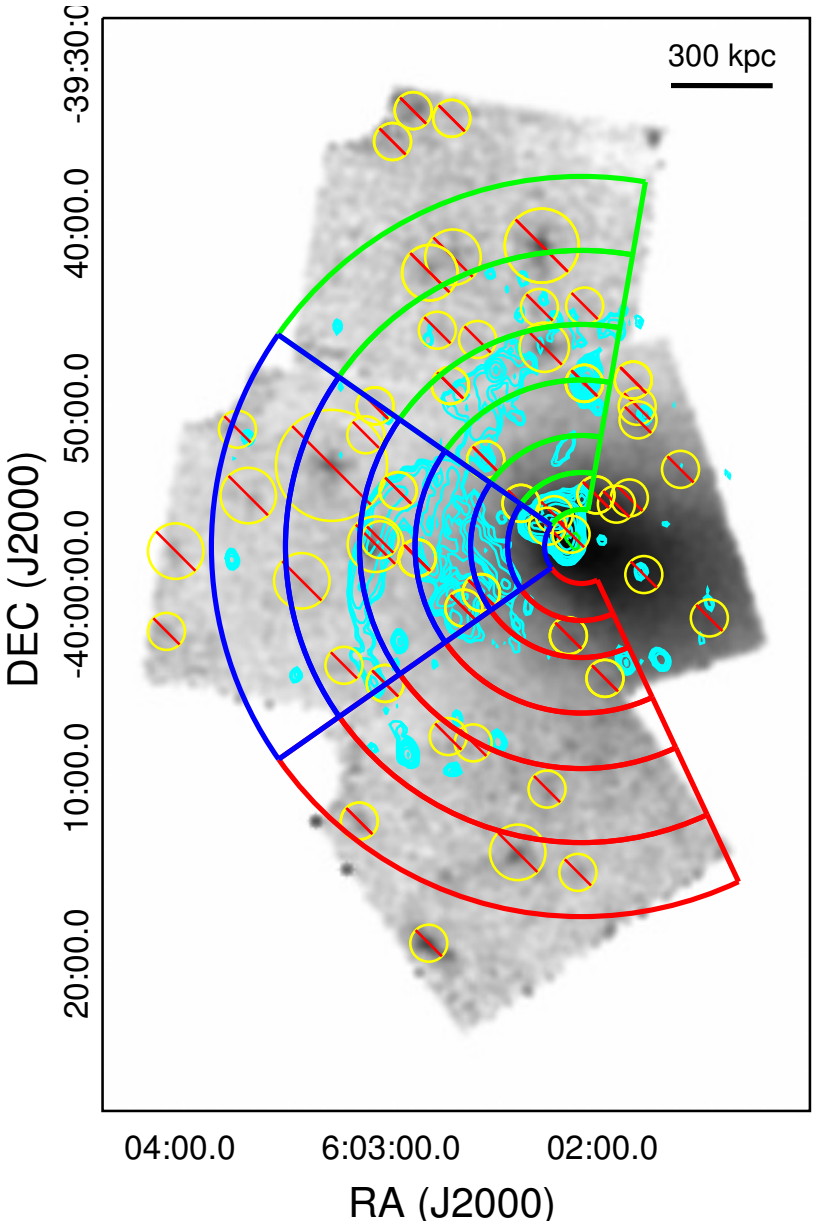

Figure 2.7: A3376 center, north, east, and south images in the band 0.5–10 keV. The cyan contours represent VLA radio observations. The yellow circles represent the extracted points sources. The green (north), blue (east) and red (south) annular regions are used for the spectral analysis detailed in Tables 2.6, 2.5, and 2.7, respectively.

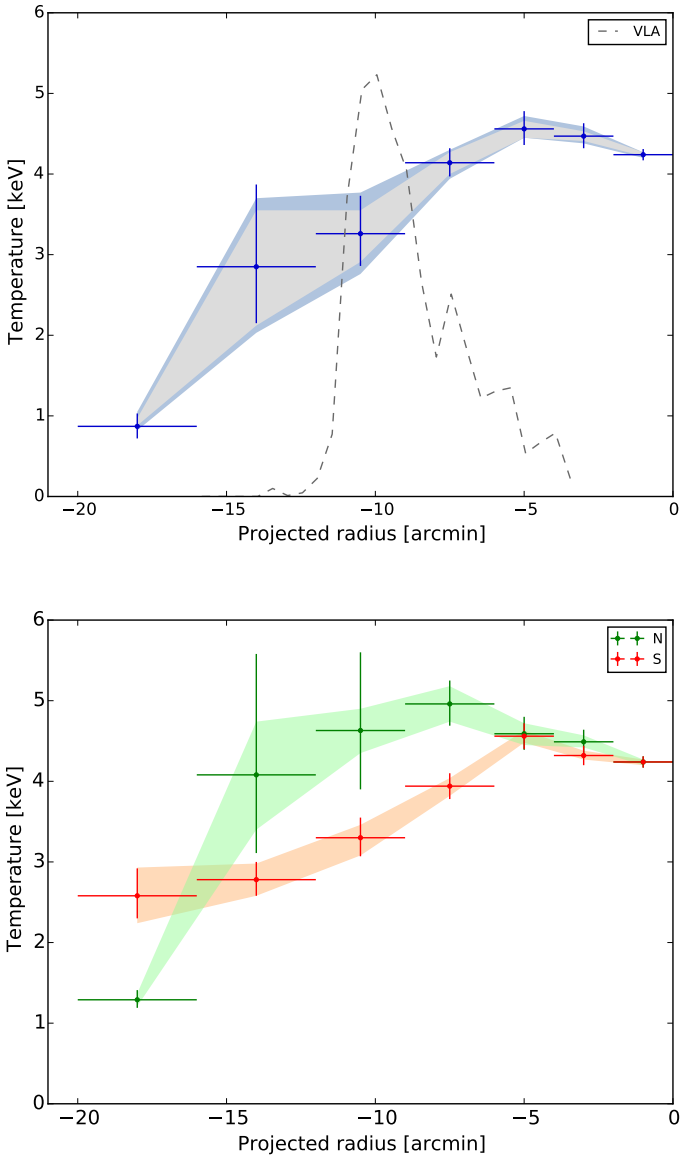

Figure 2.8: Radial temperature profile for the eastern region (top is east and bottom is north and south). Top: Gray and blue areas represent the CXB and NXB systematic uncertainties. The dashed gray line is the VLA radio radial profile. Bottom: Green and red areas represent the CXB and NXB systematic uncertainties for north and south, respectively.

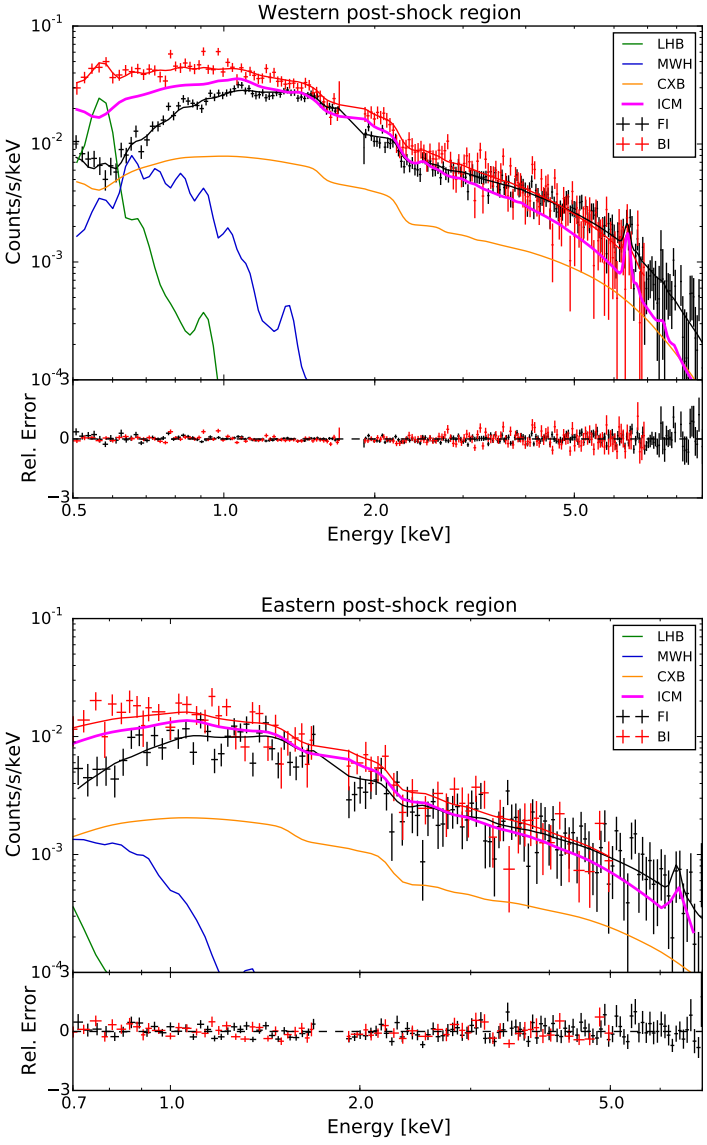

Figure 2.9: Left: NXB-subtracted spectrum of western post-shock region in the 0.5–10 keV band. Right: eastern post-shock spectrum in the 0.7–7.0 keV band. The FI (black) and BI (red) spectra are fitted with the ICM model together with the CXB and Galactic emission. The ICM is shown in magenta. The LHB, MWH and CXB are represented by green, blue and orange curves, respectively. The ICM, LHB, MWH, and CXB has been represented relative to the BI spectrum.

Table 2.5: Best-fit parameters for the center and east regions shown in Fig. 2.7.

	Radius (′)	*kT* (keV)	*Norm* (10^{73} m^{-3})	Z ($Z_\odot$)	C-stat/d.o.f.
Center	3.0 ± 1.0	4.47 ± 0.16	4.11 ± 0.11	0.33 ± 0.06	491/451
	5.0 ± 1.0	4.56 ± 0.21	1.96 ± 0.06	0.25 ± 0.07	361/340
C&E	7.5 ± 1.5	4.14 ± 0.18	0.95 ± 0.03	0.34 ± 0.08	661/630
East	10.5 ± 1.5	3.26 ± 0.44	0.36 ± 0.02	0.3 (fixed)	258/266
	14.0 ± 2.0	2.85 ± 0.86	0.12 ± 0.02	0.3 (fixed)	170/169
	18.0 ± 2.0	0.87 ± 0.16	0.02 ± 0.01	0.3 (fixed)	180/196

Table 2.6: Best-fit parameters for the center and north regions shown in Fig. 2.7.

	Radius (′)	*kT* (keV)	*Norm* (10^{73} m^{-3})	Z ($Z_\odot$)	C-stat/d.o.f.
Center	3.0 ± 1.0	4.49 ± 0.15	3.81 ± 0.09	0.38 ± 0.06	522/509
	5.0 ± 1.0	4.59 ± 0.21	1.73 ± 0.05	0.40 ± 0.09	331/363
	7.5 ± 1.5	4.96 ± 0.28	0.94 ± 0.03	0.36 ± 0.11	343/327
North	10.5 ± 1.5	4.63 ± 0.85	0.48 ± 0.04	0.3 (fixed)	129/118
	14.0 ± 2.0	4.08 ± 1.24	0.17 ± 0.02	0.3 (fixed)	126/157
	18.0 ± 2.0	1.29 ± 0.11	0.12 ± 0.02	0.3 (fixed)	192/173

Table 2.7: Best-fit parameters for the center and south regions shown in Fig. 2.7.

	Radius (′)	*kT* (keV)	*Norm* (10^{73} m^{-3})	Z ($Z_\odot$)	C-stat/d.o.f.
Center	3.0 ± 1.0	4.32 ± 0.12	5.04 ± 0.11	0.38 ± 0.06	578/559
	5.0 ± 1.0	4.56 ± 0.16	3.18 ± 0.08	0.47 ± 0.07	396/399
	7.5 ± 1.0	3.94 ± 0.16	1.82 ± 0.05	0.25 ± 0.07	326/359
South	10.5 ± 1.5	3.30 ± 0.24	0.66 ± 0.03	0.3 (fixed)	386/370
	14.0 ± 2.0	2.78 ± 0.21	0.44 ± 0.02	0.3 (fixed)	271/251
	18.0 ± 2.0	2.58 ± 0.31	0.25 ± 0.02	0.3 (fixed)	204/213

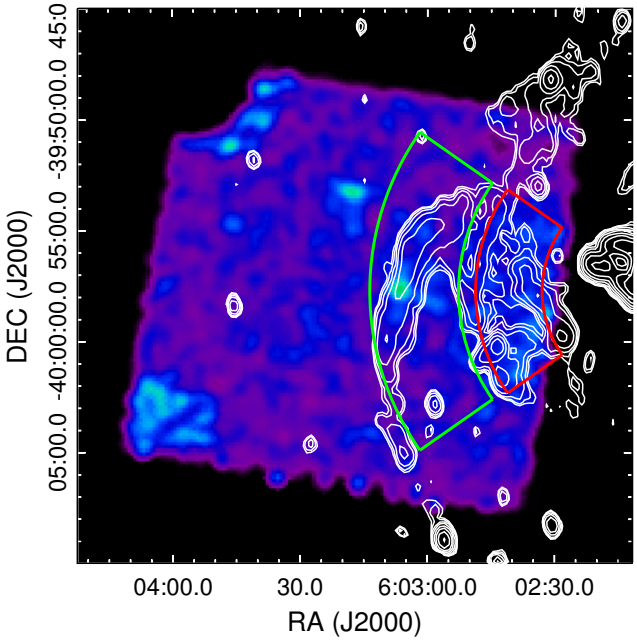

Figure 2.10: A3376 East NXB subtracted images in the band 0.5–10 keV. The white contours correspond to VLA radio observations. The green and red annular regions are the pre and post-shock regions of the eastern and northern radio relic, respectively.

Table 2.8: Best-fit parameters for the pre- and post-shock regions at the east region shown in Fig. 2.10.

	kT (keV)	*Norm* (10^{72} m^{-3})	C-stat/d.o.f.
Post	4.71 ± 0.42	11.7 ± 0.1	192/187
Pre	3.31 ± 0.44	3.2 ± 0.2	182/173

2.4 Discussion of spectral analysis

2.4.1 ICM temperature profile

The main growing mechanism of galaxy clusters includes the accretion and merging of the surrounding galaxy groups and subclusters. These processes are highly energetic and turbulent, being able to modify completely the temperature structure of the ICM (Markevitch & Vikhlinin 2007). Therefore, this temperature structure contains the signatures of how the cluster has evolved, providing relevant information on the growth and heating history.

There are fewer studies about merging galaxy clusters and the impact of the above

events to the ICM temperature structure then about relaxed clusters. A recent compilation of *Suzaku* observations shows the temperature profile up to cluster outskirts (Reiprich et al. 2013). That review shows that relaxed clusters have a similar behavior near r_{200} and that the temperature can smoothly drop by a factor of three at the periphery. Moreover, these *Suzaku* data are consistent with the ICM temperature model of relaxed galaxy clusters proposed by Burns et al. (2010).

Burns et al. (2010) obtained this 'universal' profile model based on N-body plus hydrodynamic simulations for relaxed clusters. The scaled temperature profile as a function of normalized radius is given by:

$$\frac{T}{T_{\rm avg}} = A\left[1 + B\left(\frac{r}{r_{200}}\right)\right]^{\beta}, \tag{2.4}$$

where the best-fit parameters are A = 1.74 $\pm$ 0.03, B = 0.64 $\pm$ 0.10 and β = -3.2 $\pm$ 0.4. $T_{\rm avg}$ is the average X-ray weighted temperature between 0.2–1.0r_{200}.

In Fig. 2.11 we compare Burns' radial profile with the radial temperature profile of A3376 normalized with $\langle kT \rangle$ = 4.2 keV ($\langle kT_x \rangle$ up to 0.3r_{200}, Reiprich et al. 2009) and $r_{200} \sim$ 1.76 Mpc derived from Henry et al. (2009). The western direction shows an enhancement of the temperature compared with the relaxed profile and a sharp drop close to $\sim$0.7r_{200}. This is a hint for the presence of a shock front and shock heating of the ICM at these radii. A similar, but

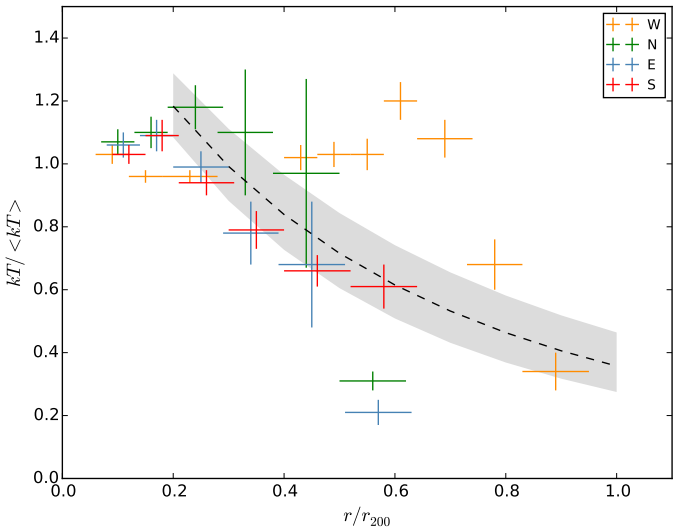

Figure 2.11: Normalized radial temperature profile of A3376 compared with relaxed clusters. The dashed line represents the Burns et al. (2010) universal profile and the gray area shows its standard deviation. The orange, green, blue and red crosses are the scaled data for the west, north, east, and south directions, respectively. We have shifted these scaled data of the different directions in r/r_{200} for clarity purpose.

less pronounced, behavior is found for the north and east, being the temperature excess higher for the north. In both cases, the temperature shows a decrease around $\sim$0.3r_{200}, where the eastern radio relic is located, with a steeper temperature profile than relaxed clusters. In the north, the large statistical errors and the weakness of the signal limit the detection of a temperature jump, and therefore, the possible evidence for a shock front. Deeper observations are needed to constrain this temperature structure in more detail. On the other hand, the southern direction seems to follow the profile of relaxed clusters. This is expected because there is no radio emission in this direction.

2.4.2 X-ray surface brightness profiles

In order to confirm the evidence of bow shocks at the western and eastern regions, we analyzed the radial X-ray surface brightness profile from the center of A3376 using the *XMM-Newton* observations. The SB was determined in the 0.3-2.0 keV band excluding the Al line at $\sim$1.5 keV. Point sources with a flux higher than $S_c = 10^{-17}$ W m^{-2} were removed (for more details see Sect. 2.3.2) and the X-ray image was corrected for exposure and background. The sky background components derived from Q0551-3637 (see Table 2.2) have been adopted together with the instrumental background for the background correction. The surface brightness profile was extracted in circular pie shaped sectors (see sectors in Fig. 2.12) and fitted with PROFFIT v1.4[7] (Eckert et al. 2011). We adopted a broken power-law density profile to describe the SB profile. Therefore, assuming spherical symmetry, the density distribution is given by

$$\begin{cases} n_2(r) = n_0 \left(\frac{r}{r_{\rm sh}}\right)^{-\alpha_2} & r \leq r_{\rm sh} \\ \\ n_1(r) = \frac{1}{C} n_0 \left(\frac{r}{r_{\rm sh}}\right)^{-\alpha_1} & r > r_{\rm sh} \end{cases} \tag{2.5}$$

where n_0 is the model density normalization, α_1 and α_2 are the power-law indices, r is the radius from the center of the sector and $r_{\rm sh}$ is the shock putative distance. At the location of the SB discontinuity n_2, the post-shock (downstream) density is higher by a factor of $C = n_2/n_1$ compared with n_1, pre-shock (upstream) density. This factor C is known as the compression factor. In the X-ray SB fitting, we left all these model parameters free to vary.

The radial SB profile across the western radio relic is shown in Fig. 2.13. The SB was accumulated in circularly shaped sectors to match the outer edge of the radio relic from an angle of 230° to 280° (measured counter-clockwise) for r = 21–28′. The data were rebinned to reach a minimum signal-to-noise ratio (S/N) of four. The best-fitting broken power-law model is shown as the blue line with C-stat/d.o.f. $\sim$ 1.2. It presents a break inside the radio relic at $r_{\rm sh} \sim 23'$ (measured from the X-ray emission peak centroid) and the compression factor is $C = 1.9 \pm 0.4$. If we apply the PSF modeling of *XMM-Newton* as described in Appendix C of Eckert et al. (2016a) for a more accurate estimate of the density profile, then the density jump increases to $C = 2.1 \pm 0.6$. We have additionally evaluated different elliptical shaped sectors to adjust them to the relic shape. They have eccentricities

[7] http://www.isdc.unige.ch/ deckert/newsite/Proffit.html

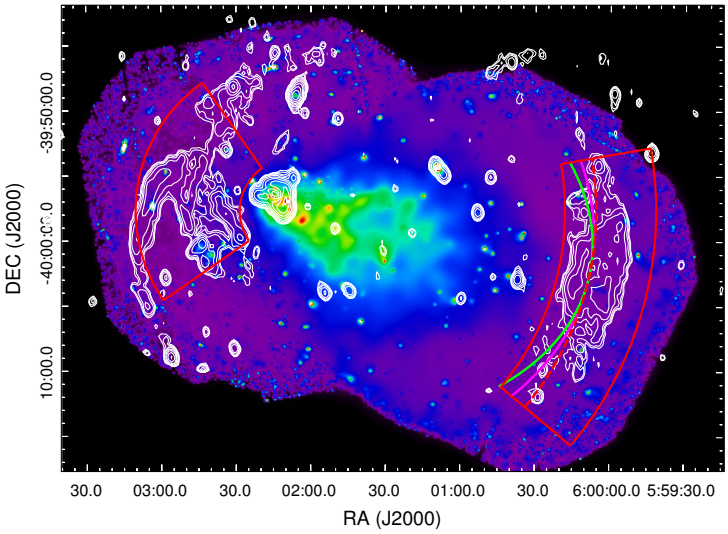

Figure 2.12: *XMM-Newton* image in the 0.5–10 keV band of A3376. The white contours correspond to VLA radio observations. The red sectors are used to extract the X-ray SB profile in the E and W directions. The dashed red line represents the circular (ε = 0) shaped sector used for the SB profiles. The magenta and green lines are the elliptical shaped sectors with ε = 0.60 and ε = 0.73, respectively.

of ε = 0.6 and ε = 0.73. The compression factors obtained in both cases are lower than for the circular sector, C = 1.7 $\pm$ 0.3 and C = 1.5 $\pm$ 0.4, respectively. The different radii for the SB discontinuity compared with the temperature jump could be caused by the *Suzaku* PSF $\sim$ 2′.

The obtained value of C = 2.1 $\pm$ 0.6 is consistent within the 1σ uncertainty bounds with the value in Table 2.9, C = 2.9 $\pm$ 0.3, although it shows a slightly lower value. This could possibly be explained because of the difficulty to model the multi-component background in the lack of any sky region where it cannot be spatially separated from the ICM. Therefore, the background modeling can play also an important role in the SB profiles located at the outskirts. Future observations with the *Athena* satellite could provide an explanation to this issue.

We obtained the radial SB profile along the E direction for circular sectors between 35° to 125° with the center at the X-ray emission peak. The data were rebinned to have a minimum S/N $\sim$ 8. For radii larger than 12′ the SB emission is low and is background dominated. For this reason, we selected the range 4–12′ for the fitting. The best-fitting broken power-law model is shown in Fig. 2.14 as a blue line with C-stat/d.o.f. $\sim$ 1.4. The SB profile contains an edge at $r \sim 8'$ and the compression factor is C = 1.9 $\pm$ 0.5, after applying the same PSF modeling as for the western SB profile. Because the radial profile of the radio relic azimutally averages various features (see VLA radio contours in Fig. 2.10 and 2.12), this edge appears to be located ahead of a secondary peak in the radio relic profile. It seems to be associated to the 'notch' described by Paul et al. (2011) and Kale et al. (2012).

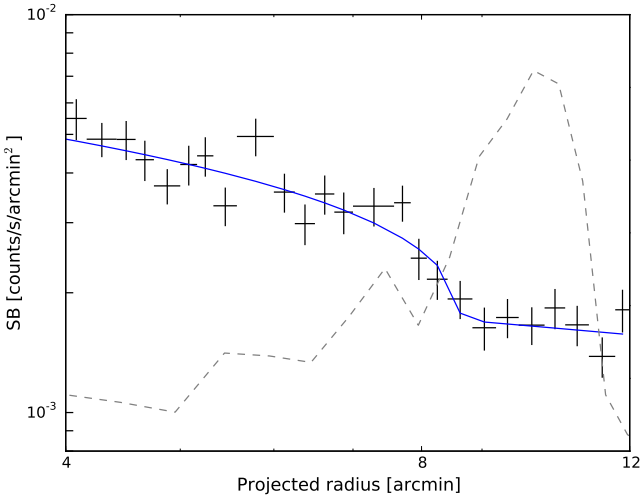

Figure 2.13: Radial X-ray surface brightness profile across the western radio relic in the 0.3–2.0 keV band using *XMM-Newton* observations. The profile is corrected for vignetting and background level, and point sources have been removed. The solid blue curve is the best-fit model and the gray dashed line is the VLA scaled radio emission. The data were rebinned to reach a minimum S/N of four and C-stat/d.o.f. ~ 1.2

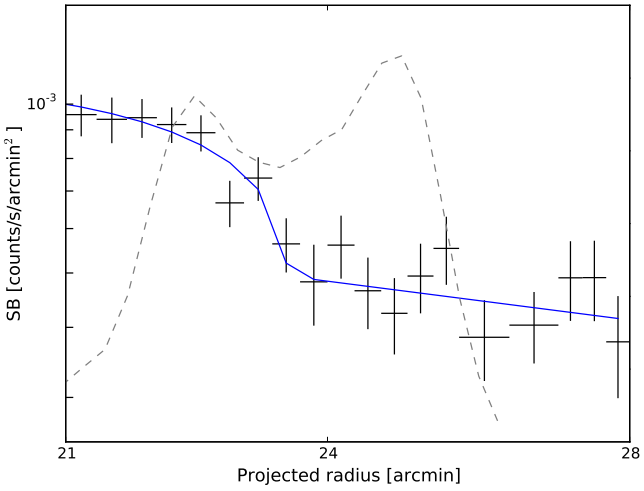

Figure 2.14: Radial X-ray surface brightness profile across the eastern radio relic in the 0.3–2.0 keV band using *XMM-Newton* observations. Same as Fig. 2.13, with a minimum S/N of eight and C-stat/d.o.f. ~ 1.4.

2.4.3 Shock jump conditions and properties

The density (surface brightness) and temperature discontinuities found along the western and eastern directions form evidence for a shock front co-spatial with the western relic (Fig. 2.13 and Table 2.4) and the 'notch' radio structure in the east (Fig. 2.14 and Table 2.8), respectively. Here, we calculate the shock properties in the western and eastern directions based on our *Suzaku* observations. The Mach number ($\mathcal{M}$) and compression factor (C) can be assessed from the Rankine-Hugoniot jump condition (Landau & Lifshitz 1959) assuming that all of the dissipated shock energy is thermalized and the ratio of specific heats (the adiabatic index) is γ = 5/3:

$$\frac{T_2}{T_1} = \frac{5\mathcal{M}^4 + 14\mathcal{M}^2 - 3}{16\mathcal{M}^2}, \tag{2.6}$$

$$C = \frac{n_2}{n_1} = \frac{4\mathcal{M}^2}{\mathcal{M}^2 + 3}, \tag{2.7}$$

where n is the electron density, and the indices 2 and 1 corresponds to post-shock and pre-shock regions, respectively. Table 2.9 shows the Mach numbers and compression factors derived from the observed temperature jumps. The Mach numbers are in good agreement with the simulations of Machado & Lima Neto (2013) and $\mathcal{M}_{\rm W}$ is consistent with previous *Suzaku* results obtained by Akamatsu et al. (2012) ($\mathcal{M}_{\rm W}$ = 3.0 $\pm$ 0.5). The Mach numbers estimated from the surface brightness discontinuities described in the previous sections are $\mathcal{M}_{\rm W_{SB}} \sim$ 1.3–2.5 and $\mathcal{M}_{\rm E_{SB}} \sim$ 1.7 $\pm$ 0.4. Both values are consistent with the value present in Table 2.9 within 1σ error. The presence of shocks with $\mathcal{M} \gtrsim 3.0$ is uncommon in galaxy clusters, only four other clusters have been found with such a high Mach number ('El Gordo', Botteon et al. 2016b; A665, Dasadia et al. 2016a; CIZA J224.8+5301, Akamatsu et al. 2015; 'Bullet', Shimwell et al. 2015).

The sound speed at the pre-shock regions is $c_{\rm s,W} \sim$ 570 km s^{-1} and $c_{\rm s,E} \sim$ 940 km s^{-1}, assuming $c_{\rm s} = \sqrt{\gamma k T_1 / \mu m_p}$ where μ = 0.6. The shock propagation speeds $v_{\rm shock} = \mathcal{M} \cdot c_{\rm s}$ for the western and eastern directions are $v_{\rm shock,W} \sim$ 1630 $\pm$ 220 km s^{-1} and $v_{\rm shock,E} \sim$ 1450 $\pm$ 150 km s^{-1}, respectively. These velocities are consistent with previous work for A3376 W (Akamatsu et al. 2012). However, the shock velocities are smaller than in other galaxy clusters with $\mathcal{M} \sim$ 2–3 as the Bullet cluster (4500 km s^{-1}, Markevitch et al. 2002), CIZA J2242.8+530 (2300 km s^{-1}, Akamatsu et al. 2017) and A520 (2300 km s^{-1}, Markevitch et al. 2005).

We have compiled the shock velocities, $v_{\rm shock}$, for several merging galaxy clusters as shown in Fig. 2.15. Black points represent data taken directly from the literature and the gray points are calculated from $\mathcal{M}$ and kT_1. Blue and red crosses are the western and eastern shock velocities, respectively. Figure 2.15 shows shock velocities as a function of average temperature of the system. To investigate the origin of driving force of the shock structure, we have examined a prediction from self-similar relationship: $v_{\rm shock} = A * \langle kT \rangle^{(3/2)} + B$, where A = 70 $\pm$ 16 and B = 550 $\pm$ 270, see orange line. As we expected, most of samples can be explained with this formula, which means that the main driving force of the merging activity is the gravitational potential of the system and no additional physics. Further sam-

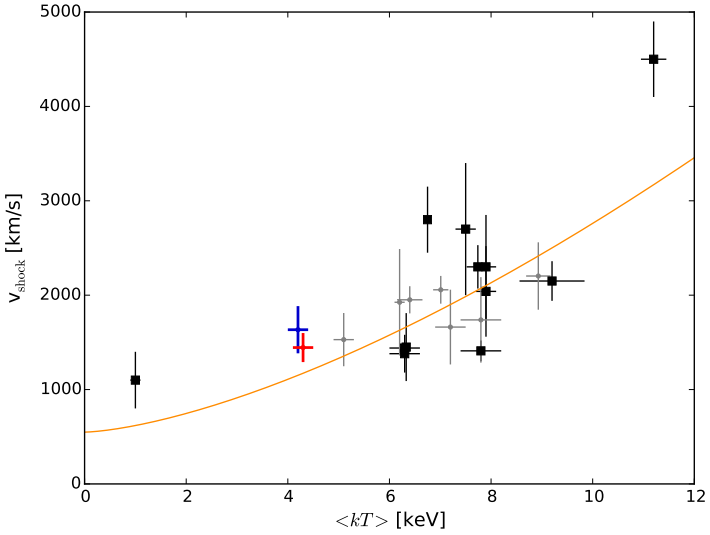

Figure 2.15: $v_{\rm shock}$ correlation with $\langle kT \rangle$. The orange line is the best-fit for $v_{\rm shock} = A * \langle kT \rangle^{(3/2)} + B$. Black crosses represent data taken directly from the literature (Akamatsu & Kawahara 2013a; Akamatsu et al. 2015, 2017; Dasadia et al. 2016a; Eckert et al. 2016b; Markevitch et al. 2002, 2005; Russell et al. 2012, 2014; Sarazin et al. 2016). Gray points are the calculated data from $\mathcal{M}$ and kT_1 (Botteon et al. 2016a; Bourdin et al. 2013; Macario et al. 2011; Ogrean & Brüggen 2013c; Owers et al. 2014; Sarazin et al. 2016; Trasatti et al. 2015) as explained in the text. Blue and red crosses correspond to the W and E shocks of A3376 as obtained in this work, respectively.

ple of shocks and proper gravitational mass estimates will enable us to extend this type of examination.

2.4.4 Mach number from X-ray and radio observations

After the first confirmation by Finoguenov et al. (2010) of a clear correlation between X-ray shock fronts and radio relics in A3667, many other observations have revealed a possible relation between them (Macario et al. 2011; Mazzota et al. 2011; Akamatsu & Kawahara 2013a). As explained in the introduction, the X-ray shock fronts may accelerate charged particles up to relativistic energies via diffusive shock acceleration (DSA, Drury 1983; Blandford & Eichler 1987), which in the presence of a magnetic field can generate synchrotron emission. The acceleration efficiency of this mechanism is low for shocks with $\mathcal{M} < 10$ and might not be sufficient to produce the observed radio spectral index (Kang et al. 2012; Pinzke et al. 2013). Therefore, alternative scenarios have been proposed like the presence of a fossil population of non-thermal electrons and re-acceleration of these electrons by shocks (Bonafede et al. 2014; van Weeren et al. 2017) or the electron re-acceleration by turbulence (Fujita et al. 2015; Kang 2017).

Table 2.9: Shock properties at the western and eastern radio relics.

	T_2 (keV)	T_1 (keV)	Mach No. $\mathcal{M}$[a]	$v_{\rm shock}$ (km s^{-1})[b]
W	4.22 ± 0.26	1.27 ± 0.29	2.8 ± 0.4	1630 ± 220
E	4.71 ± 0.42	3.3 1± 0.44	1.5 ± 0.1	1450 ± 150

	Compression C[c]	Power-law slope p[d]	Spectrum index α[e]
W	2.9 ± 0.3	2.58 ± 0.22	–0.79 ± 0.11
E	1.8 ± 0.1	4.92 ± 0.85	–1.96 ± 0.43

[a] $\mathcal{M}$ is obtained from Eq. (2.6).
[b] $v_{\rm shock} = \mathcal{M} \cdot c_{\rm s}$, $c_{\rm s} = \sqrt{\gamma k T_1/\mu m_p}$
[c] C from Eq. (2.7).
[d] $p = (C + 2)/(C - 1)$
[e] $\alpha = -(p-1)/2$

DSA is based on first order Fermi acceleration, considering that there is a stationary and continuous injection, which accelerates relativistic electrons following a power-law spectrum $n(E)dE \sim E^{-p}dE$ with $p = (C + 2)/(C - 1)$, $\alpha = -(p-1)/2$ where p is the power-law index and α is the radio spectral index for $S_\nu \propto \nu^\alpha$. The radio Mach number can be calculated from the injection spectral index as

$$\mathcal{M}_R^2 = \frac{2\alpha - 3}{2\alpha + 1}. \tag{2.8}$$

For A3376 two radio observations exist in addition to the Very Large Array (VLA) observations by Bagchi et al. (2006): Giant Metrewave Radio Telescope, GMRT, 150 and 325 MHz: Kale et al. 2012 and Murchison Widefield Array, MWA, 80-215 MHz: George et al. 2015. Kale et al. (2012) describe in detail the morphology of the E and W relics. They consider the DSA mechanism assuming that the synchrotron and inverse Compton losses have not affected the spectrum. Therefore, for the injected spectral index calculation they use the flattest spectrum in the outer edge of the spectral index map for 325–1400 MHz. Their results are $\alpha_{\rm E}$ = –0.70 ± 0.15, which implies $\mathcal{M}_{\rm E}$ = 3.31 ± 0.29; and $\alpha_{\rm W}$ = –1.0 ± 0.02 with $\mathcal{M}_{\rm W}$ = 2.23 ± 0.40. In this case, there are slight differences between the Mach number assessed from the X-ray and radio observations. George et al. (2015) have derived the integrated spectral indices of the eastern and western relic using the GMRT, MWA and VLA observations (see their Fig. 3) obtaining $\alpha_{\rm E}$ = –1.37 ± 0.08 and $\alpha_{\rm W}$ = –1.17 ± 0.06, which give the Mach numbers, assuming $\alpha_{\rm int} = \alpha_{\rm inj}$ – 0.5, $\mathcal{M}_{\rm E}$ = 2.53 ± 0.23 and $\mathcal{M}_{\rm W}$ = 3.57 ± 0.58, respectively. However, due to the low angular resolution of MWA, they can only resolve the integrated spectral index and not the injected one. For this reason, we have decided not to use the George et al. (2015) results for this study.

The differences between $\mathcal{M}_{\rm R}$ and $\mathcal{M}_{\rm X}$ are not only present in this galaxy cluster. Figure 2.16 includes several systems with similar behavior to A3376 (see Table 2.10), which

is shown by a blue cross for A3376 W. A3376 E is not included because the spectral index reported by the radio observations refers to the elongated radio relic and not to the 'notch' structure. The orange crosses represent radio data obtained with LOFAR. $\mathcal{M}_{\rm X}$ of these clusters is derived from the temperature jump and $\mathcal{M}_{\rm R}$ is calculated using Eq. (2.8) with the injection spectral index $\alpha_{\rm inj}$. In addition, some other clusters as A521 (Bourdin et al. 2013; Giacintucci et al. 2008), A2034 (Owers et al. 2014; Shimwell et al. 2016) or 'El Gordo' (Botteon et al. 2016b; Lindner et al. 2014); present evidence for a shock front based on the surface brightness jump. In order to remain consistent regarding the method used to derive $\mathcal{M}$ (in our case, the temperature jump), we do not include these measurements in Fig. 2.16. We note that Mach numbers based on the SB jump seem to be smaller than those based on temperature jump (for more details, see Sarazin et al. (2016)).

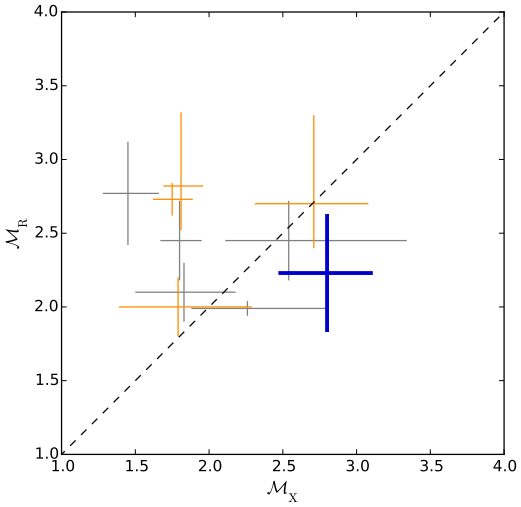

Figure 2.16: Comparison between Mach number derived from radio observations ($\mathcal{M}_{\rm R}$) based on the radio spectral index and the X-ray observations ($\mathcal{M}_{\rm X}$). The results for A3376 W is represented by the blue cross. The gray crosses show data for others clusters (see Table 2.10), orange crosses show recent radio observations done with LOFAR references. The black dashed line is the linear correlation used as reference.

Akamatsu et al. (2017) discuss several possible reasons for the Mach number discrepancies in X-rays and radio. In this study we focus on the radio ageing effect (Pacholczyk 1973; Miniati 2002; Stroe et al. 2014a), which can lead to lower radio $\mathcal{M}$ compared to X-rays. The electron ageing effect takes places when the relativistic electrons lose their energy via radiative cooling or inverse-Compton scattering after the shock passage in approximately less than $\sim 10^7$–10^8 years, which is shorter than the shock life time. As a consequence, the radio spectrum becomes steeper and the integrated spectral index decreases from $\alpha_{\rm int}$ to $\alpha_{\rm inj}$ – 0.5 in DSA model (Pacholczyk 1973; Miniati 2002). Only measurements with high angular resolution and low-frequency are able to measure $\alpha_{\rm inj}$ directly. As a consequence,

Table 2.10: The cluster sample for our $\mathcal{M}_{\rm X}$ and $\mathcal{M}_{\rm R}$ comparison.

Cluster	$\mathcal{M}_{\rm X}$ †	$\mathcal{M}_{\rm R}$
A2256*	1.8 ± 0.1 (1)	2.7 ± 0.1 (2)
A2255 NE	1.5 ± 0.2 (3)	2.8 ± 0.4 (4)
A115	1.8 ± 0.3 (5)	2.1 ± 0.2 (5)
Sausage N*	2.7 ± 0.4 (6)	2.7 ± 0.5 (8)
Sausage S*	1.8 ± 0.5 (7)	2.0 ± 0.2 (8)
A3667 NW	$2.5^{+0.8}_{-0.4}$ (9)	2.5 ± 0.3 (10)
A3667 SE	1.8 ± 0.1 (11)	2.5 ± 0.3 (10)
Coma	2.3 ± 0.5 (12)	1.99 ± 0.05 (13)
Toothbrush*	1.8 ± 0.2 (14)	2.8 ± 0.4 (15)
A3376 W	2.8 ± 0.4	2.2 ± 0.4 (16)

* Radio observations with LOFAR.
† $\mathcal{M}_{\rm X}$ has been calculated as described by Sarazin et al. (2016).

References: (1) Trasatti et al. (2015); (2) van Weeren et al. (2012b); (3) Akamatsu et al. (2017); (4) Pizzo & de Bruyn (2009); (5) Botteon et al. (2016a); (6) Akamatsu et al. (2015); (7) Storm et al. (2018); (8) Hoang et al. (2017); (9) Sarazin et al. (2016); (10) Hindson et al. (2014); (11) Akamatsu & Kawahara (2013a); (12) Akamatsu et al. (2013b); (13) Thierbach et al. (2003); (14) Itahana et al. (2015); (15) van Weeren et al. (2016); (16) Kale et al. (2012).

the calculation of $\mathcal{M}_{\rm R}$ might be underestimated. Moreover, it is thought that the simple relationship of $\alpha_{\rm int} = \alpha_{\rm inj} - 0.5$ most likely does not hold for the relics case (Kang & Ryu 2015, 2016). In the case of A3376, Kale et al. (2012) showed that the spectral distribution steepens from the outer to the inner edge in the frequency range 325–1400 MHz. However, to avoid the ageing effect they consider only the flattest spectral index as $\alpha_{\rm inj}$ at the outer edge. We calculated the distance free of ageing effect as $d = t_{\rm loss} \times v_{\rm gas}$, where $t_{\rm loss}$ is the cooling time for relativistic electrons and $v_{\rm gas} = v_{\rm shock}/C$ is the gas velocity. We estimated $t_{\rm loss} \sim 10$–5×10^7 yr from Eq. (14) of Kang et al. (2012):

$$t_{loss} \approx 8.7 \times 10^8 \ {\rm yr} \left(\frac{\rm B^{1/2}}{\rm B^2_{eff}}\right) \left(\frac{\rm v_{obs}}{1 \ {\rm GHz}}\right)^{-1/2} (1+{\rm z})^{-1/2}, \tag{2.9}$$

where we assumed a magnetic field of B ~ 1 μG and $v_{\rm obs}$ = 325 MHz–1.4 GHz. The effective magnetic field is $\rm B^2_{eff} = B^2 + B^2_{CBR}$, which includes the equivalent strength of the cosmic background radiation like $\rm B_{CBR} = 3.24$ μG $(1+z)^2$. The gas velocity is $v_{\rm gas,W} \sim 564$ km/s for the west. Therefore, the distance free of the ageing effects is $d_{\rm W}$ ∼58–28 kpc. In the case of assuming a five times higher magnetic field, B ~ 5 μG, $t_{\rm loss} \sim 4 \times 10^7$ yr (20 % lower than with B ~ 1 μG) and for B ~ 0.2 μG $t_{\rm loss} \sim 2 \times 10^7$ yr (60 %), for $v_{\rm obs}$ = 1.4 GHz. Therefore, the assumptions of B ~ 1 μG seems the most conservative one. This distance at 1.4 GHz, 28 kpc, is smaller than the radio beam at same frequency (69″ × 69″ or 65 × 65 kpc) used for the spectral index estimation (Kale et al. 2012). Thus, $\mathcal{M}_{\rm R}$ may be affected by the ageing effect.

Additionally, the X-ray SB discontinuities in the west and east (see Figs. 2.13 and 2.14) do not coincide with the outermost edges of the radio relics. There is significant radio structure outside these SB discontinuities. Therefore, while the DSA mechanism associated to these shocks is assumed to be responsible for the radio emission directly behind the shocks, it cannot explain all radio emission. There might be other shocks further outward, but these are below the detection threshold using current instruments, due to a combination of low spatial resolution (*Suzaku*) or high background (*XMM-Newton*), so we cannot test that hypothesis in the present study. Together with the ageing effect discussed before, this might contribute to the difference between the Mach number derived from the X-ray and radio observations.

2.4.5 Merger scenario

The N-body hydrodynamical simulations of A3376 by Machado & Lima Neto (2013) predict a merger scenario with two subclusters: one, eastern, which is more compact with four times more concentrated gas than the other, western subcluster. The eastern subcluster has a high initial velocity and is able to cross through the more massive western subcluster, disrupting its core and forming the dense and bright tail. This could be the reason why only one X-ray emission peak is found, probably associated to the BCG2 of the Eastern subcluster in the central region. This scenario is confirmed by the weak lensing analysis of Monteiro-Oliveira et al. (2017), which reveals that the mass peak concentration is in the stripped tail.

From the shock properties, we are able to derive the dynamical age of A3376. Assuming that the western and eastern shocks have traveled from the cluster core to the radio relic location with respective constant velocity ($v_{\rm shock,W} \sim 1630 \pm 220$ km s^{-1} and $v_{\rm shock,E} \sim 1450 \pm 150$ km s^{-1}) and the distance between both shocks is ∼1.9 Mpc, the time required to reach the current position is ∼0.6 Gyr. This value is in good agreement with the previous estimates by Monteiro-Oliveira et al. (2017), George et al. (2015) and Machado & Lima Neto (2013). It might indicate that A3376 is a young merger cluster which is still evolving and following the outgoing scenario as proposed by Akamatsu et al. (2012) and Monteiro-Oliveira et al. (2017).

We also estimated the inclination angle of the line-of-sight with respect to the merging axis, assuming that the galaxies of the infalling (eastern) subcluster are moving together with the shock front. The brightest galaxy of the E subcluster has a $z = 0.045591 \pm 0.00008$ (Smith et al. 2004) and the peculiar velocity with respect to the entire merging cluster ($z = 0.0461 \pm 0.003$, Monteiro-Oliveira et al. 2017) is $\sim 154 \pm 94$ km/s. From the relation $\theta = \arctan(v_{\rm spec}/v_{\rm shock,E})$, we estimated $\theta \sim 6^\circ \pm 4^\circ$. This means that the merger axis is close to the plane of sky.

2.5 Cold front near the center

The *Chandra* image shown in Fig. 2.17 reveals an arc-shape edge between 25–140° (measured counter-clockwise), orthogonal to the merging axis in the NE direction. For a refined spatial analysis of this feature, we extracted the X-ray surface brightness profile from the

center of A3376 to the E using the *Chandra* observations (see Table 2.1) in the 0.5–2.0 keV band. The circular pie annuli used to accumulate the SB profile cover the angle interval 50–120° from the centroid in $\mathrm{RA} = 6^{\mathrm{h}}02^{\mathrm{m}}12^{\mathrm{s}}08$, $\mathrm{Dec.} = -39°57'18''53$ (same as the red annular sectors of Fig. 2.17). The same regions are used for the spectral analysis where point sources using the criteria of $S_{\mathrm{c}} = 10^{-17}$ W m^{-2} have been excluded. Figure 2.18 shows the radial SB profile along the E direction. It shows an edge ($C = 1.78 \pm 0.15$) in the SB profile at approximately 150 kpc (∼3′) distance from the X-ray emission peak.

We determined the radial temperature profile using *XMM-Newton* and *Suzaku* observations, see Fig. 2.19, across the E direction for the four annular regions shown in Fig. 2.17. The temperature rises from ∼3.0 to ∼4.6 keV ($T_{\mathrm{in}}/T_{\mathrm{out}} = 0.65 \pm 0.08$) just outside of the SB edge location based on *XMM-Newton* observations.

The radial SB and temperature profiles show that the gas is cooler and denser (brighter) inside the edge. Using the density and temperature discontinuities of $C = 1.78 \pm 0.15$ and $T_{\mathrm{in}}/T_{\mathrm{out}} = 0.65 \pm 0.08$, respectively; the pressure jump is $P_{\mathrm{in}}/P_{\mathrm{out}} = 1.16 \pm 0.17$. Therefore, the pressure is almost continuous across the edge, which agrees with the definition of a cold front.

In addition to the two shock fronts described in the previous sections, we found evidence of a sharp edge close to the center associated to a cold front. It delimits the boundaries of a cool and dense gas cloud moving through a hotter ambient gas, which is subject to ram pressure stripping (Markevitch & Vikhlinin 2007; Vikhlinin et al. 2001). Figure 2.17

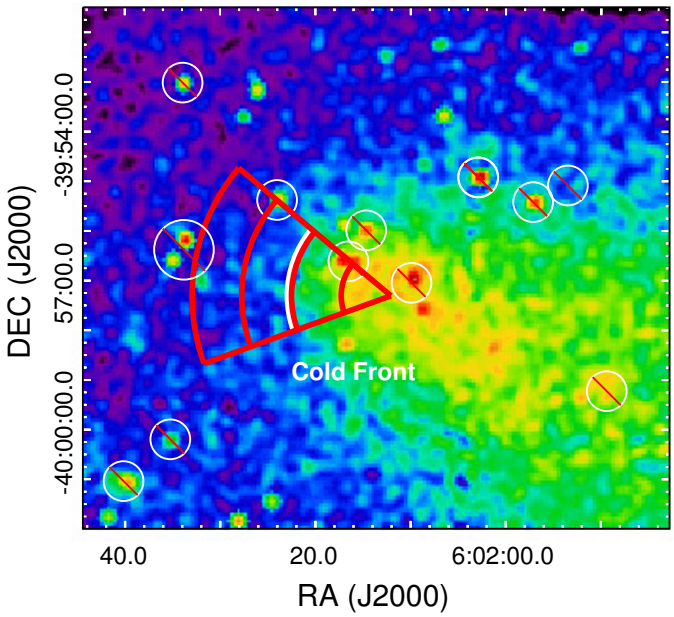

Figure 2.17: A3376 *Chandra* background and exposure corrected image in the 0.5–2.0 keV band. The red annular regions are used in the spectral analysis of the cold front and the same pie shaped annuli are used for the SB profile estimation.

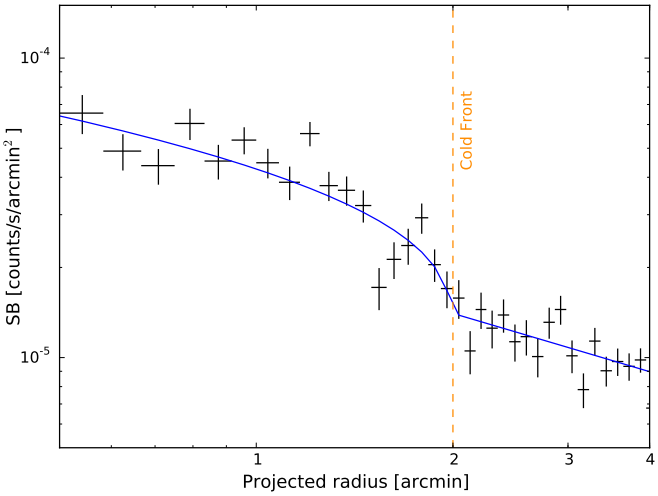

Figure 2.18: Radial X-ray surface brightness profile across the cold front in the 0.5-2.0 keV band using the *Chandra* observation. The profile is corrected for exposure and background, and point sources are removed. The solid blue curve is the best-fit model and the vertical orange line is the estimated position of the cold front.

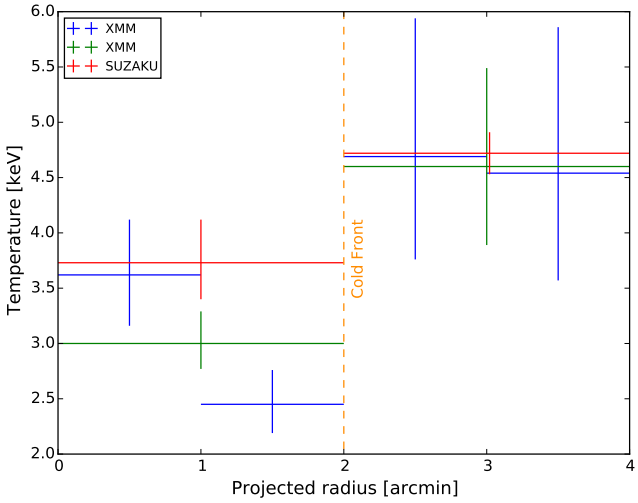

Figure 2.19: Radial temperature distribution for the red annular regions shown in Fig. 2.17. Blue and green crosses correspond to *XMM-Newton* observations and red crosses to *Suzaku*. The vertical orange line shows the estimated position of the cold front.

Table 2.11: Temperature distribution at cold front regions shown in Fig. 2.18.

	Radius (′)	*kT* (keV)
XMM-Newton	0.5 ± 0.5	3.62 ± 0.46
	1.5 ± 0.5	2.45 ± 0.29
	2.5 ± 0.5	4.69 ± 1.14
	3.5 ± 0.5	4.54 ± 1.15
XMM-Newton	1.0 ± 1.0	3.00 ± 0.27
	3.0 ± 1.0	4.60 ± 0.80
Suzaku	1.0 ± 1.0	3.73 ± 0.36
	3.0 ± 1.0	4.71 ± 0.19

shows this case, with the shape of the front perpendicular to the merger axis advancing in the NE direction. Using the temperatures and densities derived from the X-ray image and spectral analysis, we estimated the velocity of the cool gas cloud (Landau & Lifshitz 1959; Vikhlinin et al. 2001; Dasadia et al. 2016b; Ichinohe et al. 2017). We approximated the cool gas as a spherical body advancing into ambient gas. If the cloud moves with supersonic velocity, a shock front could form upstream of the gas cloud. Near the cold front edge the cool gas decelerates to zero velocity at the stagnation point, referred here with the index 0. We also assumed a free stream of gas upstream of the cold front, which is undisturbed and flows free, denoted by index 1. The ratio of pressures in the free stream and the stagnation point can be expressed as a function of the gas cloud speed v (Landau & Lifshitz 1959):

$$\frac{p_0}{p_1} = \begin{cases} \left(1 + \frac{\gamma-1}{2}\mathcal{M}_1^2\right)^{\gamma/(\gamma-1)} & (\mathcal{M}_1 \leq 1) \\ \left(\frac{\gamma+1}{2}\right)^{(\gamma+1)/(\gamma-1)} \mathcal{M}_1^2 \left(\gamma - \frac{\gamma-1}{2\mathcal{M}_1^2}\right)^{-1/(\gamma-1)} & (\mathcal{M}_1 > 1) \end{cases} \tag{2.10}$$

where $\gamma = 5/3$ is the adiabatic index; $\mathcal{M}_1 = v/c_\mathrm{s}$ and c_s are the Mach number and sound velocity of the free stream, respectively.

The gas parameter at the stagnation point cannot be measured directly, although the stagnation pressure is similar to the gas cloud inside the cold front (Vikhlinin et al. 2001). Therefore we assumed $T_0 = 3.00 \pm 0.27$ keV as the temperature inside the cold front and $T_1 = 4.60 \pm 0.80$ keV outside the cold front used as the free stream region (Vikhlinin et al. 2001; Sarazin et al. 2016). The density ratio of these regions is calculated from the best-fit parameter of the broken power-law model of Fig. 2.18, $n_0/n_1 = 3.91 \pm 0.75$. Thus, the pressure ratio between the inside of the cold front and the outside free stream region is $p_0/p_1 = 2.6 \pm 0.6$, which corresponds to $\mathcal{M}_1 = 1.2 \pm 0.2$ in the free stream. Using $c_\mathrm{cf} = \sqrt{\gamma k T_1/\mu m_p}$ with $kT_1 = 4.60$ keV, $c_\mathrm{cf} = 1100 \pm 100$ km s^{-1} and the velocity of the cool gas cloud is $v_\mathrm{cf} = 1300 \pm 250$ km s^{-1}. This value is consistent with the velocity of the shock front, $v_\mathrm{shock,E} = 1450 \pm 150$ km s^{-1}, derived in Sect. 2.4.3.

As explained in Dasadia et al. (2016b), for a rigid sphere the ratio of $d_{\rm s}/R_{cf}$, with $d_{\rm s}$ the shock 'stand-off' distance and $R_{\rm cf}$ the radius of curvature of the cold front, depends on $\mathcal{M}$ as a function of $(\mathcal{M}^2-1)^{-1}$ (see Dasadia et al. Fig. 9, Schreier 1982; Vikhlinin et al. 2001; Sarazin 2001). For a shock with $\mathcal{M}_E$ = 1.5 $\pm$ 0.1, the shock offset ratio is $d_{\rm s}/R_{\rm cf} \sim 0.8 \pm 0.1$, $d_{\rm s} \sim 120 \pm 15$ kpc ($R_{\rm cf} \sim 150$ kpc). This separation for a rigid sphere is smaller than the distance of $\sim$ 300 kpc between the cold front and shock front present in the east. This behavior is the same for most of the observed clusters (Dasadia et al. 2016b). As explained by Sarazin et al. (2016), after the first core passage the shock accelerates toward the periphery of the clusters, while the cool gas is decelerated by gravity and ram pressure. For this reason, the shock is expected to move away from the cold front and the separation between both features might be larger than the rigid sphere model predicts.

2.6 Summary

We present a spectral analysis of A3376 in four directions (west, east, north, and south) using *Suzaku* deep observations and supported by *XMM-Newton* and *Chandra* observations. A3376 is a merging galaxy cluster with two shock fronts and one cold front confirmed. One shock is coincident with the radio relic in the west and the other might be associated to the 'notch' of the eastern relic. Shocks are moving with a Mach number $\mathcal{M} \sim$ 2–3. The cold front is located at approximately 150 kpc ($r \sim 3'$) from the X-ray emission peak at the center and delimits a cool gas cloud moving with $v \sim$ 1300 km s^{-1}.

We determine the ICM structure up to 0.9r_{200} in the W, 0.6r_{200} in the E. We observe a temperature enhancement followed by a drop at $\sim$0.7r_{200} for the W and $\sim$0.5r_{200} for the E. We confirm temperature and surface brightness discontinuities in both directions. In the west it coincides with the radio relic position and in the east, it is located at 450 kpc ($r \sim 8'$). The temperature structure in the south follows the simulated profile of Burns et al. (2010) for relaxed clusters.

We estimate the Mach number based on the temperature jump, being $\mathcal{M}_{\rm W}$ = 2.8 $\pm$ 0.4 and $\mathcal{M}_{\rm E}$ = 1.5 $\pm$ 0.1, for the western and eastern region, respectively. We derive the shock speed velocity as $v_{\rm shock,W} \sim 1630 \pm 220$ km s^{-1} and $v_{\rm shock,E} \sim 1450 \pm 150$ km s^{-1}.

Assuming that the shock fronts are moving with constant velocity, the time since core passage is $\sim$0.6 Gyr, which is in good agreement with the N-body hydrodynamical simulations of Machado & Lima Neto (2013), and with earlier multiwavelength analyses of George et al. (2015) and Monteiro-Oliveira et al. (2017). Combining the eastern shock velocity and the peculiar velocity of the eastern brightest galaxy let us infer that the merger axis is close to the plane of the sky.

We compare the Mach numbers inferred from the temperature discontinuities with those derived from radio observations assuming the DSA mechanism. Not all the clusters present a consistent correlation between X-ray and radio Mach numbers. For A3376 the Mach number for the western relic estimated by Kale et al. (2012) is consistent with our result.

ACKNOWLEDGEMENTS

The authors thank the anonymous referee for constructive comments and suggestions. The authors also thank Dr. R. Kale for providing the VLA radio data. I.U. thanks H. Martínez-Rodríguez for his support in the initial stage of this work. H.A. acknowledges the support of NWO via Veni grant. T.O. and Y.I. acknowledge support by JSPS KAKENHI Grant Numbers 26220703 and 15H03642. SRON is supported financially by NWO, the Netherlands Organization for Scientific Research. This work is based on observations obtained with XMM-Newton, an ESA science mission with instruments and contributions directly funded by ESA member states and the USA (NASA).

"Caminante, no hay camino,
se hace camino al andar."

- Antonio Machado

3

X-ray study of Abell 3365 with XMM-Newton

I. Urdampilleta & A. Simionescu & J. S. Kaastra & X. Zang & G. Di Gennaro & F. Mernier & J. de Plaa &G. Brunetti

To be submitted to Astronomy and Astrophysics

Abstract

We present an X-ray spectral analysis using *XMM-Newton*/EPIC observations (∼100 ks) of the merging galaxy cluster Abell 3365 (z = 0.093). Previous radio observations suggest the presence of a peripheral elongated radio relic to the east and a smaller radio relic candidate to the west of the cluster centre. We find evidence of temperature discontinuities at the location of both radio relics, indicating the presence of a shock with a Mach number of $\mathcal{M}$ = 3.5 ± 0.6 towards the east and a second shock with $\mathcal{M}$ = 3.9 ± 0.8 towards the west. We also identify a cold front at $r \sim 1.6'$ from the X-ray emission peak. Based on the shock velocities, we estimate that the dynamical age of the main merger along the east-west direction is ∼0.6 Gyr. We find as well that the standard shock acceleration scenario from the thermal pool is consistent with the electron acceleration mechanism at the eastern radio relic. In addition, we study the distribution of the temperature, iron (Fe) abundance and pseudo-entropy along the merging axis. Our results show that remnants of a metal-rich cool-core can partially or totally survive after the merging activity. Finally, we find that the merger can displace the metal-rich and low entropy gas from the potential well towards the cold front as suggested by numerical simulations.

3.1 Introduction

Galaxy clusters are the largest virialized structures in the Universe and grow hierarchically via accretion and merging of less massive subclusters. During this merging process, turbulence, shocks and cold fronts (CF) arise in the hot intra-cluster medium (ICM) as a result of the strong merging activity (Markevitch & Vikhlinin 2007). Cold fronts delimit the boundary between the infalling subcluster's cool dense gas and the hot cluster atmosphere. Shocks are large scale structures that propagate along the hot ICM out to the cluster outskirts, where they are usually found. Both can be detected by temperature and density discontinuities in the ICM via spectral analysis and X-ray surface brightness (SB) edges, respectively. Moreover, shocks present a discontinuity as well in the pressure distribution, while cold fronts maintain it uniform across the edge (Vikhlinin et al. 2001). Shocks in galaxy clusters (typically characterized by a Mach number $\mathcal{M} \leq$ 3–5) are thought to (re)accelerate electrons in the ICM via first-order Fermi diffusive shock acceleration (hereafter DSA, Bell 1987; Blandford & Eichler 1987). These relativistic particles may produce non-thermal synchrotron emission in the form of radio relics in the presence of an amplified magnetic field. These radio features are elongated, polarized and steep-spectrum ($\alpha < -1$, being $S_\nu \propto \nu^\alpha$) structures located usually at the cluster periphery (for a theoretical and observational review, respectively, see Brunetti & Jones 2014; van Weeren et al. 2019). Turbulence generated in the merger may also (re)accelerate particles generating unpolarized cluster-wide radio phenomena known as radio haloes (Brunetti et al. 2001; Feretti et al. 2012; van Weeren et al. 2019).

Nowadays the number of shock detections in merging galaxy clusters is increasing (for recent works, e. g. Akamatsu et al. 2017; Thölken et al. 2018; Urdampilleta et al. 2018; Di Gennaro et al. 2019; Botteon et al. 2019a). In some cases these shocks appear at the same or similar location as radio relics (see Table 1 of van Weeren et al. 2019). The study of the shock-relic connection and their radial distribution throughout the ICM improves our understanding of the dynamical stage of the cluster. Moreover, a detailed spectral analysis along the merging axis, including a study of their metallicity distribution, can provide valuable information on the chemical evolution and dynamical history of the merged ICM (Urdampilleta et al. 2019).

In this paper, we analyse the temperature and surface brightness discontinuities in the outskirts and central ICM of Abell 3365 ((Abell et al. 1989), hereafter A3365), together with the temperature, Fe abundance, and pseudo-entropy distribution along the main merging axis. For this purpose we use observations taken by the *XMM-Newton* satellite. A3365 is a nearby (z = 0.093, Struble & Rood 1999) multi-merging galaxy cluster detected in X-rays by *ROSAT* and named as RXC J0548.8-2154 (Böhringer et al. 2007). A3365 has M_{500} = 1.7 $\times$ 10^{14} $M_\odot$ obtained from X-ray observations (Lovisari & Reiprich 2019). Based on this value and using the self-similar quantities described in Appendix A of Arnaud et al. (2010), we estimate r_{500} = 0.81 Mpc = 7.82′ (at this redshift) and T_{500} = 3.14 keV. A3365 hosts one radio relic at the east (hereafter relic E) and one radio relic candidate at the west (hereafter relic CW) discovered in the NVSS survey and observed by van Weeren et al. (2011a) with the VLA and WSRT at 1.4 GHz. As described by van Weeren et al. (2011a) relic E and relic CW have an angular extension of 5.5′ or 560 kpc and 2.3′ or 235 kpc, respectively at this

redshift (see Fig. 3.1).

A3365 consists of three subclusters (Golovich et al. 2018), see Fig. 3.1. They all have similar redshift, and the main components 1 and 3 are separated by a distance of 9'. They are considered as part of the same merging system (Golovich et al. 2018) named along this paper as A3365. The mass ratio between these two main subclusters is 5:1, respectively (Bonafede et al. 2017). The most massive component 1 has itself two sub-components. The X-ray emission peak (hereafter 1b) is displaced by 2.5' towards the west from sub-component 1a. The recent spectroscopic survey by Golovich et al. (2018) shows that A3365 contains 150 cluster members, is located at a redshift of 0.09273 $\pm$ 0.00028 and has a velocity dispersion of 981 $\pm$ 58 km/s. The red sequence distribution suggests that the merging system is formed by three subclusters (see their Fig. 25 for more details): one is coincident with A3365_1a towards the east, an other is in a similar position as A3365_3, in the middle, and the last one is towards the west (hereafter A3365_2), see Fig. 3.1. Golovich et al. (2018) suggest that the main merging activity occurred along the east-west direction, where A3365 has crossed the A3365_1a subcluster, stripping the gas of both subclusters in the east-west direction, highly disturbing the ICM, and forming the cometary tail towards the east. The spatial distribution seems to suggest that the merger between A3365_1a and A3365_3 is associated with the relic E. However, there is not a clear connection of this merger with the relic CW, suggesting that it might have a different origin. Golovich et al. (2018) also explain that A3365_1a shows two bright galaxies, which may indicate an ongoing merging activity. Finally, A3365_2 seems to advance towards A3365_3 and might be an indication that it has still not merged. Here we use *XMM-Newton* to investigate the merging scenario in more detail.

For this analysis, we use the values of protosolar abundances ($Z_{\odot}$) reported by Lodders et al. (2009). We assume cosmological parameters H_0 = 70 km/s/Mpc, $\Omega_{\rm M}$ = 0.27 and Ω_{Λ} = 0.73, respectively, which give 104 kpc per 1 arcmin at z = 0.093. All errors are given at 1σ (68 %) confidence level unless otherwise stated and all the spectral analysis made use of the modified Cash statistics (Cash 1979; Kaastra 2017a).

Table 3.1: Observations and net exposure times.

Sequence ID	Name	Position (J2000) (RA, Dec.)	Observation starting date	M1 (ks)	M2 (ks)	pn (ks)
0760970101	A3365-p1	(05:48:47.00, -21:54:34)	2016-03-29	71	75	65
0677181301	A3365-p2	(05:48:50.38, -21:54:43)	2011-09-02	27	27	26

3.2 Observations and data reduction

The two available *XMM-Newton* observations of A3365 are listed in Table 3.1. Both data sets are reduced using the *XMM-Newton* Science Analysis System (SAS) v17.0.0, with the

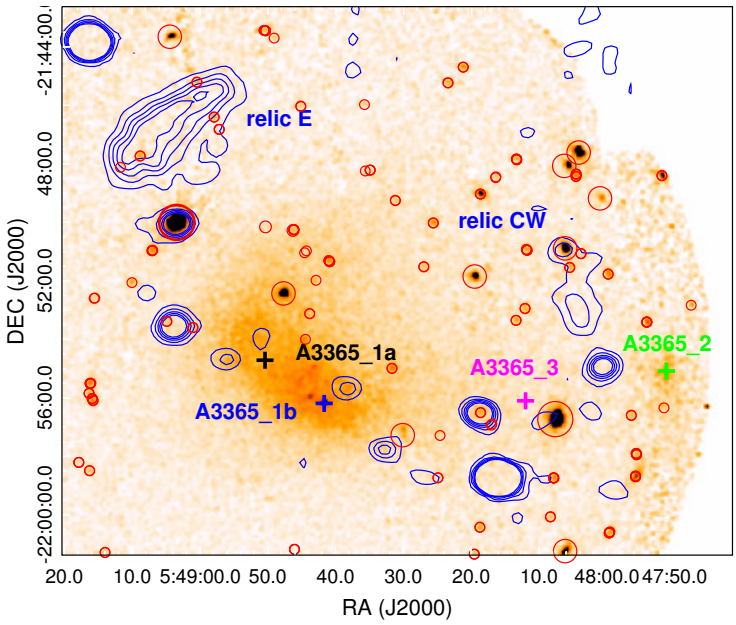

Figure 3.1: *XMM-Newton* smoothed image of A3365 in the 0.5–2 keV band. Red circles are the point sources that have been removed. VLA 1.4 GHz radio contours are shown in blue. The centre of the three subclusters: A3365_1a, A3365_2 and A3365_3, identified by Golovich et al. (2018) are marked with black, magenta and green crosses, respectively. The X-ray emission peak is shown with a blue cross, A3365_1b.

calibration files from June 2018. For this analysis we use only the observations of the EPIC instrument, containing the MOS and pn detectors. We first apply the standard pipeline commands `emproc` and `epproc`. Next, we filter the soft-proton (SP) flares by building Good Time Interval (GTI) files. For this process we use the method detailed in Urdampilleta et al. (2019) and extensively explained in Appendix A.1 of Mernier et al. (2015). We identify and exclude the point sources in the complete FOV with a circular region of 10″ radius (see Fig. 3.1), except where higher radii are needed to cover larger sources (see Appendix A.2 of Mernier et al. 2015). We use the SAS task `edetect_chain` for this purpose. We keep the single, double, triple and quadruple events in MOS (`pattern` ≤ 12) and only the single pixel events in pn (`pattern` == 0). We also correct the out-of-time events from the pn detector.

3.3 Spectral analysis

In our spectral analysis of A3365, we assume that the observed spectra include the following components: optically thin thermal plasma emission from the ICM in collisional ionization equilibrium, and the background consisting of the local hot bubble (LHB), the Milky Way halo (MWH), the cosmic X-ray background (CXB), the hard particle (HP) background

and residual soft-protons (SP). The models used for each of the background components are detailed in Urdampilleta et al. (2019) and Mernier et al. (2015). The estimation of the sky background components (LHB, MHW and CXB) is obtained from a *ROSAT* observation of an offset annullus surrounding A3365, using the X-ray Background Tool[1]. The parameters of the SP components are obtained fitting the total FOV ($r = 15'$) EPIC spectra, where the ICM *cie* (SPEX) model parameters are also left free. The best-fit parameters of the background components for each observation are listed in Table 3.2. The emission models are corrected for the cosmological redshift and absorbed by the galactic interstellar medium. We adopt the weighted total hydrogen column density $N_{\rm H,tot} = 2.94 \times 10^{20}$ cm^{-2} (Willingale et al. 2013)[2].

Table 3.2: Best-fit parameter values of the total background estimated for the A3365-p1 and A3365-p2 observations.

	Norm[a]	*kT* (keV)	Γ
MWH	0.10 ± 0.10	0.17 ± 0.02	–
LHB	0.46 ± 0.07	0.08 (fixed)	–
CXB	1.81 ± 0.22	–	1.41 (fixed)
	A3365-p1		
SP MOS1	1.32 ± 0.13	–	1.40 ± 0.02
SP MOS2	2.01 ± 0.17	–	1.40 ± 0.02
SP pn	4.88 ± 0.67	–	0.88 ± 0.03
	A3365-p2		
SP MOS1	1.65 ± 0.37	–	1.40 ± 0.02
SP MOS2	2.19 ± 0.22	–	1.40 ± 0.02
SP pn	5.05 ± 0.25	–	1.40 ± 0.10

[a] For LHB and MWH norm in units of 10^{70} m^{-3} arcmin^{-2}
For CXB norm in units of 10^{50} ph s^{-1}keV^{-1} arcmin^{-2}
For SP norm in units of 10^{45} ph s^{-1}keV^{-1} arcmin^{-2}

The spectral analysis software used in this work is SPEX[3] (Kaastra et al. 1996, 2017c) version 3.05.00 with SPEXACT (SPEX Atomic Code and Tables) version 3.05.00. We fit simultaneously the spectra of the MOS (energy range from 0.5 to 10 keV) and pn (0.6–10 keV) detectors. We apply the method of optimal binning (Kaastra & Bleeker 2016). A single temperature plasma is assumed for all the sectors in this study. We leave as free parameters the temperature, *kT*, the metal abundance, *Z*, and the normalization, *Norm*. All metal

[1] https://heasarc.gsfc.nasa.gov/cgi-bin/Tools/xraybg/xraybg.pl
[2] http://www.swift.ac.uk/analysis/nhtot/
[3] https://www.sron.nl/astrophysics-spex

abundances are tied to the Fe abundance. We account for the effect of systematic uncertainties related to the $\pm 10\%$ variation in the normalization of the sky background and non X-ray background components (Mernier et al. 2017; Urdampilleta et al. 2019). The contribution of these systematic uncertainties is further included in our analysis and results.

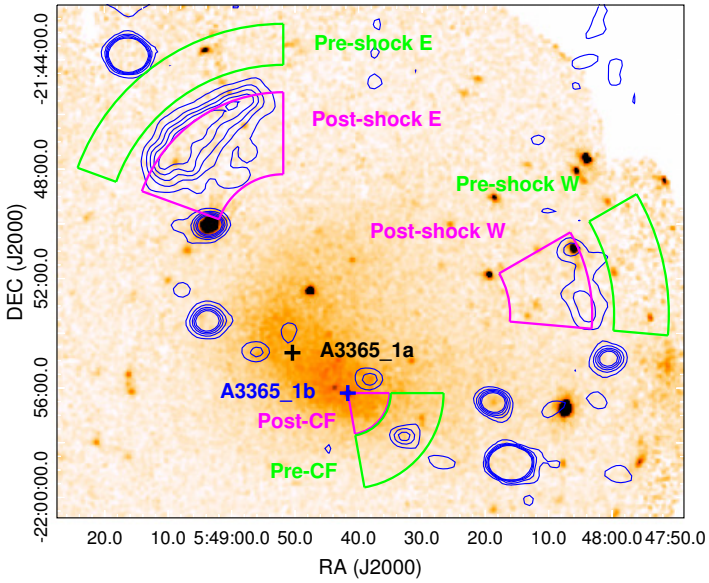

Figure 3.2: Same as Fig. 3.1, indicating spectral extraction regions. The green sectors represent the pre-shock and pre-cold front regions of relic E, relic CW and CF. The magenta sectors are the post-shock and post-cold front regions. The center of A3365_1a and A3365_1b are marked with black and blue crosses.

3.4 X-ray surface brightness profile

In order to confirm the evidence of shocks and cold fronts characteristic of merging galaxy clusters, the presence of SB profile discontinuities should be found at the same location as temperature discontinuities. We adopt a broken power-law density profile to describe the density. Assuming spherical symmetry, the density distribution is given by:

$$\begin{cases} n_2(r) = n_0 \left(\frac{r}{r_{\rm sh}}\right)^{-\alpha_2} & r \leq r_{\rm sh} \\ \\ n_1(r) = \frac{1}{C} n_0 \left(\frac{r}{r_{\rm sh}}\right)^{-\alpha_1} & r > r_{\rm sh} \end{cases} \tag{3.1}$$

where n_0 is the model density normalization, r is the radius from the centre of the sector, $r_{\rm sh}$ is the discontinuity location, α_1 and α_2 are the power-law indices. At the location of the

SB discontinuity the downstream (post-shock or post-CF) density, n_2, is higher by a factor of $C = n_2/n_1$ compared with n_1, the upstream (pre-shock or pre-CF) density. This factor C is known as the compression factor. We assume that the X-ray emissivity is proportional to the density squared ($S_X \propto n^2$) and integrate the cluster emission along the line of sight in the 0.5–2 keV energy band. For the sky background we fit the X-ray SB distribution with a constant model at large radii and we subtract it. Once the soft proton contribution and the instrumental and sky backgrounds are subtracted and all the point sources are removed we fit the X-ray SB, leaving all model parameters listed above free to vary.

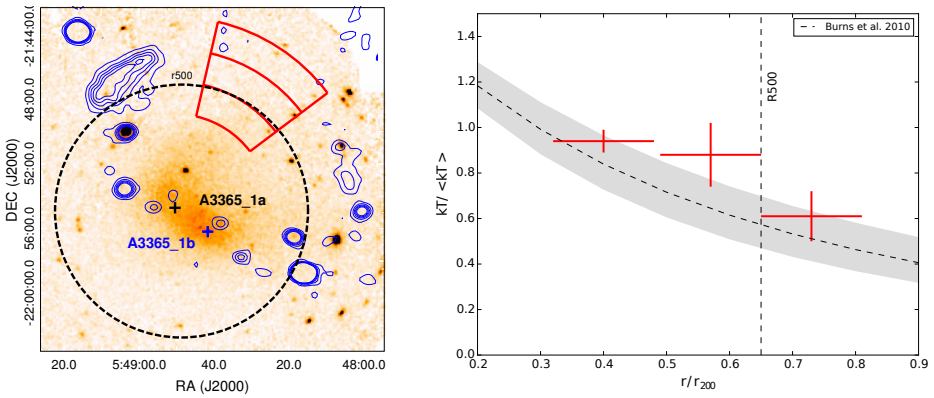

Figure 3.3: *Left panel*: Same as Fig. 3.1, showing extraction regions for the 'relaxed' direction of the cluster (orthogonal to the merging axis) in red. The black dashed circle represents r_{500}. The center of A3365_1a and A3365_1b are marked with black and blue crosses. *Right panel*: The temperature distribution of the red sectors compared with the Burns et al. (2010) 'universal' profile for relaxed clusters. The gray shaded area shows the 1σ scatter.

3.5 Results

3.5.1 Thermodynamical properties at the location of the radio relics

The diffuse radio emission in the A3365 outskirts (see Fig. 3.1) was classified as a radio relic in the east and a candidate radio relic in the west by van Weeren et al. (2011a), as described previously in Section 3.1. In this work, we investigate the possible presence of shocks associated with these radio relics analyzing the thermodynamical properties of the hot ICM. In order to search for a possible temperature discontinuity, we perform a spectral analysis of the post-shock and pre-shock E and CW regions, assuming that the candidate shocks are located at the external edge of the respective radio relics. We maintain a separation between upstream and downstream regions of $\approx 1'$ to avoid any photon leakage from the brighter region. The Fe abundance is fixed to 0.3 $Z_\odot$ in these regions. The best-fit parameters for the post and pre-shock regions at the relics E and CW are shown in Table

3.3. They both show a significant drop of the temperature. Shocks are characterized by higher temperature and pressure in the post-shock (downstream) than in the pre-shock (upstream) region. The temperature jumps ($kT_{\rm post}/kT_{\rm pre}$) are 4.6 $\pm$ 1.4 and 5.5 $\pm$ 1.2 for E and CW, respectively.

Table 3.3: Best-fit parameters for the post and pre-shock regions at the relic E and relic CW shown in Fig. 3.2.

	kT (keV)	*Norm* (10^{70} m^{-3} arcmin^{-2})	C-stat/d.o.f.
		Relic E	
Post	4.45 $\pm$ 1.08	1.10 $\pm$ 0.07	883/1009
Pre	0.97 $\pm$ 0.16	0.89 $\pm$ 0.04	1097/1024
		Relic CW	
Post	4.72 $\pm$ 0.90	2.12 $\pm$ 0.10	1056/933
Pre	0.86 $\pm$ 0.10	0.33 $\pm$ 0.07	960/923

We have also analyzed three regions (see red circular sectors in Fig. 3.3 *left*) orthogonal to the merging axis. We have compared their radial temperature profile with the 'universal' distribution of Burns et al. (2010) for relaxed clusters. For that purpose, we assume the location of A3365_1a as the centroid, the average temperature T_{500} = 3.14 keV, and $r_{200} \sim 0.65 r_{500}$ = 12′ (Reiprich et al. 2013). As shown in Fig. 3.3 *right*, the temperature profile in this direction presents a smooth decrease and is consistent with the expected distribution for relaxed clusters.

Additionally, we have determined the SB profile from circular sectors with the same angular appearing as the post and pre-shock E (centre at $\mathrm{RA} = 5^{\rm h}48^{\rm m}51^{\rm s}85$, $\mathrm{Dec.} = -21^\circ50'41''48$) regions in the east and post and pre-shock W ($\mathrm{RA} = 5^{\rm h}48^{\rm m}29^{\rm s}04$, $\mathrm{Dec.} = -21^\circ53'18''19$) in the west, shown in Fig. 3.2. The SB in these peripheral regions is too shallow, so the extracted profiles are mainly dominated by the background. Due to this low SB and reduced integration time, we are not able to detect SB discontinuities and obtain the best-fit parameters based on these SB profiles.

Furthermore, we can calculate the average density, n, in the post and pre-shock regions because $Norm \propto 1.2 n^2 V$. V is the emitting volume projected along the line-of-sight (LOS). We assume that only the sphere between the maximum and minimum radius corresponding to each circular sector contributes to the emission (Henry et al. 2004; Mahdavi et al. 2005). We estimate V as $V = 2SL/3$, with $L = 2\sqrt{(R^2_{\rm max} - R^2_{\rm min})}$, and S the area of the sectors in the plane of the sky.

For the relic E, we estimate n_1 = (1.63 $\pm$ 0.05) $\times$ 10^{-4} cm^{-3} and n_2 = (1.64 $\pm$ 0.04) $\times$ 10^{-4} cm^{-3}. At face value, this does not support the presence of a strong shock as indicated by the temperature jump. However, these measurements represent emission-weighted averages over a (presumably) steep radial gradient in both the post and pre-shock regions that

is unresolved (that is to say, the current signal to noise only allows for a single integrated measurement for each region). This, and complicated projection effects due to an aspherical shock front shape, could mask the presence of such a shock; in this case, the shock would be easier to detect in the temperature profile, where the radial gradient is relatively shallower than the density gradient.

For the relic CW, the density values are $n_1 = (0.97 \pm 0.10) \times 10^{-4}$ cm^{-3} and $n_2 = (2.41 \pm 0.06) \times 10^{-4}$ cm^{-3}. In this case, the compression factor is $C = 2.5 \pm 0.3$. This value is lower but close to the C derived from the temperature discontinuity described in Table 3.6. For the CW relic, therefore, both the density and temperature profiles show evidence for the presence of a shock.

3.5.2 Substructure in the central ICM

We search for the X-ray SB discontinuity in different edges of the bright and disturbed ICM. We find a clear discontinuity in the western side, close to the X-ray peak. We use for the X-ray SB profile analysis a circular sector centred on the X-ray peak, with exactly the same shape as the post-CF (magenta) and pre-CF (green) regions together, see Fig. 3.2. The radial X-ray SB profile obtained is shown in Fig. 3.4. The best-fit parameters of the model show a discontinuity at $r_{sh} = 1.57 \pm 0.05$ arcmin with a compression factor value of $C = 1.33 \pm 0.08$. At this same location, we measure the temperature in the post-CF ($r = 0'$–$1.57'$) and pre-CF ($r = 1.57'$–$3.5'$) regions (see Fig. 3.2 and Table 3.4) and we obtain a temperature jump of $T_1/T_2 = 0.79 \pm 0.05$. Using the temperature jump and the compression factor, we obtain a pressure ratio of $P_1/P_2 = 1.05 \pm 0.09$, consistent with a constant pressure value across the edge. This proves that the X-ray discontinuity found in the disturbed ICM edge is a cold front.

Table 3.4: Best-fit parameters for the cold front regions shown in Fig. 3.2.

	kT (keV)	*Z* ($Z_\odot$)	C-stat/d.o.f.
Post-CF	2.62 ± 0.10	0.59 ± 0.09	962/913
Pre-CF	3.30 ± 0.17	0.25 ± 0.08	1039/1003

3.5.3 Temperature and Fe abundance distributions along the merging axis

As shown in Fig. 3.5, we cover the disturbed ICM elongation with circular sectors following the X-ray emission in the east-west direction. We dedicate two circles to the subcore of the main subcluster, A3365_1a, and X-ray peak (A3365_1b). We fit the cluster emission and the background spectra, excluding the point sources as explained in Section 3.3. We use the X-ray emission peak as the centroid for our temperature and abundance distributions along the merging axis (see Fig. 3.6).

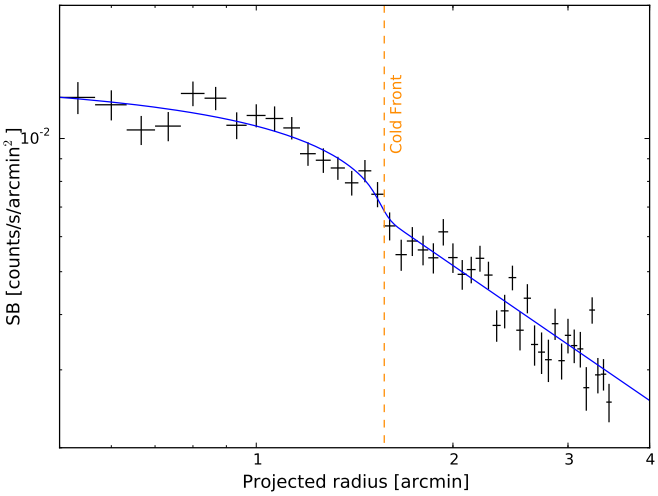

Figure 3.4: Radial X-ray SB profile across the cold front in the 0.5-2.0 keV band using the *XMM-Newton* observations. The profile is corrected for exposure, background and soft protons, and point sources are removed. The best-fit model is shown in blue and the vertical dashed orange line represents the estimated position of the cold front.

Table 3.5: Best-fit parameters for A3365 regions shown in Fig. 3.5.

Region	Radius (′)	*kT* (keV)	*Z* ($Z_\odot$)	*Norm* (10^{70} m^{-3} arcmin^{-2})	C-stat/d.o.f.
1	-4.0 ± 0.5	3.37 ± 0.13	0.31 ± 0.07	10.12 ± 0.27	1077/1006
2	-3.0 ± 0.5	3.45 ± 0.11	0.56 ± 0.07	13.46 ± 0.33	1022/999
3	-2.0 ± 0.5	3.16 ± 0.10	0.39 ± 0.06	18.16 ± 0.43	1092/996
4	-1.0 ± 0.5	3.18 ± 0.11	0.47 ± 0.08	24.92 ± 0.79	967/922
5 (A3365_1b)	0.0 ± 0.5	3.07 ± 0.14	0.55 ± 0.11	25.97 ± 0.10	927/880
6	1.0 ± 0.5	2.59 ± 0.11	0.64 ± 0.10	14.90 ± 0.65	941/893
7	2.0 ± 0.5	3.01 ± 0.17	0.34 ± 0.09	8.63 ± 0.36	1014/927
8	3.0 ± 0.5	3.77 ± 0.37	0.13 ± 0.09	4.25 ± 0.19	1046/935
A3365_1a	-2.5 ± 0.5	3.35 ± 0.19	0.53 ± 0.13	17.44 ± 0.76	929/884

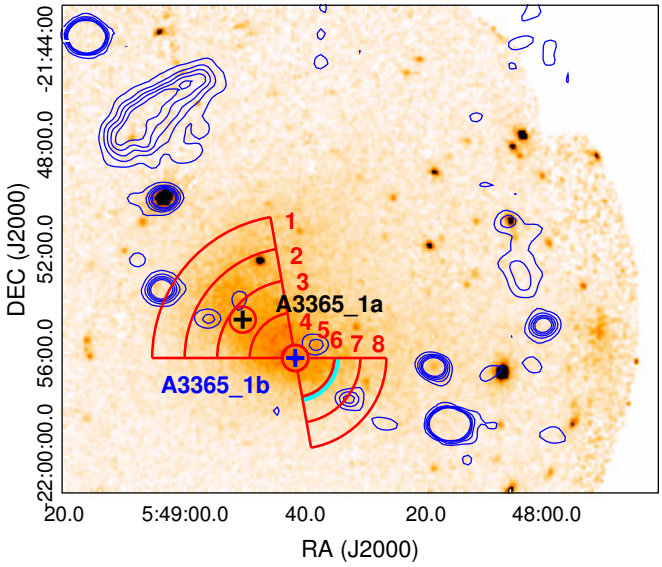

Figure 3.5: Same as Fig. 3.1, where the red sectors represent the regions used for the temperature and abundance distributions. The cyan line shows the location of the cold front. The centre of A3365_1a and the A3365_1b are marked with black and blue crosses.

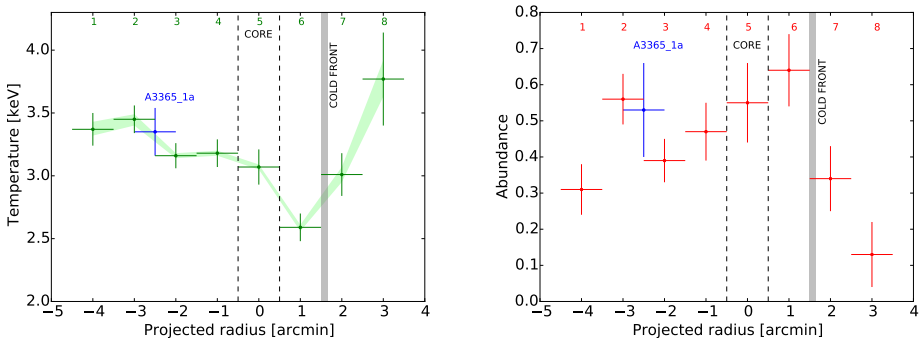

Figure 3.6: *Left panel*: The temperature distribution of A3365 along the merging direction. *Right panel*: The abundance distribution of A3365. The shaded area in the left panel represent the systematic uncertainties. Systematic errors on abundance are much smaller than statistical and thus not shown in the right panel.

The best-fit parameters of the temperature and abundance distributions are presented in Table 3.5. Sectors one to five, which are contained in the cometary tail, have a uniform temperature distribution between 3–3.5 keV. However, the temperature clearly decreases downstream of the cold front, increasing with a significant gradient in the cold front upstream region. The abundance distribution shows some signatures of two enhanced peaks, one associated with the main subcluster core, A3365_1a, and the other one with the cold

front downstream region, both with values close to ∼0.6 $Z_{\odot}$. The gas located just behind the cold front is displaced from the central potential well by the internal dynamical forces of the cold front (Heinz et al. 2003). These same effects have been already observed in Abell 3667 and Abell 665 (Lovisari et al. 2009; Urdampilleta et al. 2019).

3.6 Discussion

3.6.1 Shock jump conditions and properties

Based on the temperature jump found in the A3365 merging galaxy cluster outskirts, we repot the presence of two X-ray shock candidates associated with the relic E and relic CW. Here we present the shock properties (the Mach number, $\mathcal{M}$, the compression factor, C, and the shock velocity, v_{shock}, among others), see Table 3.6. $\mathcal{M}$ and C are calculated from the Rankine-Hugoniot jump condition (Landau & Lifshitz 1959) assuming that all of the dissipated shock energy is thermalized and the ratio of specific heats (the adiabatic index) is γ = 5/3:

$$\frac{T_2}{T_1} = \frac{5\mathcal{M}^4 + 14\mathcal{M}^2 - 3}{16\mathcal{M}^2}, \tag{3.2}$$

$$C = \frac{n_2}{n_1} = \frac{4\mathcal{M}^2}{\mathcal{M}^2 + 3}, \tag{3.3}$$

where n is the density, and the indices 2 and 1 corresponds to post-shock and pre-shock regions, respectively.

The Mach numbers estimated from the temperature discontinuities described in the previous section are $\mathcal{M}_{\rm E}$ = 3.5 ± 0.6 and $\mathcal{M}_{\rm CW}$ = 3.9 ± 0.8. The presence of shocks with $\mathcal{M} \gtrsim 3.0$ is uncommon in galaxy clusters, with only few examples known until now (CIZA J224.8+5301, Akamatsu et al. 2015; 'Bullet', Shimwell et al. 2015; 'El Gordo', Botteon et al. 2016b; A665, Dasadia et al. 2016a; A3376, Urdampilleta et al. 2018).

The sound speed at the pre-shock regions is $c_{\rm s,E} \sim$ 508 km s^{-1} and $c_{\rm s,W} \sim$ 479 km s^{-1}, assuming $c_{\rm s} = \sqrt{\gamma k T_1/\mu m_p}$ where μ = 0.6. The shock propagation speed $v_{\rm shock} = \mathcal{M} \cdot c_{\rm s}$ for the east and west is $v_{\rm shock,E}$ = 1800 ± 300 km s^{-1} and $v_{\rm shock,W}$ = 1900 ± 300 km s^{-1}, respectively. If we assume that the eastern shock is generated by the merger of A3365_1a and A3365_3 and it is moving with a constant velocity, we can calculate the dynamical age of the merger. The projected distance between A3365_1a and the relic E is ∼10′, which means ∼1.04 Mpc at z = 0.093. Thus, the time required to reach the actual position is ∼0.6 Gyr. We do the same exercise with the shock in the west assuming that is generated by the same merger. In this case, the distance between A3365_1a and relic CW is ∼11′ = 1.17 Mpc, resulting in a time of ∼0.6 Gyr. The upper limit of the merging time using the downstream gas velocity is in both cases ∼2.0 Gyr. Therefore, both shocks required the same time to propagate from the core passage up to their current location. In addition, we have no evidence of additional physical processes or mechanisms for the generation of the western shock. This might suggest that the possible origin of both shocks is the merger between A3365_1a and A3365_3.

As we explain in Section 3.1, DSA is based on first order Fermi acceleration and considers that there is a stationary and continuous injection. It accelerates relativistic electrons following a power-law spectrum $n(E)dE \sim E^{-p}dE$ with $p = (C + 2)/(C - 1)$, producing a radio synchrotron emission whose emissivity depends on the frequency as $S_\nu \propto \nu^\alpha$. The two power law indexes p and the radio injection spectral index α are related $\alpha = -(p-1)/2$. From our analysis we estimate the injection spectral index values of α_E = –0.68 ± 0.06 and α_W = –0.64 ± 0.03. Unfortunately there are no available spectral indices derived from radio observations for their comparison to date. Future radio observations are needed to confirm these results.

3.6.2 Shock acceleration efficiency

Recent studies have demonstrated that the low efficiency of the DSA mechanism for low-$\mathcal{M}$ shocks ($\mathcal{M} \leq$ 2–2.5) is not enough for the electron acceleration to proceed from the thermal pool (for observational evidences on radio relics, Botteon et al. 2019b and theoretical arguments, Vink & Yamazaki 2014,Ha et al. 2018 and Ryu et al. 2019). For this reason, alternative mechanisms have been proposed lately, as for example the re-acceleration of pre-existing cosmic ray electrons (Markevitch et al. 2005; Kang et al. 2012; Fujita et al. 2015).

Table 3.6: Shock properties at relic E and relic CW.

	Mach No. $\mathcal{M}$[a]	$v_{\rm shock}$ (km s^{-1})[b]	Compression C[c]	Power-law slope p[d]	Spectrum index α[e]
E	3.5 ± 0.6	1800 ± 300	3.2 ± 0.2	2.36 ± 0.11	–0.68 ± 0.06
CW	3.9 ± 0.8	1900 ± 300	3.3 ± 0.2	2.28 ± 0.05	–0.64 ± 0.03

[a] $\mathcal{M}$ is obtained from eq. (3.2).
[b] $v_{\rm shock} = \mathcal{M} \cdot c_{\rm S}$, $c_{\rm S} = \sqrt{\gamma k T_1/\mu m_p}$
[c] C from eq. (3.3).
[d] $p = (C + 2)/(C - 1)$
[e] $\alpha = -(p - 1)/2$ predicted

In this case, if we assume DSA as the shock acceleration mechanism of the thermal electrons in radio relics, the electron acceleration efficiency, $\eta_{\rm e}$, can be defined as the amount of kinetic energy flux at the shock moving at $v_{\rm shock}$, which is converted into relativistic electrons and produces the synchrotron luminosity $L_{\rm sync}$ of the radio relic. Both parameters, $\eta_{\rm e}$ and $L_{\rm sync}$, relate as (Brunetti & Jones 2014):

$$\eta_{\rm e} = \left[\frac{1}{2}\rho_1 v_{\rm shock}^3 \left(1 - \frac{1}{C^2}\right) \frac{B^2}{B^2 + B_{\rm CMB}^2} S\right]^{-1} \Psi(\mathcal{M}) L_{\rm sync}, \tag{3.4}$$

where ρ_1 is the total upstream density, C the compression factor, S the shock surface, $B_{\rm CMB} = 3.25(1+z)^2$ and B are the magnetic field equivalent for the Cosmic Microwave Background radiation and the magnetic field for the radio relic in μG, respectively. $\Psi(\mathcal{M})$ represents the ratio between the energy flux injected in 'all' particles and those only visible in

radio (for a more detailed description of the computation and equations see Botteon et al. 2019b).

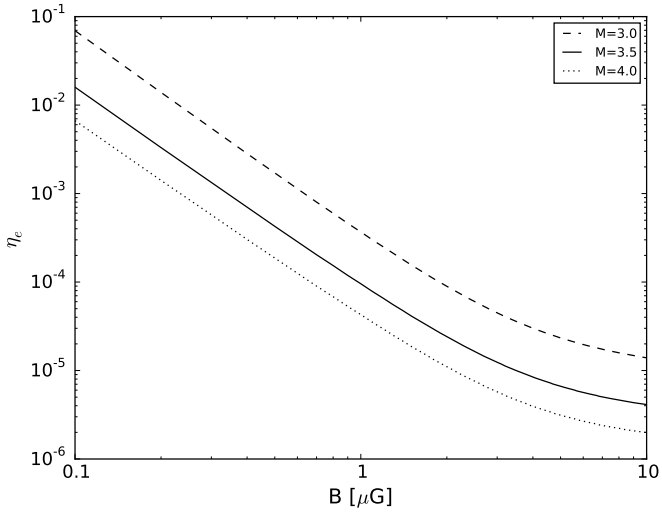

Figure 3.7: Electron acceleration efficiency, $\eta_{\rm e}$ as a function of the magnetic field, B, for $\mathcal{M}$ = 3.0, 3.5 and 4.0.

Figure 3.7 shows the electron acceleration efficiency, $\eta_{\rm e}$, as a function of the magnetic field, B, at the relic E. Radio data needed for the calculation of the electron acceleration efficiency in the relic WC are not available in the literature, therefore we only calculate it for relic E. We assume $S_{1.4\rm GHz}$ = 38.9 mJy, $S = \pi \times ((LLS/2)^2) = \pi \times ((644/2)^2)$ kpc^2 being LLS the radio relic largest linear size (see Nuza et al. 2017), the temperature and electron density in the downstream region are kT_d = 4.45 keV and n_d = 1.64 $\times$ 10^{-4} cm^{-3}, respectively. The density in the upstream region is obtained from the Eq. (3.3). We obtain $\eta_{\rm e}$ values for three different Mach numbers of $\mathcal{M}$ = 3.0, 3.5 and 4.0. In the case of $\mathcal{M}$ = 3.5, for B > 0.4 μG, the electron acceleration efficiency due to the shock is $\eta_{\rm e} \lesssim 10^{-3}$. Therefore, in this case the standard DSA scenario cannot be excluded, where efficiencies of this order are expected for weak shocks (Brunetti & Jones 2014; Caprioli & Spitkovsky 2014; Hong et al. 2014; Ha et al. 2018). These results also agree with the recent findings of Botteon et al. (2019b) and Botteon et al. (2016b) for 'El Gordo' cluster, which suggest that DSA of thermal electrons is a valid mechanism in the case of shocks with high Mach number ($\mathcal{M} \gtrsim 3$).

3.6.3 Cold front properties

We find evidence of X-ray SB and temperature discontinuities at the western edge of the highly disturbed ICM associated with a cold front. This front is perpendicular to the merging axis and moves presumably in the east-west direction, as shown in Fig. 3.2. It confines a cool and dense gas cloud moving through a hotter ambient gas (Markevitch & Vikhlinin

2007; Vikhlinin et al. 2001). The velocity of this cool gas cloud can be estimated using the density and temperature values derived from the X-ray SB and temperature discontinuities (Landau & Lifshitz 1959; Vikhlinin et al. 2001; Ichinohe et al. 2017; Urdampilleta et al. 2018). For that purpose, we assume that the cool gas is a spherical body moving through in the ambient gas.

The ratio of pressures between the stagnation point (index 0, where the fluid $v = 0$, in front of the blob) and the free stream (index 1) can be expressed as a function of the gas cloud speed v (or equivalently the Mach number assuming $\mathcal{M}_1 = v/c_\mathrm{s}$, where c_s is sound velocity of the free stream) (Landau & Lifshitz 1959):

$$\frac{p_0}{p_1} = \begin{cases} \left(1 + \frac{\gamma-1}{2}\mathcal{M}_1^2\right)^{\gamma/(\gamma-1)} & (\mathcal{M}_1 \leq 1), \\ \left(\frac{\gamma+1}{2}\right)^{(\gamma+1)/(\gamma-1)} \mathcal{M}_1^2 \left(\gamma - \frac{\gamma-1}{2\mathcal{M}_1^2}\right)^{-1/(\gamma-1)} & (\mathcal{M}_1 > 1), \end{cases} \tag{3.5}$$

where $\gamma = 5/3$ is the adiabatic index.

The gas dynamic parameters at the stagnation point cannot be measured directly. However, the pressure in the downstream region of the cold front has a similar value as the stagnation pressure as explained by Vikhlinin et al. (2001). For this reason, we assume $T_0 = 2.62 \pm 0.10$ keV as the temperature downstream the cold front and $T_1 = 3.30 \pm 0.17$ keV as the free stream region, upstream (Vikhlinin et al. 2001; Sarazin et al. 2016). The density of these regions is calculated from the best-fit parameter of the broken power-law model described in Section 3.4 and shown in Fig. 3.4. The pressure inside the cold front is $p_0 = T_0 \times n_0 = (7.7 \pm 1.0) \times 10^{-3}$ keV cm^{-3} and outside $p_1 = T_1 \times n_1 = (4.2 \pm 0.6) \times 10^{-3}$ keV cm^{-3} (both densities are calculated at the average point of the downstream and upstream regions). Thus, the pressure ratio is $p_0/p_1 = 1.9 \pm 0.4$, which corresponds to a subsonic Mach number of $\mathcal{M}_1 = 0.92 \pm 0.07$ in the free stream. This value is consistent with the cold front in A3376 ($\mathcal{M}_1 = 1.2 \pm 0.2$, Urdampilleta et al. 2018) and slight higher than A3667 ($\mathcal{M}_1 = 0.70 \pm 0.06$, Ichinohe et al. 2017). The sound speed in this region is $c_\mathrm{cf} = \sqrt{\gamma k T_1/\mu m_p} = 937 \pm 24$ km s^{-1} with $kT_1 = 3.30 \pm 0.17$ keV, giving the velocity of the cool gas cloud as $v_\mathrm{cf} = 862 \pm 69$ km s^{-1}.

3.6.4 Pseudo-entropy distribution

We aim to better understand the thermal history of the disturbed ICM of A3365. For that reason, we calculate the pseudo-entropy, $K \equiv kT \times n^{-2/3}$, for each of the sectors described in Section 3.5.3. We use the data obtained from the spectral analysis, namely the temperature, kT, and the emission measure, $Norm$, to derive the density, n.

Figure 3.8 shows the pseudo-entropy distribution along the merging axis together with the Fe abundance profile. The distribution shows a clear low entropy minimum at the location of the X-ray peak of the merging system. Urdampilleta et al. (2019) observed the same behaviour in two of the merging clusters Abell 665 and 1RXS J0603.3+4214 (known as the Toothbrush cluster). This suggests that the cool-core of the progenitor subcluster has totally or partially remained after the merging activity. As a consequence, we may be in the presence of a cool-core remnant (Rossetti & Molendi 2010). Moreover, the presence

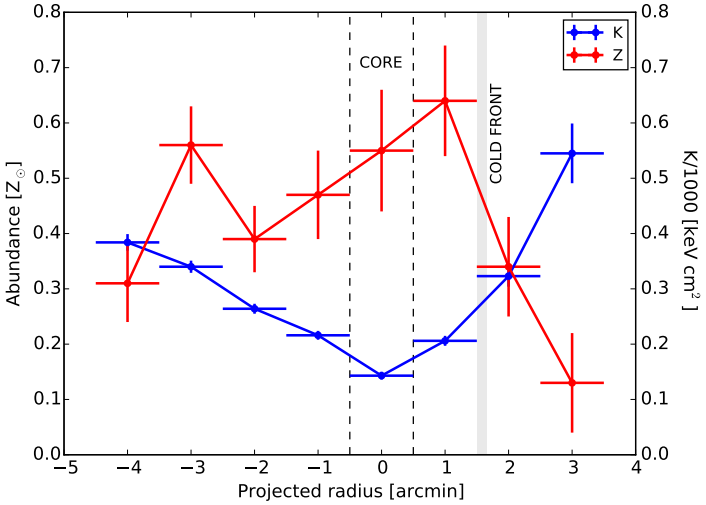

Figure 3.8: Scaled pseudo-entropy ($K/1000$) and abundance distributions along the merging axis for A3365.

of the Fe abundance enhancement and the low temperature gas towards the contact discontinuity or cold front, supports the scenario described by the simulations of Heinz et al. (2003). As an effect of the merger, the cold dense core of the cluster is displaced from the centre of the potential well. As the velocity of the core reverses in an attempt to return to equilibrium, a shear layer is created driving the gas along the cold front backwards in the direction of the background flow. This brings the material with the lowest temperature and highest abundance from the centre of the cool core towards the cold front as shown by our results in Fig. 3.8.

3.7 Summary

We have presented an imaging and spectral analysis of A3365 (z = 0.093) using *XMM-Newton* observations (∼100 ks). The recent spectroscopic survey by Golovich et al. (2018) shows that A3365 is a complex merging system formed by three subclusters. Moreover, previous radio observations (van Weeren et al. 2011a) suggest this merging galaxy cluster hosts a radio relic to the east and a radio relic candidate to the west of the merging cluster centre.

In this work, we detect abrupt temperature jumps across both radio relic edges, suggesting the presence of two shocks associated with them in the cluster outskirts. For these shocks, we estimate the Mach number and the shock velocity based on the temperature jump, being $\mathcal{M}$ = 3.5 ± 0.6 and $v_{\rm shock} \sim 1800 \pm 300$ km s^{-1} for the shock in the east, and $\mathcal{M}$ = 3.9 ± 0.8 and $v_{\rm shock} \sim 1900 \pm 300$ km s^{-1}, for the shock in the west. Assuming that

they are moving with constant velocity, the time since core passage is ∼0.6 Gyr for both shocks. This might suggest that they originate in the same merger between A3365_1a and A3365_3. For the relic E, we compute the shock acceleration efficiency as a function of the magnetic field in the relic and we find that DSA scenario is a possible acceleration mechanism. Similar results have been found for shocks with $\mathcal{M} \gtrsim 3$ as 'El Gordo' (Botteon et al. 2016b) and A3376 (Botteon et al. 2019b).

We also confirm by temperature and surface brightness discontinuities the presence of a cold front at $r \sim$1.6′ from the X-ray emission peak in the merging direction. It delimits a cool gas cloud moving with $\mathcal{M} \sim 0.9$ and a speed of $v \sim 860$ km s^{-1}.

In addition, we obtain the temperature, Fe abundance and pseudo-entropy distribution in the highly disturbed central parts of the ICM along the merging axis. We find signatures of two abundance peaks, one is coincident with A3365_1a ($\sim 0.6\ Z_{\odot}$), and the other is located towards the cold front ($\sim$0.6 $Z_{\odot}$), displaced from the potential well. This is consistent with the simulations by Heinz et al. (2003), which suggest that the shock passage can affect the internal dynamics of the cool gas and move the low entropy and metal rich gas towards the cold front. Finally, and in line with previous results shown in e.g. (Urdampilleta et al. 2019), the pseudo-entropy distribution shows a relative low entropy minimum, which might suggest that remnants of the metal-rich cool-core can survive partially or totally after the merging activity.

ACKNOWLEDGEMENTS

The authors thank Dr. R. van Weeren for the VLA radio data. A. Simionescu is supported by the Women In Science Excel (WISE) programme of the Netherlands Organization for Scientific Research (NWO), and acknowledges the MEXT World Premier Research Center Initiative (WPI) and the Kavli IPMU for the continued hospitality. SRON is supported financially by NWO, the Netherlands Organization for Scientific Research.This work is based on observations obtained with XMM-Newton, an ESA science mission with instruments and contributions directly funded by ESA member states and the USA (NASA)

"Hegoak ebaki banizkio,
nerea izango zen,
ez zuen alde egingo.
Bainan, honela
ez zen gehiago txoria izango,
eta nik txoria nuen maite."

- Joxean Artze, *Txoria txori*

4

Iron abundance distribution in the hot gas of merging galaxy clusters

I. Urdampilleta & F. Mernier & J. S. Kaastra & A. Simionescu & J. de Plaa & S. Kara & E. N. Ercan

Astronomy & Astrophysics, Volume 629, A31 (2019)

Abstract

We present *XMM-Newton*/EPIC observations of six merging galaxy clusters and study the distributions of their temperature, iron (Fe) abundance and pseudo-entropy along the merging axis. For the first time, we focused simultaneously, and in a comprehensive way, on the chemical and thermodynamic properties of the newly collided intracluster medium (ICM). The Fe distribution of these clusters along the merging axis is found to be in good agreement with the azimuthally-averaged Fe abundance profile in typical non-cool-core clusters out to r_{500}. In addition to showing a moderate central abundance peak, though less pronounced than in relaxed systems, the Fe abundance flattens at large radii towards ∼0.2–0.3 $Z_{\odot}$. Although this shallow metal distribution is in line with the idea that disturbed, non-cool-core clusters originate from the merging of relaxed, cool-core clusters, we find that in some cases, remnants of metal-rich and low entropy cool cores can persist after major mergers. While we obtain a mild anti-correlation between the Fe abundance and the pseudo-entropy in the (lower entropy, K ≈ 200-500 keV cm^2) inner regions, no clear correlation is found at (higher entropy, K ≈ 500-2300 keV cm^2) outer radii. The apparent spatial abundance uniformity that we find at large radii is difficult to explain through an efficient mixing of freshly injected metals, particularly in systems for which the time since the merger is short. Instead, our results provide important additional evidence in favour of the early enrichment scenario in which the bulk of the metals are released outside galaxies at z > 2–3, and extend it from cool-core and (moderate) non-cool-core clusters to a few of the most disturbed merging clusters as well. These results constitute a first step toward a deeper understanding of the chemical history of merging clusters.

4.1 Introduction

In order to become the largest gravitationally bound structures seen in the Universe today, galaxy clusters grow in a hierarchical way, via not only accretion but also merging of surrounding (sub) haloes. The latter case is particularly interesting as major cluster mergers are the most energetic events since the Big Bang. During the merging process, the hot intra-cluster medium (ICM) in galaxy clusters is violently compressed and heated, and large amounts of thermal and non-thermal energy are released, giving rise to shock fronts and turbulence (Markevitch & Vikhlinin 2007). Shocks can propagate into the ICM (re)accelerating electrons (Bell 1987; Blandford & Eichler 1987), which may produce elongated and polarised radio structures known as radio relics via synchrotron radio emission (for a review, see Ferrari et al. 2008; Brunetti & Jones 2014). On the other hand, particle (re)acceleration by means of the turbulence in the ICM could generate unpolarised cluster-wide sources known as radio haloes (for a review, see Brunetti et al. 2001; Feretti et al. 2012; van Weeren et al. 2019).

The ICM is also known to be rich in metals, which originate mainly from core-collapse supernovae (SNcc) and type Ia supernovae (SNIa), which have been continuously releasing their nucleosynthesis products since the epoch of major star formation, about ten billion years ago ($z \sim 2$–3) (Hopkins & Beacom 2006; Madau & Dickinson 2014). SNcc contribute primarily to the synthesis of light metals (O, Ne, Mg, Si and S). On the other hand, heavier metals (such as Ar, Ca, Mn, Fe, and Ni), together with the smaller relative contribution of Si and S, are produced by SNIa. Finally, C and N are mostly released by low-mass stars on the asymptotic giant branch (AGB). Once the metals are ejected to the ICM by SN or AGB stars, they are later transported, mixed, and redistributed via other processes, such as galactic winds (Kapferer et al. 2006, 2007; Baumgartner & Breitschwerdt 2009); ram-pressure stripping (Schindler et al. 2005; Kapferer et al. 2007); active galactic nucleus (AGN) outflows (Simionescu et al. 2008, 2009; Kapferer et al. 2009); or gas sloshing (Simionescu et al. 2010; Ghizzardi et al. 2014); among other processes. Detailed reviews on the observation of metals in the ICM include, for example Werner et al. (2008); Böhringer & Werner (2010); de Plaa (2013) and Mernier et al. (2018b).

In the last years, the Fe abundance distribution in galaxy clusters has been extensively studied using the different X-ray observatories (De Grandi & Molendi 2001; De Grandi et al. 2004; Baldi et al. 2007; Leccardi & Molendi 2008; Maughan et al. 2008; Matsushita 2011; Mernier et al. 2016, 2017; Mantz et al. 2017; Simionescu et al. 2017; Simionescu et al. 2019). The Fe radial distribution is different for cool-core (CC, i.e., dynamically relaxed) clusters and non-cool-core (NCC, i.e., dynamically disturbed) clusters. In the case of CC clusters, the Fe distribution shows a peak in the core, which decreases by up to $\sim 0.3 r_{500}$ and flattens for larger radii. NCC clusters, however, have a flat distribution in the core and follow the same universal distribution as CC for outer radii. These abundance distributions do not present evidence of evolution from now until $z \sim 1$ (McDonald et al. 2016; Mantz et al. 2017; Ettori et al. 2017). Moreover, recent X-ray observations with *Suzaku* (Fujita et al. 2008; Werner et al. 2013; Urban et al. 2017; Ezer et al. 2017; Simionescu et al. 2017) reveal a uniform radial distribution of around ~ 0.2–$0.3\ Z_{\odot}$ in the outskirts of the galaxy clusters, which suggests an early enrichment of the ICM (i.e. $z \sim 2$–3). Numerical simulations later showed that active

galactic nuclei (AGN) feedback at early times is needed to explain these observations (e.g. Biffi et al. 2017, 2018a; Biffi et al. 2018b).

Whereas metals in the ICM have been extensively and systematically studied in CC and, to some extent, NCC clusters, the ICM enrichment in the extreme case of merging clusters has been poorly explored so far (except in a few specific cases; e.g. A3376, Bagchi et al. 2006; A3667, Lovisari et al. 2009; Laganá et al. 2019). Knowing in detail how metals are distributed across merging clusters, however, is a key ingredient in our understanding of the chemical evolution of large scale structures. On one hand metals act as passive tracers and may reveal valuable information on the dynamical history of the recently merged ICM. On the other hand, merging shocks could in principle trigger star formation in neighbouring galaxies (Stroe et al. 2015a; Sobral et al. 2015), hence potentially contributing to the ICM enrichment to some extent (Elkholy et al. 2015). Metallicities in the shocked gas of such disturbed clusters, and their connection with their thermodynamical properties and star formation of their galaxies remain widely unexplored.

In this work, we present for the first time a study specifically devoted to the chemical state of merging clusters. For this purpose, we derive the spatial distribution of temperature, abundance (Fe), and pseudo-entropy from specifically selected regions of six merging galaxy clusters: CIZA J2242.8+5301, 1RXS J0603.3+4214, Abell 3376, Abell 3667, Abell 665, and Abell 2256. The principal characteristics of these clusters are summarized in Table 4.2. The first four clusters of the list are essentially major mergers hosting a double radio relic, while Abell 665 hosts a giant radio halo and Abell 2256 a prominent single radio relic together with a radio halo. The selection criteria of these clusters have been: (i) *XMM-Newton* observation availability, (ii) net exposure time > 25 ks (iii) bright and disturbed central ICM and (iv) probing a variety of diffuse radio features: we include merging clusters with double radio relics, a single radio relic and strong radio halo. This is not intended as a complete sample but rather as an exploratory first step towards future studies on metals in the ICM of merging clusters from larger observational samples. For this study, we report our results with respect to the protosolar abundances ($Z_{\odot}$) reported by Lodders et al. (2009). We assume the cosmological parameters H_0 = 70 km/s/Mpc, $\Omega_{\rm M}$ = 0.27 and Ω_{Λ} = 0.73. All errors are given at 1σ (68%) confidence level unless otherwise stated and the spectral analysis uses the modified Cash statistics (Cash 1979; Kaastra 2017a).

Table 4.1: Observations and exposure times.

Name	Sequence ID	Position (J2000) (RA, Dec.)	Observation starting date	MOS1 (ks)	MOS2 (ks)	pn (ks)
CIZA J2242.8+5301	0654030101	(22:43:01.99, 53:07:30.0)	2010-12-13	71.5	71.9	68.4
1RXS J0603.3+4214	0675060101	(06:03:13.39, 42:12:31.0)	2011-10-03	75.4	75.5	71.4
Abell 3376 East	0151900101	(06:02:08.59, -39:57:18.0)	2003-04-01	27.9	27.8	25.4
Abell 3376 West	0504140101	(06:00:51.14, -40:00:31.6)	2007-08-24	40.8	42.7	36.4
Abell 3667	0206850101	(20:13:04.79, -56:53:60.0)	2004-05-03	59.7	60.7	57.3
Abell 3667 offset	0653050201	(20:12:31.46, -56:21:39.3)	2010-09-21	28.9	28.6	24.7
Abell 665	0109890501	(08:30:57.99, 65:50:20.0)	2001-09-23	80.3	81.4	–
Abell 2256	0401610101	(17:03:02.55, 78:45:00.0)	2006-08-04	39.7	42.6	6.6
	0141380101	(17:03:02.55, 78:45:00.0)	2003-04-27	9.8	10.1	9.5

Table 4.2: Cluster sample description.

Label	z	$N_{\rm H}$[a] (10^{20} cm^{-2})	Radio features	Mass ratio	Dyn. stage[b] (Gyr)	$\langle kT \rangle$ (keV)	Scale f.[c] (kpc/″)
ClZA2242	0.192	25.8–55.7	dR, fh[1]	1–2:1[2,3]	∼0.6[4]	7.9[4]	193.0
1RXSJ0603	0.225	21.5	tR, H[5]	3:1:0.1:0.1[6]	∼2.0[7]	7.8[8]	218.0
A3376	0.046	4.8	dR[9]	3–6:1[10]	∼0.5–0.6[10]	4.2[11]	54.0
A3667	0.055	4.4	dR, MH[12,13]	5:1[14]	∼1.0[14]	6.3[15]	64.5
A665	0.182	4.3	H[16]	1–2:1[17]	∼1–2[17]	8.3[18]	184.5
A2256	0.058	4.2	R, H[19,20]	3:1:0.3[21]	∼–0.2[22]	6.4[23]	67.5

[a] Willingale et al. (2013) (http://www.swift.ac.uk/analysis/nhtot/)

[b] All dynamical stages are after core passage except A2256 (pre-merger).

[c] 1 arcmin value in kpc assuming the cosmological parameters H_0 = 70 km/s/Mpc, $\Omega_{\rm M}$ = 0.27 and Ω_Λ = 0.73 for each z.

[d] R: Relic, dR: Double relic, tR: Triple relic, fH: faint halo, H: halo, MH: mini-halo

References: [1] van Weeren et al. (2010), [2] van Weeren et al. (2011b), [3] Jee et al. (2015), [4] Akamatsu et al. (2015), [5] van Weeren et al. (2012a), [6] Jee et al. (2016), [7] Brüggen et al. (2012), [8] Ogrean et al. (2013b), [9] Bagchi et al. (2006), [10] Machado & Lima Neto (2013), [11] Urdampilleta et al. (2018), [12] Röttgering et al. (1997), [13] Riseley et al. (2015), [14] Roettiger et al. (1999), [15] Sarazin et al. (2016), [16] Moffet & Birkinshaw (1989), [17] Gomez et al. (2000), [18] Hughes & Tanaka (1992), [19] Bridle & Fomalont (1976), [20] Clarke & Ensslin (2006), [21] Berrington et al. (2002), [22] Roettiger et al. (1995), [23] Trasatti et al. (2015)

4.2 Observations and data reduction

Table 1 summarizes the *XMM-Newton* observations, the different pointings and the net exposure time used for the cluster survey analysis. All the data are reduced with the *XMM-Newton* Science Analysis System (SAS) v17.0.0, with the calibration files dated by June 2018. We used the observations from the MOS and pn detectors of the EPIC instrument and reduced them first with the standard pipeline commands `emproc` and `epproc`. Next, we filter the soft-proton (SP) flares by building Good Time Interval (GTI) files following the method detailed in Appendix A.1 of Mernier et al. (2015). This method consists of extracting light curves at the high energy range of spectrum (10–12 keV for MOS and 12–14 keV for pn) in bins of 100s. Then, the mean count rate, μ, and the standard deviation, σ, are calculated in order to apply a threshold of $\mu \pm 2\sigma$ to the generated distribution. Therefore, all the time bins with a number of counts outside the interval $\mu \pm 2\sigma$ are rejected. Afterwards, we apply the same process at the low energy range 0.3–2 keV with bins of 100s (Lumb et al. 2002). Only events satisfying the 2σ threshold in the two energy ranges mentioned above are further considered. The point source identification in the complete field of view (FOV) is done with the SAS task `edetect_chain` applied in four different bands (0.3–2.0 keV, 2.0–4.5 keV, 4.5–7.5 keV, and 7.5–12 keV). After this, we combine the detections in these four bands and exclude the point sources with a circular region of 10″ radius, except some larger sources where an appropriate radius has been applied. The 10″ radius size, as explained in Appendix A.2 of Mernier et al. (2015), is optimised for avoiding the polluting flux of the point

sources and not reducing considerably the emission of the ICM. We keep the single, double, triple and quadruple events in MOS (`pattern`≤12) and only the single pixel events in pn (`pattern`==0). We also correct the out-of-time events from the pn detector. [1]

4.3 Spectral analysis

4.3.1 Spectral analysis approach

In our spectral analysis of the clusters, we assume that the observed spectra include the following components (see EPIC MOS2 spectrum in Fig. 4.1): an optically thin thermal plasma emission from the ICM in collisional ionization equilibrium (CIE), the local hot bubble (LHB), the Milky Way halo (MWH), the cosmic X-ray background (CXB) and the non X-ray background (NXB), consisting of hard particle (HP) background and residual soft-proton (SP) component (see Sect. 4.3.2). An additional hot foreground (HF) component is included for CIZA J2242.8+5301 as suggested by Ogrean et al. (2013a) and Akamatsu et al. (2015). Further details about these components (and how we include them in the fits) are given in Sect. 3.2. The emission models are corrected for the cosmological redshift and absorbed by the galactic interstellar medium. The hydrogen column density value adopted for all the clusters is the weighted neutral hydrogen column density, $N_{\rm HI}$, estimated using the method of Willingale et al. (2013)[2]. Previous work (e.g. Mernier et al. 2016; de Plaa 2017) noted that the total $N_{\rm H}$ value (neutral + molecular hydrogen) may sometimes provide inaccurate fits whereas the weighted neutral hydrogen $N_{\rm HI}$ values are generally closer to the best-fit $N_{\rm H}$ values. Specifically, we have checked that leaving free the $N_{\rm H}$ in our fits provides values that do not deviate more than $\sim$10% from the above estimates. The only exception is CIZA J2242.8+530, for which we need to leave the value of $N_{\rm H}$ free within the range 0.8 x $N_{\rm HI}$ $\leq$ $N_{\rm H}$ $\leq$ 1.2 x $N_{\rm H,tot}$, where $N_{\rm H,tot}$ is the weighted total (neutral and molecular) hydrogen column density (Willingale et al. 2013).

In our spectral analysis, we use SPEX[3] (Kaastra et al. 1996, 2017c) version 3.04.00 with SPEXACT (SPEX Atomic Code and Tables) version 3.04.00. We carry out the spectral fitting in different regions as detailed in the sections below. The redistribution matrix file (RMF) and the ancillary response file (ARF) are processed using the SAS tasks `rmfgen` and `arfgen`, respectively. The spectra of the MOS (energy range from 0.5 to 10 keV) and pn (0.6–10 keV) detectors are fitted simultaneously and binned using the method of optimal binning described in Kaastra & Bleeker (2016). We assume a single temperature structure in the collisional ionization equilibrium (*cie* model from SPEX) component for all the clusters (this assumption is justified in Sect. 4.3.3). Because the high temperature of merging clusters does not allow to measure other metals with reasonable accuracy, their abundances are coupled to Fe. The free parameters considered in this study are the temperature *kT*, the metal abundance *Z* and the normalization *Norm*. In the case of CIZA J2242.8+5301, the column density $N_{\rm H}$ is also free to vary.

[1] https://www.cosmos.esa.int/web/xmm-newton/sas-thread-epic-oot
[2] http://www.swift.ac.uk/analysis/nhtot/
[3] https://www.sron.nl/astrophysics-spex

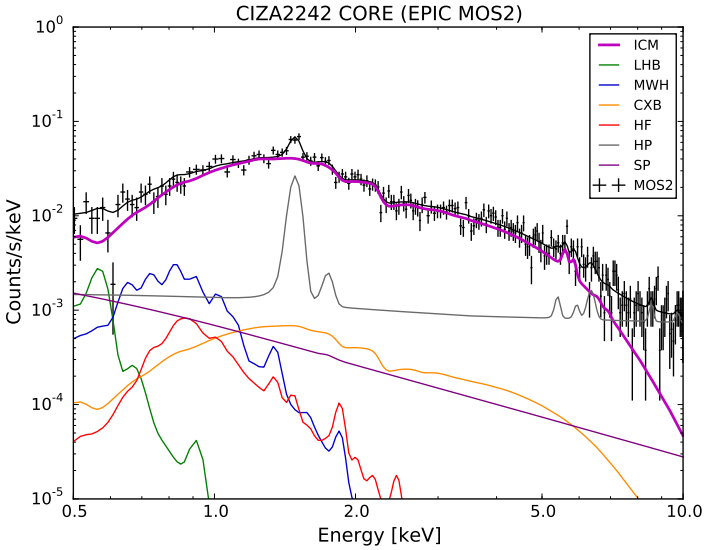

Figure 4.1: EPIC MOS2 spectrum of CIZA2242 core (r = 1.5′). The solid black line represents the best-fit model. The cluster emission ICM and all background components (LHB, MHW, CXB, HF, HP and SP) are also shown.

4.3.2 Estimation of background spectra

A proper estimation of the background components is important especially in the regions where the emission of the cluster is low. This is particularly relevant outside of the core, where the spectrum can be background dominated. In this work, we model the background components directly from our spectra (Sect. 4.3.1) using the following list of components:

- The LHB, modelled by a non-absorbed cie component with proto-solar abundance. The temperature is fixed to 0.08 keV.
- The MWH, modelled by an absorbed cie component with proto-solar abundance. The temperature is free to vary except for CIZA J2242.8+5301 and Abell 3376, where it is fixed to 0.27 keV, following the values of Akamatsu et al. (2015) and Urdampilleta et al. (2018), respectively.
- The CXB, modelled by an absorbed power law with a fixed Γ = 1.41 (De Luca & Molendi 2004). The normalization is a fixed value for each cluster assuming the CXB flux of 8.07 x 10^{-15} W m^{-2} deg^{-2}, taking into account a detection limit of S_c = 3.83 x 10^{-15} W m^{-2} and calculated with the CXBTools (de Plaa 2017). See details in Appendix B.2

of Mernier et al. (2015).[4]

- The HF, modelled by an absorbed cie component with proto-solar abundance. The temperature is fixed to 0.7 keV.
- The HP background, modelled by a broken power law (unfolded by the effective area) together with several instrumental Gaussian profiles (eight and nine for MOS and pn, respectively). The photon indices of the power laws and the centroid energies of the profiles have been taken from Table B.1 and Table B.2 of Mernier et al. (2015), see their Appendix B.1 for more details. The normalizations are left free to vary.
- The SP background, modelled by a power law (unfolded by the effective area). The power law index of the SP component is left free to vary between 0.1 and 1.4.

The estimation of the sky background components (LHB, MHW, and HF) is obtained from the offset regions (see green sectors in Fig. 4.2, 4.4, 4.8, 4.10 and 4.12) where a negligible (yet still modelled) thermal emission of the cluster is expected and the background is dominant. For Abell 3376 the values of Urdampilleta et al. (2018) are adopted. The parameters of the SP components are obtained fitting the total FOV ($r = 15'$) EPIC spectra, where the *cie* (i.e. ICM) parameters are also left free. Finally, the normalization of every background component (except the HP background) has been fixed, rescaled on the sky area of each region and corrected for vignetting if necessary. The best-fit parameters for each cluster are listed in Appendix A.

4.3.3 Systematic uncertainties

We account for the effect of systematic uncertainties related to the $\pm 10\%$ variation in the normalization of the sky background and non X-ray background components (Mernier et al. 2017). The contribution of these systematic uncertainties are further included in our analysis and results.

Mernier et al. (2017) and the posterior review of Mernier et al. (2018b) list other potential systematic uncertainties, which could affect the abundance measurements of this work. These include MOS-pn discrepancies due to residual EPIC cross-calibration, projection effects, atomic code and thermal structure uncertainties. The former has limited impact on the relative Fe abundance distribution as explained by Mernier et al. (2017). Although recent work of Liu et al. (2018) suggests that projection effects may have non-negligible observational biases on the observed abundance evolution in the core of CC clusters, the lack of strong emission gradients in merging clusters makes us confident that such a bias is limited in our case. Moreover, deprojecting merging cluster emission is very challenging, as by definition these systems are far from being spherically symmetric.

Uncertainties regarding the atomic codes are limited by the fact that we are using the update of the code SPEXACT and SPEX, which incorporate more precise modelling of the

[4] It should be noted that the flux of the faintest resolved and excluded point source, and hence the remaining unresolved CXB flux, depend on the exposure time. In our case, most of the observations have similar a exposure except two: 0151900101 and 0653050201. Even for these data sets, the SP power law norm is free to vary and will compensate for any residuals in the CXB subtraction.

atomic processes and extensive compilation of transitions. However, uncertainties due to a not complete atomic database are still present (Hitomi Collaboration et al. 2018a) and their effects can be non-negligible (Mernier et al. 2018a).

For the thermal structure, we assume a single-temperature (1T) model. This is a simplified approximation; other more complex models reproducing Gaussian (`gdem`, de Plaa et al. 2006) or power-law (`wdem`, Kaastra et al. 2004) temperature distributions could represent better the inhomogeneities of the ICM. To quantify these possible effects, we have fitted the spectra assuming a simplified version of the `gdem` model using a 3T model with one main temperature free and the other two coupled with a factor of 0.64 and 1.56, respectively. We have realised the fits in the SPEXACT version 2.07.00 in order to significantly reduce the computing time. This version includes simpler atomic code and tables, which allows to fit the spectra faster, but with a similar accuracy as the most updated version (for more details, see Mernier et al. 2018a). We verify that the best-fit temperature of the main component in our 3T model remains within $\pm$ 5% of the best-fit temperature obtained when assuming a 1T model. The relative emission measure of the other two components are less than 1% of the best-fit emission measure of the 1T model, and the variation in the abundance is less than 10%. This 1T-like behavior is not surprising as, unlike CC clusters, merging clusters do not exhibit a strong temperature gradient, and at these high temperatures the Fe abundance is almost entirely determined from the Fe-K line (which is unaffected by the Fe-bias or the inverse Fe-bias, e.g. Buote 2000, Simionescu et al. 2009). For this reason and for simplicity we decide to maintain the 1T model and we will add these uncertainties to the other background systematic uncertainties as the thermal structure contribution.

4.4 Spectral analysis: individual clusters

4.4.1 CIZA J2242.8+5301

CIZA J2242.8+5301 (hereafter CIZA2242, also known as the 'Sausage' cluster) is a massive ($\sim 10^{15} M_{\odot}$) and two-body (Jee et al. 2015) merging galaxy cluster at a redshift of $z = 0.192$. It was discovered in the second CIZA sample from the *ROSAT* All-Sky Survey and identified as a major-merger by Kocevski et al. (2007). van Weeren et al. (2010) studied CIZA2242 for the first time using WSRT, GMRT, and VLA. They observed a double radio relic feature located at $\sim$1.5 Mpc from the cluster centre. *XMM-Newton* and *Chandra* observations (Ogrean et al. 2013a, 2014) reveal a strongly disturbed and complex merger. In fact, the ICM presents an elongated X-ray morphology with a bullet shape bright edge in the south (S) and more irregular edge in the north (N), suggesting that the infalling direction is N to S. Akamatsu et al. (2015) estimate the time after the core passage to be $\sim$0.6 Gyr, in good agreement with the Sunyaev–Zel'dovich (SZ) analysis of Rumsey et al. (2017).

Finally, Stroe et al. (2014a); Stroe & Sobral (2015b); Sobral et al. (2015); Stroe et al. (2017) confirm an overdensity of H_{α} emitters, mainly cluster star-forming galaxies and AGNs, concentrated close to the subcores and northern post-shock region. The star-forming galaxies are found to be highly metal rich and to have strong outflows. The above mentioned authors propose that such an enhancement of the star formation ratio could be a shock-induced effect.

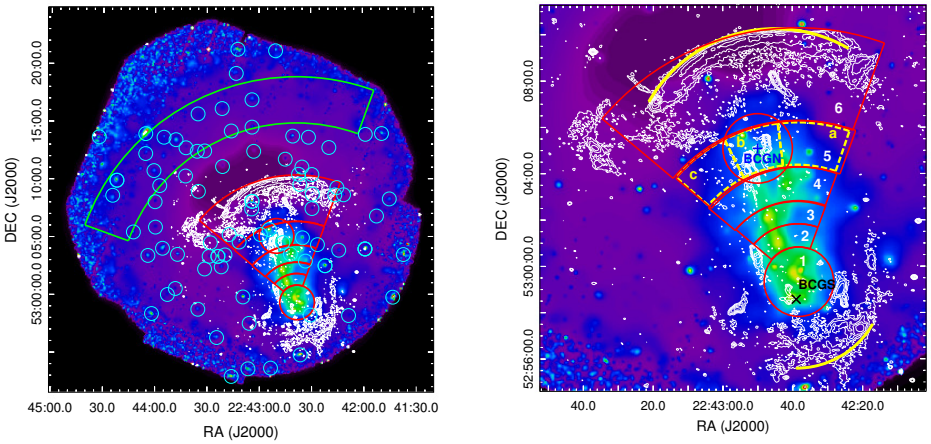

Figure 4.2: *Left panel*: *XMM-Newton* smoothed image in the 0.3–10 keV band of CIZA2242.The red sectors represent the regions used for the radial temperature and abundance profiles. The green sector is the offset region used for the sky background estimation. Cyan circles are the point sources removed (with enlarged radius for clarity purpose). White contours are LOFAR radio contours. *Right panel*: Enlarged image of CIZA2242. The BCGN and BCGS are marked with blue and black crosses, respectively. The solid yellow lines show the X-ray shocks position.

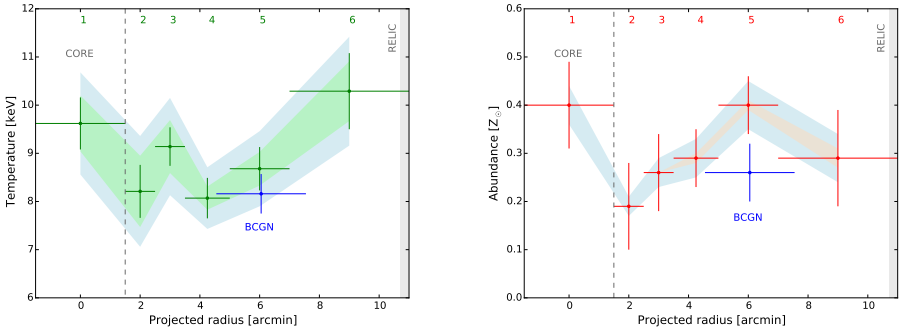

Figure 4.3: *Left panel*: Temperature distribution along the merging axis of CIZA2242. *Right panel*: Abundance distribution along the merging axis of CIZA2242. The shaded areas represent the systematic uncertainties: green and orange shadows correspond to the background normalization variation, and the blue one to the temperature structure. The shaded grey area shows the radio relic position. The dashed line shows the outer edge of the core spectral extraction region. The numbers and the BCGN blue point correspond to the regions and the red circle centred on BCGN, respectively, shown in Fig. 4.2.

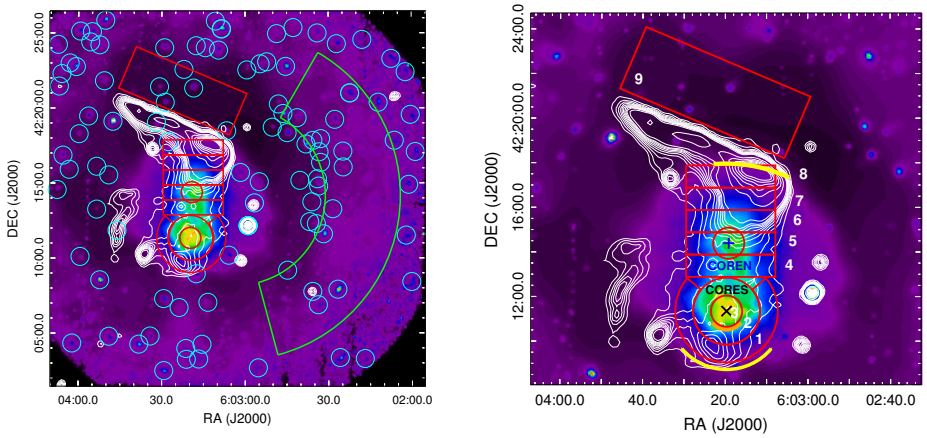

Figure 4.4: *Left panel*: *XMM-Newton* smoothed image in the 0.3–10 keV band of 1RXSJ0603. The red sectors represent the regions used for the temperature and abundance distributions. The green sector is the offset region used for the sky background estimation. Cyan circles are the point sources removed, with enlarged radius for clarity purpose. White contours are LOFAR HBA radio contours. *Right panel*: Enlarged image of 1RXSJ0603. The COREN and CORES are marked with blue and black crosses, respectively. The solid yellow and orange lines show the X-ray shock and cold front position. The numbers label the regions used in the spectral fitting.

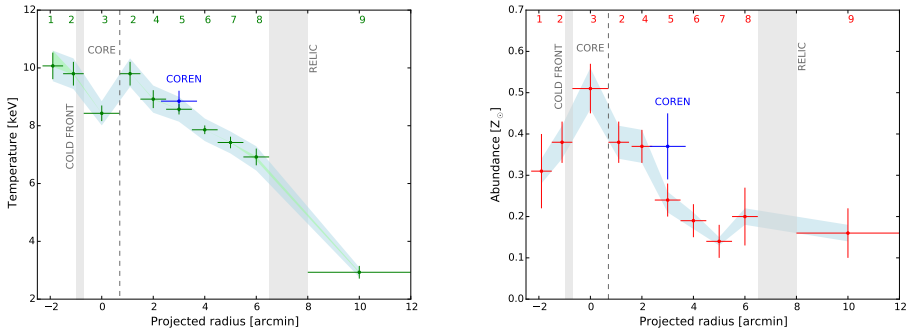

Figure 4.5: *Left panel*: Temperature distribution along the merging axis of 1RXSJ0603. *Right panel*: Abundance distribution along the merging axis of 1RXSJ0603. The shaded areas represent the systematic uncertainties: the green shadow correspond to the background normalization variation, and the blue one to the temperature structure. The shaded grey areas show the cold front and radio relic position. The dashed line shows the outer edge of the core spectral extraction region. The numbers and COREN blue point correspond to the regions and the red circle centred on COREN, respectively shown in Fig. 4.4.

We fit the cluster emission and the background spectra (see Table 4.5) in the sectors shown in Fig. 4.4, having excluded the point sources. We leave $N_{\rm H}$ free to vary between 0.8 x $N_{\rm HI} \leq\ N_{\rm H} \leq$ 1.2 x $N_{\rm HTotal}$, where $N_{\rm HI}$ = 3.22 $\times$ 10^{21} cm^{-2} and $N_{\rm HTotal}$ = 4.64 $\times$ 10^{21} cm^{-2} (Willingale et al. 2013), as explained in Section 4.3.1. The two circular regions are centred close to the two brightest cluster galaxies (BCGs) or subcores of the bimodal merger system described by Dawson et al. (2015) (BCGN: $22^{\rm h}42^{\rm m}50^{s}00$, $53^{\circ}05'06''00$; BCGS: $22^{\rm h}42^{\rm m}39^{s}00$, $52^{\circ}58'35''00$). We use as centroid the southern 'core', because it contains the X-ray peak emission and is close to the southern BCG.

The best-fit parameters are shown in Table 4.13, while the temperature and abundance distributions along the merging axis are plotted in Fig. 4.3. By convention, and for all the further relevant figures in this paper, the regions lying behind the projected main BCG trajectory are plotted with positive values on the x-axis. The temperature distribution presents a variation in the range between ∼8–10 keV within the inner regions of the X-ray emission. This temperature is higher in the last annular region, coincident with the post-shock region as described in Ogrean et al. (2014) and Akamatsu et al. (2015). These results are in good agreement within the uncertainties with the temperature map obtained by Ogrean et al. (2013a) and the radial profile of Akamatsu et al. (2015).

Between the two BCGs (sectors two to four) the Fe abundance is measured at its lowest value, between ∼0.2–0.3 $Z_{\odot}$. Moreover, the abundance profile shows an apparent enhancement with a maximum value of ∼0.4 $Z_{\odot}$ in sectors one and five, where the two BGCs are located. The northern BCG region evinces a lower abundance than the entire sector five. If we divide sector five in three regions, we obtain a gradient in the abundance and slight increase in the temperature towards the east, see Table 4.13. BCGN coincides mostly with region 5b and the enhancement in abundance in sector five is mainly driven by region 5a.

4.4.2 1RXS J0603.3+4214

1RXS J0603.3+4214 (hereafter 1RXSJ0603), also known as the 'Toothbrush' cluster, is a bright, rich and massive cluster discovered by van Weeren et al. (2012a) and located at z = 0.225. It hosts three radio relics and a giant (∼2 Mpc) radio halo elongated along the main merger axis S–N, which follows the X-ray emission morphology excluding the southernmost part (Ogrean et al. 2013b; Rajpurohit et al. 2018). Stroe et al. (2014b) found no enhancement of H_{α} emitters near the northern radio relic, with a star formation rate (SFR) consistent with that of blank field galaxies at z = 0.2. They concluded that the lack of H_{α} emitters could be possible because 1RXSJ0603 is a well evolved system, approximately ∼2 Gyr after the core passage.

As shown in Fig. 4.4, we use various sectors to fit the cluster emission and the background spectra (see Table 4.6), excluding the point sources and using $N_{\rm HI}$ = 2.15 $\times$ 10^{21} cm^{-2} (Willingale et al. 2013). We follow the X-ray emission S–N shape, coincident with the radio halo elongation with boxes four to eight, as well as the pre-shock region nine. We dedicate two circular sectors to the subcores of the main two subclusters, locating the brightest one in X-rays at the south (CORES: $6^{\rm h}03^{\rm m}13^{s}39$, $42^{\circ}12'31''00$) and the second at the north (COREN: $6^{\rm h}03^{\rm m}19^{s}17$, $42^{\circ}14'24''00$). We use CORES as centroid for our temperature

and abundance distributions along the merging axis (see Fig. 4.5).

The best-fit parameters are presented in Table 4.14 and are in good agreement with the previous X-ray studies by Ogrean et al. (2013b); Itahana et al. (2015); and van Weeren et al. (2016). The subcore temperatures (kT = 8.43 $\pm$ 0.27 keV for CORES and kT = 8.85 $\pm$ 0.36 keV for COREN) are consistent with van Weeren et al. (2016). Interestingly, we find a peak in Fe abundance located in the inner core, just behind the cold front (CF) (see Fig. 4.5; its location is approximated based on van Weeren et al. 2016). In the south, we see a slight temperature gradient towards the southern shock front, anticorrelated with a decrease in Fe abundance. The COREN shows the same abundance as the adjacent inner region, but a higher value than in the outer sectors (six to nine). It is possible that the gas belonging to this subcluster has been stripped during the merger and is mixing in that region. In the north, a gradual smooth decrease of temperature can be observed up to the post-shock region, followed by a significant drop after the radio relic. Meanwhile, the Fe abundance decreases in sector five and flattens later around $\sim$0.2 $Z_{\odot}$ for the outer sectors.

4.4.3 A3376

Abell 3376 (hereafter A3376) is a bright and nearby (z = 0.046) merging galaxy cluster located in the southern hemisphere. The N-body hydrodynamical simulations of Machado & Lima Neto (2013) suggest a two body merger scenario with a mass ratio of 3–6:1. The more massive and diffuse western subcluster core (BCG1: $6^{\rm h}00^{\rm m}41^{s}10$, $-40^{\circ}02'40''00$) has been disrupted by a dense and compact eastern subcluster (BCG2: $6^{\rm h}02^{\rm m}09^{s}70$, $-39^{\circ}57'05''00$). Recent studies suggest that the core-passing took place $\sim$0.5–0.6 Gyr ago in the W–E direction (Durret et al. 2013; Monteiro-Oliveira et al. 2017; Urdampilleta et al. 2018). Due to the merger, the inner gas of A3376 follows a cometary tail X-ray morphology as shown in Fig. 4.6. A3376 hosts two giant ($\sim$Mpc) arc-shaped radio relics (Bagchi et al. 2006) in the periphery of the cluster. X-ray analyses with the *Suzaku* satellite (Akamatsu et al. 2012; Urdampilleta et al. 2018) confirm the presence of a X-ray shock front located at the western radio relic, another shock probably associated with the eastern 'notch' (Paul et al. 2011; Kale et al. 2012) and a cold front at 3′ from the center.

In the spectral analysis of A3376 we use two different observations as listed in Table 1. Specifically, ObsI:0151900101 is used for regions one, two, and three, while ObsID:0504140101 is used for regions six and seven . In addition, both these observations are used for the overlapping regions four and five. The background modelling parameters for each of the observations are shown in Table 4.7 and Table 4.8. We fit the spectra of the annular sectors centred on BCG2, located close to the X-ray peak emission at the eastern subcluster. We assume the column density as $N_{\rm HI}$ = 4.84 $\times$ 10^{20} cm^{-2} (Willingale et al. 2013). The best-fit parameters (see Table 4.15) are in good agreement with previous studies with the *Suzaku* satellite (Akamatsu et al. 2012; Urdampilleta et al. 2018).

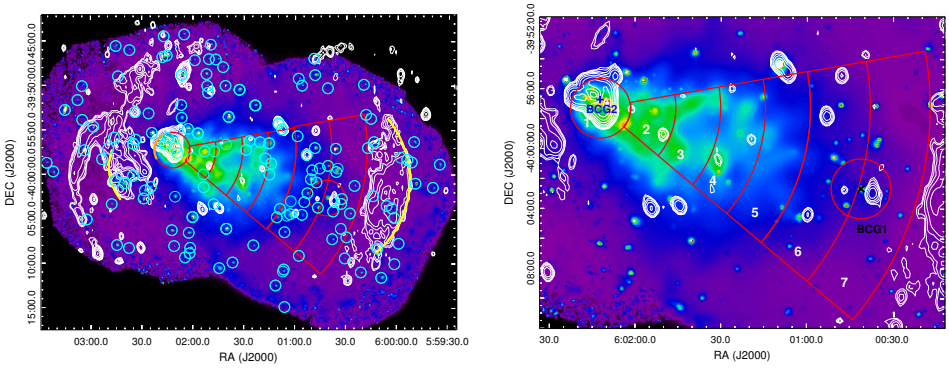

Figure 4.6: *Left panel*: *XMM-Newton* smoothed image in the 0.3–10 keV band of A3376. The red sectors represent the regions used for the temperature and abundance distributions. Cyan circles are the point sources removed, with enlarged radius for clarity purpose. White contours are VLA 1.4 GHz radio contours. The solid yellow and orange lines show the X-ray shocks and cold front position, respectively. *Right panel*: The BCG2 and BCG1 are marked with blue and black crosses. The numbers label the regions used in the spectral fitting.

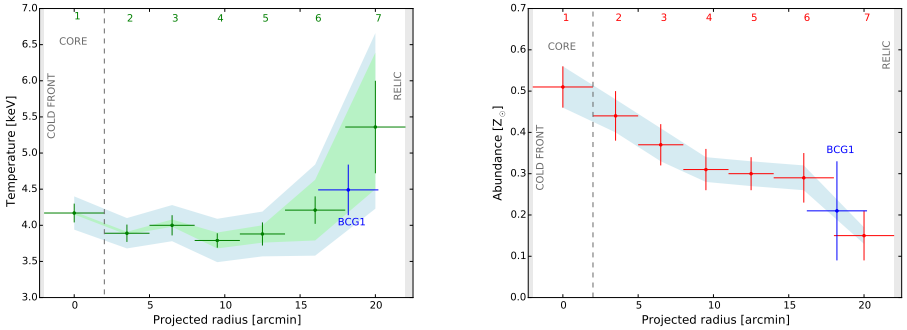

Figure 4.7: *Left panel*: Temperature distribution along the merging axis of A3376. *Right panel*: Abundance distribution along the merging axis of A3376. The shadow area represent the systematic uncertainties. The shaded areas represent the systematic uncertainties: the green shadow correspond to the background normalization variation, and the blue one to the temperature structure. The shaded grey areas show the cold front and radio relic position. The dashed shows the outer edge of the core spectral extraction region. The numbers and BCG1 blue point correspond to the regions and the red circle centred on BCG1, respectively shown in Fig. 4.6.

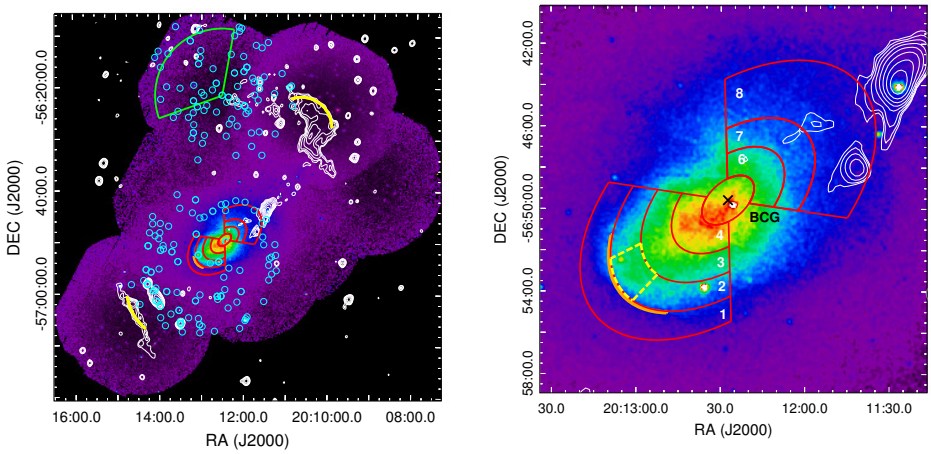

Figure 4.8: *Left panel*: *XMM-Newton* smoothed image in the 0.3–10 keV band of A3667. The red elliptical sectors represent the regions used for the temperature and abundance distributions. The green sector is the offset region used for the sky background estimation. Cyan circles are the point sources removed, with enlarged radius for clarity purpose. White contours are SUMSS radio contours. The solid yellow and orange lines show the X-ray shocks and cold front position, respectively. *Right panel*: Enlarged image of A3667. The BCG is marked with black cross. The solid orange line shows the cold front position. In addition to sector 2, the dashed yellow sector corresponds to a region considered also separately (see text). The numbers label the regions used in the spectral fitting.

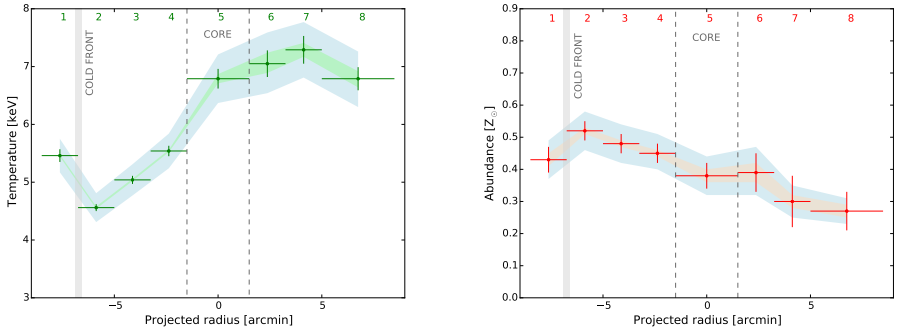

Figure 4.9: *Left panel*: Temperature distribution along the merging axis of A3667. *Right panel*: Abundance distribution along the merging axis of A3667. The shaded areas represent the systematic uncertainties: green and orange shadows correspond to the background normalization variation, and the blue one to the temperature structure. The shaded grey area shows the cold front position. The dashed lines show the outer edges of the core spectral extraction region. The numbers correspond to the regions shown in Fig. 4.8.

The temperature distribution of A3376 (Fig. 4.7) shows a central region with an average temperature ∼4 keV out to the outer radii where an increase of the temperature is seen. It is associated to the post merger region behind the western X-ray shock as described by Urdampilleta et al. (2018). The Fe abundance profile shows a peak of ∼0.5 $Z_\odot$ in the core, coincident with the BCG2. At larger distances, the abundance decreases smoothly to reach ∼0.3 $Z_\odot$ in regions four, five, and six, including BCG1 (dashed annular sector in Fig. 4.6) and in the surrounding diffuse gas. The lower abundance value appears in the outermost region of the cluster before the X-ray shock.

4.4.4 A3667

Abell 3667 (hereafter A3667) is a widely studied bright, low redshift (z = 0.0553) and bimodal merging galaxy cluster (Markevitch et al. 1999). As a consequence of a violent merger along the northwest (NW) direction, A3667 hosts two curved radio relics to the NW and SE (Röttgering et al. 1997; Johnston-Hollitt 2003; Johnston-Hollitt & Pratley 2017; Carretti et al. 2013; Hindson et al. 2014; Riseley et al. 2015). The inner central region shows an elongated morphology of high-abundance gas in SE-NW direction (Mazzotta et al. 2002; Briel et al. 2004; Lovisari et al. 2009) according to the subcluster infall direction. A3667 also includes a prominent mushroom-like cold front close to the center at SE (Vikhlinin et al. 2001; Briel et al. 2004; Owers et al. 2009; Datta et al. 2014; Ichinohe et al. 2017).

We fit the cluster emission and the background spectra (see Table 4.9) in the elliptical regions as shown in Fig. 4.8, excluding the point sources and using $N_{\rm HI}$ = 4.44 × 10^{20} cm^{-2} (Willingale et al. 2013). We use as centroid the main BCG ($20^{\rm h}12^{\rm m}27^{s}43$, $-56^\circ49'35''85$), which is close to the X-ray emission peak ($20^{\rm h}12^{\rm m}27^{s}$, $-56^\circ50'11''00$). We distribute the elliptical sectors along the merging axis assuming the BCG as the center and following the X-ray morphology described by Briel et al. (2004).

The best-fit parameters are summarized in Table 4.17 and represented in the distributions along the merging axis in Fig 4.9. The results are in good agreement with previous studies (Briel et al. 2004; Lovisari et al. 2009; Akamatsu & Kawahara 2013a; Datta et al. 2014; Ichinohe et al. 2017). The distributions show a clear temperature decrease towards the cold front at SE. It has an opposite trend with the Fe abundance, which reaches a peak just behind the cold front. The value presented here is lower than the maximum found by Briel et al. (2004) and Lovisari et al. (2009) of ∼0.7 $Z_\odot$, probably because our value includes larger azimuthal angles with lower abundance. However, if we select a smaller region in sector two (yellow dashed lines in Fig. 4.8), the temperature drops to 3.77 ± 0.09 keV and the abundance increases up to 0.64 ± 0.06 $Z_\odot$. As pointed out by Lovisari et al. (2009), this behaviour agrees with the simulations of Heinz et al. (2003), which suggest a possible displacement of the central rich and cold gas of the subcluster center well to the front during the infall, due to the internal dynamics of the cold front. The sectors in the NW direction (six to nine) show a temperature distribution close to ∼7 keV, meaning the average temperature of the cluster (Markevitch et al. 1999), and consistent with the hot tail described by Briel et al. (2004). The abundance in the central regions (two to four) is almost uniform, around ∼0.4 $Z_\odot$, but higher than the main cluster value (∼0.2–0.3 $Z_\odot$). Finally, the abundance is again flat in the outermost regions (seven to eight) close to ∼0.3 $Z_\odot$.

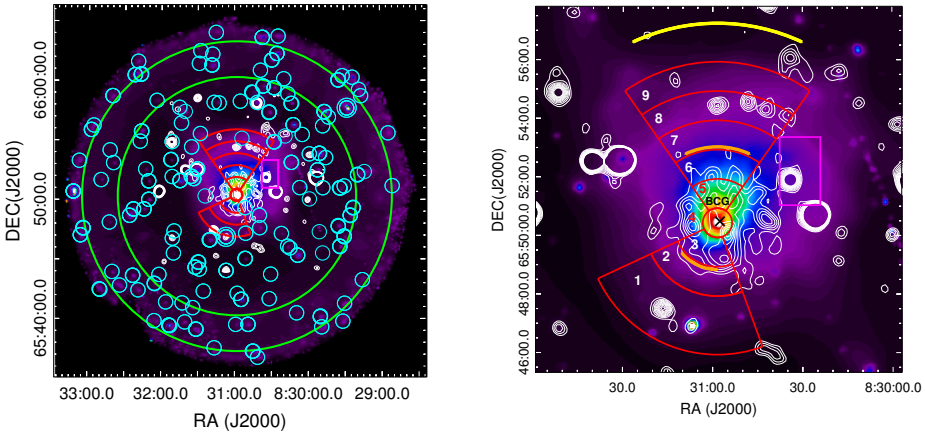

Figure 4.10: *Left panel*: *XMM-Newton* smoothed image in the 0.3–10 keV band of A665. The red sectors represent the regions used for the temperature and abundance distributions. The green annulus is the offset region used for the sky background estimation. Cyan circles are the point sources removed, with enlarged radius for clarity purpose. White contours are VLA 1.4 GHz radio contours. *Right panel*: Enlarged image of A665. The BCG is marked with a black cross. The magenta box includes the cooler gas region observed by Markevitch & Vikhlinin (2001). The solid yellow and orange lines show the X-ray shock and cold fronts position, respectively. The numbers label the regions used in the spectral fitting.

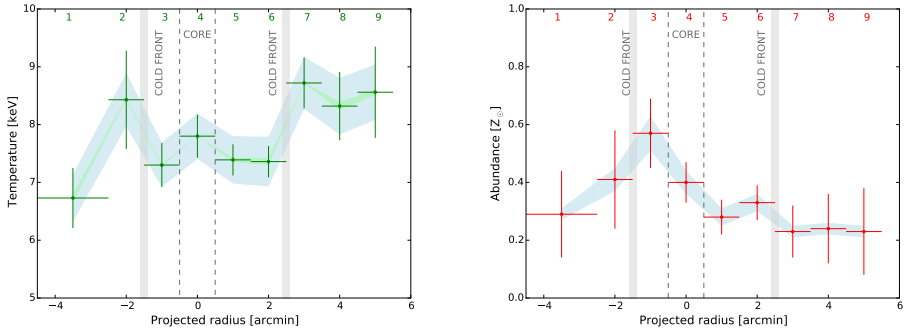

Figure 4.11: *Left panel*: Temperature distribution along the merging axis of A665. *Right panel*: Abundance distribution along the merging axis of A665. The shaded area represent the systematic uncertainties: green shadow correspond to the background normalization variation, and the blue one to the temperature structure. The shaded grey areas show the cold fronts position. The dashed lines show the outer edges of the core spectral extraction region. The numbers correspond to the regions shown in Fig. 4.10.

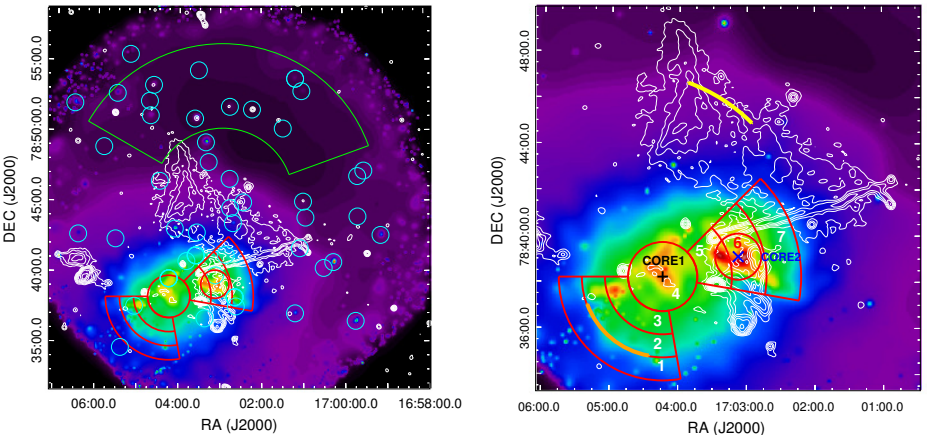

Figure 4.12: *Left panel*: *XMM-Newton* smoothed image in the 0.3–10 keV band of A2256. The red sectors represent the regions used for the temperature and abundance distributions. The green sector is the offset region used for the sky background estimation. Cyan circles are the point sources removed, with enlarged radius for clarity purpose. White contours are WRST radio contours. *Right panel*: Enlarged image of A2256. The CORE1 and CORE2 are marked with a black and blue crosses, respectively. The solid yellow and orange lines show the X-ray shocks and cold front position. The numbers label the regions used in the spectral fitting.

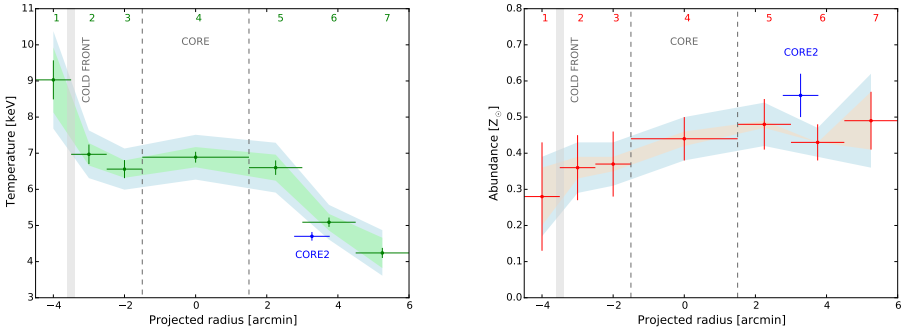

Figure 4.13: *Left panel*: Temperature distribution along the merging axis of A2256. *Right panel*: Abundance distribution along the merging axis of A2256. The shaded area represent the systematic uncertainties: green and orange shadows correspond to the background normalization variation, and the blue one to the temperature structure. The shaded grey area shows the cold front position. The dashed lines show the outer edges of the core spectral extraction region. The numbers and CORE2 blue point correspond to the regions and the red circle centred on CORE2, respectively shown in Fig. 4.12.

4.4.5 A665

The two-body merging cluster Abell 665 (hereafter A665) was discovered as a non-relaxed cluster in an optical observation of Geller & Beers (1982). The authors found the first evidence of an elongated morphology and non-relaxed galaxy cluster. A665 is a hot cluster with an average temperature of ∼8.3 keV (Hughes & Tanaka 1992) and located at z = 0.182 (Gomez et al. 2000). The N-body hydrodynamical simulations and dynamic studies of Gomez et al. (2000) suggest a subcluster merger in the NW–SE direction with two similar masses. The bright core of the infalling subcluster is moving south, crossing a more diffuse halo, before being stripped by ram pressure. A665 hosts a giant radio halo (Jones & Saunders 1996; Feretti et al. 2004b; Vacca et al. 2010), which follows the X-ray emission elongation. The X-ray observations of A665 (Markevitch & Vikhlinin 2001; Govoni et al. 2004; Dasadia et al. 2016a) have revealed only one X-ray peak ($8^{\rm h}30^{\rm m}59^{s}8$, $65^{\circ}50'31''3$), close to the BCG, which indicates that only the infalling cluster core has survived the merger. The remnant core presents a nearby cold front in the SE, followed by a hot gas (∼8–15 keV) thought to be a post-merger region of a shock (Markevitch & Vikhlinin 2001; Govoni et al. 2004).

We use spectra from MOS, the only detector available for these observations, to fit the cluster emission together with the modelled background (Table 4.10). We analyze the circular sectors centred on the BCG ($8^{\rm h}30^{\rm m}57^{s}.6$, $65^{\circ}50'29''6$) as shown in Fig. 4.10, using $N_{\rm HI}$ = 4.31 × 10^{20} cm^{-2} (Willingale et al. 2013). The best-fit parameters are presented in the Table 4.18 and plotted in Fig. 4.11.

The temperature and Fe abundance distributions along the merging axis show the presence of the two cold fronts as described by previous X-ray studies (Markevitch & Vikhlinin 2001; Govoni et al. 2004; Dasadia et al. 2016a). We see a slight temperature decrease across them towards the center. The abundance peak is found just within the south cold front and reflects the same case described by Heinz et al. (2003) for A3667. The diffuse gas in the north presents a lower abundance and a more uniform distribution (∼0.2–0.3 $Z_{\odot}$) than the gas in the core and just behind the cold front in the south. This could indicate that the gas belongs to the more diffuse cluster, which had been already disrupted by the core-crossing. The two cold fronts seem to delimit a central region with a lower temperature (∼7 keV) than the surrounding gas. We found as well the cooler gas region (kT = 7.4 ± 0.2, Z = 0.33± 0.06 $Z_{\odot}$) in the north observed by Markevitch & Vikhlinin (2001) and shown in Fig. 4.10 as a magenta box. This cooler region seems to belong to the infalling cluster coming from the NW direction as described by Markevitch & Vikhlinin (2001) and Govoni et al. (2004).

4.4.6 A2256

Abell 2256 (hereafter A2256) is a nearby (z = 0.058) rich galaxy cluster with bright X-ray emission. Optical analyses (Fabricant et al. 1989; Berrington et al. 2002; Miller et al. 2003) revealed a complex dynamical state, which consists of at least a triple merging with a mass ratio of 3:1:0.3. Berrington et al. (2002) propose that the system includes a main cluster with an infalling subcluster NW at ∼0.2 Gyr from the core passage (Roettiger et al. 1995) and another infalling group northeast (NE), possibly associated to a previous merger. Briel

et al. (1991) detected two separate X-ray peaks corresponding to the main cluster and the infalling subcluster, lately confirmed by Sun et al. (2002) and Bourdin & Mazzotta (2008). They also found bimodality in the temperature structure along the cluster elongation axis, being the low temperature component (∼4.5 keV) associated with the subcluster and the higher temperature component (∼7–8 keV) with the main cluster. In addition, Tamura et al. (2011) found bulk motion of gas of the cooler temperature component.

We use two observations (see Table 4.1) for the analysis of A2256. We divide the ICM emission region in circular sectors along the cluster major elongation axis centred in the X-ray peak of the main cluster (CORE1: $17^{\rm h}04^{\rm m}13^{s}82$, $78^{\circ}38'15''0$, Bourdin & Mazzotta 2008). We fit the cluster emission and the background spectra (see Table 4.12) using $N_{\rm HI}$ = 4.24 $\times$ 10^{20} cm^{-2} (Willingale et al. 2013). The best-fit parameters are presented in the Table 4.18 and plotted in Fig. 4.13.

The temperature profile shows the bimodal temperature structure already described by Sun et al. (2002) and Bourdin & Mazzotta (2008), as well as the hot (∼9 keV) temperature component south of the cluster center. It shows a temperature discontinuity from the adjacent region at ∼7 keV, suggested to be caused by the presence of a cold front (Bourdin & Mazzotta 2008). However, and similarly to Bourdin & Mazzotta (2008), we do not find evidence for the presence of the 'shoulder' mentioned by Sun et al. (2002) east of the CORE1. The Fe abundance distribution is in agreement with the values obtained by Sun et al. (2002). We obtain a quasi uniform abundance distribution (0.3–0.5 $Z_{\odot}$) with a slight decrease at the south. The second X-ray peak, (CORE2: $17^{\rm h}03^{\rm m}07^{s}43$, $78^{\circ}39'07''8$, Sun et al. 2002), associated to the infalling subcluster, presents the highest abundance value of ∼0.6 $Z_{\odot}$.

4.5 Discussion

4.5.1 Averaged abundance distribution

The individual Fe abundance distributions of the six merging galaxy clusters along their merging axis are compiled in Fig. 4.14 (*left*). We remind the reader that such distributions are not azimuthally averaged. Instead, in this work we have chosen to trace the central ICM elongation along the merging axis, essentially because the surface brightness allows better constraints on the Fe abundance and because no spectacular metal redistribution is expected to take place perpendicular to the merging axis. In the case of CIZA2242, 1RXSJ0603 and A3376 the interest region clearly extends the core (where the BCG resides) to the outwards direction. For A3667, A665 and A2256, sectors along two opposite directions from the core are used. In Fig. 4.14, all the clustercentric radii have been rescaled to fractions of r_{500}[5], adopting r_{500} and r_{200} values found in the literature and assuming the conversion $r_{500} \simeq 0.65 r_{200}$ of Reiprich et al. (2013). For our cosmology and redshifts we use the approximation of Henry et al. (2009):

$$r_{200} = 2.77 h_{70}^{-1} (\langle kT \rangle / 10\ {\rm keV})^{1/2} / E(z)\ {\rm Mpc}, \quad (4.1)$$

[5] r_{Δ} is formally defined as the radius within which the density is Δ times the critical density of the Universe at the redshift of the source.

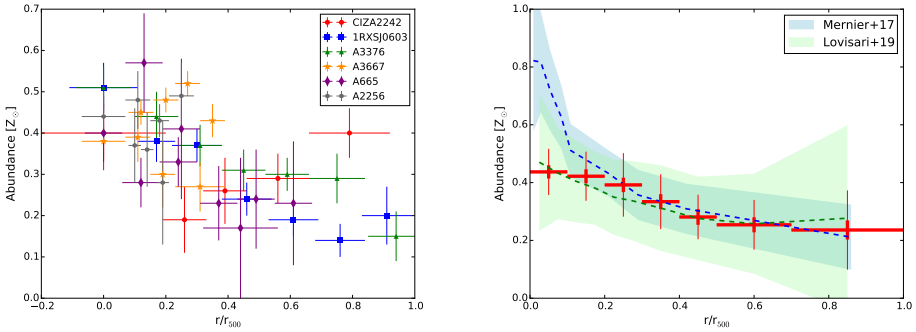

Figure 4.14: *Left panel*: Abundance distribution along the merging axis scaled by r_{500}. *Right panel*: Averaged abundance distribution scaled by r_{500}. Data points in red show the averaged value and the statistical error as a thick errorbar plus the scatter as a thinner errorbar for each bin of Table 4.3. The blue shaded area shows the average profile for clusters (>1.7 keV) , including the statistical error and the scatter, derived by Mernier et al. (2017). The green shaded area represents the mean values for disturbed systems, together with the scatter, obtained by Lovisari & Reiprich (2019). The blue and green dashed line follow the average and mean abundance value of Mernier et al. (2017) and Lovisari & Reiprich (2019), respectively.

where $E(z)$=$(\Omega_{\rm M}(1+z)^3+1-\Omega_{\rm M})^{1/2}$. The mean temperature values, $\langle kT \rangle$, are adopted from references as described in Table 4.2. Our averaged Fe abundance distribution, stacked from all the above measurements, is shown in Fig. 4.14 (*right*), and the numerical values are reported in Table 4.3.

We use the stacking method of Mernier et al. (2017) to determine this distribution. The averaged abundance distribution, $Z_{\rm ref}(k)$, as a function of the kth reference bin is defined as:

$$Z_{\rm ref(k)} = \left(\sum_{j=1}^{N} \sum_{i=1}^{M} w_{i,j,k} \frac{Z(i)_j}{\sigma^2_{Z(i)_j}} \right) \Bigg/ \left(\sum_{j=1}^{N} \sum_{i=1}^{M} w_{i,j,k} \frac{1}{\sigma^2_{Z(i)_j}} \right), \tag{4.2}$$

where $Z(i)_j$ is the individual abundance of the jth cluster at its ith region; $\sigma_{Z(i)_j}$ is its statistical error, N is the number of clusters, M is the number of regions analysed in each cluster and $w_{i,j,k}$ is the weighting factor. This factor represents the geometrical overlap of the ith region with the kth reference bin in cluster j. It varies from 0 to 1. The stacked statistical error is calculated as:

$$\sigma_{\rm stat}(k) = \frac{1}{\sqrt{\sum_{j=1}^{N} \sum_{i=1}^{M} w_{i,j,k} \frac{1}{\sigma^2_{Z(i)_j}}}}. \tag{4.3}$$

We also obtained the scatter of the measurements for each kth reference bin as:

$$\sigma_{\rm scatter}(k) = \frac{\sqrt{\sum_{j=1}^{N}\sum_{i=1}^{M} w_{i,j,k}\left(\frac{Z(i)_j - Z_{\rm ref}(k)}{\sigma_{Z(i)_j}}\right)^2}}{\sqrt{\sum_{j=1}^{N}\sum_{i=1}^{M} w_{i,j,k}\frac{1}{\sigma^2_{Z(i)_j}}}}. \tag{4.4}$$

It clearly appears from Fig. 4.14 that abundance distributions of these merging clusters are not flat. Instead, we note a decrease from the core up to $\sim 0.4 r_{500}$, followed by a flattening at larger radii. Figure 4.14 (*right*) compares our averaged distribution with the relaxed, azimuthally-averaged CC systems of Mernier et al. (2017) with $kT > 1.7$ keV and the disturbed, NCC systems of Lovisari & Reiprich (2019). In both cases we have included the statistical errors and the scatter. Remarkably, our values are in good agreement with the (azimuthally-averaged) NCC profile of Lovisari & Reiprich (2019), which shows lower abundance values in the core than relaxed clusters and a shallower decrease towards the outer radii. The averaged Fe distribution values shown in Table 4.3 are therefore consistent with Lovisari & Reiprich (2019) results. We have additionally checked the averaged abundance distribution along the BCG displacement direction (assuming only the positive radii). In this case, the agreement with the NCC systems profile of Lovisari & Reiprich (2019) improves. For more details see Appendix A.

Table 4.3: Averaged abundance profile.

Radius (r/r_{500})	Z ($Z_\odot$)	$\sigma_{\rm stat}$	$\sigma_{\rm scatter}$
0.00–0.10	0.437	0.023	0.057
0.10–0.20	0.422	0.024	0.061
0.20–0.30	0.392	0.025	0.085
0.30–0.40	0.334	0.026	0.069
0.40–0.50	0.281	0.027	0.049
0.50–0.70	0.254	0.026	0.060
0.70–1.00	0.236	0.033	0.104

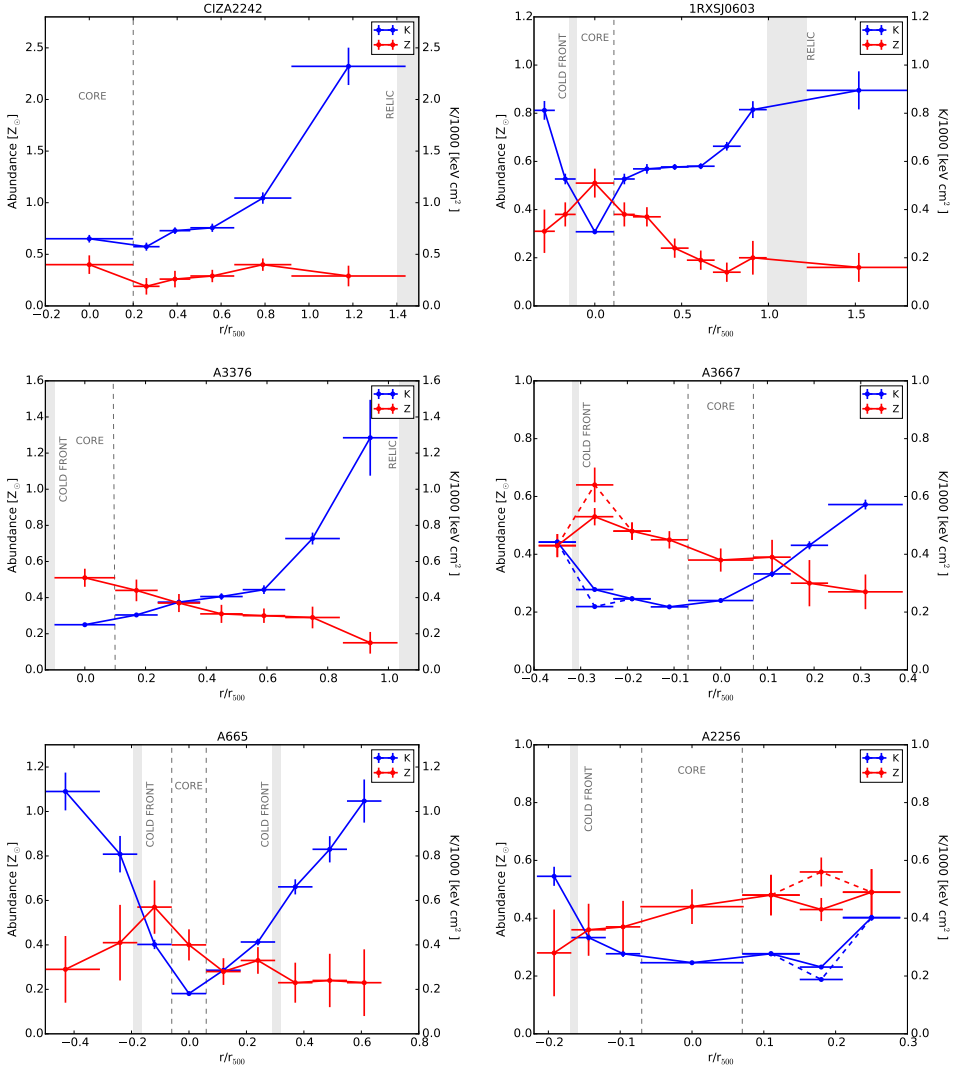

Figure 4.15: Scaled pseudo-entropy ($K/1000$) and abundance distributions along the merging axis for CIZA2242, 1RXSJ0603, A3376, A3667, A665 and A2256. Dashed lines show the values of the yellow region after the A3667 cold front (see Fig. 4.8) and the CORE2 values of A2256 (see Fig. 4.12).

The lower abundance value in the core for disturbed systems is suggested by Lovisari & Reiprich (2019) to be caused by major mergers, where in some cases the core could be disrupted. As a result, the abundance peak in the center of the (CC) progenitors is spread out and distributed across larger radii. At first glance, the similarity of the Fe distribution observed between NCC clusters and these merging clusters tends to support this scenario. However, the steeper Fe peaks observed in the core of 1RXSJ0603 and in the vicinity of the core of A665 (perhaps offset from the BCG because of important sloshing motions) suggest that remnants of previous CC clusters can partly persist to (or, at least, not be entirely disrupted by) even the most major mergers in some cases (see Sect. 5.2). While this moderate central abundance increase could be associated with either (relatively old) core passage mergers, or on the contrary, early stage mergers, we note that our sample contains both cases. In fact, most of them are massive clusters, which have undergone a major merger with a core passage more than 0.6 Gyr ago. However, A2256 is a still on going merger, before core passage, although it is thought that the main cluster center is already affected by an older merger. Future larger samples, containing an equal proportion of early and late stage mergers, will help to relate the (re)-distribution of metals with merger history.

4.5.2 Abundance vs. pseudo-entropy relation

In order to study the thermal history of the ICM, we calculate the pseudo-entropy, $K \equiv kT \times n^{-2/3}$, as a function of the region distance for each merging cluster. These pseudo-entropy distributions along the merging axis are shown together with the Fe abundance profiles in Fig. 4.15. The temperature of each region, kT, is directly obtained from the spectral analysis, and the density, n, can be inferred from the emission measure, $Norm$, as $Norm \propto 1.2 n^2 V$, where V is the emitting volume projected onto the line-of-sight (LOS). To estimate n, we assume a spherical LOS in which only the sphere between the maximum and minimum radius contributes to the emission (Henry et al. 2004; Mahdavi et al. 2005). We assume the emission volume V to be $V = 2SL/3$ for the circular and elliptical sectors, and $V = \pi SL/2$ for rectangular ones. In each case, $L = 2\sqrt{(R^2_{max} - R^2_{min})}$ and S is the area of the sectors in the plane of the sky.

Previous studies (De Grandi et al. 2004; Leccardi et al. 2010; Ghizzardi et al. 2014; Liu et al. 2018) have demonstrated, especially for relaxed (CC) clusters, the existence of a negative correlation between the Fe abundance and the gas entropy. Low-entropy cores, where the cooling of the ICM might take place, are in fact associated with central abundance peaks. However, disturbed (NCC) clusters are not well characterized by this behaviour as mentioned by Leccardi et al. (2010) and Rossetti & Molendi (2010).

Pseudo-entropy quantifies the internal energy variation due to thermal processes such as, for example cooling, turbulent dissipation or shock heating. Regions under the influence of the latter, in particular, can be easily identified because they exhibit a positive gradient proportional to $r^{1.1}$ (Tozzi & Norman 2001). In particular for our merging cluster selection, we observe a similar trend in the post-shock regions, see Fig. 4.15 and Fig. 4.16 (*left*), although some systems (e.g. 1RXSJ0603, A3376) significantly deviate from this relation. If we fit simultaneously all our pseudo-entropy distributions with a power-law ($\sim r^{\alpha}$), we obtain a slope of $\alpha = 1.34 \pm 0.63$ (Fig. 4.16 *left*). In the case of 1RXSJ0603, we see a flat

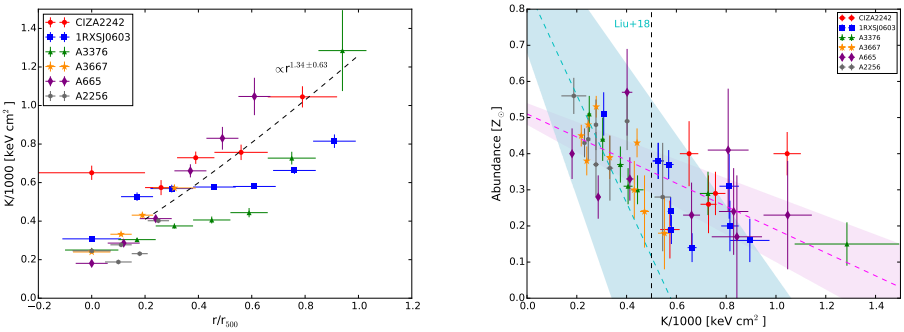

Figure 4.16: *Left panel*: Pseudo-entropy distribution scaled by r_{500}. *Right panel*: The distribution of Fe abundance versus the scaled pseudo-entropy of all the measured regions of the clusters: CIZA2242, 1RXSJ0603, A3376, A3667, A665 and A2256. The magenta dashed line is the best-fit linear model and the shaded area shows the 1σ uncertainties of the best-fit parameter. The cyan line and shadow are the results of Liu et al. (2018) for relaxed galaxy clusters.

profile between ∼0.2–0.4 r_{500}, coincident with the COREN location, possibly indicating a sign of the subcluster core remnant after the merger event. A similar flattening is observed in A3376, although its origin may be rather related to the central low-entropy gas stripped during the merger, thereby forming the cometary shape ICM.

Most of NCC clusters are thought to have undergone a CC phase, before the (cool) core being disrupted completely or partially by major mergers (Leccardi et al. 2010; Rossetti & Molendi 2010; ZuHone 2011). The on-going interactions heat and increase the entropy in the core. Therefore, NCC tend to have high-entropy cores and smaller entropy gradients. Some of these clusters present regions with lower entropy that have associated an abundance excess, in most of the cases associated with the BCG or a giant elliptical galaxy, and known as 'CC-remnants' (Rossetti & Molendi 2010). It is suggested that these regions are the reminiscent of CC after the merging activity. Another consequence of merger events is the decrease of the abundance excess in the core, which can be erased by the shock-heating and gas mixing processes.

Figure 4.15 shows simultaneously the pseudo-entropy and Fe abundance distributions scaled by r_{500} for our six merging galaxy clusters. In the case of CIZA2242 and A3376, the entropy is slightly flat in the core and the profile increases smoothly (though with a larger gradient) out to the recently shocked region. Interestingly, 1RXSJ0603 exhibits a relative low-entropy core associated with the abundance peak. One natural interpretation is that this region is the remainder of cool core after the merging activity, which agrees with ZuHone (2011) simulations taking into account the mass ratio of 3:1 and it is found in twelve clusters of Rossetti & Molendi (2010). An alternative scenario could be that 1RXSJ0603, as a well evolved merger (∼2 Gyr since the shock producing the radio relic; e.g. Brüggen et al. 2012, Stroe et al. 2015a), has started to recover its potential well and to re-build its entropy (and metal) stratification after the merger. For A3667 and A2256, we identify possible CC-remnants characterized by somewhat lower entropy and higher metallicity values (Rossetti

& Molendi 2010). These remnants clearly appear after we include the measurements of the truncated yellow region after the A3667 cold front (see Fig. 4.8) and the CORE2 values of A2256 (see Fig. 4.12), in dashed lines in Fig. 4.15. A2256 also contains a second minimum corresponding to the CORE1. As explained in Leccardi et al. (2010), two low-entropy clumps can be found if we are in the presence of an early stage merger, as in this case, or an off-axis merger event. A665 also shows a relative low-entropy drop in the core, but in this case the abundance peak is displaced towards the cold front, as explained in Section 4.5.1, possibly due to the effect of the internal dynamics of the cold front during the infall of the subcluster. The above examples, and in particular the case of 1RXSJ0603, strongly suggest that in some cases, signatures of cool cores can remain even after the most major ICM merger events.

Table 4.4: Best-fit parameters of abundance vs pseudo-entropy distributions.

K (keV cm^2)	α (Z$_\odot$ keV^{-1} cm^{-2})	Z$_0$ ($Z_\odot$)
200–2300	0.32 ± 0.06	0.51 ± 0.03
200–500	0.61 ± 0.17	0.61 ± 0.05
500–2300	0.07 ± 0.07	0.32 ± 0.05
10–1000[a]	1.49 ± 0.51	0.86 ± 0.18

[a] Liu et al. (2018) distribution best-fit parameters.

Furthermore, we try to determine a correlation between Fe abundance and pseudo-entropy for our merging clusters. Figure 4.16 (*right*) shows the distribution of Z-K. Generally speaking, our measured entropies are clearly higher than in the distribution of Liu et al. (2018), with our lowest value being $\sim$200 keV cm^2 and the maximum abundance value being $\sim$0.5 $Z_\odot$. In fact, these values are characteristic of merging clusters (Leccardi et al. 2010; ZuHone 2011). We fit the distribution with a linear function $Z \sim Z_0 - \alpha K/1000$. Our best-fit parameters are Z_0 = 0.51 ± 0.03 and α = 0.32 ± 0.06. This correlation shows a flatter slope than obtained by Liu et al. (2018) for relaxed (CC) galaxy clusters (Z_0 = 0.86 ± 0.18 and α = 1.49 ± 0.51). Our results suggest that the abundance and pseudo-entropy relation are not always tightly related. Instead, it is likely that, when a merger occurs, the entropy gets boosted in post-shock regions more rapidly than metals diffuse out. Interestingly, when we consider the values of pseudo-entropy only below $\sim$500 keV cm^2 – which were presumably less affected by shock-heating, or which start to relax again (see vertical black dashed line in Fig. 4.16), the slope of the relation considerably increases (Table 4.4). This might suggest that in the lowest entropy regions ($\sim$200–500 keV cm^2) of these merging clusters (NCC) – usually associated with the core remnant (see Fig. 4.15), the metal-rich gas (originally still coming from the BCG) gets mixed and redistributed at a moderate rate compared to the entropy changes during the merger event (ZuHone 2011). Alternatively, chemical histories may differ between relaxed and merging systems. Although beyond the scope of this paper, in some cases we cannot rule out the possibility of an extra Fe

enrichment, produced by a boost of star formation or SNIa explosions, triggered by major mergers (e.g. Stroe et al. 2015a; Sobral et al. 2015).

Finally, we do not find evidence of a correlation in the higher (>500 keV cm^2) entropy range, meaning beyond $\sim$0.4–0.6 r_{500}. In these outer regions, the Fe abundance remains rather uniform around 0.2–0.3 $Z_\odot$, with no notable trend with cluster mass, radius or azimuth (Fig. 4.14). Combined with the previous observations of a uniform $\sim$0.3 $Z_\odot$ Fe abundance in the outskirts of (mostly) CC clusters (Fujita et al. 2008; Werner et al. 2013; Thölken et al. 2016b; Urban et al. 2017; Ezer et al. 2017), we conclude that Fe distribution in cluster outskirts of these merging clusters depends very weakly (or not at all) on the dynamical state of the cluster. This has important consequences regarding the chemical history of large-scale structures. In fact, although these previous measurements in relaxed systems strongly suggested that the most of the ICM enrichment took place in early stages of cluster formation (i.e. at z > 2–3; for recent reviews, see Mernier et al. 2018b; Biffi et al. 2018b), the alternative scenario of late enrichment coupled with a very efficient mixing of metals in the ICM, could not be totally excluded. Among the entire cluster population, merging clusters are systems in which metals had the least time to mix and diffuse out since their last merger event. Consequently, if the bulk of metals were mixed efficiently in the entire cluster volume (after being injected into the ICM at late stages), one would expect to find important variations of the Fe abundance at large radii in such dynamically disturbed systems, with values considerably higher than 0.2–0.3 $Z_\odot$ in some specific outer regions. Instead, the remarkable similarity of the Fe distribution in the outskirts of CC and these six merging clusters, and the above indication that in inner regions metal mixing lags somewhat behind entropy changes, constitute valuable additional evidence in favour of the early enrichment scenario.

4.6 Summary

In this work, we analyse for the first time the Fe distribution along the merging axis of six merging galaxy clusters (0.05 < z < 0.23) observed with *XMM-Newton*/EPIC. We obtain and specifically studied the temperature, abundance and pseudo-entropy distributions across the ICM of these disturbed systems. Specifically, we provide a first estimate of the averaged Fe distribution out to r_{500} – as well as the relation between Fe abundance and pseudo-entropy – in six merging clusters. The main results can be summarized as follows.

Firstly, the Fe distribution is far from being universal, as it strongly varies from one merging cluster to another. While in some cases (e.g. CIZA2242, A2256) no Fe peak nor pseudo-entropy drop is detected in central regions, some of our observations (e.g. 1RXSJ0603, A665) strongly suggest that remnants of previous (metal-rich) cool-cores can persist after major mergers.

Secondly, our averaged Fe distribution in these six merging clusters is in excellent agreement with that in (non-merging) non-cool-core clusters presented by Lovisari & Reiprich (2019). The average profile clearly shows a moderate abundance central excess, thus present not only in CC systems but even in many spectacular mergers. Compared to the former, however, the central ($\lesssim 0.3 r_{500}$) Fe profile in these merging clusters is significantly less steep. This can be interpreted as the metal-rich gas of the CC progenitors being mixed

and spread across moderate radii by merging processes.

Thirdly, the minimum pseudo-entropy value obtained for these six merging clusters is $\sim$200 keV cm^2. This value is characteristic of typical unrelaxed systems, whose internal activity is dominated by turbulence, large-scale motions and/or AGN feedback. Whereas some clusters exhibit a pseudo-entropy distribution that tends to follow the behaviour $\propto r^{1.1}$ described by Tozzi & Norman (2001), some systems (e.g. 1RXSJ0603, A3376) deviate from this relation due to stripped cold gas from disrupted cores.

Fourthly, we find a mild negative correlation between abundance and pseudo-entropy for the inner core region (K = 200-500 keV cm^2), shallower than the anti-correlation obtained by Liu et al. (2018) for relaxed clusters. This might suggest that mergers affect the gas entropy more rapidly than they re-distribute metals (via gas mixing).

Finally, in the outermost, high-entropy regions (K = 500-2300 keV cm^2) studied here, we have no evidence of a correlation between metallicity and pseudo-entropy and the abundance is consistent with the uniform abundance value of 0.2–0.3 $Z_\odot$. This demonstrates that the lack of dependence of Fe abundance at such high entropies (and large radii) applies not only to the mass, radius and azimuthal characteristics of clusters, but also to the dynamical stage. In other words, our results provide important additional evidence towards the scenario of an early enrichment of the inter galactic medium (z >2–3).

ACKNOWLEDGEMENTS

The authors thank Dr. R. van Weeren for the LOFAR radio data, Dr. R. Kale, Dr. T. Shimwell and Dr. V. Vacca for providing the VLA radio data and Dr. A. Botteon for the SUMMSS data. S. Kara and. E. N. Ercan would like to thank TUBITAK for financial support through a 1002 project under the code 118F023. A. Simionescu is supported by the Women In Science Excel (WISE) programme of the Netherlands Organisation for Scientific Research (NWO), and acknowledges the MEXT World Premier Research Center Initiative (WPI) and the Kavli IPMU for the continued hospitality. SRON is supported financially by NWO, the Netherlands Organization for Scientific Research. This work is based on observations obtained with XMM-Newton, an ESA science mission with instruments and contributions directly funded by ESA member states and the USA (NASA).

4.A Averaged abundance distribution along BCG displacement direction

In addition to stacking our measurements over the entire merger axis as explained in Section 4.5.1, we can alternatively choose to trace the ICM only from the BCG region (i.e. typically including the cluster X-ray peak), down to the freshly collided gas, meaning along its cometary structure (defined in Figs. 4.3, 4.5, 4.7, 4.9, 4.11, and 4.13 as positive values on the x-axis). These regions better trace the disturbed and mixed plasma while avoiding special features such as cold fronts ahead of the merger (e.g. A3667, Fig. 4.9); therefore the effects of the merging activity in the ICM are expected to be more significant. For CIZA2242, 1RXSJ0603, and A3376 this covers the complete elongation or cometary tail present in the ICM. For A3367 and A665 this includes the sectors five to eight and four to nine, respectively. In the case of A2256, we consider the sectors four to seven, where the ICM of the main subclusters is predominantly affected by the presence of the infalling subclsuter. The individual Fe abundance distribution of the six merging galaxy clusters included in this analysis are plotted in Fig. 4.17 (*left*), the averaged values obtained with the stacking method described in Section 4.5.1 are shown in Fig. 4.17 (*right*).

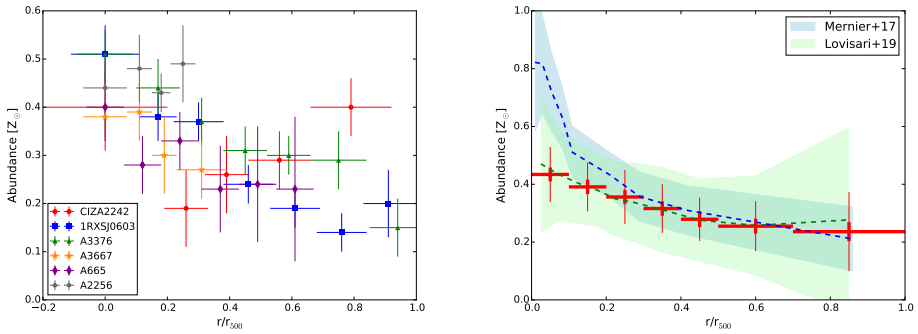

Figure 4.17: *Left panel*: Abundance distribution along the BCG displacement direction scaled by r_{500}. *Right panel*: Averaged abundance distribution scaled by r_{500}. Data points in red show the averaged value and the statistical error as a thick errorbar plus the scatter as a thinner errorbar for each bin of Table 4.3. The blue shaded area shows the average profile for clusters (>1.7 keV) , including the statistical error and the scatter, derived by Mernier et al. (2017). The green shaded area represents the mean values for disturbed systems, together with the scatter, obtained by Lovisari & Reiprich (2019). The blue and green dashed line follow the average and mean abundance value of Mernier et al. (2017) and Lovisari & Reiprich (2019), respectively.

Interestingly, the Fe averaged distribution is now in excellent agreement with the Fe average profile of NCC systems by Lovisari & Reiprich (2019). The major differences with respect to the distribution shown in Section 4.5.1 appear in the 0.1–0.2 r_{500} (8% lower) and 0.2–0.3 r_{500} (10% lower) radii. These lower values are obtained because the displaced Fe peak outside cluster center (see Section 4.5.1 and 4.5.2 for more details) of A3667 and A665 are not included.

4.B EPIC background modelling for the cluster sample & Temperature and abundance analysis for the cluster sample

The following tables summarise the EPIC background model parameters used of each one of the galaxy clusters using the method described in Section 4.3.2. The norms are given in standard SPEX definition, which are intrinsically dependent of the distance to the source.

Table 4.5: Background components derived from the CIZA2242 observation.

	Norm[a]	*kT* (keV)	Γ
MWH	57.55 ± 0.28	0.27 (fixed)	–
LHB	258.33 ± 0.68	0.08 (fixed)	–
CXB	6.75 (fixed)	–	1.41 (fixed)
HF	6.24 ± 2.56	0.7 (fixed)	–
SP MOS1	13.25 ± 1.98	–	1.40 ± 0.19
SP MOS2	18.10 ± 1.77	–	1.40 ± 0.19
SP PN	58.86 ± 11.51	–	1.20 ± 0.15

[a] For LHB and MWH norm in units of 10^{69} m^{-3} arcmin^{-2}
For CXB norm in units of 10^{49} ph s^{-1} keV^{-1} arcmin^{-2}
For SP norm in units of 10^{44} ph s^{-1} keV^{-1} arcmin^{-2}

Table 4.6: Background components derived from the 1RXSJ0603 observation.

	Norm[a]	*kT* (keV)	Γ
MWH	2.58 ± 0.07	0.21 ± 0.02	–
LHB	13.40 ± 0.06	0.08 (fixed)	–
CXB	1.57 (fixed)	–	1.41 (fixed)
SP MOS1	5.22 ± 0.46	–	1.40 ± 0.01
SP MOS2	6.34 ± 1.0	–	1.40 ± 0.01
SP PN	42.71 ± 0.90	–	1.40 ± 0.04

[a] For LHB and MWH norm in units of 10^{70} m^{-3} arcmin^{-2}
For CXB norm in units of 10^{50} ph s^{-1} keV^{-1} arcmin^{-2}
For SP norm in units of 10^{44} ph s^{-1} keV^{-1} arcmin^{-2}

Table 4.7: Best-fit parameter values of the total background estimated for A3376 E observation.

	Norm[a]	*kT* (keV)	Γ
MWH	2.31 (fixed)	0.27 (fixed)	–
LHB	86.00 (fixed)	0.08 (fixed)	–
CXB	3.90 (fixed)	–	1.41 (fixed)
SP MOS1	2.18 ± 0.37	–	1.40 ± 0.04
SP MOS2	1.30 ± 0.37	–	1.40 ± 0.04
SP PN	2.77 ± 0.66	–	1.09 ± 0.12

[a] For LHB and MWH norm in units of 10^{68} m^{-3} arcmin^{-2}
For CXB norm in units of 10^{48} ph s^{-1} keV^{-1} arcmin^{-2}
For SP norm in units of 10^{45} ph s^{-1} keV^{-1} arcmin^{-2}

Table 4.8: Best-fit parameter values of the total background estimated for A3376 W observation.

	Norm[a]	*kT* (keV)	Γ
MWH	2.31 (fixed)	0.27 (fixed)	–
LHB	86.00 (fixed)	0.08 (fixed)	–
CXB	3.90 (fixed)	–	1.41 (fixed)
SP MOS1	2.87 ± 0.40	–	1.40 ± 0.01
SP MOS2	23.65 ± 0.45	–	1.40 ± 0.01
SP PN	7.57 ± 0.57	–	1.21 ± 0.04

[a] For LHB and MWH norm in units of 10^{68} m^{-3} arcmin^{-2}
For CXB norm in units of 10^{48} ph s^{-1} keV^{-1} arcmin^{-2}
For SP norm in units of 10^{45} ph s^{-1} keV^{-1} arcmin^{-2}

Table 4.9: Background components derived from the A3667 observation.

	Norm[a]	*kT* (keV)	Γ
MWH	1.49 ± 0.07	0.26 ± 0.01	–
LHB	26.21 ± 1.56	0.08 (fixed)	–
CXB	0.74 (fixed)	–	1.41 (fixed)
SP MOS1	12.26 ± 1.82	–	1.40 ± 0.09
SP MOS2	7.55 ± 3.12	–	1.40 ± 0.09
SP PN	0.40 ± 0.06	–	0.35 ± 0.07

[a] For LHB and MWH norm in units of 10^{69} m^{-3} arcmin^{-2}
For CXB norm in units of 10^{49} ph s^{-1} keV^{-1} arcmin^{-2}
For SP norm in units of 10^{44} ph s^{-1} keV^{-1} arcmin^{-2}

Table 4.10: Background components derived from the A665 observation.

	Norm[a]	*kT* (keV)	Γ
MWH	0.89 ± 0.06	0.19 ± 0.03	–
LHB	15.00 ± 3.54	0.08 (fixed)	–
CXB	0.41 (fixed)	–	1.41 (fixed)
SP MOS1	22.12 ± 1.17	–	1.40 ± 0.04
SP MOS2	9.88 ± 0.48	–	1.40 ± 0.04

[a] For LHB and MWH norm in units of 10^{70} m^{-3} arcmin^{-2}
For CXB norm in units of 10^{50} ph s^{-1}keV^{-1} arcmin^{-2}
For SP norm in units of 10^{44} ph s^{-1}keV^{-1} arcmin^{-2}

Table 4.11: Background components derived from the A2256 pointing 1 observation.

	Norm[a]	*kT* (keV)	Γ
MWH	4.77 ± 0.18	0.31 ± 0.04	–
LHB	54.50 ± 1.70	0.08 (fixed)	–
CXB	8.17 (fixed)	–	1.41 (fixed)
SP MOS1	9.66 ± 0.61	–	0.91 ± 0.02
SP MOS2	9.99 ± 0.72	–	0.91 ± 0.02
SP PN	20.94 ± 3.51	–	1.08 ± 0.08

[a] For LHB and MWH norm in units of 10^{68} m^{-3} arcmin^{-2}
For CXB norm in units of 10^{48} ph s^{-1}keV^{-1} arcmin^{-2}
For SP norm in units of 10^{45} ph s^{-1}keV^{-1} arcmin^{-2}

Table 4.12: Background components derived from the A2256 pointing 2 observation.

	Norm[a]	*kT* (keV)	Γ
MWH	4.77 ± 0.18	0.31 ± 0.04	–
LHB	54.50 ± 1.70	0.08 (fixed)	–
CXB	8.17 (fixed)	–	1.41 (fixed)
SP MOS1	3.23 ± 0.52	–	1.40 ± 0.02
SP MOS2	3.13 ± 0.46	–	1.40 ± 0.02
SP PN	5.02 ± 0.88	–	1.40 ± 0.03

[a] For LHB and MWH norm in units of 10^{68} m^{-3} arcmin^{-2}
For CXB norm in units of 10^{48} ph s^{-1}keV^{-1} arcmin^{-2}
For SP norm in units of 10^{45} ph s^{-1}keV^{-1} arcmin^{-2}

Table 4.13: Best-fit parameters for CIZA2242 regions shown in Fig. 4.2.

Region	Radius (′)	*kT* (keV)	*Z* ($Z_\odot$)	*Norm* (10^{72} m^{-3} arcmin^{-2})	N_H (10^{21} cm^{-2})	C-stat/d.o.f.
1	0.0 ± 1.5	9.62 ± 0.54	0.40 ± 0.09	1.64 ± 0.04	3.60 ± 0.10	603/574
2	2.0 ± 0.5	8.21 ± 0.55	0.19 ± 0.09	1.98 ± 0.06	3.79 ± 0.13	553/539
3	3.0 ± 0.5	9.14 ± 0.40	0.26 ± 0.08	1.63 ± 0.04	3.85 ± 0.11	570/560
4	4.3 ± 0.8	8.07 ± 0.42	0.29 ± 0.06	1.46 ± 0.05	3.85 ± 0.07	624/606
5	6.0 ± 1.0	8.68 ± 0.45	0.40 ± 0.06	0.95 ± 0.03	4.27 ± 0.09	653/619
5a	6.0 ± 1.0	7.41 ± 0.56	0.58 ± 0.11	0.79 ± 0.03	4.10 ± 0.13	561/546
5b	6.0 ± 1.0	8.69 ± 0.67	0.29 ± 0.09	1.44 ± 0.04	4.32 ± 0.14	525/559
5c	6.0 ± 1.0	9.61 ± 1.03	0.18 ± 0.10	0.83 ± 0.03	5.57 ± 0.07	566/551
6	9.0 ± 2.0	10.29 ± 0.79	0.29 ± 0.10	0.25 ± 0.01	5.13 ± 0.07	662/643
BCGN	6.0 ± 1.5	8.16 ± 0.41	0.26 ± 0.06	1.37 ± 0.03	4.33 ± 0.10	645/591

Table 4.14: Best-fit parameters for 1RXSJ0603 regions shown in Fig. 4.4.

Region	Radius (′)	*kT* (keV)	*Z* ($Z_\odot$)	*Norm* (10^{72} m^{-3} arcmin^{-2})	C-stat/d.o.f.
1	-1.9 ± 0.4	10.07 ± 0.46	0.31 ± 0.09	1.62 ± 0.09	524/590
2	-1.1 ± 0.4	9.80 ± 0.41	0.38 ± 0.05	4.16 ± 0.07	606/625
3 (CORES)	0.0 ± 0.7	8.43 ± 0.27	0.51 ± 0.06	7.02 ± 0.13	613/572
4	2.0 ± 0.5	8.92 ± 0.31	0.37 ± 0.04	8.85 ± 0.13	640/647
5	3.0 ± 0.5	8.57 ± 0.18	0.24 ± 0.04	9.20 ± 0.08	717/652
6	4.0 ± 0.5	7.86 ± 0.15	0.19 ± 0.04	8.10 ± 0.10	783/652
7	5.0 ± 0.5	7.42 ± 0.20	0.14 ± 0.04	5.08 ± 0.05	729/631
8	6.0 ± 0.5	6.92 ± 0.29	0.20 ± 0.07	2.43 ± 0.03	619/602
9	10.0 ± 2.0	2.93 ± 0.22	0.16 ± 0.06	0.36 ± 0.02	974/661
COREN	3.0 ± 0.4	8.85 ± 0.36	0.37 ± 0.08	5.05 ± 0.01	606/562

Table 4.15: Best-fit parameters for A3376 regions shown in Fig. 4.6.

Region	Radius (′)	*kT* (keV)	*Z* ($Z_\odot$)	*Norm* (10^{72} m^{-3} arcmin^{-2})	C-stat/d.o.f.
1 (BCG2)	0.0 ± 2.0	4.17 ± 0.13	0.51 ± 0.05	6.88 ± 0.12	553/607
2	3.5 ± 1.5	3.89 ± 0.12	0.44 ± 0.06	7.14 ± 0.18	642/579
3	6.5 ± 1.5	4.00 ± 0.14	0.37 ± 0.05	5.61 ± 0.13	647/603
4	9.5 ± 1.5	3.79 ± 0.10	0.31 ± 0.05	4.54 ± 0.68	1250/1185
5	12.5 ± 1.5	3.88 ± 0.16	0.30 ± 0.04	4.29 ± 0.58	1276/1195
6	16.0 ± 2.0	4.21 ± 0.19	0.29 ± 0.06	1.63 ± 0.03	617/643
7	20.0 ± 2.0	5.36 ± 0.84	0.15 ± 0.06	0.68 ± 0.10	657/599
BCG1	18.2 ± 2.0	4.49 ± 0.35	0.21 ± 0.12	1.35 ± 0.01	512/544

Table 4.16: Best-fit parameters for A3667 regions shown in Fig. 4.8.

Region	Radius (′)	*kT* (keV)	*Z* ($Z_\odot$)	*Norm* (10^{72} m^{-3} arcmin^{-2})	C-stat/d.o.f.
1	-7.6 ± 0.9	5.46 ± 0.11	0.43 ± 0.04	1.24 ± 0.01	802/664
2	-5.9 ± 0.9	4.56 ± 0.06	0.52 ± 0.03	2.57 ± 0.02	843/682
3	-4.1 ± 0.9	5.04 ± 0.07	0.48 ± 0.03	4.16 ± 0.02	761/685
4	-2.4 ± 0.9	5.54 ± 0.09	0.45 ± 0.03	6.12 ± 0.47	756/651
5	0.0 ± 1.5	6.79 ± 0.17	0.38 ± 0.04	4.29 ± 0.05	760/652
6	2.4 ± 0.9	7.05 ± 0.23	0.39 ± 0.06	3.54 ± 0.05	675/618
7	4.1 ± 0.9	7.29 ± 0.24	0.30 ± 0.08	2.35 ± 0.04	729/631
8	6.8 ± 1.8	6.79 ± 0.20	0.27 ± 0.06	1.48 ± 0.02	733/673

Table 4.17: Best-fit parameters for A665 regions shown in Fig. 4.10.

Region	Radius (′)	*kT* (keV)	*Z* ($Z_\odot$)	*Norm* (10^{72} m^{-3} arcmin^{-2})	C-stat/d.o.f.
1	-3.5 ± 1.0	6.73 ± 0.52	0.29 ± 0.15	0.26 ± 0.01	393/400
2	-2.0 ± 0.5	8.43 ± 0.85	0.41 ± 0.17	0.67 ± 0.02	373/362
3	-1.0 ± 0.5	7.30 ± 0.38	0.57 ± 0.12	2.51 ± 0.05	413/372
4	0.0 ± 0.5	7.80 ± 0.37	0.40 ± 0.07	11.79 ± 0.21	431/421
5	1.0 ± 0.5	7.39 ± 0.27	0.28 ± 0.06	7.17 ± 0.09	452/405
6	2.0 ± 0.5	7.36 ± 0.27	0.33 ± 0.06	3.35 ± 0.03	476/405
7	3.0 ± 0.5	8.72 ± 0.44	0.23 ± 0.09	1.66 ± 0.03	412/395
8	4.0 ± 0.5	8.32 ± 0.59	0.24 ± 0.12	0.84 ± 0.02	393/386
9	5.0 ± 0.5	8.56 ± 0.79	0.23 ± 0.15	0.51 ± 0.01	375/374

Table 4.18: Best-fit parameters for A2256 regions shown in Fig. 4.12.

Region	Radius (′)	*kT* (keV)	*Z* ($Z_\odot$)	*Norm* (10^{72} m^{-3} arcmin^{-2})	C-stat/d.o.f.
1	-4.0 ± 0.5	9.03 ± 0.54	0.28 ± 0.15	1.86 ± 0.06	1203/1095
2	-3.0 ± 0.5	6.97 ± 0.27	0.36 ± 0.09	3.25 ± 0.08	1161/1101
3	-2.0 ± 0.5	6.56 ± 0.25	0.37 ± 0.09	3.83 ± 0.09	1149/1081
4 (CORE1)	0.0 ± 1.5	6.89 ± 0.15	0.44 ± 0.06	4.78 ± 0.07	1218/1192
4	2.3 ± 0.8	6.60 ± 0.20	0.48 ± 0.07	5.33 ± 0.09	1077/1073
5	3.8 ± 0.8	5.09 ± 0.13	0.43 ± 0.04	5.41 ± 0.09	1308/1145
6	5.3 ± 0.8	4.24 ± 0.14	0.49 ± 0.08	0.70 ± 0.02	1145/1024
CORE2	-3.3 ± 0.5	4.70 ± 0.12	0.56 ± 0.05	5.79 ± 0.09	1259/1096

"You're simply the BEST,
better than all the rest,
better than anyone."

- Tina Turner, *The Best*

5

X-ray emission from thin plasmas. Collisional ionization for atoms and ions of H to Zn

I. Urdampilleta & J. S. Kaastra & M. Mehdipour

Astronomy & Astrophysics, Volume 601, A85 (2017)

Abstract

Every observation of astrophysical objects involving a spectrum requires atomic data for the interpretation of line fluxes, line ratios and ionization state of the emitting plasma. One of the processes which determines it is collisional ionization. In this study an update of the direct ionization (DI) and excitation-autoionization (EA) processes is discussed for the H to Zn-like isoelectronic sequences. In the last years new laboratory measurements and theoretical calculations of ionization cross sections have become available. We provide an extension and update of previous published reviews in the literature. We include the most recent experimental measurements and fit the cross sections of all individual shells of all ions from H to Zn. These data are described using an extension of Younger's and Mewe's formula, suitable for integration over a Maxwellian velocity distribution to derive the subshell ionization rate coefficients. These ionization rate coefficients are incorporated in the high-resolution plasma code and spectral fitting tool SPEX V3.0.

5.1 Introduction

In calculations of thermal X-ray radiation from hot optically thin plasmas, it is important to have accurate estimates of the ion fractions of the plasma, since the predicted line fluxes sometimes depend sensitively on the ion concentrations. The ion concentrations are determined from the total ionization and recombination rates. In this paper, we focus on collisional ionization rates. Radiative recombination rates (Mao & Kaastra 2016) and charge exchange rates (Gu et al. 2016) are treated in separate papers. These rates are essential for the analysis and interpretation of high-resolution astrophysical X-ray spectra, in particular for the future era of X-ray astronomy with Athena.

An often used compilation of ionization and recombination rates is given by Arnaud & Rothenflug (1985), AR hereafter. AR treat the rates for 15 of the most abundant chemical elements. Since that time, however, many new laboratory measurements and theoretical calculations of the relevant ionization processes have become available. A good example is given by Arnaud & Raymond (1992), who re-investigated the ionization balance of Fe using new data. Their newly derived equilibrium concentrations deviate sometimes even by a factor of 2–3 from AR. The most recent review has been performed by Dere (2007), D07 hereafter. D07 presents total ionization rates for all elements up to the Zn isoelectronic sequence that were derived mainly from laboratory measurements or Flexible Atomic Data (FAC, Gu 2002) calculations.

Motivated by the findings of AR and D07, we started an update of the ionization rates, extending it to all shells of 30 elements from H to Zn. Since we want to use the rates not only for equilibrium plasmas but also for non-equilibrium situations, it is important to know the contributions from different atomic subshells separately. Under non-equilibrium conditions inner shell ionization may play an important role, both in the determination of the ionization balance and in producing fluorescent lines.

In the following Section 5.2, we give an overview of the fitting procedure used in this work. In Section 5.3, we review the ionization cross-sections obtained from experimental measurements or theoretical calculations along isoelectronic sequences. Details of the ion rate coefficients analytical approach are given in Section 5.4, Appendix 5.B and 5.C. In Section 5.5 we compare and discuss the results of this work. The references used for the cross-sections are included in Appendix 5.A.

5.2 Fitting procedure

Collisional ionization is mainly dominated by two mechanisms: direct ionization (DI), where the impact of a free electron on an atom liberates a bound electron; and excitation-autoionization (EA), when a free electron excites an atom into an autoionizing state during a collision.

5.2.1 Direct Ionization cross-sections

An important notion in treating DI is the scaling law along the isoelectronic sequence, as first obtained by Thomson (1912):

$$uI^2Q = f(u), \tag{5.1}$$

where $u = E_\mathrm{e}/I$ with E_e (keV) the incoming electron energy and I (keV) the ionization potential of the atomic subshell; Q (10^{-24} m^2) is the ionization cross-section. The function $f(u)$ does not – in lowest order – depend upon the nuclear charge Z of the ion, and is a unique function for each subshell of all elements in each isoelectronic sequence.

Direct ionization cross-sections are most readily fitted using the following formula, which is an extension of the parametric formula originally proposed by Younger (1981a):

$$uI^2Q_{DI} = A\left(1-\frac{1}{u}\right) + B\left(1-\frac{1}{u}\right)^2 + CR\ln u + D\frac{\ln u}{\sqrt{u}} + E\frac{\ln u}{u}. \tag{5.2}$$

The parameters A, B, D, and E are in units of 10^{-24} m^{2}keV^2 and can be adjusted to fit the observed or calculated DI cross-sections, see Section 5.2.3 for more details. R is a relativistic correction discussed below. C is the Bethe constant and corresponds to the high energy limit of the cross-section.

The parameter C is given by Younger (1981c):

$$C = \frac{IE_\mathrm{H}}{\pi\alpha}\int\frac{\sigma(E)}{E}\mathrm{d}E, \tag{5.3}$$

where $\sigma(E)$ is the photo-ionization cross-section of the current subshell, E_H the ionization energy of Hydrogen and α the fine structure constant. The Bethe constants used in this paper are derived from the fits to the Hartree-Dirac-Slater photoionization cross-sections, as presented by Verner & Yakovlev (1995).

As mentioned above, Eq. 5.2 is an extension of Younger's formula, where we have added the term with $D\ln u/\sqrt{u}$. The main reason to introduce this term is that in some cases the fitted value for C, as determined from a fit over a relatively low energy range, differs considerably from the theoretical limit for $u \to \infty$ as determined from Eq. (5.3). For example, AR give C = 12.0$\times10^{-24}$ m^{2}keV^2 for their fit to the 2p cross-section of C I, while the Bethe coefficient derived from Eq. (5.3) is 6.0$\times10^{-24}$ m^{2}keV^2. However, if we fix C to the Bethe value in the fit, the resulting fit sometimes shows systematic deviations with a magnitude of 10% of the maximum cross-section. This is because the three remaining parameters A, B, and E are insufficient to model all details at lower energies. Therefore, we need an extra fit component which, for small u is close to $\ln u$, but vanishes for large u, to accommodate for the discrepancy in C.

The relativistic correction R in Eq. (5.2) becomes important for large nuclear charge Z (or equivalently large ionization potential I) and large incoming electron energy E (Zhang & Sampson 1990; Moores & Pindzola 1990; Kao et al. 1992). This expression is only valid for the midly relativistic ($\epsilon \lesssim 1$, where $\epsilon \equiv E/m_\mathrm{e}c^2$) regime. Our approximations and cross-sections do not apply to the fully relativistic regime ($\epsilon \gtrsim 1$). The presence of this correction is clearly visible for the hydrogen and helium sequences, as shown in Fig. 5.2. Using a

classical approach the relativistic correction can be written here as given by, for example, Quarles (1976) and Tinschert et al. (1989):

$$R = \left(\frac{\tau+2}{\epsilon+2}\right)\left(\frac{\epsilon+1}{\tau+1}\right)^2\left[\frac{(\tau+\epsilon)(\epsilon+2)(\tau+1)^2}{\epsilon(\epsilon+2)(\tau+1)^2+\tau(\tau+2)}\right]^{3/2}, \tag{5.4}$$

where $\tau \equiv I/m_e c^2$, with m_e the rest mass of the electron and c the speed of light. The above correction factor R, when applied to the simple Lotz-approximation (Lotz 1967), is consistent with the available observational data for a wide range of nuclear charge values (Z=1–83) and 5 magnitudes of energy, within a range of about 15% (Quarles 1976).

For the present range of ions up to Zn (Z=30), the ionization potential is small compared to $m_e c^2$ and, hence, τ is small. On the other hand, we are interested in the cross-section up to high energies (∼100 keV) that applies to the hottest thin astrophysical plasmas, and therefore ϵ is not always negligible. By making a Taylor's expansion in ϵ of Eq. (5.4) for small τ we obtain

$$R \approx 1 + 1.5\epsilon + 0.25\epsilon^2. \tag{5.5}$$

We will use this approximation Eq. (5.5) in our formula for the DI cross-section Eq. (5.2).

Analysing the asymptotic behaviour of Eq. (5.2)

$$\lim_{u\to 1} uI^2 Q_{DI} = (A + C + D + E)(u-1), \tag{5.6}$$

$$\lim_{u\to \infty} uI^2 Q_{DI} = C \ln u. \tag{5.7}$$

Therefore, it is evident from Eq. (5.6) that the fit parameters A to E must satisfy the constraint $A+C+D+E > 0$. Further, the Bethe constant C gives the asymptotic behaviour at high energies.

It appears that when u is not too large, $\ln u$ can be decomposed as (see Fig. 5.1)

$$\begin{aligned}\ln u \quad &\approx 6.5597\left(1-\tfrac{1}{u}\right) + 0.4407\left(1-\tfrac{1}{u}\right)^2 \\ &\quad -5.3622\tfrac{\ln u}{\sqrt{u}} - 0.1998\tfrac{\ln u}{u}.\end{aligned} \tag{5.8}$$

Equation (5.8) has a relative accuracy that is better than 1, 3, and 16% for u smaller than 50, 100, and 1000, respectively; and the corresponding cross-section contribution $\ln u/u$ deviates never more from the true cross-section than 0.5% of the corresponding maximum cross-section (which occurs at $u = e$).

In all cases, where we do not fit the cross-section, based on Eq. (5.8), we use the following expression for the calculation of Younger's formula parameter (with $A(\mathrm{ref})$, $B(\mathrm{ref})$, $C(\mathrm{ref})$, $D(\mathrm{ref})$ and $E(\mathrm{ref})$), as given by the parameters of the isoelectronic sequence that we use as reference. For example, the Li-sequence is used as reference for the 1s cross-sections of the Be to Zn-sequences as detailed in Section 5.3.4.

$$\begin{aligned} A &= A(\mathrm{ref}) + 6.5597[C(\mathrm{ref}) - C(\mathrm{Bethe})], \\ B &= B(\mathrm{ref}) + 0.4407[C(\mathrm{ref}) - C(\mathrm{Bethe})], \\ C &= C(\mathrm{Bethe}), \\ D &= D(\mathrm{ref}) - 5.3622[C(\mathrm{ref}) - C(\mathrm{Bethe})], \\ E &= E(\mathrm{ref}) - 0.1998[C(\mathrm{ref}) - C(\mathrm{Bethe})]. \end{aligned} \tag{5.9}$$

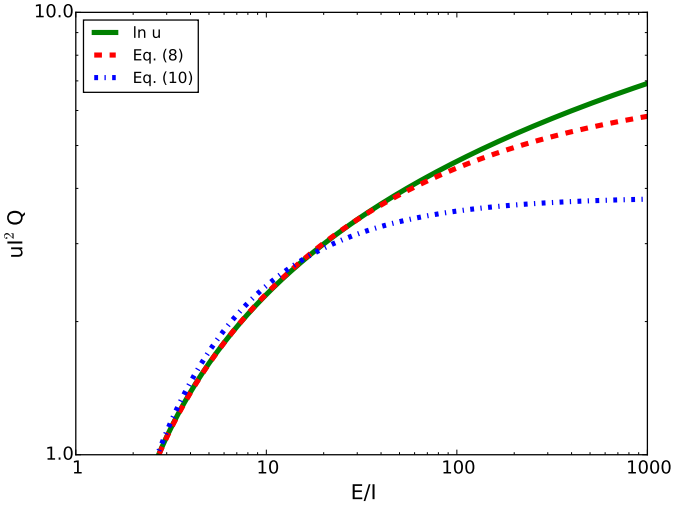

Figure 5.1: Approximation to the Bethe cross-section.

This assures that, for most of the lower energies, the scaled cross-section is identical to the reference cross-section, while at high energies it has the correct asymptotic behaviour.

In some cases, we can get acceptable fits with $D = 0$. In these cases, we obtain a somewhat less accurate approximation for the logarithm:

$$\begin{aligned} \ln u \quad &\approx 6.5867\left(1-\tfrac{1}{u}\right) - 2.7655\left(1-\tfrac{1}{u}\right)^2 \\ &\quad -5.5528\tfrac{\ln u}{u}. \end{aligned} \tag{5.10}$$

Equation (5.10) has a relative accuracy better than 14, 23, and 45% for u smaller than 50, 100, and 1000, respectively; and the corresponding cross-section never deviates more from the true cross-section than 5.6% of the maximum cross-section (which occurs at $u = e$).

In the case of $D = 0$, the equivalent of Eq. (5.9) becomes

$$\begin{aligned} A &= A(\mathrm{ref}) + 6.5867[C(\mathrm{ref}) - C(\mathrm{Bethe})], \\ B &= B(\mathrm{ref}) - 2.7655[C(\mathrm{ref}) - C(\mathrm{Bethe})], \\ C &= C(\mathrm{Bethe}), \\ D &= 0, \\ E &= E(\mathrm{ref}) - 5.5528[C(\mathrm{ref}) - C(\mathrm{Bethe})]. \end{aligned} \tag{5.11}$$

5.2.2 Excitation-autoionization cross-sections

The excitation-autoionization (EA) process occurs when a free electron excites an atom or ion during a collision. In some cases, especially for the Li and Na isoelectronic sequence,

the excited states are often unstable owing to Auger transitions, leading to simultaneous ejection of one electron and decay to a lower energy level of another electron. Many different excited energy levels can contribute to the EA process. In general, this leads to a complicated total EA cross-section, showing many discontinuous jumps at the different excitation threshold energies. Since in most astrophysical applications we are not interested in the details of the EA cross-section, but only in its value averaged over a broad electron distribution, it is reasonable to approximate the true EA cross-section by a simplified fitting formula.

The EA cross-section is most readily fitted using Mewe's formula, originally proposed to fit excitation cross-sections by Mewe (1972):

$$u{I_{EA}}^2 Q_{EA} = A_{EA} + B_{EA}/u + C_{EA}/u^2 + 2D_{EA}/u^3 + E_{EA} \ln u, \tag{5.12}$$

where $u \equiv E_\mathrm{e}/I_{EA}$ with E_e the incoming electron energy; Q_{EA} is the EA cross-section. The parameters A_{EA} to E_{EA} and I_{EA} can be adjusted to fit the observed or calculated EA cross-sections. We note that Arnaud & Raymond (1992) first proposed to use this formula for EA cross-sections, although they used a slightly different definition of the parameters.

For the Li, Be, and B isoelectronic sequences, we used the calculations of Sampson & Golden (1981). All the necessary formulae can be found in their paper. The scaled collision strengths needed were obtained from Golden & Sampson (1978), Table 5.5. For these sequences, we used the sum of two terms with Eq. (5.12), the first term corresponding to excitation 1s-2ℓ, and the second term corresponding to all excitations 1s-$n\ell$ with $n > 2$. The total fitted EA cross-section deviates no more than 5% of the maximum EA contribution, using the exact expressions of Sampson & Golden. Since, for these sequences, the EA contribution is typically less than 10% of the total cross-section, our fit accuracy is sufficient given the systematic uncertainties in measurements and theory.

For the Na to Ar isoelectronic sequences, AR recommends to extend the calculations for the Na-sequence of Sampson (1982) to the Mg-Ar sequences. In doing so, they recommend to put all the branching ratios to unity. We follow the AR recommendations and use the method described in Sampson (1982), extended to the Mg-Ar sequences, to calculate the EA cross-section. We consider the branching ratio unity for these calculations. We include excitation from the 2s and 2p subshells to the ns, np, and nd subshells with n ranging from 3–5. We then fit these cross-sections to Eq. (5.12), splitting it into two components: transitions towards $n = 3$ and $n = 4, 5$. The advantage of this approach is that we can estimate the EA contribution for all relevant energies. Other theoretical EA calculations are often only presented for a limited energy range.

For the K to Cr isoelectronic sequences we obtain the EA parameters by fitting to Eq. (5.12) the FAC EA cross-sections of D07, which are the same used by CHIANTI.

5.2.3 Fitting experimental and theoretical data

The main purpose of our fitting procedure is to obtain the parameters A, B, D, and E of Eq. (5.2) for all inner and outer shells that contribute to DI process, together with the EA parameters, which are calculated as explained above.

For the H and He-sequences, the DI parameters are obtained directly by fitting the cross-sections from experimental measurements and theoretical calculations listed in Ap-

pendix 5.A. The rest of sequences include the DI contribution of the outer and one or several inner shells. In this case, we cannot perform a direct fit to the data because most papers in the literature only present the total cross-sections, which are not split into subshells, while our purpose is to obtain the individual outer and inner shell cross-sections separately.

For this reason, we calculate first the EA and inner shell DI parameters and cross-sections. The particular method used for each isoelectronic sequence is explained in Section 5.3. Afterwards, to obtain the outer shell cross-section (for example for the Li-like sequence, 2s), we subtract the inner shell (in the Li-like case, 1s) and EA contributions from total cross-section. We then fit this outer shell contribution using Eq. (5.2) and obtain the parameters A, B, D, and E.

The remaining cross-sections, for which no data are present are obtained, using Eq. (5.2) with interpolated or extrapolated DI parameters. In this case, A, B, D, and E are calculated by applying linear interpolation or extrapolation of the DI parameters derived from the fitting of experimental or theoretical data along the same shell and isoelectronic sequence. The parameter C is always calculated using Eq. (5.3).

5.3 Ionization cross-sections

The detailed discussion of the available data used for fitting the cross-sections can be found in the following subsections. In general, we follow the recommendations of AR and D07 in selecting the most reliable data sets, but also other reviews like Kallman & Palmeri (2007) have been take into account. We do not repeat their arguments here, therefore only the relevant differences in the selection criteria and application in the code have been highlighted . Moreover, the multi-searching platform GENIE[1] has additionally been used as cross-check. The references for the cross-section data sets used for each isoelectronic sequence (experimental data e or theoretical calculation t) are listed in Appendix 5.A.

5.3.1 H isoelectronic sequence

The cross-sections for this sequence include only the direct ionization process from the 1s shell. For He II, the cross-sections of Peart et al. (1969) have been selected instead of Dolder et al. (1961), Defrance et al. (1987) and Achenbach et al. (1984), because they have a larger extension to the highest energies and an acceptable uncertainty of 12%, compared to Dolder et al. (1961) with 25%.

Relativistic effects are important for the high Z elements of this sequence. This is the reason why the relativistic cross-sections of Kao et al. (1992) and Fontes et al. (1999) for Ne X; Kao et al. (1992) and Moores & Pindzola (1990) for Fe XXVI; and Moores & Pindzola (1990) for Cu XXIX have been chosen. They are, in general, around 5–10% larger than the non-relativistic ones. These effects are mainly present for high Z elements of the H and He isoelectronic sequences, as can be seen in Fig. 5.2, where the total DI normalized cross-section of Fe XXVI is shown. For this ion the cross-section increases asymptotically with the energy beyond $u = 100$. The measurements of O'Rouke et al. (2001) for Fe XXVI has

[1] https://www-amdis.iaea.org/GENIE/

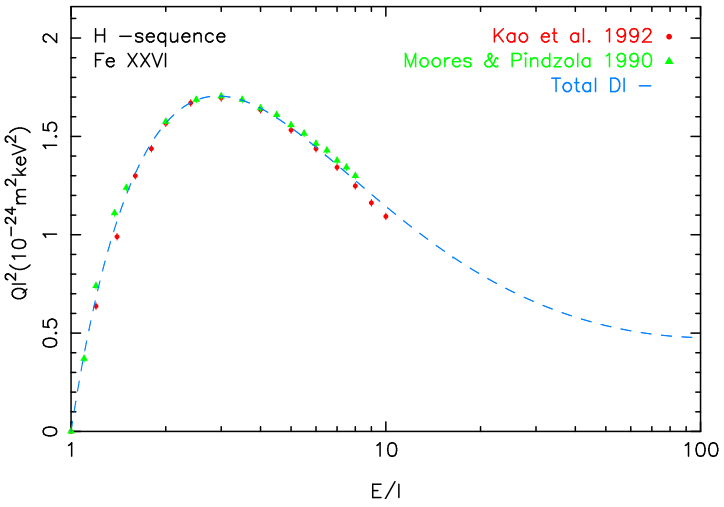

Figure 5.2: Total DI normalized cross-section for Fe XXVI (dashed blue line) and the measurements of Kao et al. (1992) (red dots) and Moores & Pindzola (1990) (green triangles). Note the presence of relativistic effects for high energies.

been neglected because they present a considerable experimental error and are in poor agreement with the selected calculations.

The cross-section comparison of this sequence with D07 shows a good agreement for all the elements except for Be IV. We calculate by linear interpolation in $1/Z$ between Li III and B V, which are fitted by experimental measurements. The value at the peak for our interpolation is 20% lower than the values used by D07. However, it follows a smooth increase, which is consistent with the trend of the rest of the elements in this sequence.

5.3.2 He isoelectronic sequence

The He-like ions have an $1s^2$ structure and the DI process includes ionization of the 1s shell. For He I, the experimental data of Shah et al. (1988) and Montague et al. (1984b) have been used together with the more recent measurements of Rejoub et al. (2002). These data sets are in very good agreement with the cross-sections presented in Rapp & Englander-Golden (1965), although the value at the peak is 6% lower. The final fit has an uncertainty less than 6%. For Li II, the measurements of Peart & Dolder (1968) and Peart et al. (1969) were selected, as shown in Fig. 5.3, an example of the 1s shell DI fitting. For Be III the same difference with D07 as described for the H-like sequence occurs as well. The peak value using our linear interpolation in $1/(Z-1)$ is 30% lower than D07.

Since the data range for Ne IX, as measured by Duponchelle et al. (1997), is rather limited, we have supplemented their data by adding the cross-sections at $u = 100$, as interpolated from the calculations of Zhang & Sampson (1990) for O VII and Fe XXV.

The relativistic calculations for O VII, Fe XXV, and Zn XXIX of Zhang & Sampson (1990)

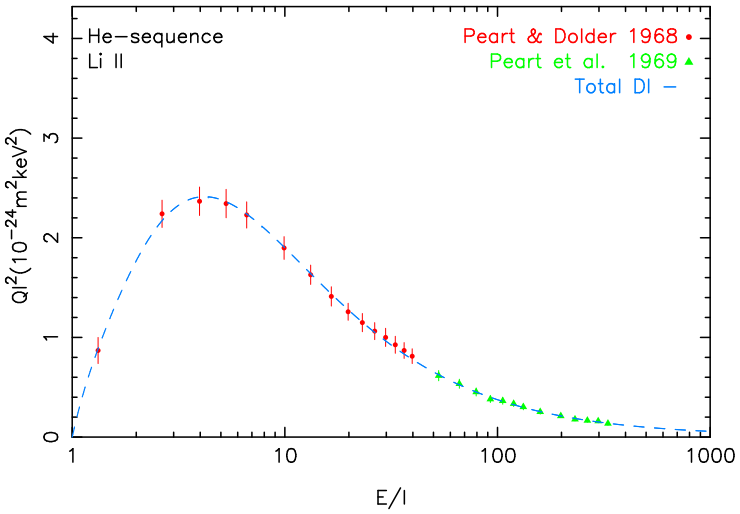

Figure 5.3: Total DI normalized cross-section for Li II (dashed blue line) and the measurements of Peart & Dolder (1968) (red dots) and Peart et al. (1969) (green triangles) with their respective experimental error.

yield cross-sections that are about 15% larger at the higher energies than the corresponding cross-sections interpolated from the theoretical results for N, Na and Fe (Younger 1981a, 1982a). This is similar to what we find for the H-like sequence, and is in agreement with the relativistic effects expected for high Z elements.

5.3.3 Li isoelectronic sequence

Li sequence ions have a structure of $1s^2 2s$ and can experience DI in both the 1s and 2s shell with a significant presence of an EA contribution in the outer shell, mainly for highly ionized elements. The DI and EA cross-sections are calculated with the equations described in Section 5.2.1 and 5.2.2, respectively.

DI: 1s cross-sections

Younger (1981a) showed that, except for the lower end of the sequence, the cross-sections are similar to the values for the He-sequence. This is confirmed by the work of Zhang & Sampson (1990) for O, Fe, Zn, and U. Wherever needed, we have corrected for a difference in the Bethe constant between the He-like and Li-like sequence using Eq. 5.11. We note that, again for Ni, the cross-sections of Pindzola et al. (1991) are 15–25% lower than those of Zhang & Sampson (1990).

In summary, we used Younger (1981a) for Li I, Be II; the corresponding cross-section of the He-sequence for B III, C IV, N V; Zhang & Sampson (1990) for O VI, Fe XXIV and Zn XXVIII; and linear interpolation in $1/(Z-1)$ for the remaining cross-sections.

DI: 2s cross-sections

For Li I, we follow the recommendations of McGuire (1997) and we fit the convergent close-coupling calculations of Bray (1995) below 70 eV, together with the measurements of Jalin et al. (1973) above 100 eV.

For B III, C IV, N V, O VI, and F VII, high resolution measurements exist near the EA threshold (Hofmann et al. 1990). These measurements are systematically higher than the measurements of Crandall et al. (1979) and Crandall et al. (1986), ranging from 9% for B III, 24% for N V to 31% for O VI. Moreover, for C IV Hofmann's data above the EA onset are inconsistent in shape with both Crandall's measurements and the calculations of Reed & Chen (1992). Therefore we did not use the measurements of Hofmann et al. (1990).

For N V, the measurements of Crandall et al. (1979) are ∼10% smaller than Defrance et al. (1990) below 300 eV, but 10% larger above 1000 eV. In the intermediate range, where the EA onset occurs, the agreement is better than 5%. We used Crandall et al. (1979), together with the high energy data of Donets & Ovsyannikov (1981).

For O VI, the measurements of Crandall et al. (1986) are ∼10% smaller than those of Defrance et al. (1990) below 450 eV and above 800 eV. In the intermediate range, where the EA onset occurs the agreement is good. We have used both data sets in our fit, but scaled the measurements of Defrance et al. by a factor of 0.95, and also we have included the high energy data of Donets & Ovsyannikov (1981). Using the statistical errors in the data sets, the relative weights used in the fit are approximately 5:1:2 for Crandall et al., Defrance et al., and Donets & Ovsyannikov, respectively.

For Fe XXIV and Zn XXVIII, we again considered the relativistic calculations of Zhang & Sampson (1990). Their scaled cross-sections for O VI, Fe XXIV, and Zn XXVIII are not too different; therefore we interpolate linearly in $1/(Z-1)$ all elements between Ne and Fe, and similarly between Fe and Zn.

For Ti to Fe, measurements also exist at about 2.3 times the ionization threshold (Wong et al. 1993) with an uncertainty of 10%, which are also proposed by D07. The ratio of these observed cross-sections to the calculations are 0.83, 0.81, 0.85, 0.84, and 0.97, respectively for $Z = 22$–26. Given the measurement uncertainty, and the agreement of the calculations of Zhang & Sampson in the region of overlap with those of Chen & Reed (1992), we finally decided to use the calculations of Zhang & Sampson.

As for the 1s cross-sections in the H, He, and Li sequences, the cross-sections of Younger (1982a) for Fe XXIV are 5% smaller than those of Zhang & Sampson at the highest energies, instead of the typically 15% for the 1s cross-sections. Thus relativistic effects are slightly less important, which can be understood given the lower ionization potential for the 2s shell, compared to the 1s shell.

EA contribution

Fits to the calculations of Sampson & Golden (1981) were used to approximate the shape of the EA contribution. The contributions, which are due to excitation towards n=2, 3, 4, and 5, are treated separately. A comparison of the results of Sampson & Golden ($Q_{\rm SG}$) with the more sophisticated calculations of Reed & Chen (1992) and Chen & Reed (1992) ($Q_{\rm RC}$) just above the $1s-2p$ excitation threshold for Z= 6, 9, 18, 26, and 36 gives for the ratio $Q_{\rm RC}/Q_{\rm SG}$

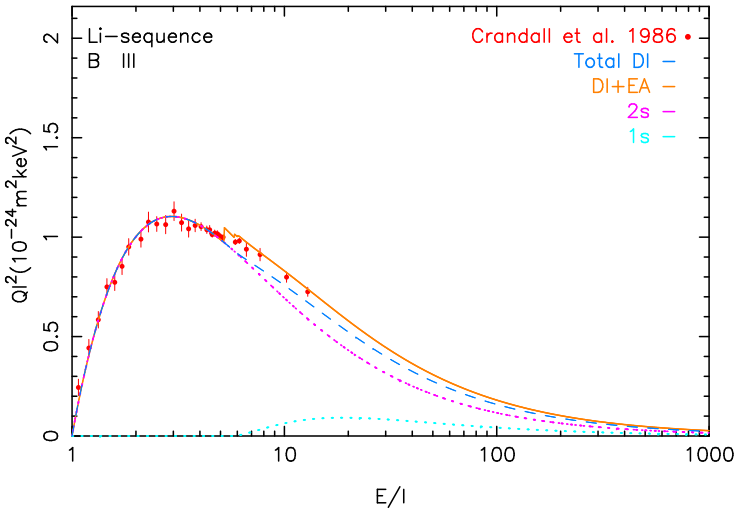

Figure 5.4: Total DI (dashed blue line) and DI plus EA (orange line) normalized cross-section for B III, where the DI contribution of the 1s shell is shown as the dotted cyan line and the 2s shell in magenta. The measurements of Crandall et al. (1986) (red dots) with the experimental uncertainties are also included.

values of 0.52, 0.64, 0.77, 1.18, and 2.02, respectively. The following approximation has been made to these data:

$$Q_{\rm RC} = [0.54 + 1.33 \times 10^{-4}\ Z^{2.6}]Q_{\rm SG}. \tag{5.13}$$

A similar tendency is noted by AR. A more detailed analysis shows that for larger energies the discrepancy is slightly smaller. Unfortunately, Reed & Chen and Chen & Reed only give the EA cross-section near the excitation thresholds. Therefore, we decided to retain the calculations of Sampson & Golden (1981), but to scale all EA cross-sections using Eq. (5.13). We note that, for this isoelectronic sequence, the EA contribution is, in general, smaller than ∼10%, and thus slight uncertainties in the EA cross-section are not very great in the total ionization cross-section. Figure 5.4 shows an example of Li-like ion cross-sections scaling.

5.3.4 Be isoelectronic sequence

The Be sequence elements have a structure of $1s^2 2s^2$ and can experience DI through collisions in the 1s and 2s shells. There is also an EA contribution. Moreover, in experimental data, some elements, like C III, N VI, and O V often show a high population of ions in metastable levels $1s^2 2s2p$.

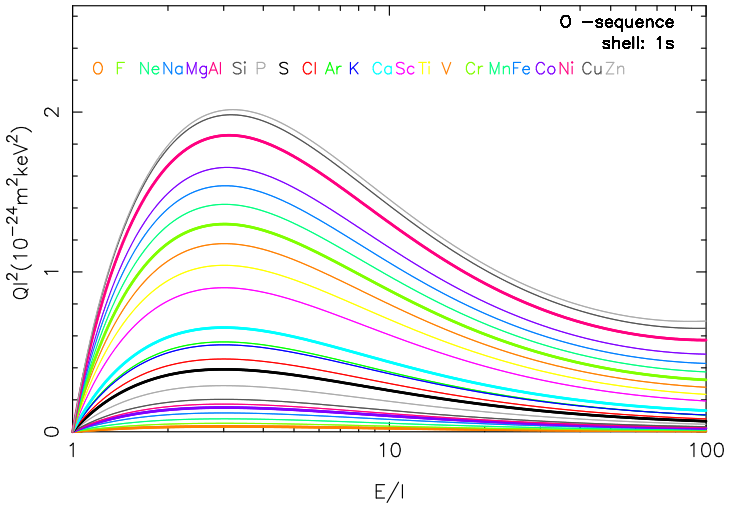

Figure 5.5: Total DI cross-section for the 1s subshell for all elements of the oxygen sequence using interpolation with Eq. (5.11).

DI: 1s cross-sections

The 1s cross-sections for all elements in the Be to Zn isoelectronic sequences have been calculated with Eq. (5.11) and, using as a reference, the parameters obtained for the 1s inner shell of Li-like ions. An example can be seen in Fig. 5.5 for the oxygen isoelectronic sequence.

A comparison of some K-shell measurements compiled by Llovet et al. (2014), for example for C I, Al I, and Ti I (Limandri et al. 2012), demonstrated a good agreement with the maximum difference between the measurements and the calculations with Eq. (5.11) at the peak for Ti I of less than 15%.

DI: 2s cross-sections

The measurements in this sequence are often greatly affected by metastable ions (see the discussion in AR). As mentioned in Loch et al. (2003) and Loch et al. (2005), it is essential to know the ratio of the metastable configuration for an accurate determination of the ground-state cross-section.

D07 proposes using the measurements of Falk et al. (1983a) for B II, which we discard owinge to the existence of a significant population of ions in metastable levels, which results in a ground-state cross-section higher than that proposed by Fogle et al. (2008) for C III, N IV, and O V. Fogle's measurements use the crossed-beam apparatus at Oak Ridge National Laboratory. In this experiment, it was possible to measure the metastable ion fractions present in the ion beams in the $1s^2 2s2p$ levels, which were used to infer the rate coefficients for the electron-impact single ionization from the ground state and metastable term of each ion. Considering these mentioned rates in the paper for the ground cross-

sections calculations, they are in good agreement (error of ∼7% for C III and ∼2% for N IV and O V) with the cross-sections obtained by the Younger (1981d) theoretical calculation. The measurements of Loch et al. (2003) for O V have been neglected because it was not possible to determine the metastable fraction at the experimental crossed-beam.

The measurements of Bannister for Ne VII are consistent with the Duponchelle et al. (1997) ones at high energies, but show a bump around 280 eV, and are finally rejected. For S XIII, Hahn et al. (2012a) eliminated all metastable levels using hyperfine induced decays, combined with an ion storage ring, obtaining a total cross-section with 1σ uncertainty of 15%. The measurements are in very good agreement with the theoretical data of Younger (1981c) and distorted-wave calculation of D07.

Lacking more reliable measurements for this isoelectronic sequence, and given the reasonable agreement with the measurements for Ne VII, we base our cross-sections on the theoretical calculations of Younger (Younger 1981d, 1982a) for F VI, Ar XV, and Fe XXIII. The calculations of Fe XXIII have been multiplied by a scaling factor of 1.05, to account for these effects, as are present in the Li-sequence for 2s electrons.

EA contribution

For all ions of this sequence, we also include the EA contribution according to Sampson & Golden (1981), although the contribution is small (in general smaller than ∼5%). A comparison of the results of Sampson & Golden ($Q_{\rm SG}$) with the more recent calculations of Badnell & Pindzola (1993) ($Q_{\rm BP}$), which include calculations for only Fe, Kr, and Xe just above the 1s-2p excitation threshold, was performed. This shows a systematic trend that can be approximated by

$$Q_{\rm BP} = [0.70 + 1.46.10^{-3}\ Z^2]Q_{\rm SG}. \tag{5.14}$$

We assume that the rest of the elements of this isoelectronic sequence present the same behaviour. Therefore, we use the calculations of Sampson & Golden (1981), but scale all EA cross-sections to the results of Badnell & Pindzola using Eq. (5.14).

5.3.5 B isoelectronic sequence

The elements of the B-like sequence ($1s^2 2s^2 2p$) have an EA contribution in the outer shell that is relatively small (Yamada et al. 1989a; Duponchelle et al. 1997; Loch et al. 2003).

DI: 2s cross-sections

Younger (1982a) shows that, for the iron ions of the Be to Ne sequences, the 2s cross-section is approximately a linear function of the number of the 2p electrons present in the ion. Following AR, we assume such a linear dependence to hold for all ions of these sequences. Thus, from the 2s cross-sections for the Be-sequence and those of the Ne-sequence, the 2s cross-sections for all ions between Na–Zn for intermediate sequences (B-like, C-like, N-like, O-like, and F-like) are obtained by linear interpolation plus the Bethe coefficient difference correction applying Eq. (5.9).

For ions of B to F in the B-F isoelectronic sequences, we cannot use the above interpolation since, in this case, there are no ions in the Ne-sequence. AR assume that the 2s cross-section of the Ne-sequence minus the 2s cross-section of the Be-sequence depends linearly upon the atomic number Z; since our procedure is slightly different from Arnaud & Rothenflug, we cannot confirm clear linear trends in our data. For that reason, we use for the ions from B to F a linear extrapolation of the difference coefficients given by AR:

$$\begin{aligned} A(\text{Ne seq.}, 2\text{s}) - A(\text{Be seq.}, 2\text{s}) &= 4.20 - 0.1658\ Z, \\ B(\text{Ne seq.}, 2\text{s}) - B(\text{Be seq.}, 2\text{s}) &= -0.42 - 0.1313\ Z, \\ C(\text{Ne seq.}, 2\text{s}) - C(\text{Be seq.}, 2\text{s}) &= -0.05 + 0.0088\ Z, \\ E(\text{Ne seq.}, 2\text{s}) - E(\text{Be seq.}, 2\text{s}) &= -18.87 + 0.8240\ Z, \end{aligned} \tag{5.15}$$

where Z is the atomic number and A, B, and E are in units of 10^{-24} m^{2}keV^2.

DI: 2p cross-sections

For B I, we included the CHIANTI data obtained from Tawara (2002) (D07). The data of Aitken et al. (1971) for C II are slightly higher than the measurements of Yamada et al. (1989a), especially near the threshold. Nevertheless, we use both data sets in our fit, with a larger weight given to the data of Yamada et al.

For N III, we chose Aitken et al. (1971) and Bannister & Haverner (1996b) proposed by D07 because both data sets extend from near threshold to $u = 20$ and, besides, they are in relatively good agreement, except below the peak where the data of Bannister & Haverner (1996b) are ∼5% higher.

The most recent measurement for the B-sequence is that of Hahn et al. (2010) for Mg VIII. The innovative aspect of the Hahn et al. data is the use of an ion storage ring (TSR) for the measurements. This new experimental technique achieves a radiative relaxation of ions to the ground state after being previously stored long enough in the TSR, decreasing considerably the contribution of possible metastable ions. The data show a 15% systematic uncertainty owing to the ion current measurement. Nevertheless, the data are in good agreement with the distorted-wave calculations with the GIPPER (Magee et al. 1995) and FAC (Gu 2002) codes, within the experimental uncertainties.

The theoretical data for Fe XXII are based upon Zhang & Sampson (1990) for Ne-like iron. Following Younger (1982a), we assume that the scaled 2p cross-section for B-like to Ne-like iron is a linear function of the number of 2p-electrons; we account for the slight difference in $2p_{1/2}$ and $2p_{3/2}$ cross-sections in the work of Zhang & Sampson. Finally, we use their data for Se (Z=34) to interpolate the ions between Fe and Zn on these sequences.

EA contribution

For all ions of this sequence, we include the EA contribution according to Sampson & Golden (1981), although the contribution is small (in general less than ∼2.5%). A comparison of the results of Sampson & Golden ($Q_{\rm SG}$) with the calculations of Badnell & Pindzola (1993) ($Q_{\rm BP}$) for Fe, Kr and Xe just above the 1s-2p excitation threshold, shows a systematic

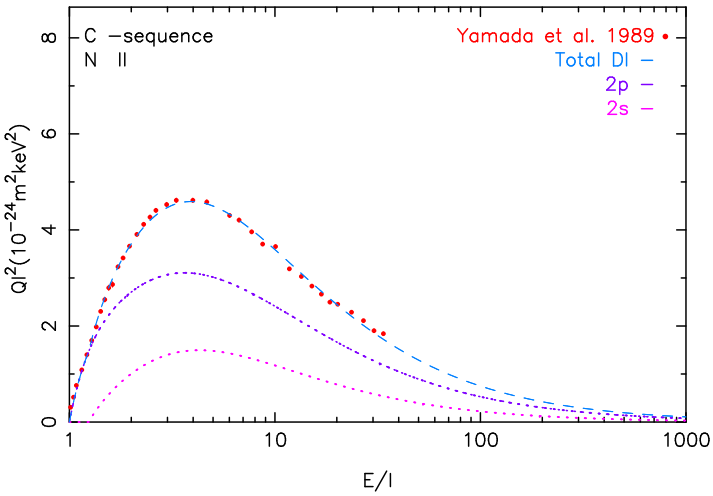

Figure 5.6: Total DI normalized cross-section for Ne II (dashed blue line) and the measurements of Yamada et al. (1989a) (red dots) with the experimental uncertainties.

trend that can be approximated by

$$Q_{\mathrm{BP}} = [0.92 + 7.45 \times 10^{-5}\ Z^2] Q_{\mathrm{SG}}. \tag{5.16}$$

We retain the calculations of Sampson & Golden, but scaled all EA cross-sections to the results of Badnell & Pindzola using Eq. (5.16).

5.3.6 C isoelectronic sequence

The ions of the carbon isoelectronic sequence ($1s^2 2s^2 2p^2$) can be directly ionized by the collision of a free electron with electrons in the 1s, 2s, and 2p shells; the same holds for all sequences up to the Ne-like sequence. There is no evidence for a significant EA processes in the C to Ne sequences.

DI: 2p cross-section

For O III, we use the measurements of Aitken et al. (1971), Donets & Ovsyannikov (1981), and Falk (1980). The first two are provided up to ten times the threshold. The Aitken et al. (1971) measurements are ∼15% lower than those of Falk (1980) beyond the cross-section peak. We also use the data of Donets & Ovsyannikov (1981) for the high energy range. Figure 5.6 shows an example of the DI contribution for the 2s and 2p shells.

5.3.7 N isoelectronic sequence

DI: 2p cross-section

The measurements for Si VIII (Zeijlmans van Emmichoven et al. 1993) were correctly fitted using Eq. (5.2), obtaining a maximum uncertainty of ∼6%. The peak value of Si VIII compared with CHIANTI data is ∼10% lower. This difference also affects the cross-sections of interpolated components between Ne IV and Si VIII.

The data of Yamada et al. (1989a) for O II are about 5% higher than the older data of Aitken et al. (1971); our fit lies between both sets of measurements. For O II and Ne IV, the high energy measurements of Donets & Ovsyannikov (1981) are significantly higher than our fit, including that data set; we have therefore discarded these measurements for these ions.

5.3.8 O isoelectronic sequence

DI: 2p cross section

We note that the measurements for Si VII (Zeijlmans van Emmichoven et al. 1993) could be affected by metastable ions that show an increase between 10-20% of the cross-section at the peak compared with the distorted-wave calculations. This is the reason we neglect this data set. For Ne III, we discard the high energy measurements of Donets & Ovsyannikov since these are 30% below our fit including those data.

5.3.9 F isoelectronic sequence

DI: 2p cross-section

The Yamada et al. (1989a) measurements were included for F I up to $u = 10$. The most recent measurements in this sequence are from Hahn et al. (2013) for Fe XVIII up to energies of $u = 3$. The measurements given by Hahn et al. (2013) are 30% lower than the values provided by Arnaud & Raymond (1992) and 20% lower than D07. This is achieved by the new experimental technique of the ion storage ring. We combine these data with the theoretical calculations of Zhang & Sampson (1990) for high energies. These theoretical data were obtained directly from the total cross-section modelling for the 2p shell, as explained in Section 5.3.5. The Fig. 5.7 above shows the DI fitting of four different experimental measurements for Ne II.

5.3.10 Ne isoelectronic sequence

DI: 2s cross-section

For Na, Mg and Al Younger (1981c) calculates the 2s cross-sections in the Na-like sequence. For the high Z end of the sequence (Ar and Fe), the difference between the Ne-like and Na-like 2s cross-section is, in general, at most a few percent. Accordingly, we assume that,

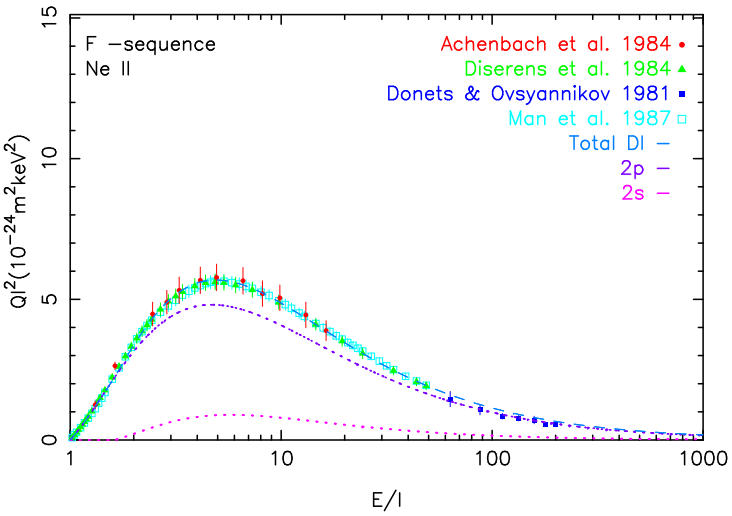

Figure 5.7: The DI normalized cross-section for Ne II (dashed blue line) and the measurements of Achenbach et al. (1984) (red dots), Diserens et al. (1984) (green triangle), Donets & Ovsyannikov (1981) (blue square) and Man et al. (1987a) (cyan square) with their respective experimental uncertainties.

for the low Z end of the Ne-sequence, the shape of the cross-section is at least similar to that of the Na-sequence.

Therefore, we have extrapolated the Na-like data of Younger (1981c) to obtain the cross-sections of Na II, Mg III, Al IV, P VI, and Ar IX. We found that the ratio of the Ne-like to the Na-like 2s cross-section is about 1.38, 1.23, 1.06, and 1.00 for the elements Na, Mg, Al, and Ar. We included a scaling factor of 1.00 for P. Our adopted 2s ionization cross-section for the Ne-like ions Na II, Mg III, Al IV, P VI, and Ar IX are thus based upon the corresponding Na-like cross-section, multiplied by the above scaling factors. Lacking other data, for Ne I we simply used the correlation Eq. (5.15) between Ne-like and Be-like 2s cross-sections. For the remaining elements from Si and higher, we use linear interpolation in $1/(Z-3)$.

DI: 2p cross-sections

We used the calculations of Younger (1981b) for the 2p shell of Al IV instead of the Aichele et al. (2001) measurements because, as they explain, their data contain a 20% contribution from metastable ions contamination.

For Ar IX, we did not use the data of Zhang et al. (1991), because they contain a 3% contribution of a metastable state, which is strongly auto-ionising. The contribution of this metastable state, which is described well by the calculations of Pindzola et al. (1991), makes the measured cross-section ∼5% higher at 1 keV; however, owing to the complex ionization cross-section of this metastable state, we do not attempt to subtract it, but merely use the data of Defrance et al. (1987) and Zhang et al. (2002) for this ion, which appears to be free of metastable contributions.

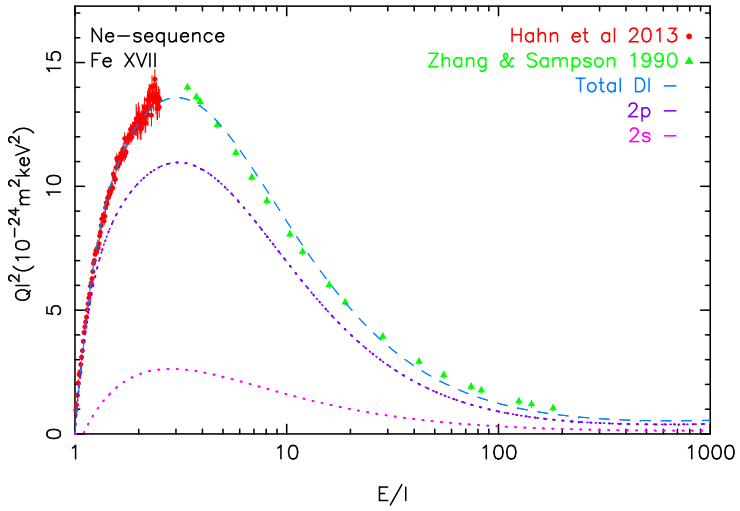

Figure 5.8: Total DI normalized cross-section for Fe XVII (dashed blue line) and the measurements of Hahn et al. (2013) (red dots), and calculations of Zhang & Sampson (1990) (green triangles).

We have used the measurements of Hahn et al. (2013) for Fe XVII up to energies close to $u = 3$, together with Zhang & Sampson (1990) for high energies, as in the same case of Fe XVIII, see Fig. 5.8.

5.3.11 Na isoeletronic sequence

DI: 2s and 2p cross-section

We use the theoretical calculations of Younger (1981c) for Mg II, Al III, P V, and Ar VIII and Pindzola et al. (1991) for Ni XVIII. The remaining elements have been interpolated, except for Na I, for which we adopted the scaled Mg II parameters.

DI: 3s cross-section

We decided not to include the measurements for Ar VIII (Rachafi et al. 1991; Zhang et al. 2002) and Cr XIV (Gregory et al. 1990), because they are higher and lower, respectively, compared with the other elements on this sequence. The Ar VIII measurements are probably affected by the presence of resonant excitation double Auger ionization (REDA).

Ti XII was fitted using Gregory et al. (1990), although there are only measurements up to $u = 3$. For this reason we included some values from Griffin et al. (1987) calculation for higher energies. The data of Gregory et al. (1990) are about 10% higher than the calculations of Griffin et al. (1987), therefore we decided to apply a scaling factor of 0.9.

For Fe XVI, the measurements of Gregory et al. (1987) and Linkemann et al. (1995) were used, which extend till $u = 2$. The data of Gregory et al. (1987) are 30% higher than those of Linkemann et al. (1995), resulting in a fit with values around 15% higher than proposed

by the Griffin et al. (1987). To achieve a better agreement of 5-10%, we applied a scaling factor of 0.9 to the Gregory et al. (1987) measurements. Finally, we included the theoretical calculations of Pindzola et al. (1991) for Ni XVIII, which agree with Griffin et al. (1987) better than 10%.

The total cross-sections obtained with our method are systematically higher than D07 by 10-30%. For several elements, the DI level seems to be of the same order and the main difference is related to EA contributions. A possible explanation could be that we use the calculations of Sampson (1982), which include more excitation transitions (from 2s, 2p, and 3s subshells to the ns, np and nd subshells with n=3–5), while D07 use the FAC EA calculation scaled by a certain factor for excitation into $2^7\ 3l3l'$ and $2^7\ 3l4l'$.

EA contribution

For the low Z elements of this sequence (Mg II, Al III and Si IV) the theoretical calculations of Griffin et al. (1982) for the EA contribution fail to correctly model the measurements, mainly due to too large 2p→3p and 2p→4p cross-sections, but also becuase of the presence of REDA contributions in the measured cross-sections (Müller et al. 1990; Peart et al. 1991b). The measured cross-sections show a distinct EA contribution, but not with the sharp edges that are usually produced by theory owing to limitations in the way the EA contribution is calculated. Therefore, we fitted the measured cross-sections of Mg II, Al III, and Si IV to (5.12) after subtracting the DI contributions.

For Na I and Mg II, there are no signs of the EA onset owing to the regularity of the measurements although some REDA contributions could be present. For Al III and Si IV, we have followed the same procedure chosen by D07 for scaling all the EA cross-sections to recreate the measured values. Therefore, we retained the calculations of Sampson (1982), but scaled by a factor of 0.4 for Al III and 0.5 for Si IV. The rest of elements have been maintained with a scaling factor equal to 1.0.

5.3.12 Mg isoelectronic sequence

DI: 2s and 2p cross-section

The 2s and 2p cross-sections for all elements from the Mg to Zn isoelectronic sequences have been calculated with Eq. 5.9 using, as a reference, the parameters obtained for the 2s and 2p subshell, respectively, of the previous isoelectronic sequence. Therefore, for the Mg-sequence, the reference parameters for all elements are taken from the Na-sequence.

To evaluate the robustness of this method, we introduced a 10% and 20% increase in the A to E parameters of the Fe XV 2s shell and analysed how it affects the 2s shells of Fe ions for the following isoelectronic sequences. If we compare the difference in the peak of the cross-sections, from the Al to Ti sequences (there is no 2s shell contribution for the V to Fe-sequence) the error is reduced to 5-6% and 11%, respectively. This difference is maintained almost constantly for all the sequences as seen in Fig. 5.9. We also evaluated the impact in the calculation of the outer shell DI cross-sections using the fitting procedure explained in Section 5.2.3 and the effects are negligible, being the maximum difference of 0.03%, 0.07%, and 0.06%, for an initial increase of 10%, 20%, and 50%, respectively. The main reason for

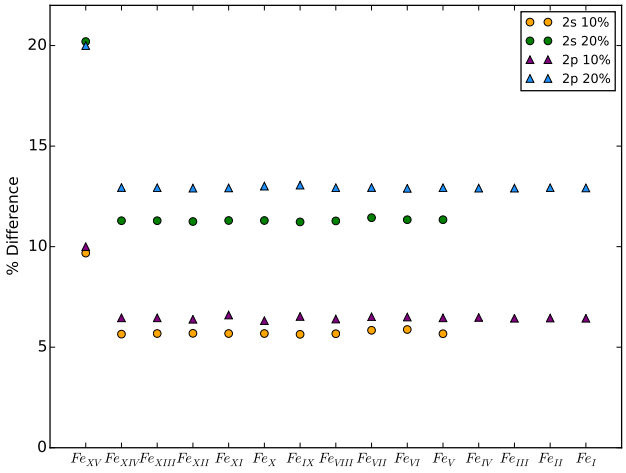

Figure 5.9: Error propagation along Fe ions after applying a 10% and 20% increase in the 2s shell (orange and green circles) and the 2p shell (purple and blue triangles) DI parameters of Fe XV.

this behaviour is because the 2s shell cross-sections and their contribution to the single ionization is much lower than the outer shells. Therefore, a variation in the DI parameters of the 2s shell has no appreciable effects on the other shell cross-sections.

We performed the same study for the 2p shell as explained above for the 2s shell. The results are slightly similar and the same conclusions are applicable in this case.

DI: 3s cross-sections

Following the discussion in McGuire (1997), we scaled-down the experimental results for Mg I and Al II by multiplying by a factor of 0.8. For Si III and S V the measurements of Djuric et al. (1993b) and Howald et al. (1986), respectively, were omitted because the measurements present clear evidence of metastable ions.

In the case of Ar VII, the measurements of Chung (1996) do not show evidence of 3s3p ^{3}P metastable ions unlike Djuric et al. (1993b), Howald et al. (1986) and Zhang et al. (2002). However, they only extend up to $u = 6$, where they seem to be in good agreement with Zhang et al. (2002), which contains data till 30 times the threshold. For this reason, we used the Chung (1996) measurement adding the Zhang et al. (2002) cross-sections above $u = 5$.

Bernhardt et al. (2014) present recent measurements for Fe XV in the range 0–2600 eV. Bernhardt et al. use the TSR storage-ring technique, also applied to several measurements of Hahn et al., which allows them to reduce the fraction of metastable ions in the stored ion beam.

Figure 5.10 shows the total cross-section calculated as the sum of 3s shell data of

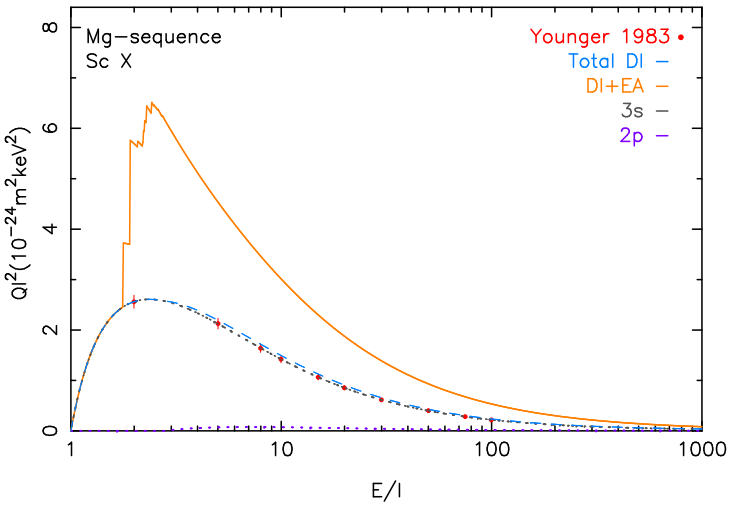

Figure 5.10: Total normalized cross-section for Sc X (orange line), DI cross-section (dashed blue line), 3s (pointed grey line), 2p (pointed purple line) and the calculations for the 3s shell of Younger (1982b) (red dots).

Younger (1983) for Sc X with the rest of the inner-shell contributions. In this case, the main contributor to the total DI cross-section is the 3s shell followed by the 2p shell in a very low proportion. The EA contribution was added from Sampson (1982) after applying a scaling factor, as explained in the following section. As in the case of the Na-like sequence, the total cross-section compared to D07 is systematically 10-40% higher, probably for the same reason.

EA contribution

For the Mg-sequence, we compared the EA contributions calculated with the method explained in Section 5.2.2 to other calculations available for Z =13, 16, 17 and 18 (Tayal & Henry 1986), and Z =28 (Pindzola et al. 1991). We have compared Sampson's cross-sections $Q_{\rm SG}$ at about twice the EA onset towards these other calculations $Q_{\rm TP}$, and have found the following relation for these elements. We assume the same relation for Z >14 of the Mg-sequence:

$$Q_{\rm TP} = [-0.07 + 0.03306\ Z]Q_{\rm SG}. \tag{5.17}$$

For Al II and Si III the scaling factor is smaller: 0.20. The observations for neutral Mg I (Freund et al. 1990; McCallion et al. 1992a) show no evidence for EA and therefore we neglected this process for neutral Mg. The available measurements (Chung 1996; Bernhardt et al. 2014) show EA enhancements that are consistent with the above scaling.

5.3.13 Al isoelectronic sequence

DI: 3s cross-sections

For the Al-sequence up to the Ar-sequence the 3s inner-shell contribution is interpolated from the theoretical calculations of Younger (1982a) for Ar, Sc, and Fe ions. For the P-like and S-like sequences, we included the data for Ni ions from Pindzola et al. (1991) because they correctly follow the trend of the rest of the elements in the same sequence, which is not the case for the other sequences.

DI: 3p cross-sections

For Fe XIV, the recent measurements of Hahn et al. (2013) using the TSR ion ring storage confirm the existence of a considerably lower cross-section than previous measurements (Gregory et al. 1987) or calculations (AR; D07). Hahn's results agree with Gregory's from threshold up to 700 eV, and after that they decrease until they show a difference of 40%. One of the reason for this difference could be the presence of the metastable ions in Gregory's experiment. The major discrepancies with the theory could come from the fact that theory overestimates the EA component, specially the $n = 2 \rightarrow 4$ transitions, in the case of D07.

EA contribution

For the Al to Ar-sequences, the EA calculations of Pindzola et al. (1991) for Ni ions can be used for comparison with the EA parameters derived from Sampson (1982). The scaling factors needed to bring the Sampson data in accordance with the Pindzola data are given in Table 5.1. These data show that the scaling factor gets smaller for higher sequences. This is no surprise since Sampson's calculations were, in particular, designed for the Na-sequence. We note that the relative importance of the EA process diminishes anyway for the higher sequences.

Lacking other information we assumed that, for all other ions of these isoelectronic sequences, the same scaling factors apply as for the Ni-ions. Where there are measurements available with clear indications of the EA process, this scaling appeared to be justified. The possible exception is Ni XIII (S-sequence), where Pindzola et al. (1991) suggest that there is an additional contribution in the measurements of Wang et al. (1988) owing to resonant recombination followed by double autoionization. However, we decided to apply the same process as explained above for calculating the scaling factor of the S-sequence, only taking into consideration the Pindzola data.

5.3.14 Si isoelectronic sequence

DI: 3p cross-sections

The experimental data available for Ar V (Crandall et al. 1979; Müller et al. 1980; Sataka et al. 1989) agree well below 200 eV but, above this energy, the Crandall et al. data are slightly

higher. The three data sets are about 20% larger than expected based upon Younger's calculations, probably due to some contamination by metastable levels in the beam. For this reason, theoretical calculations were obtained for Ar V, taking the A, B, C, and D parameters proposed by AR for Younger's formula.The same situation occurs for Cr XI (Sataka et al. 1989) and the data were discarded.

The measurements of Hahn (Hahn et al. 2011b, 2012b) are used for Fe XIII. These data are 20% lower than the Arnaud & Raymond (1992) calculations and 15% lower above ∼680 eV, compared with the FAC calculations of D07. The Hahn et al. experimental data show a faster increase of the cross-section in the onset compared with the calculations, probably owing to the excitation of the 3s shell electron, which the calculations did not include. The possible explanation for the higher EA contribution above the threshold proposed by Hahn is that the calculations overestimate the branching ratio of the autoionization and, additionally, the intermediate states could decay by double ionization rather than single ionization.

5.3.15 P isoelectronic sequence

DI: 3p cross-sections

The measurements of Freund et al. (1990) for P I are used for the 3p cross-section fitting with an error less than 6%. In the case of S II, two data set are available, Yamada et al. (1988) and Djuric et al. (1993a), which agree within ±15%. Yamada's measurements extent up to $u = 12$. However, the cross-section at the peak appears about ∼40-50% larger than expected base on the general trend of the elements in this sequence. The measurements are probably affected by metastable ions in the beam. For this reason, we decided to use interpolation for this element. The measurements of Hahn et al. (2011a) are used for Fe XII instead of Gregory et al. (1983) because the latter data are compromised owing to metastable ions in the beam. Hahn's data are about ∼30% lower than the data of Gregory et al. (1983) and the calculations of Arnaud & Raymond (1992), and are in agreement with

Table 5.1: EA scaling factors for the Al–Ar isoelectronic sequences needed to bring the Sampson data in accordance with the Pindzola data.

Isoelectronic sequence	Scaling factor
Al	0.79
Si	0.81
P	0.75
S	0.62
Cl	0.64
Ar	0.52

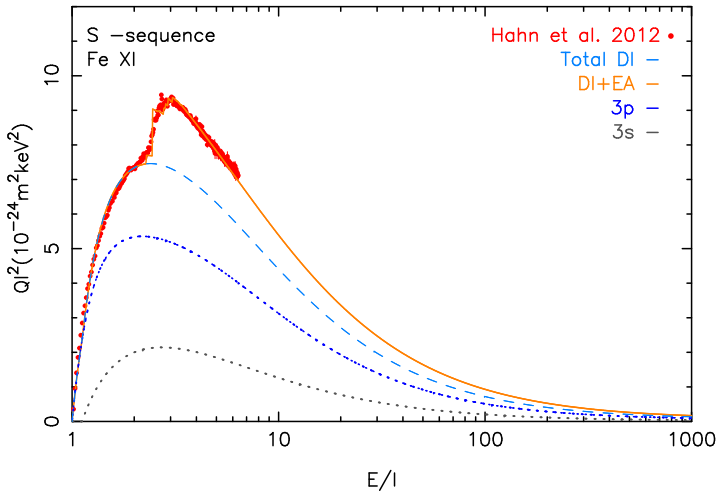

Figure 5.11: Total normalized cross-section for Fe XI (orange line), DI cross-section (dashed blue line), 3p (dotted blue line), 3s (dotted grey line) and the measurements of Hahn et al. (2012c) (red dots).

the theoretical cross-section of D07 within $\pm 20\%$.

5.3.16 S isoelectronic sequence

DI: 3p cross-sections

For Ar III, we followed the discussion in Diserens et al. (1988) and did not include the data of Müller et al. (1980), Mueller et al. (1985), and Danjo et al. (1984),whose data are larger at high energies than the presently adopted data of Diserens et al. (1988) and Man et al. (1993). As explained by Diserens, the increased cross-sections may indicate the presence of metastable ions in the beam.

The measurements of Hahn et al. (2012c) for Fe XI are about 35% lower than the Arnaud & Raymond (1992) theoretical calculations and are in reasonable good agreement with D07. The main differences are twofold. First, at 650 eV, a step appears in the cross-section owing to $n = 2 \rightarrow 3$ excitations not included in D07; and secondly, for higher energies D07 considers the $n = 2 \rightarrow 4$ and $n = 2 \rightarrow 5$ EA transitions, resulting in a higher cross-section. However, the experiments do not show evidence for these last processes.

5.3.17 Cl isoelectronic sequence

DI: 3p cross-sections

For K III and Sc V, the theoretical calculations of Younger (1982c) for the 3p shell were used. For Ni XII, the measurements of Cherkani-Hassani et al. (2001) and the calculations of Pindzola et al. (1991) seem to be in good agreement, see Fig. 5.13.

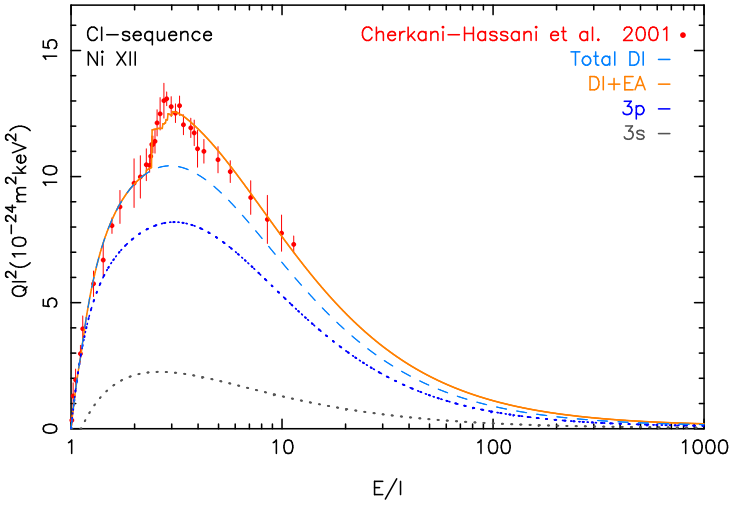

Figure 5.12: Total normalized cross-section for Ni XII (orange line), DI cross-section (dashed blue line), 3p (dotted blue line), 3s (dotted grey line) and the measurements of Cherkani-Hassani et al. (2001) (red dots).

The measurements of Hahn et al. (2012c) are used for Fe X. These are 35% lower than the Gregory et al. (1987) measurements. The theoretical calculations of Arnaud & Raymond (1992) and D07 lie within the experimental uncertainties, although some discrepancies can be found owing to the non-identical EA processes modeling. The reason for these differences are the same as for Fe XI, explained in Section 5.3.16.

5.3.18 Ar isoelectronic sequence

DI: 3p cross-sections

The theoretical data of Younger (1982d) for the 3p shell of Sc IV were taken into account, which are in good agreement with the D07 FAC calculations. Otherwise, for Fe IX recent measurements of Hahn et al. (2016) are available. In this case, the storage ring could not eliminate all the metastable ions from the beam. However, Hahn et al. are able to estimate a metastable fraction of 30% in the $3p^5 3d$ level and they obtain a new estimated ground state cross-section (subtracting the metastable states from the experimental data), which is 15-40% lower than the AR and D07 calculations, and 20% lower than the total cross-section derived from the Younger (1982d) data for the 3p shell. Owing to those lower values of the total cross-section, the rest of the elements interpolated or extrapolated based on Fe IX will be affected as well by a systematic decrease of their total cross-section.

5.3.19 K isoelectronic sequence

The K-like ($3s^2 3p^6 4s$) ions have the 3p and 3d shells as the main contributors to the DI and the EA process is dominated by excitation from $3p^6 3d$ to the $3p^5 3d nl$ levels with $n = 4, 5$. The DI contribution of 4s is taken into account for the elements that have some electrons in the 4s shell, such as K I and Ca II with a structure of $3s^2 3p^6 4s$. The same process has been followed for the ions up to the Zn-like sequence that have the 4s shell contribution.

DI: 3s & 3p cross-sections

For the calculation of the 3s and 3p shells DI cross-section contribution, we have followed the same procedure as for the 2s and 2p shells, explained in Section 5.3.12. We calculated the A, B, D, and E parameters with Eq. (5.9) using, as reference, the parameters of the previous isoelectronic sequence. The same process was applied for all elements from the K-sequence up to the Zn-sequence.

DI: 3d & 4s cross-sections

For K I and Ni X we used the theoretical data of McCarthy & Stelbovics (1983) and Pindzola et al. (1991), respectively, which are well fitted. For Fe VIII, the recent measurements of Hahn et al. (2015) were used, from the ionization threshold up to 1200 eV. They remain 30-40% lower than theoretical calculations of Arnaud & Raymond (1992), based on Pindzola et al. (1987), and are in good agreement (10%) with D07. The reason for these discrepancies are similar to the case of Fe XI, as explained in Section 5.3.16.

EA contribution

We adopted the EA parameters calculated by D07 from his FAC EA calculations, which are the same as used by CHIANTI for all the sequences from the K-like up to the Cr-like sequences.

5.3.20 Ca isoelectronic sequence

DI: 3d & 4s cross-sections

For Ca I we selected three data sets (McGuire 1977, 1997; Roy & Kai 1983) of theoretical calculations. The first two sets of McGuire are in reasonably good agreement, although they are ∼30% higher than Roy's. There are no apparent reasons for discarding any of the three sets and therefore we decided to include all of them. For Fe VII we use the sets of Gregory et al. (1986) and Stenke et al. (1999) and forNi IX the calculations of Pindzola et al. (1991) and Wang et al. (1988).

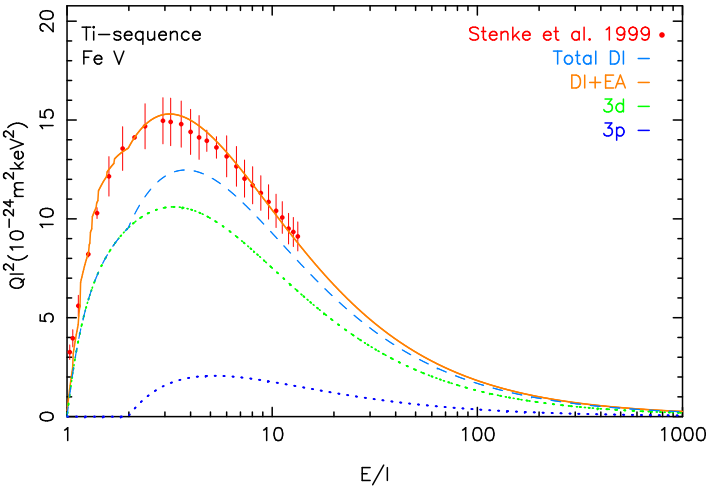

Figure 5.13: Total normalized cross-section for Fe V (orange line), DI cross-section (dashed blue line), 3d (dotted blue line), 3p (dotted blue line) and the measurements of Stenke et al. (1999) (red dots).

5.3.21 Sc isoelectronic sequence

DI: 3d & 4s cross-sections

We include measurements of Ti II, Fe VI, and Ni VIII to obtain the DI and EA cross-sections of the scandium ($3p^6 3d^3$) sequence. The rest of the elements are interpolated or extrapolated. For Fe VI, the measurements of Gregory et al. (1987) and Stenke et al. (1999) are in good agreement with our fit. The data sets of Wang et al. (1988) and Pindzola et al. (1991) were used for Ni VIII.

5.3.22 Ti isoelectronic sequence

DI: 3d & 4s cross-sections

For the titanium sequence ($3p^6 3d^4$) the measurements of Stenke et al. (1999) for the Fe V, as can be seen in Fig. 5.13, and Ni VII 3d shell, respectively, were selected. In the case of Ti I, with an irregular structure of $3d^2 4s^2$, the McGuire (1977) theoretical calculations are used to obtain the 4s shell contribution.

5.3.23 V isoelectronic sequence

DI: 3d & 4s cross-sections

The measurements used for the V-like sequence are Tawara (2002) for V I (obtained directly from CHIANTI), Man et al. (1987b) for Cr II, Stenke et al. (1999) for Fe IV and Wang et al.

(1988) for Ni VI, which are well fitted. The remaining elements are interpolated or extrapolated.

5.3.24 Cr isoelectronic sequence

DI: 3d & 4s cross-sections

For Cr I there are no measurements available and we use the calculations of Reid et al. (1992) and McGuire (1977) for high energies. The measurements of Bannister & Guo (1993) and calculations of Pindzola et al. (1991) are in good agreement for Ni V.

5.3.25 Mn isoelectronic sequence

DI: 3d & 4s cross-sections

For the manganese sequence ($3p^6 3d^7$) elements 3d shell DI cross-section, we use the theoretical calculation of Younger (1983) for Fe II and the measurements of Gregory et al. (1986) for Ni IV. Since the Fe II element has a ground state configuration of $3d^6 4s$, we considered the measurements of the total DI cross-section of Montague et al. (1984a) for subtracting the contribution of the rest of the inner-shells and for obtaining the 4s shell DI cross-sections. Mn I was fitted with data of Tawara (2002) taken from CHIANTI (D07). The remaining elements of the sequence are interpolated.

5.3.26 Fe isoelectronic sequence

DI: 3d & 4s cross-sections

For Fe I, we included the measurements of Freund et al. (1990) and the FAC DI calculations of D07 for Co II. We use the Pindzola et al. (1991) theoretical calculations for Ni III, which are in good agreement with Stenke et al. (1999) at high energies; and Gregory et al. (1986) for Cu IV. The rest of the elements of the sequence are interpolated.

5.3.27 Co isoelectronic sequence

DI: 3d & 4s cross-sections

The measurements found for the cobalt sequence are Montague et al. (1984a) for Ni II and Gregory et al. (1986) for Cu III, which are well fitted. Co I was fitted with data of Tawara (2002) taken from CHIANTI (D07) and Zn IV with the extrapolation of Ni II and Cu III.

5.3.28 Ni isoelectronic sequence

DI: 3d & 4s cross-sections

For Ni I (with ground configuration $3d^8 4s^2$) the Pindzola et al. (1991) and McGuire (1977) data were selected for the 3d and 4s DI contribution, respectively. For Cu II and Zn III, there

are no known measurements, therefore, the 3d DI cross-sections were calculated as the extrapolation of Pindzola's data for Ni I.

5.3.29 Cu isoelectronic sequence

DI: 3d & 4s cross-sections

The measurements considered for the 4s shell DI fit of the copper sequence ($3d^{10}4s$) are for Cu I, Bolorizadeh et al. (1994) and Bartlett & Stelbovics (2002); and for Zn II, Peart et al. (1991a) and Rogers et al. (1982). The fit is in a reasonably good agreement with the measurements. The 3d shell DI contribution of both elements were calculated with FAC.

5.3.30 Zn isoelectronic sequence

DI: 3d & 4s cross-sections

For the Zn I ion, which has a $3d^{10}4s^2$ ground configuration, the calculations of Omidvar & Rule (1977) were used for the fit of the 4s DI cross-section contribution instead of McGuire (1977), because they are around 5-10% higher than Omidvar's values before the cross-section peak and more than 20% lower after, which disagrees with the contribution of the inner-shells. Otherwise, FAC was used forthe 3d DI cross-section calculation.

5.4 Ionization rate coefficients

In the previous section, we obtained the ionization cross-sections for all subshells of all elements from H to Zn isoelectronic sequence by applying Eq. (5.2) for DI and Eq. (5.12) for EA. The total cross-section for DI can be written as the sum of j inner-shells, where $u_j = E_\mathrm{e}/I_j$ with E_e the incoming electron energy (in keV) and I_j the ionization potential of the atomic subshell (in keV):

$$Q_{DI} = \sum_j \frac{1}{u_j I_j^2}\left[A_j\left(1-\frac{1}{u_j}\right) + B_j\left(1-\frac{1}{u_j}\right)^2 + C_j R_j \ln u_j + D_j \frac{\ln u_j}{\sqrt{u_j}} + E_j \frac{\ln u_j}{u_j}\right]. \quad (5.18)$$

The parameters A_j, B_j, C_j, D_j, and E_j (in units of 10^{-24}m^{2}keV^2) for Si-like Fe XI are given in Table 5.3.

The direct ionization rate is written as a function of the temperature kT as

$$C_{DI} = \frac{2\sqrt{2}n_e n_i}{[\pi(kT)^3 m_e]^{\frac{1}{2}}} \sum_i C_i \cdot g_i(u_j), \quad (5.19)$$

where n_e and n_i are the electron and ion density, respectively, m_e the electron mass, and C_i and $g_i(u_j)$ are given in Appendix 5.B. The same approach can be taken with the EA

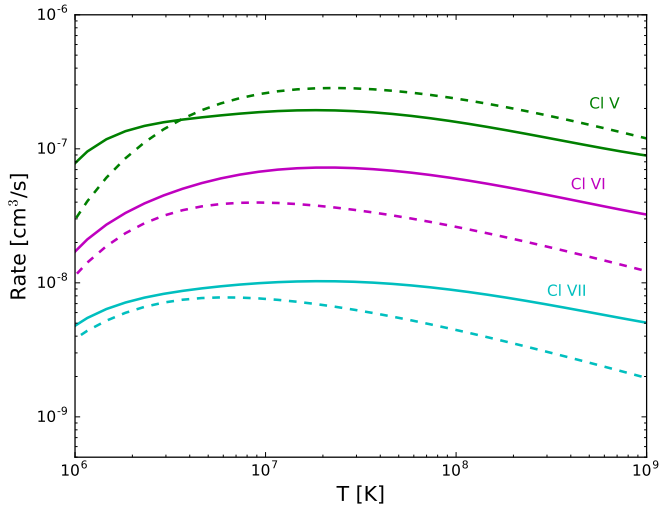

Figure 5.14: Left axis: Ionization rates comparison between Bryans et al. (2009) (dashed lines) and the present work (solid lines) for Cl VII (Na-like), Cl VI (Mg-like, rate multiplied by factor 10) and Cl V (Al-like, rate multiplied by factor 50).

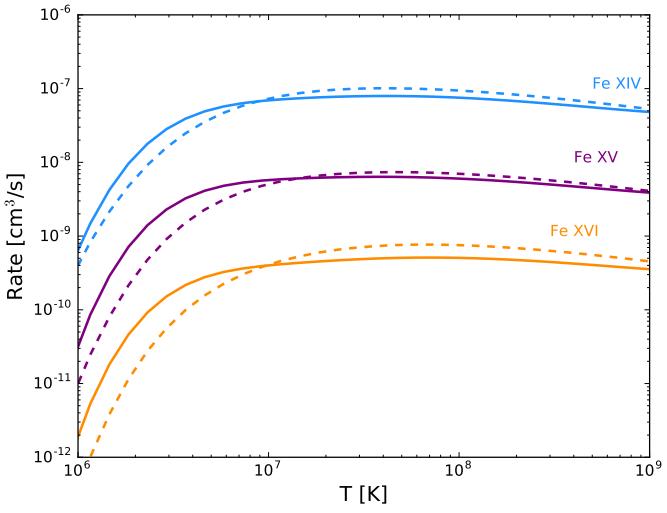

Figure 5.15: Ionization rates comparison between Bryans et al. (2009) (dashed lines) and the present work (solid lines) for Fe XVI (Na-like), Fe XV (Mg-like, rate multiplied by factor 10), and Fe XIV (Al-like, rate multiplied by factor 100).

process. The EA cross-section contribution to the outer shell of each ion, is the sum of k energy level transitions with I_{EAk} the excitation-autoionization threshold (in keV):

$$Q_{EA} = \sum_k \frac{1}{u_k I_{EAk}^2}\left[A_{EAk} + \frac{B_{EAk}}{u_k} + \frac{C_{EAk}}{u_k^2} + \frac{2D_{EAk}}{u_k^3} + E_{EAk}\ln u_k\right], \tag{5.20}$$

where A_{EAk}, B_{EAk}, C_{EAk}, D_{EAk}, and E_{EAk} (in units of 10^{-24}m^{2}keV^2) are the parameters obtained for each ion in presence of the EA process.

Moreover, the total excitation-autoionization rate coefficient is expressed as

$$C_{EA} = \frac{2\sqrt{2}n_e n_i}{[\pi(kT)^3 m_e]^{\frac{1}{2}}} \sum_i D_i \cdot m_i(u_k). \tag{5.21}$$

A detailed description of the D_i and $m_i(u_k)$ terms of this parametric formula is shown in Appendix 5.C.

The total ionization rate coefficient is given by the sum of Eq. (5.19) and (5.21) and includes the contributions from all inner-shells.

5.5 Discussion

A systematic comparison was made with the Bryans et al. (2009) atomic data, which adopt the D07 electron-impact ionization rates. This shows that the present work and Bryans et al. (2009) rates are in good agreement (differences less than 10-20%) for more than 85% of the elements. The highest differences appear for the isoelectronic sequences of Na, Mg (Si III, P IV, S V and Cl VI), and Al (P III, S IV, Cl V and Ar VI), where some of the ions show a difference of 30-40% in the cross-sections compared with D07. As a consequence, the ionization rates for these ions are up to 2-3 times higher than D07 for high temperatures. An example for Cl is shown in Fig. 5.14. This difference decreases for high Z elements as can be seen in Fig. 5.15 where the ionization rates for Fe are represented.

A possible explanation could be that the D07 cross-sections are mainly calculated with FAC, instead of fitted to experimental data, as performed in the present work (see Appendix A). The measurements represent a more realistic scenario and include more transitions, since REDA or multiple ionization are not usually incorporated in the theoretical calculations.

As explained in the previous sections, the most recent experimental measurements included in this work are Fe XVIII, Fe XVII, and Fe XIV (Hahn et al. 2013), Fe XIII (Hahn et al. 2012b), Fe XII (Hahn et al. 2011a), Fe XI and Fe X (Hahn et al. 2012c), Fe IX (Hahn et al. 2016) and Fe VIII (Hahn et al. 2015), and Bernhardt et al. (2014) for Fe XV. They used the new TSR technique to reduce the metastable ion levels to obtain lower cross-sections than AR for all the ions. D07's cross-sections are about 20% higher than Hahn's for Fe XIV, Fe XIII, Fe XII, Fe XI, Fe X, Fe IX, and Fe VIII. For the other ions, the cross-sections are comparable, with the difference that the D07 EA threshold is located at higher energy, probably because D07 does not include the $n = 2 \rightarrow 3$ excitations, see Fig. 5.16.

Figure 5.17 contains the ionization comparison rates for some ions: Fe XVIII, Fe XVII, Fe XIV, Fe XII, and Fe IX. The plot shows that the ionization rates are similar or lower than D07, as

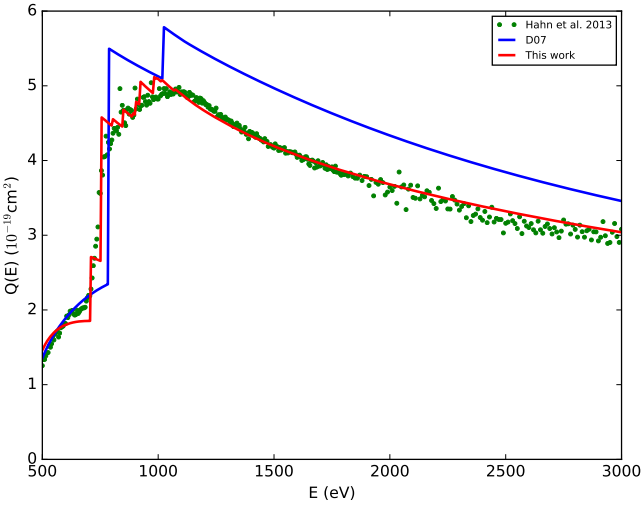

Figure 5.16: Fe XIV total cross-section. The experimental results of Hahn et al. are shown by the green dots. The theoretical calculations of D07 are given by the blue line and the results of this work derived from the fitting process described in section 5.3.13 by the red line.

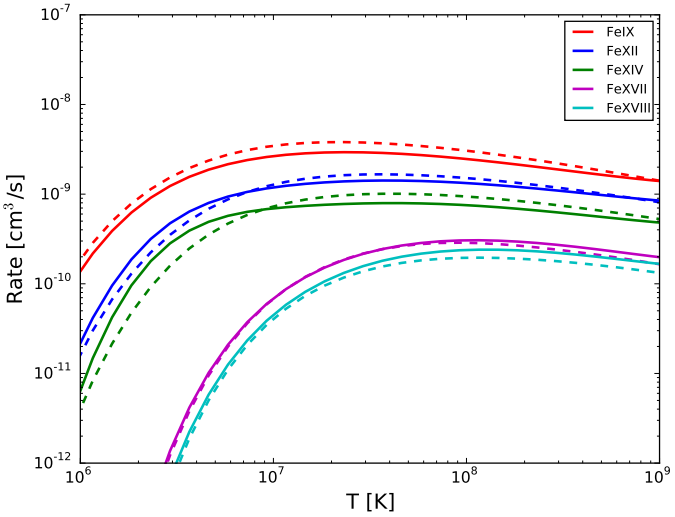

Figure 5.17: Ionization rates comparison between Bryans et al. (2009) (dashed lines) and the present work (solid lines).

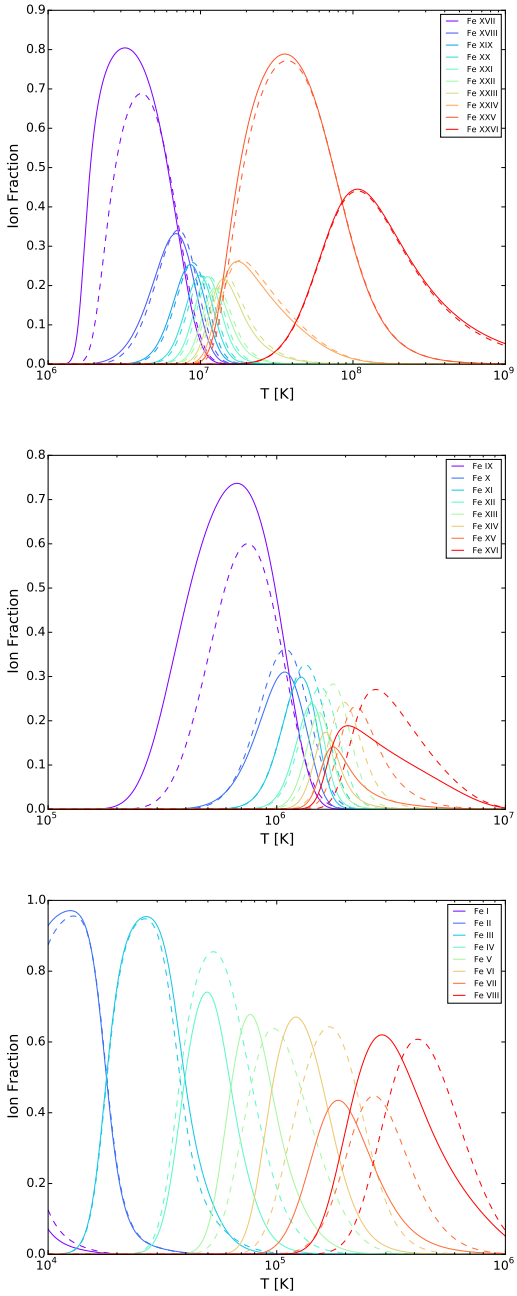

Figure 5.18: Top: Ion fraction for H-like to Ne-like Fe including the ionization rates of Bryans et al. (2009) (dashed lines) and present work (solid lines). Middle: Ion fraction for Na-like to Ar-like. Bottom: Ion fraction for K-like to Fe-like.

expected from the experimental measurements. For Fe XI to Fe XV we obtain a higher value than D07 for low temperature. The reason for this is probably that, at low temperature, the rates are very sensitive to the weighting of the cross-section with the Maxwellians velocity and a small variance in the cross-section fit at low energies could have a major impact in this region.

The major impact of the new cross-sections used in this work is on the ion fractions obtained by the ionization balance. As an example, we compared the ion fractions from Bryans et al. (2009) with the present work for all ions of Fe. In this comparison, we used the same recombination rates as Bryans et al. (2009), so the only differences are the ionization rates.

Figure 5.18 (top) shows the first ten ions from Fe XXVI to Fe XVII. The ion fraction is relatively similar for all ions, except for Ne-like Fe XVII. The lower temperature ionic fraction in this work is clearly higher than using Bryans et al. (2009). This is mainly influenced by ions of adjacent isoelectronic sequences such as Na-like or Mg-like, which have higher ionization rates, as explained above.

Figure 5.18 (middle) presents the ion fraction for Fe IX up to Fe XVI. In this case, there is a more appreciable difference. The peak ion concentration in the present work is lower than in Bryans et al. and it seems to be slightly displaced to lower temperatures. However, for Fe XVI the ion concentration behaviour is similar to Fe XVII. The least ionized Fe (Fe VIII up to Fe I) ion fractions are plotted in Fig. 5.18 (bottom). From Fe VIII to Fe VI, the values at the peak of the ion fractions are similar but they are displaced at lower temperatures around $\sim 10^4$-10^5 K. For Fe III, the value at the peak is $\sim$20% lower. The Fe I and Fe II ions are in good agreement.

5.6 Summary and conclusions

We produced a complete set of electron direct collisional ionization cross-sections together with excitation-autoionization cross-sections. We were able to obtain not only the total cross-sections, such as D07, but all the individual inner shells cross-section of all elements from the H to Zn isoelectronic sequences. They were obtained from experimental measurements, theoretical calculations, and interpolation/extrapolation among the data sets. We incorporated the most recent experimental measurements available at the moment, taken by Fogle et al. (2008), Hahn et al. (2011a,b, 2012a,b,c, 2013, 2015, 2016), and Bernhardt et al. (2014).

This method enables a much more efficient analytical calculation of ionization rate coefficients than other plasma codes with a comparable accuracy. The corresponding rates are in good agreement with Bryans et al. (2009) in at least 85% of the cases. This capability is essential to resolve emission lines and line fluxes in a high-resolution X-ray spectra.

The results of the present work are included in the SPEX[2] (Kaastra et al. 1996) software, utilized for X-ray spectra modeling, fitting, and analysis.

[2] https://www.sron.nl/spex

ACKNOWLEDGEMENTS

SRON is supported financially by NWO, the Netherlands Organization for Scientific Research. We thank J. Mao, L. Gu, T. Raassen and J. de Plaa for their support in the different stages of this project.

5.A References for used cross-section data

Table 5.2: List of references for used cross-section data

Ion	Type [1]	Reference	Uncertainty
		H-sequence	
H I	e	Shah et al. (1987)	7%
He II	e	Peart et al. (1969)	12%
Li III	e	Tinschert et al. (1989)	10%
B V	e	Aichele et al. (1998)	10%
C VI	e	Aichele et al. (1998)	10%
N VII	e	Aichele et al. (1998)	10%
O VIII	e	Aichele et al. (1998)	10%
Ne X	t	Fontes et al. (1999)	–
	t	Kao et al. (1992)	–
Fe XXVI	t	Kao et al. (1992)	–
	t	Moores & Pindzola (1990)	–
Cu XXIX	t	Moores & Pindzola (1990)	–
		He-sequence	
He I	e	Montague et al. (1984b)	4%
	e	Rejoub et al. (2002)	5%
	e	Shah et al. (1988)	6%
Li II	e	Peart & Dolder (1968)	6%
	e	Peart et al. (1969)	11%
B IV	e	Crandall et al. (1979)	4%
C V	e	Crandall et al. (1979)	7%
	e	Donets & Ovsyannikov (1981)	6%
O VII	t	Zhang & Sampson (1990)	–
Ne IX	e	Duponchelle et al. (1997)	11%
	t	Zhang & Sampson (1990)	–
Fe XXV	t	Zhang & Sampson (1990)	–
Zn XXIX	t	Zhang & Sampson (1990)	–
		Li-sequence (1s)	
Li I	t	Younger (1981a)	–
Be II	t	Younger (1981a)	–
O VI	t	Zhang & Sampson (1990)	–
Fe XXIV	t	Zhang & Sampson (1990)	–
Zn XXVIII	t	Zhang & Sampson (1990)	–

[1] e: experimental data, t: theoretical calculations

Ion	Type[1]	Reference	Uncertainty
		Li-sequence (2s)	
Li I	t	Bray (1995)	–
	e	Jalin et al. (1973)	18%
Be II	e	Falk & Dunn (1983b)	8%
B III	e	Crandall et al. (1986)	7%
C IV	e	Crandall et al. (1979)	7%
	e	Teng et al. (2000)	14%
N V	e	Crandall et al. (1979)	7%
	e	Donets & Ovsyannikov (1981)	–
O VI	e	Crandall et al. (1986)	16%
	e	Defrance et al. (1990)	7%
	e	Donets & Ovsyannikov (1981)	7%
Ne VIII	e	Riahi et al. (2001)	–
Fe XXIV	t	Zhang & Sampson (1990)	–
Zn XXVIII	t	Zhang & Sampson (1990)	–
		Be-sequence (2s)	
C III	e	Fogle et al. (2008)	8%
N IV	e	Fogle et al. (2008)	8%
O V	e	Fogle et al. (2008)	8%
F VI	t	Younger (1981d)	–
Ne VII	t	Duponchelle et al. (1997)	6%
S XIII	e	Hahn et al. (2012a)	15%
Ar XV	t	Younger (1981d)	–
Fe XXIII	t	Younger (1982a)	–
		B-sequence (2p)	
B I	e	Tawara (2002) (CHIANTI)	–
C II	e	Aitken et al. (1971)	7%
	e	Yamada et al. (1989a)	10%
N III	e	Aitken et al. (1971)	7%
	e	Bannister & Haverner (1996b)	8%
O IV	e	Crandall et al. (1979)	8%
Ne VI	e	Bannister (1996a)	11%
	e	Duponchelle et al. (1997)	6%
Mg VIII	e	Hahn et al. (2010)	15%
Fe XXII	t	Zhang & Sampson (1990)	–
Zn XXVI	t	Zhang & Sampson (1990)	–

Ion	Type[1]	Reference	Uncertainty
		C-sequence (2p)	
C I	e	Brook et al. (1978)	5%
N II	e	Yamada et al. (1989a)	10%
O III	e	Aitken et al. (1971)	7%
	e	Donets & Ovsyannikov (1981)	–
	e	Falk (1980)	10%
Ne V	e	Bannister (1996a)	9%
	e	Duponchelle et al. (1997)	5%
Fe XXI	t	Zhang & Sampson (1990)	–
Zn XXV	t	Zhang & Sampson (1990)	–
		N-sequence (2p)	
N I	e	Brook et al. (1978)	4%
O II	e	Aitken et al. (1971)	–
	e	Yamada et al. (1989a)	7%
F III	e	Mueller et al. (1985)	9%
Ne IV	e	Gregory et al. (1983)	8%
Si VIII	e	Zeijlmans van Emmichoven et al. (1993)	7%
Fe XX	t	Zhang & Sampson (1990)	–
Zn XXIV	t	Zhang & Sampson (1990)	–
		O-sequence (2p)	
O I	e	Brook et al. (1978)	5%
	e	Thompson et al. (1995)	5%
F II	e	Yamada et al. (1989b)	10%
Ne III	e	Bannister (1996a)	9%
Ar XI	e	Zhang et al. (2002)	9%
Fe XIX	t	Zhang & Sampson (1990)	–
Zn XXIII	t	Zhang & Sampson (1990)	–
		F-sequence (2p)	
F I	e	Hayes et al. (1987)	20%
Ne II	e	Achenbach et al. (1984)	10%
	e	Diserens et al. (1984)	3%
	e	Donets & Ovsyannikov (1981)	–
	e	Man et al. (1987a)	3%
Al V	e	Aichele et al. (2001)	8%
	t	McGuire (1982)	–
Si VI	e	Thompson & Gregory (1994)	4%
Fe XVIII	e	Hahn et al. (2013)	17%
	t	Zhang & Sampson (1990)	–
Zn XXII	t	Zhang & Sampson (1990)	–

Ion	Type[1]	Reference	Uncertainty
		Ne-sequence (2s)	
Na II	e	Younger (1981c)	–
Mg III	e	Younger (1981c)	–
Al IV	e	Younger (1981c)	–
P VI	e	Younger (1981c)	–
Ar IX	e	Younger (1981c)	–
Fe XVII	e	Zhang & Sampson (1990)	–
Zn XXI	e	Zhang & Sampson (1990)	–
		Ne-sequence (2p)	
Ne I	e	Almeida et al. (1995)	8%
	e	Nagy et al. (1980)	7%
	e	Stephan et al. (1980)	8%
	e	Wetzel et al. (1987)	15%
Na II	e	Hirayama et al. (1986)	13%
	e	Hooper et al. (1966)	10%
	e	Peart & Dolder (1968)	6%
Mg III	e	Peart et al. (1969)	8%
Al IV	t	Younger (1981b)	–
Ar IX	e	Defrance et al. (1987)	10%
	e	Zhang et al. (2002)	5%
Fe XVII	e	Hahn et al. (2013)	16%
	t	Zhang & Sampson (1990)	–
Zn XXI	t	Zhang & Sampson (1990)	–
		Na-sequence (2s & 2p)	
Mg II	t	Younger (1981c)	–
Al III	t	Younger (1981c)	–
P V	t	Younger (1981c)	–
Ar VIII	t	Younger (1981c)	–
Ni XVIII	t	Pindzola et al. (1991)	–
		Na-sequence (3s)	
Na I	e	McFarland & Kinney (1965)	8%
	e	Zapesochnyi & Aleksakhin (1969)	15%
Mg II	e	Becker et al. (2004)	10%
	e	Martin et al. (1968)	11%
	e	Peart et al. (1991b)	9%
Al III	e	Thomason & Peart (1998)	8%
Si IV	e	Crandall et al. (1982)	12%
Ti XII	e	Gregory et al. (1990)	7%
	t	Griffin et al. (1987)	–
Fe XVI	e	Gregory et al. (1987)	14%
	e	Linkemann et al. (1995)	20%
Ni XVIII	t	Pindzola et al. (1991)	–

Ion	Type[1]	Reference	Uncertainty
		Mg-sequence (3s)	
Mg I	e	Boivin & Srivastava (1998)	11%
	e	Freund et al. (1990)	10%
	e	McCallion et al. (1992a)	12%
Al II	e	Belic et al. (1987)	9%
Cl VI	e	Howald et al. (1986)	10%
Ar VII	e	Chung (1996)	6%
	e	Zhang et al. (2002)	7%
Sc X	t	Younger (1983)	–
Fe XV	t	Bernhardt et al. (2014)	26%
		Al-sequence (3p)	
Al I	e	Freund et al. (1990)	10%
Si II	e	Djuric et al. (1993b)	9%
Cl V	e	Bannister & Guo (1993)	9%
Ar VI	e	Gregory & Crandall (1982)	11%
Sc IX	t	Younger (1983)	–
Fe XIV	e	Hahn et al. (2013)	16%
		Si-sequence (3p)	
Si I	e	Freund et al. (1990)	10%
P II	e	Yamada et al. (1989a)	10%
S III	e	Yamada et al. (1988)	10%
Ar V	t	Arnaud & Rothenflug (1985)	–
Sc VIII	t	Younger (1983)	–
Fe XIII	e	Hahn et al. (2012b)	12%
		P-sequence (3p)	
P I	e	Freund et al. (1990)	10%
Cl III	e	Mueller et al. (1985)	10%
Sc VII	t	Younger (1983)	–
Fe XII	e	Hahn et al. (2011a)	16%
Ni XIV	e	Cherkani-Hassani et al. (2001)	14%
		S-sequence (3p)	
S I	e	Freund et al. (1990)	10%
Cl II	e	Djuric et al. (1993b)	7%
Ar III	e	Diserens et al. (1988)	3%
	e	Man et al. (1993)	3%
Sc VI	t	Younger (1983)	–
Fe XI	e	Hahn et al. (2012c)	9%

Ion	Type[1]	Reference	Uncertainty
		Cl-sequence (3p)	
Cl I	e	Hayes et al. (1987)	14%
Ar II	e	Gao et al. (1997)	10%
	e	Man et al. (1987a)	3%
	e	Mueller et al. (1985)	10%
	e	Yamada et al. (1989b)	10%
K III	t	Younger (1982c)	–
Sc V	t	Younger (1982c)	–
Fe X	e	Hahn et al. (2012c)	9%
Ni XII	e	Cherkani-Hassani et al. (2001)	14%
		Ar-sequence (3p)	
Ar I	e	Ma et al. (1991)	15%
	e	McCallion et al. (1992b)	6%
	e	Nagy et al. (1980)	6%
	e	Straub et al. (1995)	8%
	e	Wetzel et al. (1987)	3%
K II	e	Hirayama et al. (1986)	15%
	t	Kumar & Roy (1979)	–
	e	Peart & Dolder (1968)	15%
Sc IV	t	Younger (1982d)	–
Fe IX	e	Hahn et al. (2016)	16%
		K-sequence (3d & 4s)	
K I	t	McCarthy & Stelbovics (1983)	–
Ca II	e	Peart & Dolder (1975)	10%
	e	Peart et al. (1989)	8%
Sc III	e	Pindzola et al. (1994)	8%
Ti IV	e	Falk et al. (1983c)	7%
Fe VIII	e	Hahn et al. (2015)	12%
Ni X	t	Pindzola et al. (1991)	–
		Ca-sequence (3d & 4s)	
Ca I	t	Roy & Kai (1983)	–
	t	McGuire (1977)	–
	t	McGuire (1997)	–
Sc II	e	Jacobi et al. (2004)	15%
Ti III	e	Diserens et al. (1988)	3%
	e	Mueller et al. (1985)	9%
Fe VII	e	Gregory et al. (1986)	5%
	e	Stenke et al. (1999)	8%
Ni IX	t	Pindzola et al. (1991)	–
	e	Wang et al. (1988)	6%

Ion	Type[1]	Reference	Uncertainty
		Sc-sequence (3d & 4s)	
Sc I	e	Tawara (2002) (CHIANTI)	–
Ti II	e	Diserens et al. (1988)	3%
Fe VI	e	Gregory et al. (1986)	5%
	e	Stenke et al. (1999)	8%
Ni VIII	t	Pindzola et al. (1991)	–
	e	Wang et al. (1988)	6%
		Ti-sequence (3d & 4s)	
Ti I	t	McGuire (1977)	–
Fe V	e	Stenke et al. (1999)	8%
Ni VII	e	Wang et al. (1988)	6%
		V-sequence (3d & 4s)	
V I	e	Tawara (2002) (CHIANTI)	–
Cr II	e	Man et al. (1987b)	2.5%
Fe IV	e	Stenke et al. (1999)	–
Ni VI	e	Wang et al. (1988)	6%
		Cr-sequence (3d & 4s)	
Cr I	t	Reid et al. (1992)	–
	t	McGuire (1977)	–
Fe III	t	FAC (CHIANTI)	–
Ni V	e	Bannister & Guo (1993)	7%
	t	Pindzola et al. (1991)	–
		Mn-sequence (3d & 4s)	
Mn I	e	Tawara (2002) (CHIANTI)	–
Fe II	t	Younger (1983) (3d)	–
	e	Montague et al. (1984b) (4s)	–
		Fe-sequence (3d & 4s)	
Fe I	e	Freund et al. (1990)	7%
Co II	t	FAC (CHIANTI)	–
Ni III	t	Pindzola et al. (1991)	–
Cu IV	e	Gregory et al. (1986)	4%
		Co-sequence (3d & 4s)	
Co I	e	Tawara (2002) (CHIANTI)	–
Ni II	e	Montague et al. (1984a)	3%
Cu III	e	Gregory et al. (1986)	4%
		Ni-sequence (3d & 4s)	
Ni I	t	Pindzola et al. (1991) (3d)	–
	t	McGuire (1977) (4s)	–

Ion	Type[1]	Reference	Uncertainty
		Cu-sequence (3d & 4s)	
Cu I	t	FAC (3d)	–
	e	Bolorizadeh et al. (1994) (4s)	10%
	t	Bartlett & Stelbovics (2002) (4s)	–
Zn II	t	FAC (3d)	–
	e	Peart et al. (1991a) (4s)	10%
	e	Rogers et al. (1982) (4s)	10%
		Zn-sequence (3d & 4s)	
Zn I	t	FAC (3d)	–
	t	McGuire (1977) (4s)	–
	t	Omidvar & Rule (1977) (4s)	–

5.B Calculation of DI ionization rate coefficients

As explained in Section 5.2, for the direct ionization cross-section calculation, the extended Younger's Eq. (5.2) was used:

$$uI^2Q_{DI} = A\left(1-\frac{1}{u}\right) + B\left(1-\frac{1}{u}\right)^2 + CR\ln u + D\frac{\ln u}{\sqrt{u}} + E\frac{\ln u}{u}, \tag{5.22}$$

where

$$R \simeq 1 + 1.5\epsilon + 0.25\epsilon^2$$
$$\epsilon \equiv E/mc^2 \equiv uI/mc^2$$
$$I/mc^2 \equiv \lambda \ll 1$$
$$u = E/I$$

with E the kinetic energy of the colliding electron and I the ionisation potential of the relevant subshell.

If we generalize the formula for all the inner shells j and the summation over all shells is taken into account for the total direct ionization cross-section, the parametric formula is

$$u_jI_j^2Q_{DI} = \sum_j \left[A_j\left(1-\frac{1}{u_j}\right) + B_j\left(1-\frac{1}{u_j}\right)^2 + C_jR_j\ln u_j + D_j\frac{\ln u_j}{\sqrt{u_j}} + E_j\frac{\ln u_j}{u_j}\right]. \tag{5.23}$$

Eq. (5.22) can be written as follows being $u_j = E/I_j$:

$$u_jI_j^2Q_{DI} = \sum_{i=1}^{8} c_i \cdot f_i(u_j), \tag{5.24}$$

with

$c_1 = (A_j + B_j)$	$f_1(u) = 1$
$c_2 = (-A_j - 2B_j)$	$f_2(u) = \frac{1}{u}$
$c_3 = B_j$	$f_3(u) = \frac{1}{u^2}$
$c_4 = C_j$	$f_4(u) = \ln u$
$c_5 = \frac{3}{2}\lambda C_j$	$f_5(u) = u\ln u$
$c_6 = \frac{1}{4}\lambda^2 C_j$	$f_6(u) = u^2\ln u$
$c_7 = D_j$	$f_7(u) = \frac{\ln u}{\sqrt{u}}$
$c_8 = E_j$	$f_8(u) = \frac{\ln u}{u}$

As a consequence, the direct ionization rate coefficients versus the temperature [T] are:

$$C_{DI} = r_0\int_1^\infty (u_jI_j^2Q_{DI})e^{-u_jy}\mathrm{d}u_j \equiv r_0\sum_{i\approx 1}^{\infty} c_i \cdot g_i(u_j), \tag{5.25}$$

with $y \equiv I/kT$ and $r_0 \equiv \frac{2\sqrt{2}n_e n_i}{[\pi(kT)^3 m_e]^{\frac{1}{2}}}$

$$g_i(y) = \int_1^\infty f_i(u) e^{-uy} \mathrm{d}u \tag{5.26}$$

with

$$g_1(y) = \int_1^\infty e^{-uy} \mathrm{d}u = \frac{1}{y} e^{-y} \tag{5.27}$$

$$g_2(y) = \int_1^\infty \frac{e^{-uy}}{u} \mathrm{d}u = E_1(y) \tag{5.28}$$

$$\tag{5.29}$$

being E_1 the first exponential integral function.

$$g_3(y) = \int_1^\infty \frac{e^{-uy}}{u^2} \mathrm{d}u = e^{-y} - yE_1(y) \tag{5.30}$$

$$g_4(y) = \int_1^\infty \ln u e^{-uy} \mathrm{d}u = \frac{1}{y} E_1(y) \tag{5.31}$$

$$g_5(y) = \int_1^\infty u \ln u e^{-uy} \mathrm{d}u = \frac{1}{y^2}[e^{-y} + E_1(y)] \tag{5.32}$$

$$g_6(y) = \int_1^\infty u^2 \ln u e^{-uy} \mathrm{d}u = \frac{3+y}{y^3} e^{-y} + \frac{2}{y^3} E_1(y) \tag{5.33}$$

$$g_7(y) = \int_1^\infty \frac{\ln u}{\sqrt{u}} e^{-uy} \mathrm{d}u \tag{5.34}$$

For small y (y<0.6):

$$g_7(y) \simeq -\sqrt{\frac{\pi}{y}}(\gamma + \ln 4 + \ln y) + 4 - \frac{4y}{9} + \frac{2y^2}{25} - \frac{2y^3}{147} + \frac{y^4}{486}, \tag{5.35}$$

where γ=0.577216 is the Euler-Mascheroni constant.

For intermediate y $(0.6 \leq y \geq 20)$:

$$g_7(y) \simeq \frac{e^{-y}[p_1 + \frac{p_2}{\sqrt{y}} + \frac{p_3}{y} + \frac{p_4 \ln y}{\sqrt{y}}]}{(y + p_5)(y + p_6)} \tag{5.36}$$

with,

$$p_1 = 1.000224$$
$$p_2 = -0.11301$$
$$p_3 = 1.851039$$
$$p_4 = 0.019731$$
$$p_5 = 0.921832$$
$$p_6 = 2.651957$$

For large y (y>20):

$$g_7(y) \simeq \frac{e^{-y}}{y^2}[1 - \frac{2}{y} + \frac{23}{4y^2} - \frac{22}{y^3} + \frac{1689}{16y^4} - \frac{4881}{8y^5}] \tag{5.37}$$

$$g_8(y) = \int_1^\infty \frac{\ln u}{u} e^{-uy} \mathrm{d}u \tag{5.38}$$

For small y (y<0.5):

$$g_8(y) \simeq \gamma \ln y + \frac{1}{2}(\ln y)^2 - y + \frac{y^2}{8} - \frac{y^3}{54} + \frac{y^4}{384} - \frac{y^5}{3000} + 0.989056 \tag{5.39}$$

For intermediate y ($0.5 \leq y \geq 20$):

$$g_8(y) \simeq \frac{e^{-y}[a_o + \frac{a_1}{y} + \frac{a_2}{y^2} + \frac{a_3}{y^3} + \frac{a_4}{y^4}]}{(y + b_1)(y + b_2)} \tag{5.40}$$

with,

$a_0 = 0.999610841$
$a_1 = 3.50020361$
$a_2 = -0.247885719$
$a_3 = 0.00100539168$
$a_4 = 1.3907539.10^{-3}$
$b_1 = 1.84193516$
$b_2 = 4.64044905$

For large y (y>20):

$$g_8(y) \simeq \frac{e^{-y}}{y} \sum_{n=1}^{7} \frac{a_n}{y^n} \tag{5.41}$$

with,

$a_1 = 1$
$a_2 = -3$
$a_3 = 11$
$a_4 = -50$
$a_5 = 274$
$a_6 = -1764$
$a_7 = 13068$

5.C Calculation of EA ionization rate coefficients

The excitation-autoionization ion rate coefficients were calculated applying the integral to a Maxwellian velocity distribution of Mewe's equation, mentioned in Section 5.2.2:

$$uI_{EA}^2 Q_{EA} = \left[A_{EA} + \frac{B_{EA}}{u} + \frac{C_{EA}}{u^2} + \frac{2D_{EA}}{u^3} + E_{EA} \ln u \right].$$

The EA cross-section contribution that affects the outer shell of each element, is the summation over k energy level transitions with I_{EAk} the excitation-autoionization potential being $u_k = E/I_E Ak$:

$$u_k I_{EAk}^2 Q_{EA} = \sum_{i=1}^{5} d_i \cdot l_i(u_k), \tag{5.42}$$

with,

$$\begin{array}{ll} d_1 = A_{EAk} & l_1(u_k) = 1 \\ d_2 = B_{EAk} & l_2(u_k) = \frac{1}{u_k} \\ d_3 = C_{EAk} & l_3(u_k) = \frac{1}{u_k^2} \\ d_4 = 2D_{EAk} & l_4(u_k) = \frac{1}{u_k^3} \\ d_5 = E_{EAk} & l_5(u_k) = \ln u_k \end{array}$$

Therefore, the EA ionization rate coefficients versus the temperature [T] are

$$C_{EA} = r_0 \int_1^\infty (u_k I_{EAk}^2 Q_{EA}) e^{-u_k y} \mathrm{d}u \equiv r_0 \sum_{i=1}^{5} d_i \cdot m_i(u_k), \tag{5.43}$$

with $y \equiv I_{EA}/kT$ and $r_0 \equiv \frac{2\sqrt{2} n_e n_i}{[\pi (kT)^3 m_]]^{\frac{1}{2}}}$

$$m_i(y) = \int_1^\infty l_i(u_k) e^{-u_k y} \mathrm{d}u, \tag{5.44}$$

with:

$$m_1(y) = \int_1^\infty e^{-uy} \mathrm{d}u = \frac{1}{y} e^{-y} \tag{5.45}$$

$$m_2(y) = \int_1^\infty \frac{e^{-uy}}{u} \mathrm{d}u = E_1(y) \tag{5.46}$$

$$m_3(y) = \int_1^\infty \frac{e^{-uy}}{u^2} \mathrm{d}u = e^{-y} - yE_1(y) \tag{5.47}$$

$$m_4(y) = \int_1^\infty \frac{e^{-uy}}{u^3} \mathrm{d}u = (1-y)\frac{e^{-y}}{2} + \frac{y^2}{2} E_1(y) \tag{5.48}$$

$$m_5(y) = \int_1^\infty \ln u e^{-uy} \mathrm{d}u = \frac{1}{y} E_1(y) \tag{5.49}$$

5.D The DI and EA coefficients

The tables below shows an example of the DI coefficients calculated by Eq. (5.2) for Si-like Fe XI.

Table 5.3: The DI coefficients

ii[a]	ir[b]	iz[c]	I_{DI} (eV)[d]	A	B	C	D	E[e]
16	1	26	7585.000	28.28	-11.62	4.80	0.00	-24.12
16	2	26	1164.000	18.21	-3.73	3.56	-3.85	-9.85
16	3	26	1048.687	59.57	-26.85	13.230	14.61	-51.29
16	4	26	324.400	21.91	-11.03	2.25	4.09	-18.89
16	5	26	290.300	80.28	-72.24	6.22	33.59	-92.87

[a] ii: Isoelectronic sequence
[b] ir: Shell number 1-7 (1s,2s,2p,3s,3p,3d,4s)
[c] iz: Element
[d] I_{DI}: Ionization potential
[e] A,B,C,D and E units: 10^{-24} m^{2}keV^2

The table below shows an example of the EA coefficients calculated by Eq. (5.12) for Si-like Fe XI.

Table 5.4: The EA coefficients

ii[a]	iz[b]	k[c]	I_{EA} (eV)[d]	A	B	C	D	E[e]
16	26	1	757.000	-0.465	0.812	-0.037	-0.062	0.608
16	26	2	802.500	2.809	-4.408	4.904	-1.017	-0.056
16	26	3	902.200	0.260	-0.062	0.006	0.006	0.000
16	26	4	916.900	-0.136	0.223	0.248	-0.087	0.378
16	26	5	936.300	0.372	-0.409	0.434	-0.068	0.000
16	26	6	977.500	0.217	-0.143	0.322	-0.062	0.143
16	26	7	662.900	1.302	-0.484	0.794	-0.174	0.006
16	26	8	709.000	-0.831	7.738	5.871	-2.344	9.653
16	26	9	809.300	0.186	-0.068	0.409	-0.099	0.093
16	26	10	823.800	0.955	-0.384	0.818	-0.149	0.000
16	26	11	843.400	1.048	-0.651	2.883	-0.670	1.445
16	26	12	884.700	0.942	-0.725	1.910	-0.378	0.521

[a] ii: Isoelectronic sequence
[b] iz: Element
[c] k: Number of transitions
[d] I_{EA}: Ionization potential
[e] A,B,C,D and E units: 10^{-24} m^{2}keV^2

Bibliography

Abell, G. O., Corwin, Jr., H. G., & Olowin, R. P. 1989, ApJS, 70, 1

Achenbach, C., Müller, A., Salzborn, E., & Becker, R. 1984, J. Phys. B: At. Mol. Phys., 17, 1405

Aichele, K., Steidl, M., Hartenfeller, U., et al. 2001, J. Phys. B: At. Mol. Opt. Phys., 34, 4113

Aichele, K., Hartenfeller, U., Hathiramani, D., et al. 1998, J. Phys. B: At. Mol. Opt. Phys., 31, 2369

Aitken, K. L., Harrison, M. F. A., & Rundel, R. D. 1971, J. Phys. B: At. Mol. Phys., 4, 1189

Akamatsu, H., Inoue, S., Sato, T., et al. 2013b, PASJ, 65, 89

Akamatsu, H., & Kawahara, H. 2013a, PASJ, 65, 16

Akamatsu, H., Takizawa, M., Nakazawa, K., et al. 2012, PASJ, 64

Akamatsu, H., van Weeren, R. J., Ogrean, G. A., et al. 2015, A&A, 582, A20

Akamatsu, H., Mizuno, M., Ota, N., et al. 2017, A&A, 600, A100

Almeida, D. P., Fontes, A. C., & Godinho, C. F. L. 1995, J. Phys. B: At. Mol. Opt. Phys., 28, 3335

Arnaud, K. A. 1996, in Astronomical Society of the Pacific Conference Series, Vol. 101, Astronomical Data Analysis Software and Systems V, ed. G. H. Jacoby & J. Barnes

Arnaud, M., Pratt, G. W., Piffaretti, R., et al. 2010, A&A, 517, A92

Arnaud, M., & Raymond, J. 1992, ApJ, 398, 394

Arnaud, M., & Rothenflug, R. 1985, A&AS, 60, 425

Badnell, N. R., & Pindzola, M. S. 1993, Phys. Rev. A, 47

Bagchi, J., Durret, F., Lima Neto, G. B., & Paul, S. 2006, Science, 314, 791

Baldi, A., Ettori, S., Mazzotta, P., Tozzi, P., & Borgani, S. 2007, ApJ, 666, 835

Ballarati, B., Feretti, L., Ficarra, A., et al. 1981, A&A, 100, 323

Bannister, M. E. 1996a, Phys. Rev. A, 54, 1435

Bannister, M. E., & Guo, X. Q. 1993, Unpublished, http://www-cfadc.phy.ornl.gov/xbeam/xbmintro.html

Bannister, M. E., & Haverner, C. C. 1996b, Unpublished, http://www-cfadc.phy.ornl.gov/xbeam/xbmintro.html

Barret, D., Lam Trong, T., den Herder, J.-W., et al. 2018, in Space Telescopes and Instru-

mentation 2018: Ultraviolet to Gamma Ray, Society of Photo-Optical Instrumentation Engineers (SPIE) Conference Series
Bartlett, P. L., & Stelbovics, A. T. 2002, Phys. Rev. A, 66, 012707
Baumgartner, V., & Breitschwerdt, D. 2009, Astronomische Nachrichten, 330, 898
Becker, C., Knopp, H., Jacobi, J., et al. 2004, J. Phys. B: At. Mol. Opt. Phys., 37, 1503
Belic, D. S., Falk, R. A., Timmer, C., & Dunn, G. H. 1987, Phys. Rev A, 36, 1073
Bell, A. R. 1987, MNRAS, 225, 615
Bernhardt, D., Becker, A., Grieser, M., et al. 2014, Phys. Rev. A, 90, 012702
Berrington, R. C., Lugger, P. M., & Cohn, H. N. 2002, AJ, 123, 2261
Biffi, V., Mernier, F., & Medvedev, P. 2018b, Space Sci. Rev., 214, 123
Biffi, V., Planelles, S., Borgani, S., et al. 2018a, MNRAS, 476, 2689
Biffi, V., Planelles, S., Borgani, S., et al. 2017, MNRAS, 468, 531
Blandford, R., & Eichler, D. 1987, Phys. Rep., 154, 1
Blanton, E. L., Sarazin, C. L., & McNamara, B. R. 2003, ApJ, 585, 227
Blumenthal, G. R., Faber, S. M., Primack, J. R., & Rees, M. J. 1984, Nature, 311, 517
Böhringer, H., Schuecker, P., Pratt, G. W., et al. 2007, A&A, 469, 363
Böhringer, H., & Werner, N. 2010, A&A Rev., 18, 127
Boivin, R. F., & Srivastava, S. K. 1998, J. Phys. B: At. Mol. Opt. Phys., 31, 2381
Bolorizadeh, M. A., Patton, C. J., Shah, M. B., & Gilbody, H. B. 1994, J. Phys. B: At. Mol. Opt. Phys., 27, 175
Bonafede, A., Intena, H. T., Brüggen, M., et al. 2014, ApJ, 785, 1
Bonafede, A., Feretti, L., Giovannini, G., et al. 2009, A&A, 503, 707
Bonafede, A., Cassano, R., Bruggen, M., et al. 2017, MNRAS, 470, 3465
Botteon, A., Brunetti, G., Ryu, D., & Roh, S. 2019b, arXiv e-prints [arXiv:1907.00966]
Botteon, A., Gastaldello, F., Brunetti, G., & Dallacasa, D. 2016a, MNRAS, 460, 84
Botteon, A., Gastaldello, F., Brunetti, G., & Kale, R. 2016b, MNRAS, 463, 1534
Botteon, A., Shimwell, T. W., Bonafede, A., et al. 2019a, A&A, 622, A19
Bourdin, H., & Mazzotta, P. 2008, A&A, 479, 307
Bourdin, H., Mazzotta, P., Markevitch, M., Giacintucci, S., & Brunetti, G. 2013, ApJ, 764, 82
Bray, I. 1995, J. Phys. B: At. Mol. Opt. Phys., 28, 247
Bridle, A. H., & Fomalont, E. B. 1976, A&A, 52, 107
Briel, U. G., Finoguenov, A., & Henry, J. P. 2004, A&A, 426, 1
Briel, U. G., Herny, J. P., Schwarz, R. A., et al. 1991, A&A, 246, L10
Brook, E., Harrison, M. F. A., & Smith, A. C. H. 1978, J. Phys. B: At. Mol. Phys., 11, 3115
Brüggen, M., Bykov, A., Ryu, D., & Röttgering, H. 2012b, Space Sci. Rev., 166, 187
Brüggen, M., van Weeren, R. J., & Röttgering, H. J. 2012, MNRAS, 425, L76
Brüggen, M., Rafferty, D., Bonafede, A., et al. 2018, MNRAS, 477, 3461
Brunetti, G., & Jones, T. W. 2014, IJMPD, 23, 1430007
Brunetti, G., Setti, G., Feretti, L., & Giovannini, G. 2001, MNRAS, 320, 365
Bryans, P., Landi, E., & Savin, D. W. 2009, ApJ, 691, 1540
Buote, D. A. 2000, MNRAS, 311, 176
Buote, D. A. 2001, ApJ, 553, L15
Burns, J. O., Skillman, S. W., & O'Shea, B. W. 2010, ApJ, 721, 1105
Cappelluti, N., Li, Y., Ricarte, A., et al. 2017, ApJ, 837, 19

Caprioli, D., & Spitkovsky, A. 2014, ApJ, 783, 91
Carretti, E., Brown, S., Staveley-Smith, L., et al. 2013, MNRAS, 430, 1414
Cash, W. 1979, ApJ, 228, 939
Cassano, R., Ettori, S., Giacintucci, S., et al. 2010, ApJ, 721, L82
Chen, M. H., & Reed, K. J. 1992, Phys. Rev. A, 45, 4525
Cherkani-Hassani, S., Khouilid, M., & Defrance, P. 2001, Physica Scripta, 92, 287
Chung, S. 1996, Unpublished ORNL data, http://www-cfadc.phy.ornl.gov/xbeam/xbmintro.html
Clarke, T. E., & Ensslin, T. A. 2006, ApJ, 131, 2900
Crandall, D. H., Phaneuf, A., Falk, A., Belic, D. S., & Dunn, H. 1982, Phys. Rev. A, 25
Crandall, D. H., Phaneuf, R. A., Gregory, D. C., et al. 1986, Phys. Rev. A, 34, 1757
Crandall, D. H., Phaneuf, R. A., Hasselquist, B. E., & Gregory, D. C. 1979, J. Phys. B: At. Mol. Phys., 12, 249
Cuciti, V., Brunetti, G., van Weeren, R., et al. 2018, A&A, 609, A61
Danjo, A., Matsumoto, A., Ohtani, S., et al. 1984, J. Phys. Soc. Jpn, 53, 4091
Dasadia, S., Sun, M., Sarazin, C., et al. 2016a, ApJ, 820, L20
Dasadia, S., Sun, M., Morandi, A., et al. 2016b, MNRAS, 458, 681
Datta, A., Schenck, D. E., Burns, J. O., Skillman, S. W., & Hallman, E. J. 2014, ApJ, 793, 80
Dawson, W. A., Jee, M. J., Stroe, A., et al. 2015, ApJ, 805, 143
De Gasperin, F., Intema, H. T., Shimwell, T. W., et al. 2017, Sci. Adv., 3, e1701634
De Grandi, S., Ettori, S., Longhetti, M., & Molendi, S. 2004, A&A, 419, 7
De Grandi, S., & Molendi, S. 2001, ApJ, 551, 153
De Grandi, S., & Molendi, S. 2002, ApJ, 567, 163
De Luca, A., & Molendi, S. 2004, A&A, 419, 837
de Plaa, J. 2013, Astronomische Nachrichten, 334, 416
de Plaa, J. 2017, CXBTools, Zenodo, doi:10.5281/zenodo.2575495
de Plaa, J., Werner, N., Bykov, A. M., et al. 2006, A&A, 452, 397
Defrance, P., Chantrenne, S., Rachafi, S., et al. 1990, J. Phys. B: At. Mol. Opt. Phys., 23, 2333
Defrance, P., Rachafi, S., Jureta, J., Meyer, F., & Chantrenne, S. 1987, Nuclear Instruments and Methods in Physics Research Section B: Beam Interactions with Materials and Atoms, 23, 265
Del Zanna, G., Dere, K. P., Young, P. R., Landi, E., & Mason, H. E. 2015, A&A, 582, A56
Dere, K. P. 2007, A&A, 466, 771
Di Gennaro, G., van Weeren, R. J., Andrade-Santos, F., et al. 2019, ApJ, 873, 64
Diserens, M. J., Harrison, M. F. A., & Smith, A. C. H. 1984, J. Phys. B: At. Mol. Phys., 17, 621
Diserens, M. J., Smith, A. C. H., & Harrison, M. F. A. 1988, J. Phys. B: At. Mol. Opt. Phys., 21, 2129
Djuric, N., Bell, E. W., & Dunn, G. H. 1993a, Internationa Journal of Mass Spectrometry and Ion Processes, 123, 187
Djuric, N., Bell, W., Guo, Q., et al. 1993b, Phys. Rev. A, 47, 4786
Dolder, K. T., Harrison, M. F. A., & Thonemann, P. C. 1961, Proceedings of the Royal Society of London. Series A, Mathematical and Physical Sciences, 264, 367
Donets, E. D., & Ovsyannikov, V. P. 1981, Sov. Phys. JETP, 53, 466
Drury, L. O. 1983, Reports on Progress in Physics, 46, 973

Duponchelle, M., Khouilid, M., Oualim, E. M., Zhang, H., & Defrance, P. 1997, J. Phys. B: At. Mol. Opt. Phys., 30, 729
Durret, F., Perrot, C., Lima Neto, G. B., et al. 2013, A&A, 560, A78
Eckert, D., Jauzac, M., Vazza, F., et al. 2016b, MNRAS, 461, 1302
Eckert, D., Molendi, S., & Paltani, S. 2011, A&A, 526, A79
Eckert, D., Ettori, S., Coupon, J., et al. 2016a, A&A, 592, A12
Elkholy, T. Y., Bautz, M. W., & Canizares, C. R. 2015, ApJ, 805, 3
Ettori, S., Baldi, A., Balestra, I., et al. 2015, A&A, 578, A46
Ettori, S., Ghirardini, V., Eckert, D., Dubath, F., & Pointecouteau, E. 2017, MNRAS, 470, L29
Ettori, S., Pratt, G. W., de Plaa, J., et al. 2013, arXiv e-prints [arXiv:1306.2322]
Ezer, C., Bulbul, E., Nihal Ercan, E., et al. 2017, ApJ, 836, 110
Fabian, A. C. 1994, ARA&A, 32, 277
Fabricant, D. G., Kent, S. M., & Kurtz, M. J. 1989, ApJ, 336, 77
Falk, R. 1980, Unpublished, http://www-cfadc.phy.ornl.gov/xbeam/xbmintro.html
Falk, R. A., Dunn, G. H., G. D., & Crandall, D. H. 1983c, Phys. Rev. A, 27, 762
Falk, R. A., & Dunn, G. H. 1983b, Phys. Rev. A, 27, 754
Falk, R. A., Stefani, G., Camilloni, R., et al. 1983a, Phys. Rev. A, 28, 91
Feretti, L., Giovannini, G., Govoni, F., & Murgia, M. 2012, A&A Rev., 20, 54
Feretti, L., Orrù, E., Brunetti, G., et al. 2004b, A&A, 423, 111
Ferland, G. J., Chatzikos, M., Guzmán, F., et al. 2017, Rev. Mexicana Astron. Astrofis., 53, 385
Ferrari, C., Govoni, F., Schindler, S., Bykov, A. M., & Rephaeli, Y. 2008, Space Sc. Rev., 134, 93
Finoguenov, A., Sarazin, C. L., Nakazawa, K., Wik, D. R., & Clarke, T. E. 2010, ApJ, 715, 1143
Fogle, M., Bahati, E. M., Bannister, M. E., et al. 2008, ApJS, 58, 543
Fontes, C. J., Sampson, D. H., & Zhang, H. L. 1999, Phys. Rev. A, 59, 1329
Forman, W., & Jones, C. 1982, ARA&A, 20, 547
Freund, R. S., Wetzel, R. C., Shul, R. J., & Hayes, T. R. 1990, Phys. Rev. A, 41, 7
Fujita, Y., Akamatsu, H., & Kimura, S. S. 2016, PASJ, 68, 34
Fujita, Y., Takizawa, M., Yamazaki, R., Akamatsu, H., & Ohno, H. 2015, ApJ, 815, 116
Fujita, Y., Tawa, N., Hayashida, K., et al. 2008, PASJ, 60, 343
Gabici, S., & Blasi, P. 2003, ApJ, 583, 695
Gao, H., Fang, D., Lu, F., et al. 1997, Nucl. Instr. Meth. Phys. Res. B, 132, 364
Geller, M. J., & Beers, T. C. 1982, PASP, 94, 421
George, L. T., Dwarakanath, K. S., Johnston-Hollitt, M., et al. 2015, MNRAS, 451, 4207
Ghizzardi, S., De Grandi, S., & Molendi, S. 2014, A&A, 570, A117
Giacintucci, S., Markevitch, M., Cassano, R., et al. 2017, ApJ, 841, 71
Giacintucci, S., Venturi, T., Macario, G., et al. 2008, A&A, 486, 347
Giovannini, G., Bonafede, A., Feretti, L., et al. 2009, A&A, 507, 1257
Giovannini, G., Taylor, G. B., Arbizzani, E., et al. 1999, New A Rev., 43, 651
Gitti, M., Ferrari, C., Domainko, W., Feretti, L., & Schindler, S. 2007, A&A, 470, L25
Gitti, M., Tozzi, P., Brunetti, G., et al. 2015, Advancing Astrophysics with the Square Kilometre Array (AASKA14), 76
Golden, L. B., & Sampson, D. H. 1978, ApJS, 38, 19
Golovich, N., Dawson, W. A., Wittman, D. M., et al. 2018, ArXiv e-prints [arXiv:1806.10619v1]
Gomez, P. L., Hughes, J. P., & Birkinshaw, M. 2000, ApJ, 540, 726

Govoni, F., Markevitch, M., Vikhlinin, A., et al. 2004, ApJ, 605, 695
Gregory, D. C., & Crandall, D. H. 1982, Unpublished, http://www-cfadc.phy.ornl.gov/xbeam/xbmintro.html
Gregory, D. C., Dittner, P. F., & Crandall, D. H. 1983, Phys. Rev. A, 27, 724
Gregory, D. C., Meyer, F. W., Mueller, A., & Defrance, P. 1986, Phys. Rev. A, 34, 1
Gregory, D. C., Wang, L. J., Meyer, F. W., & Rinn, K. 1987, Phys. Rev. A, 35, 3256
Gregory, D. C., Wang, L. J., Swenson, D. R., Sataka, M., & Chantrenne, S. J. 1990, Phys. Rev. A, 41, 6512
Griffin, D. C., Bottcher, C., & Pindzola, M. S. 1982, Phys. Rev. A, 25, 154
Griffin, D. C., Pindzola, M., & Bottcher, C. 1987, Phys. Rev. A, 36, 3642
Gu, L., Kaastra, J., & Raassen, T. 2016, arXiv:1601.05958, 588, 1
Gu, M. F. 2002, ApJ, 579, 103
Guainazzi, M., & Tashiro, M. S. 2018, arXiv e-prints [arXiv:1807.06903]
Guo, X., Sironi, L., & Narayan, R. 2014a, ApJ, 794, 153
Guo, X., Sironi, L., & Narayan, R. 2014b, ApJ, 797, 47
Guo, X., Sironi, L., & Narayan, R. 2017, ApJ, 851, 134
Ha, J.-H., Ryu, D., & Kang, H. 2018, ApJ, 857, 26
Hahn, M., Bernhardt, D., Lestinsky, M., et al. 2010, ApJ, 712, 1166
Hahn, M., Bernhardt, D., Grieser, M., et al. 2011a, ApJ, 729, 76
Hahn, M., Grieser, M., Krantz, C., et al. 2011b, ApJ, 735, 105
Hahn, M., Bernhardt, D., Grieser, M., et al. 2012a, Phys. Rev. A, 85, 042713
Hahn, M., Grieser, M., Krantz, C., et al. 2012b, ApJ, 761, 79
Hahn, M., Becker, A., Grieser, M., et al. 2012c, ApJ, 760, 80
Hahn, M., Becker, A., Bernhardt, D., et al. 2013, ApJ, 767, 47
Hahn, M., Becker, A., Bernhardt, D., et al. 2015, ApJ, 813, 16
Hahn, M., Becker, A., Bernhardt, D., et al. 2016, J. Phys. B: At. Mol. Opt. Phys., 49, 084006
Hayes, T. R., Wetzel, R. C., & Freund, R. S. 1987, Phys. Rev. A, 35, 578
Heinz, S., Churazov, E., Forman, W., Jones, C., & Briel, U. G. 2003, MNRAS, 346, 13
Henry, J. P., Evrard, A. E., Hoekstra, H., Babul, A., & Mahdavi, A. 2009, ApJ, 691, 1307
Henry, J. P., Finoguenov, A., & Briel, U. G. 2004, ApJ, 615, 181
Hindson, L., Johnston-Hollitt, M., Hurley-Walker, N., et al. 2014, MNRAS, 445, 330
Hirayama, T., Oda, K., Morikawa, Y., et al. 1986, J. Phys. Soc. Jpn, 55, 1411
Hitomi Collaboration, Aharonian, F., Akamatsu, H., et al. 2016, Nature, 535, 117
Hitomi Collaboration, Aharonian, F., Akamatsu, H., et al. 2018a, PASJ, 70, 12
Hitomi Collaboration, Aharonian, F., Akamatsu, H., et al. 2018b, PASJ, 70, 10
Hitomi Collaboration, Aharonian, F., Akamatsu, H., et al. 2018c, PASJ, 70, 11
Hitomi Collaboration, Aharonian, F., Akamatsu, H., et al. 2018d, PASJ, 70, 9
Hoang, D. N., Shimwell, T. W., Stroe, A., et al. 2017, MNRAS, 471, 1107
Hofmann, G., Müller, A., Tinschert, K., & Salzborn, E. 1990, Z. Phys. D-Atoms, Molecules and Clusters, 16, 113
Hong, S. E., Ryu, D., Kang, H., & Cen, R. 2014, ApJ, 785, 133
Hooper, J. W., Lineberger, W. C., & Bacon, F. M. 1966, Physical Review, 141
Hopkins, A. M., & Beacom, J. F. 2006, ApJ, 651, 142
Hoshino, A., Henry, J. P., Sato, K., et al. 2010, PASJ, 62, 371

Howald, A. M., Gregory, D. C., Ridge, O., et al. 1986, Phys. Rev. A, 33, 3779
Hughes, J. P., & Tanaka, Y. 1992, ApJ, 398, 62
Ichinohe, Y., Simionescu, A., Werner, N., & Takahashi, T. 2017, MNRAS, 467, 3662
Ishisaki, Y., Maeda, Y., Fujimoto, R., et al. 2007, PASJ, 59, 113
Itahana, M., Takizawa, M., Akamatsu, H., et al. 2015, PASJ, 67, 113
Jacobi, J., Knopp, H., Schippers, S., & Müller, A. 2004, Phys. Rev. A, 042717, 2015
Jaffe, W. J., & Rudnick, L. 1979, ApJ, 233, 453
Jalin, R., Hagemann, R., & Botter, R. 1973, The Journal of Chemical Physics, 59, 952
Jee, M. J., Dawson, W. A., Stroe, A., et al. 2016, ApJ, 817, 179
Jee, M. J., Stroe, A., Dawson, W., et al. 2015, ApJ, 802, 46
Johnston-Hollitt, M. 2003, PhD thesis, University of Adelaide
Johnston-Hollitt, M., & Pratley, L. 2017, ArXiv e-prints [arXiv:1706.04930v1]
Jones, M., & Saunders, R. 1996, in Röntgenstrahlung from the Universe, MPE Report, 263,553
Kaastra, J. S. 2017a, A&A, 605, A51
Kaastra, J. S., & Bleeker, J. A. M. 2016, A&A, 587, A151
Kaastra, J. S., Bykov, A. M., & Werner, N. 2009, A&A, 503, 373
Kaastra, J. S., Ferrigno, C., Tamura, T., et al. 2001, A&A, 365, L99
Kaastra, J. S., Gu, L., Mao, J., et al. 2017b, Journal of Instrumentation, 12, C08008
Kaastra, J. S., Mewe, R., & Nieuwenhuijzen, H. 1996, in UV and X-ray Spectroscopy of Astrophysical and Laboratory Plasmas, ed. K. Yamashita & T. Watanabe, 411
Kaastra, J. S., Paerels, F. B. S., Durret, F., Schindler, S., & Richter, P. 2008, Space Sci. Rev., 134, 155
Kaastra, J. S., Raassen, A. J. J., de Plaa, J., & Gu, L. 2017c, SPEX X-ray spectral fitting package, Zenodo
Kaastra, J. S., Tamura, T., Peterson, J. R., et al. 2004, A&A, 413, 415
Kale, R., Dwarakanath, K. S., Bagchi, J., & Paul, S. 2012, MNRAS, 426, 1204
Kale, R., Venturi, T., Giacintucci, S., et al. 2015, A&A, 579, A92
Kallman, T. R., & McCray, R. 1982, ApJS, 50, 263
Kallman, T. R., & Palmeri, P. 2007, Reviews of Modern Physics, 79, 79:133
Kang, H. 2017, JKAS, 50, 93
Kang, H., & Ryu, D. 2015, ApJ, 809, 186
Kang, H., & Ryu, D. 2016, ApJ, 823, 13
Kang, H., Ryu, D., & Jones, T. W. 2012, ApJ, 756, 97
Kao, H. C., Kuo, T. Y., Yen, H. P., Wei, C. M., & Huang, K. N. 1992, Phys. Rev. A, 45, 4646
Kapferer, W., Ferrari, C., Domainko, W., et al. 2006, A&A, 447, 827
Kapferer, W., Kronberger, T., Weratschnig, J., et al. 2007, A&A, 466, 813
Kapferer, W., Kronberger, T., Breitschwerdt, D., et al. 2009, A&A, 504, 719
Kawano, N., Fukazawa, Y., Nishino, S., et al. 2009, PASJ, 61, 377
Kempner, J. C., & David, L. P. 2004, MNRAS, 349, 385
Kocevski, D. D., Ebeling, H., Mullis, C. R., & Tully, R. B. 2007, ApJ, 662, 224
Koyama, K., Tsunemi, H., Dotani, T., et al. 2007, PASJ, 59, S23
Kumar, A., & Roy, B. N. 1979, J. Phys. B: At. Mol. Phys., 12, 3979
Kushino, A., Ishisaki, Y., Morita, U., et al. 2002, PASJ, 54, 327

Laganá, T. F., Durret, F., & Lopes, P. A. A. 2019, MNRAS, 484, 2807
Landau, L. D., & Lifshitz, E. M. 1959, Fluid mechanics, Course of theoretical physics, Oxford: Pergamon Press
Landi, E., Del Zanna, G., Young, P. R., et al. 2006, ApJS, 162, 261
Large, M. I., Mathewson, D. S., & Haslam, C. G. T. 1959, Nature, 183, 1663
Leccardi, A., & Molendi, S. 2008, A&A, 487, 461
Leccardi, A., Rossetti, M., & Molendi, S. 2010, A&A, 510, A82
Limandri, S. P., Vasconcellos, M. A. Z., Hinrichs, R., & Trincavelli, J. C. 2012, Phys. Rev. A, 86, 042701
Lindner, R. R., Baker, A. J., Hughes, J. P., et al. 2014, ApJ, 786, 49
Linkemann, J., Müller, A., Kenntner, J., et al. 1995, Physical Review Letters, 74, 4173
Liu, A., Tozzi, P., Yu, H., De Grandi, S., & Ettori, S. 2018, MNRAS, 481, 361
Llovet, X., Powell, C. J., Salvat, F., & Jablonski, A. 2014, J. Phys. Chem. Ref. Data, 43, 013102
Loch, S. D., Colgan, J., Pindzola, M. S., et al. 2003, Phys. Rev. A, 67, 042714
Loch, S. D., Witthoeft, M., Pindzola, M. S., et al. 2005, Phys. Rev. A, 71, 012716
Lodders, K., Palme, H., & Gail, H.-P. 2009, Landolt Bömstein, New Series, Astronomy and Astrophysics, Springer Verlag„ VI/4B, 560
Lotz, W. 1967, Z. Phys., 206, 205
Lovisari, L., Kapferer, W., Schindler, S., & Ferrari, C. 2009, A&A, 508, 191
Lovisari, L., & Reiprich, T. H. 2019, MNRAS, 483, 540
Lumb, D. H., Warwick, R. S., Page, M., & De Luca, A. 2002, A&A, 389, 93
Ma, C., Sporleder, C. R., & Bonham, R. A. 1991, Review of Scientific Instruments, 62, 909
Macario, G., Markevitch, M., Giacintucci, S., et al. 2011, ApJ, 782, 82
Machado, R. E. G., & Lima Neto, G. B. 2013, MNRAS, 430, 3249
Madau, P., & Dickinson, M. 2014, ARA&A, 52, 415
Magee, N. H., Abdallah, J., JR., et al. 1995, Astropyshical Applications of Powerful New Databases, ASP Conf., 78, 51
Mahdavi, A., Finoguenov, A., Böhringer, H., Geller, M. J., & Henry, J. P. 2005, ApJ, 622, 187
Man, K. F., Smith, A. C. H., & Harrison, M. F. A. 1987a, J. Phys. B: At. Mol. Phys., 20, 5865
Man, K. F., Smith, A. C. H., & Harrison, M. F. A. 1987b, J. Phys. B: At. Mol. Phys., 20, 2571
Man, K. F., Smith, A. C. H., & Harrison, M. F. A. 1993, J. Phys. B: At. Mol. Opt. Phys., 26, 1365
Mandal, S., Intema, H. T., Shimwell, T. W., et al. 2019, A&A, 622, A22
Mantz, A. B., Allen, S. W., Morris, R. G., et al. 2017, MNRAS, 472, 2877
Mao, J., & Kaastra, J. 2016, A&A, 587, A84
Mao, J., Kaastra, J., & Badnell, N. R. 2017, A&A, 599, A10
Mao, J., de Plaa, J., Kaastra, J. S., et al. 2019, A&A, 621, A9
Markevitch, M., Gonzalez, A. H., David, L., et al. 2002, ApJ, 567, L27
Markevitch, M., Govoni, F., Brunetti, G., & Jerius, D. 2005, ApJ, 627, 733
Markevitch, M., Sarazin, C. L., & Vikhlinin, A. 1999, ApJ, 521, 526
Markevitch, M., & Vikhlinin, A. 2001, ApJ, 563, 95
Markevitch, M., & Vikhlinin, A. 2007, Phys. Rep., 443, 1
Martin, S. O., Peart, B., & Dolder, K. T. 1968, J. Phys. B, 1, 537
Matsushita, K. 2011, A&A, 527, A134
Maughan, B. J., Jones, C., Forman, W., & van Speybroeck, L. 2008, ApJS, 174, 117

Mazzota, P., Bourdin, H., Giacintucci, S., Markevitch, M., & Venturi, T. 2011, Mem. Soc. Astron. Italiana, 82, 495
Mazzotta, P., Fusco-Femiano, R., & Vikhlinin, A. 2002, ApJ, 569, L31
Mazzotta, P., & Giacintucci, S. 2008, ApJ, 675, L9
McCallion, P., Shah, M. B., & Gilbody, H. B. 1992a, J. Phys. B: At. Mol. Opt. Phys., 25, 1051
McCallion, P., Shah, M. B., & Gilbody, H. B. 1992b, J. Phys. B: At. Mol. Opt. Phys., 25, 1061
McCarthy, I. E., & Stelbovics, A. T. 1983, Phys. Rev. A, 28, 1322
McDonald, M., Bulbul, E., de Haan, T., et al. 2016, ApJ, 826, 124
McFarland, R. H., & Kinney, J. D. 1965, Physical Review, 137, A1058
McGuire, E. J. 1977, Phys. Rev. A, 16, 62
McGuire, E. J. 1982, Phys. Rev. A, 26, 125
McGuire, E. J. 1997, J. Phys. B: At. Mol. Opt. Phys., 30, 1563
Mehdipour, M., Kaastra, J. S., & Kallman, T. 2016, A&A, 596, A65
Meidinger, N., Nandra, K., & Plattner, M. 2018, in Society of Photo-Optical Instrumentation Engineers (SPIE) Conference Series, Vol. 10699, Space Telescopes and Instrumentation 2018: Ultraviolet to Gamma Ray, 106991F
Mernier, F., de Plaa, J., Lovisari, L., et al. 2015, A&A, 575, A37
Mernier, F., de Plaa, J., Pinto, C., et al. 2016, A&A, 595, A126
Mernier, F., de Plaa, J., Kaastra, J. S., et al. 2017, A&A, 603, A80
Mernier, F., de Plaa, J., Werner, N., et al. 2018a, MNRAS, 478, L116
Mernier, F., Biffi, V., Yamaguchi, H., et al. 2018b, Space Sci. Rev., 214, 129
Merten, J., Coe, D., Dupke, R., et al. 2011, MNRAS, 417, 333
Mewe, R. 1972, A&A, 20, 215
Mewe, R., Gronenschild, E. H. B. M., & van den Oord, G. H. J. 1985, A&AS, 62, 197
Mewe, R., Lemen, J. R., & van den Oord, G. H. J. 1986, A&AS, 65, 511
Miley, G. K., & Perola, G. C. 1975, A&A, 45, 223
Miller, N. A., Owen, F. N., & Hill, J. M. 2003, AJ, 125, 2393
Miniati, F. 2002, MNRAS, 337, 199
Mitchell, R. J., Culhane, J. L., Davison, P. J. N., & Ives, J. C. 1976, MNRAS, 175, 29P
Mitsuda, K., Bautz, M., Inoue, H., et al. 2007, PASJ, 59, 1
Moffet, A. T., & Birkinshaw, M. 1989, ApJ, 98, 1148
Montague, R. G., Diserens, M. J., & Harrison, M. F. A. 1984a, J. Phys. B: Atom. Molec. Phys., 17, 2085
Montague, R. G., Harrison, M. F. A., & Smith, A. C. H. 1984b, J. Phys. B: At. Mol. Phys., 17, 3295
Monteiro-Oliveira, R., Neto, G. B. L., Cypriano, E. S., et al. 2017, MNRAS, 468, 4566
Moores, D. L., & Pindzola, M. S. 1990, Phys. Rev. A, 42, 5384
Mueller, D. W., Morgan, T. J., Dunn, G. H., Gregory, D. C., & Crandall, D. H. 1985, Phys. Rev. A, 31, 2905
Müller, A., Hofmann, G., Tinschert, K., Weibecker, B., & Salzborn, E. 1990, Z. Phys. D-Atoms, Molecules and Clusters, 15, 145
Müller, A., Salzborn, E., Frodl, R., et al. 1980, J. Phys. B: At. Mol. Phys., 13, 1877
Nagy, P., Skutlartz, A., & Schmidt, V. 1980, J. Phys. B: At. Mol. Phys., 13, 1249
Nandra, K., Barret, D., Barcons, X., et al. 2013, ArXiv e-prints [arXiv:1306.2307]
Nuza, S. E., Gelszinnis, J., Hoeft, M., & Yepes, G. 2017, MNRAS, 470, 240

Ogrean, G., Brüggen, M., Simionescu, A., et al. 2013a, MNRAS, 429, 2617
Ogrean, G. A., & Brüggen, M. 2013c, MNRAS, 433, 1701
Ogrean, G. A., Brüggen, M., van Weeren, R. J., Burgmeier, A., & Simionescu, A. 2014, MNRAS, 443, 2463
Ogrean, G. A., Brüggen, M., van Weeren, R. J., et al. 2013b, MNRAS, 433, 812
Omidvar, K., & Rule, D. 1977, International Conference on the Physics of Electronic and Atomic Collisions: ICPEAC X, 544
O'Rouke, B., Currell, F. J., Kuramoto, H., et al. 2001, J. Phys. B: At. Mol. Opt. Phys., 34, 4003
Owers, M. S., Couch, W. J., & Nulsen, P. E. J. 2009, ApJ, 693, 901
Owers, M. S., Nulsen, P. E. J., Couch, W. J., et al. 2014, ApJ, 780, 163
Pacholczyk, A. G. 1973, Radio astrophysics. Nonthermal processes in galactic and extra-galactic sources, Moskva: Mir
Paul, S., Iapichino, L., Miniati, F., Bagchi, J., & Mannheim, K. 2011, ApJ, 726, 17
Peart, B., & Dolder, K. 1975, J. Phys. B: At. Mol. Phys., 8, 56
Peart, B., & Dolder, K. T. 1968, J. Phys. B, 1, 872
Peart, B., Thomason, J. W. G., & Dolder, K. 1991a, J. Quant. Spectrosc. Radiat. Transfer, 24, 489
Peart, B., Thomason, J. W. G., & Dolder, K. 1991b, J. Phys. B: At. Mol. Opt. Phys., 24, 4453
Peart, B., Underwood, J. R. A., & Dolder, K. 1989, J. Phys. B: At. Mol. Opt. Phys., 22, 2789
Peart, B., Walton, D. S., & Dolder, K. T. 1969, J. Phys. B, 2, 1347
Pedlar, A., Ghataure, H. S., Davies, R. D., et al. 1990, MNRAS, 246, 477
Peterson, J. R., Paerels, F. B. S., Kaastra, J. S., et al. 2001, A&A, 365, L104
Pindzola, M. S., Gorczyca, T. W., Badnell, N. R., et al. 1994, Phys. Rev. A, 49, 943
Pindzola, M. S., Griffin, D. C., Bottcher, C., Buie, M. J., & Gregory, D. C. 1991, Physica Scripta, 37, 35
Pindzola, M. S., Griffin, D. C., Bottcher, C., Younger, S. M., & Hunter, H. T. 1987, Nucl. Fusion Special Suppl., 27, 21
Pinzke, A., Oh, S. P., & Pfrommer, C. 2013, MNRAS, 435, 1061
Pizzo, R. F., & de Bruyn, a. G. 2009, A&A, 507, 639
Quarles, C. A. 1976, Phys. Rev. A, 13, 1278
Rachafi, S., Belic, D. S., Duponchelle, M., et al. 1991, J. Phys. B: At. Mol. Opt. Phys., 24, 1037
Rajpurohit, K., Hoeft, M., van Weeren, R. J., et al. 2018, ApJ, 852, 65
Rapp, D., & Englander-Golden, P. 1965, J. Phys. Chem., 43, 1464
Reed, K. J., & Chen, M. H. 1992, Phys. Rev. A, 45, 4519
Reid, R. H. G., Bartschat, K., & Burke, P. G. 1992, J. Phys. B: At. Mol. Opt. Phys., 25, 3175
Reiprich, T. H., Basu, K., Ettori, S., et al. 2013, Space Sci. Rev., 177, 195
Reiprich, T. H., Hudson, D. S., Zhang, Y. Y., et al. 2009, A&A, 501, 899
Rejoub, R., Lindsay, B. G., & Stebbings, R. F. 2002, Phys. Rev. A, 65, 042713
Riahi, A., Laghdas, K., Reid, R. H. G., et al. 2001, J. Phys. B: At. Mol. Opt. Phys., 34, 175
Riseley, C. J., Scaife, A. M., Oozeer, N., Magnus, L., & Wise, M. W. 2015, MNRAS, 447, 1895
Roettiger, K., Burns, J. O., & Pinkney, J. 1995, ApJ, 453, 634
Roettiger, K., Burns, J. O., & Stone, J. M. 1999, ApJ, 518, 603
Rogers, W. T., Stefani, G., Camilloni, R., et al. 1982, Phys. Rev. A, 25
Rossetti, M., & Molendi, S. 2010, A&A, 510, A83

Röttgering, H. J., Wieringa, M. H., Hunstead, R. W., & Ekers, R. D. 1997, MNRAS, 290, 577
Roy, B. N., & Kai, D. K. 1983, J. Phys. B: At. Mol. Phys., 16, 4677
Rumsey, C., Perrott, Y. C., Olamaie, M., et al. 2017, MNRAS, 470, 4638
Russell, H. R., Mcnamara, B. R., Sanders, J. S., et al. 2012, MNRAS, 423, 236
Russell, H. R., Fabian, A. C., McNamara, B. R., et al. 2014, MNRAS, 444, 629
Ryu, D., Kang, H., & Ha, J.-H. 2019, arXiv e-prints, arXiv:1905.04476
Ryu, D., Kang, H., Hallman, E., & Jones, T. W. 2003, ApJ, 593, 599
Sampson, D. H. 1982, J. Phys. B: At. Mol. Phys., 15, 2087
Sampson, D. H., & Golden, L. B. 1981, J. Phys. B: At. Mol. Phys., 14, 903
Sanderson, A. J. R., Ponman, T. J., Finoguenov, A., Lloyd-Davies, E. J., & Markevitch, M. 2003, MNRAS, 340, 989
Sarazin, C. L. 2001, Merging Processes in Clusters of Galaxies, Astrophysics and Space Science Library, Vol. 272. Kluwer Academic Publishers, Dordrecht, 1
Sarazin, C. L., Finoguenov, A., Wik, D. R., & Clarke, T. E. 2016, ArXiv e-prints [arXiv:1606.07433]
Sataka, M., Ohtani, S., Swanson, D., & Gregory, D. C. 1989, Phys. Rev. A, 39, 2397
Schindler, S., Kapferer, W., Domainko, W., et al. 2005, A&A, 435, L25
Schreier, S. 1982, in Compressible Flow.Wiley, New York
Serlemitsos, P. J., Smith, B. W., Boldt, E. A., Holt, S. S., & Swank, J. H. 1977, ApJ, 211, L63
Serlemitsos, P. J., Soong, Y., Chan, K. W., et al. 2007, PASJ, 59, 9
Shah, M. B., Elliott, D. S., & Gilbody, H. B. 1987, J. Phys. B: At. Mol. Phys., 20, 3501
Shah, M. B., Elliott, D. S., McCallion, P., & Gilbody, H. B. 1988, J. Phys. B: At. Mol. Opt. Phys., 21, 2751
Shimwell, T. W., Markevitch, M., Brown, S., et al. 2015, MNRAS, 449, 1486
Shimwell, T. W., Luckin, J., Br, M., et al. 2016, MNRAS, 459, 277
Simionescu, A., Werner, N., Böhringer, H., et al. 2009, A&A, 493, 409
Simionescu, A., Werner, N., Finoguenov, A., Böhringer, H., & Brüggen, M. 2008, A&A, 482, 97
Simionescu, A., Werner, N., Forman, W. R., et al. 2010, MNRAS, 405, 91
Simionescu, A., Werner, N., Mantz, A., Allen, S. W., & Urban, O. 2017, MNRAS, 496, 1476
Simionescu, A., Nakashima, S., Yamaguchi, H., et al. 2019, MNRAS, 483, 1701
Skillman, S. W., Xu, H., Hallman, E. J., et al. 2013, ApJ, 765
Smith, R. J., Hudson, M. J., Nelan, J. E., et al. 2004, ApJ, 128, 1558
Sobral, D., Stroe, A., Dawson, W. A., et al. 2015, MNRAS, 450, 630
Stenke, M., Aichele, K., Hartenfeller, U., et al. 1999, J. Phys. B: At. Mol. Opt. Phys., 32, 3627
Stephan, K., Helm, H., & Märk, T. D. 1980, J. Phys. Chem., 73, 3763
Storm, E., Vink, J., Zandanel, F., & Akamatsu, H. 2018, MNRAS, 479, 553S
Straub, H., Renault, P., Lindsay, B., Smith, K., & Stebbings, R. 1995, Phys. Rev. A, 52, 1115
Stroe, A., Harwood, J. J., Hardcastle, M. J., & Röttgering, H. J. 2014a, MNRAS, 445, 1213
Stroe, A., Oosterloo, T., Röttgering, H. J., et al. 2015a, MNARS, 452, 2731
Stroe, A., & Sobral, D. 2015b, MNRAS, 453, 242
Stroe, A., Sobral, D., Paulino-Afonso, A., et al. 2017, MNRAS, 465, 2916
Stroe, A., Sobral, D., Röttgering, H. J., & van Weeren, R. J. 2014b, MNARS, 438, 1377
Struble, M. F., & Rood, H. J. 1999, ApJS, 125, 35
Sun, M., Murray, S. S., Markevitch, M., & Vikhlinin, A. 2002, ApJ, 565, 867

Tamura, T., Bleeker, J. A. M., Kaastra, J. S., Ferrigno, C., & Molendi, S. 2001, A&A, 379, 107
Tamura, T., Hayashida, K., Ueda, S., & Nagai, M. 2011, PASJ, 63, S1009
Tashiro, M., Maejima, H., Toda, K., et al. 2018, in Society of Photo-Optical Instrumentation Engineers (SPIE) Conference Series, Vol. 10699, Space Telescopes and Instrumentation 2018: Ultraviolet to Gamma Ray, 1069922
Tawa, N., Hayashida, K., Nagai, M., et al. 2008, PASJ, 60, 11
Tawara, H. 2002, Numerical Data and Functional Relationships in Science and Technology, ed. Y. Hahn, A. K. Pradhan, H. Tawara, H. L. Zhang and Itakawa (gen. ed.), Landolt-Bornstein, 103
Tayal, S. S., & Henry, R. J. W. 1986, Phys. Rev. A, 33, 3825
Teng, H., Knopp, H., Ricz, S., et al. 2000, Phys. Rev. A, 61, 060704
Thierbach, M., Klein, U., & Wielebinski, R. 2003, A&A, 397, 53
Thölken, S., Lovisari, L., Reiprich, T. H., & Hasenbusch, J. 2016a, A&A, 592, A37
Thölken, S., Lovisari, L., Reiprich, T. H., & Hasenbusch, J. 2016b, A&A, 592, A37
Thölken, S., Reiprich, T. H., Sommer, M. W., & Ota, N. 2018, A&A, 619, A68
Thomason, J. W. G., & Peart, B. 1998, J. Phys. B: At. Mol. Opt. Phys., 31, 201
Thompson, J. S., & Gregory, D. C. 1994, Phys. Rev. A, 50, 1377
Thompson, W. R., Shah, M. B., & Gilbody, H. B. 1995, J. Phys. B: At. Mol. Opt. Phys., 28, 1321
Thomson, J. J. 1912, Phil. Mag., 23, 449
Tinschert, K., Müller, A., Hofmann, G., et al. 1989, J. Phys. B: At. Mol. Opt. Phys., 22, 531
Tozzi, P., & Norman, C. 2001, ApJ, 546, 63
Trasatti, M., Akamatsu, H., Lovisari, L., et al. 2015, A&A, 575, A45
Urban, O., Werner, N., Allen, S. W., Simionescu, A., & Mantz, A. 2017, MNRAS, 470, 4583
Urdampilleta, I., Akamatsu, H., Mernier, F., et al. 2018, A&A, 618, A74
Urdampilleta, I., Kaastra, J. S., & Mehdipour, M. 2017, A&A, 601, A85
Urdampilleta, I., Mernier, F., Kaastra, J. S., et al. 2019, A&A, 629, A31
Vacca, V., Govoni, F., Murgia, M., et al. 2010, A&A, 541, A71
van Weeren, R. J., Brüggen, M., Röttgering, H. J., & Hoeft, M. 2011b, MNARS, 418, 230
van Weeren, R. J., Brüggen, M., Röttgering, H. J. A., et al. 2011a, A&A, 533, A35
van Weeren, R. J., de Gasperin, F., Akamatsu, H., et al. 2019, Space Sci. Rev., 215, 16
van Weeren, R. J., Intema, H. T., Oonk, J. B. R., Röttgering, H. J. A., & Clarke, T. E. 2009, A&A, 508, 1269
van Weeren, R. J., Rottgering, H. J. A., Bruggen, M., & Hoeft, M. 2010, Science, 330, 347
van Weeren, R. J., Röttgering, H. J. A., Intema, H. T., et al. 2012a, A&A, 546, A124
van Weeren, R. J., Röttgering, H. J. A., Rafferty, D. A., et al. 2012b, A&A, 543, A43
van Weeren, R. J., Intema, H. T., Lal, D. V., et al. 2014, ApJ, 786, L17
van Weeren, R. J., Brunetti, G., Brüggen, M., et al. 2016, ApJ, 818, 204
van Weeren, R. J., Andrade-Santos, F., Dawson, W. A., et al. 2017, Nature Astronomy, 1, 5
Vazza, F., & Brüggen, M. 2014, MNRAS, 437, 2291
Verner, D. A., & Yakovlev, D. G. 1995, A&AS, 109, 125
Vikhlinin, A., Kravtsov, A., Forman, W., et al. 2006, ApJ, 640, 691
Vikhlinin, A., Markevitch, M., & Murray, S. S. 2001, ApJ, 551, 160
Vink, J., & Yamazaki, R. 2014, ApJ, 780, 125
Vogelsberger, M., Marinacci, F., Torrey, P., et al. 2018, MNRAS, 474, 2073

Wang, L. J., Rinn, K., & Gregory, D. C. 1988, J. Phys. B: Atom. Molec. Phys., 21, 2117
Werner, N., Durret, F., Ohashi, T., Schindler, S., & Wiersma, R. P. C. 2008, Space Sci. Rev., 134, 337
Werner, N., Urban, O., Simionescu, A., & Allen, S. W. 2013, Nature, 502, 656
Wetzel, R. C., Baiocchi, F. A., Hayes, T. R., & Freund, R. S. 1987, Phys. Rev. A, 35, 559
Wilber, A., Brüggen, M., Bonafede, A., et al. 2019, A&A, 622, A25
Willingale, R., Starling, R. L. C., Beardmore, A. P., Tanvir, N. R., & O'Brien, P. T. 2013, MNRAS, 431, 394
Willson, M. A. G. 1970, MNRAS, 151, 1
Wong, K. L., Beiersdorfer, P., Chen, M. H., et al. 1993, Phys. Rev. A, 48, 2850
Yamada, I., Danjo, A., Hirayama, T., et al. 1988, J. Phys. Soc. Jpn, 57, 2699
Yamada, I., Danjo, A., Hirayama, T., et al. 1989a, J. Phys. Soc. Jpn, 58, 1585
Yamada, I., Danjo, A., Hirayama, T., et al. 1989b, J. Phys. Soc. Jpn, 58, 3151
Younger, S. M. 1981a, J. Quant. Spectrosc. Radiat. Transfer, 26, 329
Younger, S. M. 1981b, Phys. Rev. A, 23, 1138
Younger, S. M. 1981c, Phys. Rev. A, 24, 1272
Younger, S. M. 1981d, Phys. Rev. A, 24, 1278
Younger, S. M. 1982a, J. Quant. Spectrosc. Radiat. Transfer, 27, 541
Younger, S. M. 1982b, Journal of research of the national Bureau of Standards, 87, 49
Younger, S. M. 1982c, Phys. Rev. A, 25, 3396
Younger, S. M. 1982d, Phys. Rev. A, 26, 3177
Younger, S. M. 1983, J. Quant. Spectrosc. Radiat. Transfer, 29, 61
Zapesochnyi, I. P., & Aleksakhin, I. S. 1969, Soviet Physics Jetp, 28, 41
Zeijlmans van Emmichoven, P., Bannister, M., Gregory, D., et al. 1993, Phys. Rev. A, 47, 2888
Zhang, H., Cherkani-Hassani, S., B lenger, C., et al. 2002, J. Phys. B: At. Mol. Opt. Phys., 35, 3829
Zhang, H. L., & Sampson, D. H. 1990, Phys. Rev. A, 42, 5378
Zhang, Y., Reddy, C. B., Smith, R. S., et al. 1991, Phys. Rev. A, 44, 4368
ZuHone, J. A. 2011, ApJ, 728, 54

Nederlandse Samenvatting

Clusters van sterrenstelsels zijn de grootste objecten in het universum. Ze bevatten tussen de honderd tot duizend sterrenstelsels. Deze sterrenstels worden omringd door heet geionseerd plasma, het zogenaamde intracluster medium (ICM) wat geobserveerd kan worden met behulp van röntgenstraling. De sterrenstelsels vormen slechts 5% van de totale massa, terwijl het ICM 15% van de massa van het totale cluster omvat. De rest van de massa, ∼80%, bestaat vooral uit donkere materie. Clusters van sterrenstelsels worden waargenomen op verschillende golflengtes. In dit proefschrift zijn de meest relevante waarnemingen gedaan in optisch-, röntgen- en radio golflengten (zie Fig. A). Optische waarnemingen onthullen de individuele sterrenstelsels en hun over-dichtheid (nl. een hogere dichtheid dan gemiddeld in het cluster) op een vergelijkbare roodverschuiving. Met behulp van röntgenstraling kunnen de eigenschappen van het ICM worden afgeleid, zoals onder andere de dichtheid, temperatuur en abundantie van elementen. Daarbij onthullen radio waarnemingen discrete en langgerekte radiobronnen, traceren ze de kosmische straling en de versnelling van energetische deeltjes. Clusters van sterrenstelsels worden gewoonlijk geklassificeerd in verschillende groepen op basis van hun dynamische toestand: gerelaxeerde of koele-kern clusters (CC), verstoorde of niet-koele-kern (NCC) en extreem verstoorde of fuserende clusters.

Clusters van sterrenstelsels groeien hiërarchisch door middel van accretie en fusie van minder zware groepen of subclusters. Deze fuserende stelsels, ook wel cluster mergers genaamd, zijn de meest energetische gebeurtenissen in het universum sinds de Oerknal. Tubulentie, schokken en koufronten ontstaan in het hete ICM als gevolg van deze sterke fusieactiviteit. Schokken zijn grootschalige structuren die zich voortplanten vanuit het centrum naar de rand van het cluster, waar ze meestal worden gedetecteerd. Ze kunnen worden waargenomen door middel van spectrale analyse dankzij temperatuur en dichtheidsdiscontinuiteiten in het ICM en door middel van de scherpe randen waarneembaar in röntgen. Men denkt dat schokken ($\mathcal{M} \leq 3$–5) elektronen (opnieuw) versnellen via eerste-orde Fermi Diffusive Shock Acceleration (DSA). Tegenwoordig worden er ook alternatieve mechanismen voorgesteld, zoals het opnieuw versnellen van reeds bestaande komische stralingselektronen. Deze relativistische deeltjes zouden niet-thermische synchrotron emissie kunnen produceren in de vorm van langwerpige, gepolariseerde en steile spectrumstruc-

Figuur A: Samengestelde afbeelding (optisch, röntgen in oranje en radio in blaauw) van het cluster van sterrenstelsel Abell 3376. Credit: X-ray (NASA/CXC/SAO/A. Vikhlinin; ROSAT), Optical (DSS), Radio (NSF/NRAO/VLA/IUCAA/J. Bagchi).

turen ook bekend als radio relieken. In sommige fuserende clusters verschijnt deze radio emissie (radio relieken) samen met röntgen emissie (röntgen schokken).

Het ICM van clusters is rijk aan metalen, die voornamelijk hun oorsprong vinden in supernovae met ineenstortende kernen (SNcc), type Ia super novae (SNIa) en sterren met een lage massa op de asymptotische reuzentak (AGB). SNcc produceren met name lichtere metalen (O, Ne, Mg, Si en S), terwijl zwaardere metalen (zoals Ar, Ca, Mn, Fe en Ni) door SNIa worden uitgestoten. AGB sterren dragen het meest bij aan de productie van C en N. Als de metalen eenmaal in het ICM zijn uitgestoten, worden ze getransporteerd, gemengd en opnieuw verdeeld. In de afgelopen jaren is de Fe abundantie van CC en NCC uitgebreid geanalyseerd. Er zijn echter maar weinig onderzoeken gedaan die gericht zijn op fuserende sterrenstelsels. Een beter begrip van de verdeling van metalen langs de as waarop de sterrenstelsels fuseren, kan de chemische geschiedenis en evolutie van deze grootschalige structuren onthullen. De radiele Fe verdeling van CC clusters vertoont een hoge metaalrijke piek vergeleken met NCC clusters, die op grote radiele afstanden afvlakt naar een uniforme verdeling rond $\sim$0.2–0.3 $Z_{\odot}$. Hetzelfde gedrag wordt waargenomen in NCC clusters, wat wijst op een scenario waarin het ICM al vroeg met metalen is verrijkt ($z \sim 2$–3).

Röntgen spectroscopie biedt een nuttig hulpmiddel om al deze hier boven genoemde thermodynamische en chemische eigenschappen van het ICM af te leiden. We hebben

daarom actuele spectrale plasma codes met hoge nauwkeurigheid en volledigheid nodig om röntgenspectra van clusters van sterrenstelsels te modelleren en te fitten. SPEX is een van deze software programma's voor het modelleren, fitten en analyseren van spectra. SPEX is recentelijk geupdate naar v3.0 om te kunnen voldoen aan de hoge observationele eisen m.b.t. tot de spectroscopische waarnemingen die werden verwacht van de Hitomi satelliet en van toekomstige missies: XRISM en Athena. De belangrijkste verbeteringen waren gericht op het updaten van stralingsprocessen zoals stralingsrecombinatie, botsingsionisatie, ladingsuitwisseling of foto-ionisatie en de integratie van een groot aantal emissie- en overgangslijnen.

Dit proefschrift richt zich op de röntgenanalyse van fuserende clusters van sterrenstelsels en de ontwikkeling van de plasma code voor toekomstige spectrocoscopische waarnemingen met hoge resolutie. Dit werk is gewijd aan een beter begrip van twee concrete aspecten van deze fuserende clusters: ten eerste, de correlatie tussen de thermische (röntgen) en de niet-thermische (radio) componenten, en als tweede, hun metaalverrijkingsgeschiedenis. Het eerste punt kan de fysieke associatie tussen de röntgen- en radiocomponenten onthullen. Het tweede kan licht werpen op de dynamische geschiedenis van de fusies en hun rol in de metaalverrijking van de clusters.

In hoofdstuk 2 behandelen we de röntgenstudie van het fuserende sterrenstelsel Abell 3376 waargenomen met *Suzaku*. We bestuderen de ruimtelijke verdeling van de thermische component van het ICM inclusief de randen van het cluster. Hiervoor bepalen we de temperatuurverdeling in vier verschillende radiale richtingen (west, oost, noord en zuid). We vergelÿlen deze verdelingen met universele profielen van gerelaxeerde clusters en we vinden een afwijking in alle richtingen behalve het zuiden, wat een mogelijke aanwezigheid van schokken suggereert. We vinden echter alleen aanwijzingen voor twee schokken in het westen en oosten. De ene is gekoppeld aan de westerse radio-reliek met $\mathcal{M} \sim 2.8$ en de andere aan de oostelijke 'inkeping' met een $\mathcal{M} \sim 1.5$. We detecteren ook een koud front ten oosten van de röntgenemissiepiek. Het Mach-nummer van de oostelijke schok is consistent met eerdere radio-waarnemingen, terwijl die van het westerse radio-reliek iets lager is, waarschijnlijk door verouderingseffecten. Tot slot beschouwen we het fusiescenario en beargumenteren een mogelijke fusie dicht bij het hemelvlak met een dynamische leeftijd van $\sim$0.6 Gyr na kernpassage.

In Hoofdstuk 3 onderzoeken we de thermodynamische eigenschappen van het hete plasma in het fuserende cluster van sterrenstelsels Abell 3365 met behulp van waarnemingen met *XMM-Newton*. We zoeken hiervoor als eerste naar de discontinuiteiten in de röngtenoppervlaktehelderheid en temperatuur aan de randen van het cluster en de centrale ICM-randen. Ten tweede verkrijgen we de temperatuur, Fe-abundantie en pseudo-entropieverdelingen langs de fuserende as in het centrale heldere gebied. We vinden twee sterke schokken ($\mathcal{M} > 3$) geassocieerd met het oostelijke radio-relikwie en het westelijke kandidaat-relikwie en één koud front ten westen van de röntgenemissiepiek. De schokversnellingsefficiëntie bij het oostelijke relikwie is consistent met het DSA-mechanisme, wat suggereert dat dit een gunstig scenario is voor schokken met $\mathcal{M} > 3$. De abundantieverdeling laat tekenen zien van twee pieken met een waarde van $\sim$0.6 $Z_{\odot}$. De ene komt overeen met de locatie van de hoofdsubcluster en de andere is verplaatst ten opzichte van de röngtenemissie piek richting het houdefront. We vinden ook een laag entropie minimum, wat

suggereert dat de koelekern van het voormalige sterrenstelsel de fusieactiviteit gedeeltelijk of volledig kan overleven.

In Hoofdstuk 4 presenteren we een spectrale röngtenanalyse van zes fuserende clusters (CIZA J2242.8+5301, 1RXS J0603.3+4214, Abell 3376, Abell 3667, Abell 665 and Abell 2256) waargenomen met XMM-Newton. We verkrijgen de temperatuur, Fe abundantie en pseudo-entropieverdelingen langs de fuserende as tot r_{500}. We leiden het gemiddelde Fe-profiel af, dat een matige centrale piek vertoont, lager dan ontspannen clusters, gevolgd door een gladde afvlakking tot een uniforme waarde van $\sim$0.2–0.3 $Z_{\odot}$ bij grote radii. Bovendien suggereren de pseudo-entropieverdelingen dat in sommige gevallen de relatief lage entropiekern kan overleven bij grote fusies. We bestuderen ook de correlatie tussen Fe abundantie en pseudo-entropie. We vinden een bescheiden correlatie tussen de centrale regio's, waarschijnlijk als gevolg van de fusieactiviteit en de verspreiding van de metalen. Er is echter geen bewijs voor correlaties op grote afstand van het centrum aan de randen van het cluster. Dit resultaat samen met de uniformiteit van de abundantie lijkt aanvullend bewijs te leveren voor het pre-verrijkingsscenario.

Ten slotte updaten we in hoofdstuk 5 de werkzame doorsnede voor enkelvoudige ionisatie voor ionen van H tot Zn, waarbij we rekening houden met nieuwe theoretische berekeningen en laboratorium experimenten. De doorsneden van de rest van de ionen zonder dataset worden geïnterpoleerd of geëxtrapoleerd. We kunnen niet alleen de totale werkzame doorsnede, maar ook voor het eerst die van de binnenste elektronen schillen atzonderlÿk bepalen. Deze dwarsdoorsnedes omvatten twee verschillende stralingsprocessen: de directe ionisatie (DI) en excitatie-autoionisatie (EA). We modelleren en fitten de DI- en EA-processen met behulp van een uitbreiding van de vergelijkingen van Younger en Mewe om zo de DI- en EA-coëfficiënten te verkrijgen. We leiden de subshell-ionisatiecoëfficiënten af, waarbij we integreren over een Maxwelliaanse snelheidsverdeling. Tot slot nemen we de DI-, EA- en ionisatiesnelheidcoëfficiënten op in de nieuwe versie van SPEX v3.0.

Summary

Galaxy clusters are the largest virialized objects in the Universe, which contain between a hundred to a thousand of galaxies. These galaxies are surrounded by hot ionized plasma, known as intracluster medium (ICM) and it is observed in X-rays. The galaxies constitute only $\sim$5% of the total mass, while the ICM includes around $\sim$15%. The rest of the mass, $\sim$80%, is dominated by dark matter. Galaxy clusters can be observed using different wavelengths, although the most relevant for this work are optical, X-ray and radio observations (see Fig. A). Optical observations reveal the individual galaxies and their overdensity at a similar redshift. In X-rays the spectral properties (for example, temperature, density or abundance) of the ICM can be derived. Moreover, radio observations show discrete and extended radio sources, trace the cosmic rays and the energetic particles acceleration. Galaxy clusters are usually classified in different groups based on their dynamical state: relaxed or cool-core (CC) clusters, disturbed or non-cool-core (NCC) clusters and extremely disturbed or merging galaxy clusters.

Galaxy clusters grow hierarchically via accretion and merging of less massive groups or subclusters. Cluster mergers are the most energetic events in the Universe since the Big Bang. Turbulence, shocks and cold fronts arise in the hot ICM as a result of the strong merging activity. Shocks are large scale structures that propagate from the cluster center to the periphery, where they are usually found. They can be detected by temperature and density discontinuities in the ICM via spectral analysis and detection of X-ray surface brightness edges, respectively. Shocks ($\mathcal{M} \leq$ 3–5) are thought to (re)accelerate electrons, in the presence of an amplified magnetic field, via first-order Fermi diffusive shock acceleration (DSA). Nowadays alternative acceleration mechanisms have been also proposed such as the re-acceleration of the pre-existing cosmic ray electrons, among others. These relativistic particles may produce non-thermal synchrotron emission in the form of elongated, polarized and steep-spectrum structures known as radio relics. In some merging clusters this radio emission appears associated to an X-ray counterpart (X-ray shocks).

The ICM of galaxy clusters is rich in metals, which originate mainly from core-collapse supernovae (SNcc), type Ia supernovae (SNIa) and low-mass stars on the asymptotic giant branch (AGB). SNcc release primary light metals (O, Ne, Mg, Si and S), while heavier metals (such as Ar, Ca, Mn, Fe, and Ni) are expelled by SNIa. The main contribution of C and N

Figure A: Composite image (optical, X-ray in orange and radio in blue) of the galaxy cluster Abell 3376. Credit: X-ray (NASA/CXC/SAO/A. Vikhlinin; ROSAT), Optical (DSS), Radio (NSF/NRAO/VLA/IUCAA/J. Bagchi).

come from AGB. Once the metals are ejected to the ICM, they are later transported, mixed, and redistributed. During the last years, the Fe abundance distribution of CC and NCC clusters has been widely analyzed. However, few studies have been done centered on the merging galaxy clusters. A better understanding of the metals distribution along the merging axis can reveal the chemical evolution and history of these large scale structures. The Fe radial distribution of CC clusters present a high central metal-rich peak compared with NCC clusters, which flattens at large radii towards a uniform distribution around $\sim$0.2–0.3 $Z_{\odot}$. This same behavior is observed in NCC clusters, which suggest an early enrichment scenario of the ICM ($z \sim$ 2–3).

X-ray spectroscopy represents a useful tool to determine all these thermodynamical and chemical properties of the ICM mentioned above. For this reason updated spectral plasma codes with high accuracy are completely needed to model and fit X-ray spectra of galaxy clusters. SPEX is one of these spectral modeling, fitting and analysis software packages. SPEX has been recently updated to v3.0 driven by the high-resolution observation requirements expected by the *Hitomi* and future missions, *XRISM* and *Athena*. The major improvements have been focused on the update of the radiative processes such as radiative recombination, collisional ionization, charge exchange or photoionization and the incorporation of a large number of emission and transition lines.

This thesis focuses on the X-ray analysis of merging galaxy clusters and the plasma

code development for future high-resolution X-ray spectroscopic observations. This work is devoted to a better understanding of two concrete aspect of these merging clusters: one, the correlation between the thermal (X-ray) and the non-thermal (radio) components, and two, their metal enrichment history. The first issue can reveal the physical association between the X-ray and radio components. The second one can seed light on the dynamical history of the mergers and their role in the metal enrichment of the clusters.

In Chapter 2, we show the X-ray study of the merging galaxy cluster Abell 3376 observed with *Suzaku*. We study the spatial distribution of the thermal component of the ICM including the cluster outskirts. For this purpose, we obtain the temperature distribution in four different radial directions (west, east, north and south). We compare these distributions with the universal profile of relaxed clusters and we find a deviation for all the directions except for the south, suggesting the possible presence of shocks. However, we only find evidence of two shocks at west and east. One is associated to the western radio relic with $\mathcal{M} \sim 2.8$ and the other to the eastern 'notch' with a $\mathcal{M} \sim 1.5$. We detect as well a cold front at the east of the X-ray emission peak. The Mach number of the eastern shock is consistent with previous radio observations, while the western radio relic present a slightly lower one, probably due to radio ageing effects. Finally we investigate the merger scenario, which suggests a merger close to the plane of the sky with a dynamical age of $\sim$0.6 Gyr after core passage.

In Chapter 3, we investigate the thermodynamical properties of the hot plasma across the merging galaxy cluster Abell 3365 using *XMM-Newton* observations. For this purpose, first, we search for X-ray surface brightness and temperature discontinuities at the clusters outskirts and central ICM edges. Second, we obtain the temperature, Fe abundance and pseudo-entropy distributions along the merging axis in the central bright region. We find two strong shocks ($\mathcal{M} > 3$) associated to the eastern radio relic and western candidate relic and one cold front at the west of the X-ray emission peak. The shock acceleration efficiency at the eastern relic is consistent with the DSA mechanism, suggesting that this is a favorable scenario for shocks with $\mathcal{M} > 3$. The abundance distribution presents signatures of two peaks with a value of $\sim$0.6 $Z_{\odot}$. One corresponds to the location of the main subcluster and the other one is displaced from the X-ray emission peak towards the cold front. We also find a low entropy minimum, which suggests that the progenitor cool-core can partially or totally survived to the merging activity.

In Chapter 4, we present an X-ray spectral analysis of six merging galaxy clusters (CIZA J2242.8+5301, 1RXS J0603.3+4214, Abell 3376, Abell 3667, Abell 665 and Abell 2256) observed with *XMM-Newton*. We obtain the temperature, Fe abundance and pseudo-entropy distributions along the merging axis up to r_{500}. We derive the averaged Fe profile, which presents a moderate central peak, lower than relaxed clusters, followed by a smooth flattening up to a uniform value of $\sim$0.2–0.3 $Z_{\odot}$ at large radii. Moreover, the pseudo-entropy distributions suggest that in some cases the relative low entropy core can survive to major mergers. We also study the correlation between Fe abundance and pseudo-entropy. We find a mild correlation in the central regions, probably due to the merging activity and the spread out of the metals. However, there is no evidence of correlation at large radii, in the cluster outskirts. This result together with the abundance uniformity seems to suggest an additional evidence in favor of the pre-enrichment scenario.

Lastly, in Chapter 5, we update with 45 new data sets the single ionization cross sections for ions from H to Zn, taking into account the new theoretical calculations and laboratory measurements. The cross sections of the rest of the ions with no data sets, are interpolated or extrapolated. We are able to obtain not only the total, but all the inner shells cross sections for the first time. These cross sections include two different radiative processes: the Direct Ionization (DI) and Excitation-Autoionization (EA). We model and fit the DI and EA processes using an extension of Younger's and Mewe's equations to obtain the DI and EA coefficients. We derive the subshell ionization rate coefficients applying the integral to a Maxwellian velocity distribution of these equations. Finally, we incorporate the DI, EA and ionization rate coefficients to the new version of SPEX v3.0.

Resumen

Los cúmulos de galaxias son los mayores objetos virializados en el Universo, compuestos de centenares a miles de galaxias. Estas galaxias están rodeadas de un plasma caliente ionizado conocido como medio intracumular (ICM) y es observado en rayos-X. Las galaxias constituyen sólo un $\sim$5% de la masa total del cúmulo, mientras que el ICM el $\sim$15%. El resto de la masa, $\sim$80%, está dominada por la materia oscura. Los cúmulos de galaxias pueden observarse en diferentes longitudes de onda, aunque las más relevantes para este estudio son las asociadas al espectro visible, rayos-X y radio (ver Fig. A). Las observaciones en el óptico proporcionan información sobre las galaxias individuales y su sobredensidad a distancias similares. Las propiedades espectrales (tales como la temperatura, densidad o abundancia) pueden derivarse en rayos-X. Por otra parte, las observaciones en radio muestran objetos radio discretos y extensos, trazan los rayos cósmicos y la aceleración de partículas energéticas. Los cúmulos de galaxias se clasifican en diferentes grupos basados en su estado dinámico: cúmulos relajados o 'cool-core' (CC), cúmulos distorsionados o 'non-cool-core' (NCC) y cúmulos extremádamente distorsionados o cúmulo de galaxias en colisión .

Los cúmulos de galaxias crecen jerárquicamente via acreción o colisión de grupos o subcúmulos menos masivos. La colisión de cúmulos es el evento más energético en el Universo desde el Big Bang. Turbulencias, ondas de choque y frentes fríos emergen en el ICM como resultado de una fuerte colisión . Las ondas de choque son estructuras de gran escala que se propagan desde el centro a la periferia de los cúmulos, donde normalmente se observan. Pueden ser detectados por discontinuidades en la temperatura y la densidad en el ICM a través del análisis espectral y la detección de saltos en el brillo superficial, respectivamente. Se cree que estas ondas de choque (con un número de Mach $\mathcal{M} \leq 3$–5) (re)aceleran electrones, en presencia de un campo magnético amplificado, vía el mecanismo de Fermi de primer orden, la aceleración difusa de onda de choque (DSA). Hoy en día han sido propuestos nuevos mecanismos de aceleración como la re-aceleración de rayos cósmicos preexistentes, entre otros. Estas partículas relativistas pueden producir emisión sincrotrón formando estructuras alargadas, polarizadas y de espectro inclinado o 'steep-spectrum', conocidos como 'radio relics'. En algunos cúmulos esta emisión en radio ('radio relics') aparece asociada a una emisión en rayos-X (ondas de choque en rayos-X).

Figure A: Imagen compuesta (óptico, rayos-X en naranja y radio en azul) del cúmulo de galaxias Abell 3376. Créditos: Rayos-X (NASA/CXC/SAO/A. Vikhlinin; ROSAT), Óptico (DSS), Radio (NSF/NRAO/VLA/IUCAA/J. Bagchi).

El ICM de los cúmulos de galaxias son ricos en metales que se originan principalmente de las supernovas de colapso gravitatorio (SNcc), supernovas de tipo Ia (SNIa) y estrellas de baja masa de la rama asintótica gigante (AGB). Las SNcc liberan metales ligeros (O, Ne, Mg, Si and S), mientras que los metales pesados son expulsados por las SNIa. La principal contribución de C y N proviene de las AGB. Una vez que los metales son depositados en el ICM, éstos son posteriormente transportados, mezclados y redistribuidos. En los últimos años, la distribución radial de la abundancia (Fe) de los cúmulos relajados y distorsionados ha sido analizada extensamente. Sin embargo, pocos estudios se han centrado en los cúmulos de galaxias en colisión. Una mayor comprensión de la distribución de metales a lo largo del eje de colisión podría revelar la evolución química de estas estructuras de gran escala. La distribución radial del Fe en los cúmulos relajados presenta un gran pico central rico en metales comparado con los cúmulos distorsionados. Este pico disminuye a radios lejanos hasta alcanzar un valor uniforme cercano a $\sim$0.2–0.3 $Z_{\odot}$. Este mismo comportamiento puede observarse en los cúmulos distorsionados, lo que indicaría un enriquecimiento temprano del ICM ($z \sim 2$–3).

La espectroscopía de rayos-X es una herramienta útil para determinar las propiedades termodinámicas y químicas del ICM mencionadas anteriormente. Por esta razón los códigos espectrales de gran precisión son completamente necesarios para modelar y ajustar los espectros de cúmulos de galaxias en rayos-X. SPEX es uno de los programas utilizados

para el modelado, ajuste y análisis de espectros. SPEX ha sido recientemente actualizado a v3.0 debido a los requisitos de las observaciones de alta resolución esperadas por el satélite *Hitomi* y las futuras misiones, *XRISM* y *Athena*. Las mejoras de la nueva versión se han centrado en la actualización de los procesos radiativos como la recombinación radiativa, la ionización colisional, intercambio de carga y la fotoionización, y la incorporación de un extenso número de líneas de emisión y transición.

Esta tesis se centra en el análisis espectral de cúmulo de galaxias en colisión y el desarrollo de un código para futuras observaciones espectroscópicas de rayos-X de alta resolución. Este trabajo está dedicado a una mejor comprensión de dos aspectos concretos de estos cúmulos en colisión: uno, la correlación entre la componente térmica (rayos-X) y la no-térmica (radio), y dos, su historia sobre el enriquecimiento de metales. El primer tema puede revelar la asociación física de las componentes de rayos-X y radio. El segundo puede arrojar luz sobre la historia dinámica de las colisiones y su papel en el enriquecimiento en metales de los cúmulos.

En el Capítulo 2, mostramos el estudio en rayos X del cúmulo de galaxias en colisión Abell 3376 observado con *Suzaku*. Estudiamos la distribución espacial de la componente térmica del ICM incluyendo la periferia de los cúmulos. Para este propósito obtenemos la distribición de la temperatura en cuatro direcciones radiales (norte, sur, este y oeste). Comparamos estas distribuciones con el perfil universal para cúmulos relajados y encontramos una desviación para todas las direcciones excepto para el sur, sugiriendo la posible presencia de ondas de choque en esas direcciones. Sin embargo, sólo encontramos evidencias de dos ondas de choque al oeste y este. Una está asociada al 'radio relic' del oeste con un $\mathcal{M} \sim 2.8$ y la otra al 'notch' del este con un $\mathcal{M} \sim 1.5$. Detectamos además un frente frío al este del pico de emisión de rayos-X. El número de Mach de la onda de choque del este es consistente con las observaciones de radio previas, mientras que el 'radio relic' del oeste presenta un número de Mach ligéramente inferior, probablemente debido a los efectos de envejecimiento. Finalmente, estimamos el escenario de la colisión, el cuál sugiere una colisión cerca del plano del cielo con una edad dinámica de $\sim$0.6 Gyr después de cruzar el núcleo del subcúmulo principal.

En el Capítulo 3, investigamos las propiedades termodinámicas del plasma caliente en el cúmulo de galaxias en colisión Abell 3365 usando observaciones de *XMM-Newton*. Para este propósito, en primer lugar, buscamos discontinuidades en el brillo superficial y temperatura en las regiones periféricas y centrales del ICM. En segundo lugar, obtenemos las distribuciones de temperatura, abundancia (Fe) y pseudo-entropía a lo largo del eje de colisión en la region central. Encontramos dos ondas de choque prominentes ($\mathcal{M} > 3$) asociadas al 'radio relic' del este y al candidato de 'radio relic' del oeste además de un frente frío al oeste del pico de emisión de rayos-X. La eficiencia de aceleración de la onda de choque en el 'radio relic' del este es consistente con el mecanismo DSA, sugiriendo que es un escenario favorable para ondas de choque con $\mathcal{M} > 3$. La distribución de abundancia presenta signos de dos picos de valor $\sim$0.6 $Z_{\odot}$. Uno corresponde con la localización del subcúmulo principal y el otro está desplazado del pico de emisión hacia el frente frío. Además encontramos un mínimo de entropía que sugiere que el núcleo o 'cool-core' del cúmulo progenitor ha sobrevivido partial o totalmente a la colisión.

En el Capítulo 4, presentamos el análisis espectral en rayos-X de seis cúmulos de

galaxias en colisión (CIZA J2242.8+5301, 1RXS J0603.3+4214, Abell 3376, Abell 3667, Abell 665 and Abell 2256) observados con *XMM-Newton*. Obtenemos las distribuciones de temperatura, abundancia (Fe) y pseudo-entropía a lo largo del eje de choque hasta r_{500}. De estas distribuciones derivamos el perfil promedio de Fe que presenta un pico moderado central, menor que los cúmulos relajados, seguido de una disminución hasta un valor uniforme de $\sim$0.2–0.3 $Z_{\odot}$ para radios lejanos. Además, las distribuciones de pseudo-entropía sugieren que en algunos casos el núcleo de baja entropía relativa puede sobrevivir a colisiones mayores. También estudiamos la correlación entre la abundancia y la pseudo-entropía. Encontramos que existe una leve correlación para las regiones centrales, probablemente debido a que la actividad de la colisión esparce los metales. Sin embargo, no hay evidencias de ninguna correlación a radios lejanos, en la periferia de los cúmulos. Este resultado junto con la uniformidad de la abundancia parece aportar una evidencia adicional en favor del escenario de enriquecimiento temprano.

Por último, en el Capítulo 5, actualizamos las secciones cruzadas de ionización para iones desde H a Zn con 45 nuevas bases de datos, teniendo en cuenta los nuevos cálculos teóricos y nuevas medidas de laboratorio. Las secciones cruzada del resto de iones que no tengan una base de datos han sido interpoladas o extrapoladas. En este estudio somos capaces de obtener por primera vez no sólo la sección total, sino la sección de cada celda interna. Estas secciones cruzadas incluyen dos procesos radiativos diferentes: la Ionización Directa (DI) y la Excitación-Autoionización (EA). Modelamos y ajustamos estos procesos de DI y EA con las ecuaciones extendidas de Younger y Mewe, respectivamente, para obtener los coeficientes de ajuste. Derivamos los coeficientes del ratio de ionización aplicando la integral a la distribución de velocidades Maxwelliana de estas ecuaciones. Finalmente, hemos incorporado los coeficientes de DI, EA y el ratio de ionización a SPEX v3.0.

Publications

First-author articles

1. **Urdampilleta, I.**, Kaastra, J. S., & Mehdipour, M., 2017.
   A&A, 601, A85. (**Chapter 5**)
   X-ray emission from thin plasmas. Collisional ionization for atoms and ions of H to Zn
2. **Urdampilleta, I.**, Akamatsu H., Mernier, F., Kaastra, J. S., de Plaa, J., Ohashi, T., Ishisaki, Y., & Kawahara, H., 2018.
   A&A, 618, A74. (**Chapter 2**)
   X-ray study of the double radio relic Abell 3376 with Suzaku
3. **Urdampilleta, I.**, Mernier, F., Simionescu, A., Kaastra, J. S., de Plaa, J., Kara, S. & Ercan, E. N., 2019.
   A&A, 629, A31. (**Chapter 4**)
   Iron abundance distribution in the hot gas of merging galaxy clusters
4. **Urdampilleta, I.**, Simionescu, A., Kaastra, J. S., Zhang, X., Di Gennaro, G., Mernier, F., de Plaa, J., &, Brunetti, G., 2019.
   To be submitted to A&A. (**Chapter 3**)
   X-ray study of Abell 3365 with XMM-Newton

Co-authored articles

1. Liyi, G., Akamatsu, H., Shimwell, T. W., Intema, H. T., van Weeren, J. R., de Gasperin, F., Mernier, F., Mao, J., **Urdampilleta, I.**, de Plaa, J., Parekh, V., Röttgering, H. J. A. & Kaastra, J. K., 2019.
   Nature Astronomy.
   Observational Evidence for a Pre-Merger Shock in Colliding Clusters of Galaxies
2. Mernier, F., Werner, N., de Plaa, J., Kaastra, J. S., Raassen, A. J. J., Gu, L., Mao, J., **Urdampilleta, I.**, & Simionescu, A., 2018.
   MNRAS, 480 L95.

Solar chemical composition in the hot gas of cool-core ellipticals, groups, and clusters of galaxies

3. Mernier, F., de Plaa, J., Werner, N., Kaastra, J. S., Raassen, A. J. J., Gu, L., Mao, J., **Urdampilleta, I.**, Truong, N., & Simionescu, A., 2018.
MNRAS, 478 L116.
Mass-invariance of the iron enrichment in the hot haloes of massive ellipticals, groups, and clusters of galaxies
4. Kaastra, J. S., Gu, L., Mao, J., Mehdipour, M., Mernier, F., de Plaa, J., Raassen, A. J. J., , & **Urdampilleta, I.**, 2017.
Journal of Instrumentation, 12, C08008.
Science with hot astrophysical plasmas
5. Akamatsu H., Gu, L., Shimwell, T. W., Mernier, F., Mao, J., **Urdampilleta, I.**, de Plaa, J., Röttgering, H. J. A. , & Kaastra, J. S, 2016.
A&A, 593, L7
Suzaku and XMM-Newton observations of the newly discovered early-stage cluster merger of 1E2216.0-0401 and 1E2215.7-0404

Additional articles

1. Ruiz, M., **Urdampilleta, I.**, Bombardelli, C., Ahedo, E., Merino, M., Cichocki, F. , 2014.
Proceeding of Space Propulsion Conference 2014
The FP7 LEOSWEEP project: Improving low earth orbit security with enhanced electric propulsion
2. Ruiz, M., **Urdampilleta, I.**, del Cura, J. M., Ahedo, E., Navarro-Cavallé, J., 2013.
Proceeding of 33$^{\mathrm{rd}}$ International Electric Propulsion Conference 2013, IEPC-2013-273
Space Missions potentially benefit or enabled by prospective use of Helicon Plasma Thrusters
3. **Urdampilleta, I.**, Prieto-Ballesteros, O., Rebolo, R., Sancho, J., 2012.
Proceeding of European Planetary Science Congress 2012, EPSC2012-64
TALISE: Titan Lake In-situ Sampling Propelled Explorer
4. Fuente, I., Ruiz, M., Gutirérrez, J., **Urdampilleta, I.**, Del Campo, D., Nieto, S., 2004.
Proceeding of 55$^{\mathrm{th}}$ International Astronautical Congress 2004, IAC.04-P.Q.12
LMG: A Multi-scenario Sample Return Mission to Mars
5. Anton, A., Carretero, D., Gutiérrez, J., **Urdampilleta, I.**, 2004.
Proceeding of 55$^{\mathrm{th}}$ International Astronautical Congress 2004, IAC.04-J.6.09
Vibration Isolation in Microgravity Environments
6. Gutiérrez, J., Cuadra, D., Flores, C., Fernández, P., Fuente, I., Martín, S., Meije, R., Pérez, M., Ruiz, M., Sabín, M., Torres, R., **Urdampilleta, I.**, Yarza, A., 2003.
Proceeding of 54$^{\mathrm{th}}$ International Astronautical Congress 2003, IAC.03-W.P.01
Tethered inherently safe re-entry capsule

Curriculum Vitae

I was born on 20 August 1981, in San Sebastian (Gipuzkoa), Spain. I attended the High School in the same city, I. E. S. Jose María Usandizaga, where I obtained the International Baccalaureate (IB) Diploma. In 1999, I moved to Madrid to study Aerospace Engineering in the School of Aeronautical and Space Engineering (ETSIA), Universidad Politécnica de Madrid, at that time the only university of Spain offering this degree. I graduated in November 2006 with a thesis on an Earth Observation Satellite project.

During my university period, I participated actively in different programs offered by the European Space Agency (ESA) Education Office. In 2002, I was granted to attend the World Space Congress in Houston (US), an event only happening every 10 years, where COSPAR and the 53th International Astronautical Congress (IAC) took place together for two weeks. The same year, I also participated in the reentry capsule design, YES 2 (Young Engineering Satellite), as part of the ETSIA team. In 2003, I was finalist in the 1st Aurora Design Contest with a multi-landing Mars Sample Return mission called LMG (Little Martian Grasshopper). This year I was also granted to attend the 54th IAC in Bremen (Germany). In 2004, I was selected to participate in the 7th Parabolic Flight Campaign with the experiment VMD (Microvibration Measurements Device).

In addition to all these space related activities, in 2003 I attended a summer course in Patras (Greece) organized by the student association BEST (Board of European Students of Technology). After this experience, I decided to join them in the Madrid local group, where I was an active member from 2003 to 2006. I participated in the organization of the summer courses in 2004 and 2005, being one of the main organizers in 2005. I also was part of the Board as the treasurer in the course 2004-2005. Thanks to BEST I travelled around Europe to attend different engineering and technology courses at the University of Patras, L'École Polytechnique of Paris and Tallinn University of Technology.

In December 2006 I started to work at INTA (National Institute of Aerospace Technology) in the helicopters airworthiness department with Angel Centenera and Alfonso Barrado. In June 2007 I moved to GMV as Mission Analysis specialist. There I worked on the phase 0 study of the 7th Earth Explorers of ESA (TRAQ, Biomass, FLEX, CoreH2O, Premier y A-Scope) together with Fernando Alemán and Javier Atapuerca in the Earth Observation group.

At the end of 2007 I was selected by the Education Ministry to participate in the International Organizations grant. For this reason, in May 2008, I joined the Earth Observation Programme Future Mission Division, at ESA-ESTEC (The Netherlands) under the supervision of Miguel Aguirre and Luca Massotti. In this period my labour was focused on the development of an AOCS (Attitude and Orbital Control Subsystem) Simulator for Geostationary satellites (Meteosat Third Generation and GEO-Oculus), which would be integrated into the INR (Image and Navigation Registration) end-to-end simulator. Afterwards, I carried out the feasibility study and the preliminary design of the C-band Bistatic InSAR (Synthetic Aperture Radar) Concept for Coastal Current Estimation.

In September 2009 I came back to Madrid to the Aerospace Division at the engineering company SENER. During five years I was involved in many different projects such as validation and documentation of AOCS simulator under the supervision of Lorenzo Tarabini, preparation of Proba 3 Ground Demonstration to be carried out in JPL working with Antonio Ayuso, development of Solar Orbiter and Interplanetary Mission Simulator together with Guillermo Rodríguez, and development of a Mission Analysis Tool for 3MI instrument on board of Metop-SG satellite, project led by Jaime Sanchez Paramo, among others.

During 2010, I participated as Project Manager and System Engineer in the space project known as Future Science Mission Analysis, in collaboration with the Spanish Astrobiology Center, CAB. This project was initiated by Juan Manuel del Cura and I could work closely with CAB scientists as Miguel Mass-Hesse on the conceptual design of a Far Infrared Interferometer Mission, and Olga Prieto-Ballesteros on a Titan lakes Exploration Mission. From this last project we came out, together with Rafael Rebolo and Jaime Sancho, with a conceptual design of a Titan lakes zodiac called TALISE (Titan Lake In-situ Sampling Propelled Explorer).

In 2011, I collaborated on the Vega ISVV (Independent Software Verification and Validation) project led by Alfonso López as GNC (Guidance, Navigation and Control) specialist. In 2012, I supported the HPT (Helicon Plasma Thruster) project led by Mercedes Ruiz as Mission Analysis specialist and I joined the System Engineering Team of PROBA-3 with José María Fernández. During my last year in SENER, 2013–2014, I worked as System Engineer of the LEOSWEEP (Improving Low Earth Orbit Security With Entranced Electric Propulsion) project managed by Mercedes Ruiz.

Encouraged by my experience working with scientists of CAB in 2011, I decided to start the Master's Degree in Astrophysics at the Universidad Complutense de Madrid, UCM. During the course 2011-2012 I attended some courses of the master. I restarted the classes again in September 2013, finishing the master in 2014 with a Master Thesis focused on the Observation and Analysis of Geomagnetic Field Effects on the Imaging Technique of Very High Energy Gamma-Rays with MAGIC Telescope, under the supervision of Emiliano Carmona.

In 2014 I started my PhD with Jelle Kaastra in SRON (Utrecht) and Leiden Observatory centered on *X-ray spectroscopy of merging galaxy clusters*. In my first project, I updated the plasma code SPEX, concretely the Collisional Ionization model, as part of the SPEX development team. Our duties were focused on preparing SRON plasma code for the upcoming observations from *Hitomi* satellite. For this reason, as part of this activity, in 2015 I attended a JP/NL bilateral workshop in Tokyo (Japan), the AtomDB workshop and

The Universe in High-Resolution X-ray Spectra conference in Boston (US). During my second project, I worked with Hiroki Akamatsu on the merging galaxy cluster Abell 3376. I presented the results of this study at SEA (Spanish Astronomy Society) Scientific Meeting 2016 in Bilbao (Spain), The X-ray Universe conference in Rome (Italy), Diffusive Synchrotron Emission in Clusters of Galaxies-What?s Next? workshop in Leiden (The Netherlands) and SnowCluster in Utah (US). In the third project I performed together with François Mernier the study of iron abundance distribution of six merging galaxy clusters. It has been recently presented in the astrophysics of hot plasma in extended X-ray sources conference in Madrid (Spain). The last project is devoted to the X-ray study of the merging galaxy cluster Abell 3365 using *XMM-Newton* observations and I worked under supervision of Aurora Simionescu. From December 2019 I will start working in the Space Surveillance and Tracking (SST) program of the European Commission in the CDTI (Centre for the Development of Industrial Technology) as Aerospace Engineer.

Acknowledgements

Life is a grand adventure that we live day by day. Only those ones that decide to take a risk can live it intensively, although it means to have good and bad moments along the way. For this reason, some years ago I decided to come back to the Netherlands to start a new adventure of doing a PhD on Astrophysics. This wouldn't be possible without the unconditional support of my beloved travel mate, David. He decided to follow me and live this adventure together. He has made the way easier, being close to me in all the moments, giving me strength to continue and finish it. Thank you very much my love. Two years ago a new traveler joined us, Shiva, my sweetie cat. I don't know what I would have done without her and her furry hugs.

This adventure wouldn't have started without Jelle Kaastra and Jelle de Plaa. Thank you for giving me the opportunity of beginning this PhD at SRON and knowing better the scientific part of the space missions. I have learned a lot from you and my stay at SRON. Thanks as well for all your support not only in the professional but also in the personal aspects during all these years. I thank Hiroki for introducing me in the amazing world of the merging galaxy clusters. I have enjoyed a lot working in this topic and being part of a great scientific community. I couldn't be more grateful with Francois, you have done things easy and straightforward, you have trusted on me and given the motivation I needed to finish the PhD. Finally, Aurora thanks for your help in the fourth paper and your useful advices. I thank as well the Top Grant of NWO for the financial support.

In SRON I had the opportunity to be part of the SPEX Team (Jelle Kaastra, Jelle de Plaa, Ton, Liyi, Junjie and Misssagh). Thanks for the atomic physics meetings, specially to Ton for teaching me new vocabulary like triplet, quatruplet and all the possible transitions. Thanks to Junjie and Francois for helping me during the PhD and being part of the nice group of galaxy clusters. I am very grateful to my officemates Manuel, Carlo and Aurora, we had interesting conversations and shared great moments. Carlo, you know that since you left I missed you a lot, your happiness everyday, always with a smile. In SRON I could also meet some exceptional scientists, which have inspired and motivated me, thanks to Elisa, Margherita, Laura, Marianne, Catia, Sascha, Kristhell, Francesca, Zuzanna, Aurora and Ioanna. Elisa, thank you so much for being there and for your motivation. Catia, I am so glad that our paths crossed at SRON, thanks for listening, for the good advices and for always

encouraging me. Sascha, thanks for all the good moments shared together, all the nice conversations in the car and it was an honor to be your paranymph. Kristhell, I won't never forget your consolation and support, thank you very much for listening to me always when I needed. And I can't forget as well the Italian troop always with a smile, willing to delight with a funny conversation and a good coffee, thanks Daniele, Davide and Giacomo. I would like to thanks also to everyone who has made so pleasant my stay at SRON as Cor, Lucien, Jean, Theo, Peter, Lydia, Xiaoyuan, Patrick, Deepak, Katy, Jeroen, Jan-Willem, Esther and Frank.

Thanks to the wonderful colleagues and friends I met at the Leiden observatory, who have shared this PhD with me. Thanks to all the officemates of 1105 (Gabi, Ele, Mieke, Aayush, Marcelo, Christos, Tommaso, Mher and MJ) and after 571 (Gabriella and MJ), for making me feel one more in spite of going there only once per week. Thanks to the galaxy clusters group (Emma, Andra, Jit, Francesco, Gabriella, Tim, Reinout, Andrea, Duy, Huib, Julius, Fabio, Michael, Martijn and Huub) for such an interesting discussions and meetings along these years, where I could learn so much. Many thanks for all the moments, lunch and parties together, apart from all mentioned before to Kim, Maria Cristina, Valerya, Freeze, Andrej, Turgay, Josh, Matus, Xabier, Marco, Daniel, Mattia and Leah. Gabi, I met you already in the PhD interviews and since then you have been a key person in the observatory. Thank you so much for listening and share experiences with me. Mieke, in the last year you have helped me a lot to cope with the end and I thank so much your support. And I couldn't miss the group of latino/hispanos, with whom I could share so many conversations in Spanish and parties where we could dance with good music, thanks for making me feel a bit closer from home (Santiago, Francisca, Heather, Pedro, Pablo, Javi, Cristina, Liz, Yanett, Carmen and Álvaro). Finally, a huge thank you to Xander for his enormous labor, which has made possible that today I can write these lines. Thanks for guiding me until the end and don't letting me to give up.

I couldn't either finish this PhD without the support of my astro girls (Laura, Alba, Belén and Maider). Thanks, you are awesome. Each of us in a different place of Europe doing our own PhD, we have shared the experiences and difficulties. You are great scientists and an example to follow, we did it! Héctor, who undoubtedly has shared the experiences of this PhD as well. Thank you very much for being always available to talk and listen even the silliest thing in spite of being to the other side of the world. Thanks for helping me especially in the beginning of the PhD.

And I wouldn't arrive to this PhD without the support of my SENER colleagues, thanks to all, thanks to JR, Juanma and Mertxe, who encouraged me to start the Master on Astrophysics and allowed me to combine it with the work. I want to thank especially the Comité de Jóvenes Imberbes (Dani, Patri, Marta and Yolanda) for all the special moments in SENER and thanks to them I could survive the last year there. I would like to thank too all my master colleagues and all great professors (África, Pablo, Armando, José Antonio, David, Gorgas, Jaime, Jesús, Nicolás, Juan Abel and María José). I deeply enjoyed your classes, in spite of the big effort I had to make to combine them with my job. You achieved that everyday I wanted to attend the classes and continued still learning.

This journey wouldn't be the same without all the people, who has been with me in the Netherlands outside the PhD environment. Starting from Inés, Celia and Elena, who has

been always there for absolutely everything since we met the first time in 2008, I would be deeply grateful forever. And of course, thanks to eazie al sol group (Gaba, Carol, Jesús Hidalgo, Jesús, Ana, Jonathan and César) for all the eazies, lunchs and dinners together, trips in Panecuquen I and patxaranes. This experience without all of you wouldn't be the same. A massive thank you to my choir, Singlarísimo, thanks to each of one: David, Marta, Alicia, Ana Collado, Ana, Monika, Robert, Álvaro, Xavi, Montse, Agustín, Eva, Víctor, Inés, Begoña, Suzanne, Ramón and Germán. You made me really happy every Saturday with our rehearsals, surrounded by nice music and a better wine. I want to thank my football teams Lugdunum and Wonderbrains (Irene, Alicia, Nerea, Eli, Miri, Inés Alonso, Inés, Celia, Maria, Kim, Cristina, Ana and Ann-Marie). Thanks for all the great moments, matches and derbies, specially against Dream Team and ESOC. I would like to thank as well to my yoga studio, especially to my teachers Santa, Nancy, Jerry and Robinson, for teaching me to enjoy the yoga and show me my safe place in the studio. Thanks to Marieke and Yoga per tutti for your wonderful classes and give me so much peace. Thanks to Borja and Francis, for all the evenings of dinner and cinema. Thanks to Franchu and Tami for the great dinners at your place. Thanks to ESA people Pedro, Isa, Susana, Jonan, Judith, Berta, Xevi, Ana Laura, Laura, Gonzalo and Bernardo. And finally I would like to thank Adriaan Goslinga, for making things much easier and helping us as much as you could.

And what I can say of my dear kukis (Coro, Laura, Elena, Ester and Tina). You are the best, you have been there supporting and encouraging me till the end, without doubting that I could make it. Thank you very much! You have achieved that every time I come back home I feel that the time would haven't passed. You have managed that all the Christmas and parties have been memorable. Coro, you know that you are special for me, mi oldest friend since my childhood, you have been always by my side despite of the distance. You have worried to send me everyday a "how are you doing?" that made me feel you so close. I cannot express my gratitude. I love you fea!

Thank you so much for all the people who have been close despite of the distance. Thanks to Ainara, Laura, Izas, Mertxe, Marta, Paula and Szil, a group of courageous women, who inspires me, gives me strength and I am so proud of having as friends. Thanks to the supernenas, Irenne and MC, all the time there despite of the years. Thanks to Nacho and Mario for being so authentic, don't change never. Thanks to those in the neighborhood (Lore, David, Iñaki, Emi, Sanza, Marina, Lucía, Javi. Manila and Carlos), continuously in good mood. Thanks to Fernando, Ana, Claudia, Bea, Carmen, Celia, Rául, Óscar and Carlos. To finish, thank you very much Edurne for the last year and a half. Thanks for teaching me to think in the present moment, to prioritize and relativize all the situations. This thesis wouldn't have an end without your help.

Lastly, I would like to thank my family for their unconditional support. Starting with my parents, they have been an example of fight and perseverance. Even don't having an easy life, they have done everything for giving me a better future. To my mom, she knows that I am very grateful, because without her support and determination I wouldn't have never gone to study to Madrid and I wouldn't be the person I am today. Mila esker ama! To my brother Martin, thanks for your support and comprehension, I know that eventually you feel proud of your sister. To Marta, I am glad that you have joined to the family, thanks for your happiness and positivity. Thanks to my brother and sister in law and family, Juan Pablo,

Bea, Sergio and Marta, for showing me everyday that I can count on you. Thanks to Mari Jose and Txomin, rest in peace, I am glad that we recovered the contact some years ago. Finally, thanks a lot to my cousins Asier, Garbiñe, Izarne, Gari, Amets and Mikel. We should always see the beautiful side of life and you were the special present, which came from the goodbye to Txomin. I am so happy that we are again in contact and I hope it will be for a lot of years.

Agradecimientos

La vida es una gran aventura que vivimos día a día. Sólo aquellos que deciden arriesgarse pueden vivirla intensamente, aunque eso suponga tener buenos y malos momentos por el camino. Por esa misma razón, ya hace unos años, decidí volver a los Países Bajos y embarcarme en la nueva aventura de hacer un doctorado en astrofísica. Esta no hubiera sido posible sin el apoyo incondicional de mi querido compañero de viaje, David. Él decidió seguirme, venir aquí y vivir esta aventura junto a mí. Ha hecho que todo el camino sea mucho más fácil, estando a mí lado en todos los momentos, dándome fuerzas para seguir adelante y poder terminarlo. Muchas gracias mi vida. Hace dos años también se unió una nueva viajera, Shiva, mi preciosa gata. No sé que hubiera hecho sin ella y sin esos achuchones peludos que me han ayudado tanto.

Esta aventura no hubiera comenzado sin Jelle Kaastra y Jelle de Plaa. Gracias por darme la oportunidad de empezar este doctorado en SRON y conocer de cerca la parte científica de las misiones espaciales. He aprendido mucho de vosotros y de mi estancia en SRON. Gracias además por vuestro apoyo y compresión no sólo en lo profesional si no también en lo personal durante estos años. Gracias a Hiroki por introducirme en el apasionado mundo de los choques de cúmulos de galaxias. He disfrutado mucho trabajando en este tema y siendo parte de una gran comunidad. Estoy enormemente agradecida a Francois, has hecho que las cosas sean fáciles y directas, has confiado en mí y me has dado la motivación que me hacía falta para poder terminar este doctorado. Estaré siempre en deuda contigo. Por último, gracias Aurora por haberme ayudado en el cuarto proyecto, darme buenos consejos y saber guiarme para poder sacarlo adelante. Gracias además al Top Grant de NWO por el apoyo en la parte financiera.

En SRON he tenido la oportunidad de formar parte del SPEX Team (Jelle Kaastra, Jelle de Plaa, Ton, Liyi, Junjie, Misssagh). Gracias por esas reuniones sobre física atómica, especialmente a Ton por enseñarme el uso de nuevas palabras como triplet, quadruplet, o todas las posibles transiciones. Gracias a Junjie y Francois por acompañarme y ayudarme en este doctorado, me ha alegrado mucho haber compartido nuestro tiempo juntos como parte del grupo de cúmulo de galaxias. Quiero agradecer a mis compañeros de despacho Manuel, Carlo y Aurora, con los que he tenido grandes conversaciones y he compartido muy buenos momentos. Carlo, ya sabes que desde te fuiste he echado de menos esa gran

alegría que me transmitías todos los días, siempre te tendré presente. En SRON también he tenido la oportunidad de conocer a científicas excepcionales que me han servido de inspiración y motivación, y por ello quiero dar las gracias a Elisa, Margherita, Laura, Marianne, Catia, Sascha, Kristhell, Francesca, Zuzanna, Aurora y Ioanna. Elisa, muchas gracias por estar siempre ahí, por tu motivación y creer en mí. Catia, me alegro mucho de que nuestros caminos se cruzaran, gracias por escucharme, por tus buenos consejos, y siempre darme mucho ánimos. Sascha, gracias por todos los momentos vividos juntas, esas conversaciones en los trayectos de coche y fue un honor ser tu paraninfo. Kristhell, nunca voy a olvidar tu consuelo y apoyo, muchas gracias por escucharme siempre que lo he necesitado. Cómo olvidarme además de la tropa italiana siempre con la sonrisa puesta, dispuestos a deleitarnos con un divertida conversación y un buen café, gracias Danielle, Davide y Giacomo. También quiero agradecer a todos los que habéis hecho mi estancia en SRON más agradable como Cor, Lucien, Jean, Theo, Peter, Lydia, Xiaoyuan, Patrick, Deepak, Katy, Lydia, Jeroen, Jan-Willem, Esther y Frank.

Gracias a todos mis compañeros y amigos del observatorio de Leiden que han compartido este doctorado conmigo. Gracias a todos aquellos que han pasado por la oficina 1105 (Gabi, Ele, Mieke, Aayush, Marcelo, Christos, Tommaso, Mher y MJ) y después por la oficina 571 (Gabriella y MJ) por haberme hecho sentir una más a pesar de sólo ir una vez por semana. Gracias al grupo de cúmulo de galaxias (Emma, Andra, Jit, Francesco, Gabriella, Tim, Reinout, Andrea, Duy, Huib, Julius, Fabio, Michael, Martijn y Huub) por las discusiones y reuniones tan interesantes que hemos tenido a lo largo de estos años, de los que he podido aprender muchísimo. Gracias por todos los momentos, comidas y fiestas compartidas por la gente del observatorio además de los ya mencionados (Kim, Maria Cristina, Valerya, Freeze, Andrej, Turgay, Josh, Matus, Xabier, Marco, Daniel, Mattia y Leah). Gabi, te conocí ya en las entrevistas para los PhDs y desde entonces has sido un pilar fundamental allí en el observatorio. Muchas gracias por estar siempre dispuesta a escuchar y compartir experiencias conmigo. Mieke, en este último año me has ayudado mucho a sobrellevar todo y te agradezco muchísimo tu apoyo. Y no podían faltar el grupo de los latino/hispanos, con los que he podido compartir tantas conversaciones en español y fiestas donde hemos podido mover el esqueleto al son de la buena música, gracias por haberme hecho sentir un poco más cerca de casa (Santiago, Francisca, Heather, Pedro, Pablo, Javi, Cristina, Liz, Yanett, Carmen y Álvaro). Por último quiero agradecer su enorme labor a Xander que ha hecho posible que hoy pueda estar escribiendo estas líneas. Gracias por saberme guiar hasta el final y no dejar que me rindiera por el camino.

Tampoco hubiera podido terminar este doctorado sin la gran ayuda y apoyo de mis chicas astro (Laura, Alba, Belén y Maider). Gracias, sois geniales. Cada una en una punta diferente de Europa haciendo todas el doctorado, hemos compartido experiencias y penas. Sois unas grandes científicas y todo un ejemplo a seguir, al final sí, lo hemos conseguido. El que sin duda también ha seguido de cerca y compartido las experiencias del doctorado ha sido Héctor. Mucha gracias por estar siempre disponible para hablar a pesar de encontrarte al otro lado del charco y estar siempre dispuesto a escuchar por tonta que fuera la situación. Gracias por ayudarme sobre todo al comienzo del doctorado cuando estuve atascada.

Y no hubiera llegado a este doctorado sin el apoyo de mis antiguos compañeros de trabajo de SENER, gracias a todos, entre ellos a JR, Juanma y Mertxe, que me animaron a empezar el Máster en Astrofísica de la UCM y me permitieron compaginar el trabajo con los estudios. Pero en especial quiero agradecer al Comité de Jóvenes Imberbes (Dani, Patri, Marta y Yolanda) por todos esos buenos momentos juntos en SENER y gracias a los cuales no sucumbí el último año allí. Gracias también a todos mis compañeros del máster y a todos grandes profesores (África, Pablo, Armando, José Antonio, David, Gorgas, Jaime, Jesús, Nicolás, Juan Abel y María José). Disfruté muchísimo volviendo a clase y sobre todo conseguisteis que a pesar del gran esfuerzo que suponía para mí asistir a clase y compatibilizarlo con el trabajo, todos los días estuviera deseando coger la mochila e ir allí a seguir aprendiendo.

Este viaje no sería lo mismo sin toda esa gente que ha estado a mi lado en los Países Bajos a parte del trabajo. Empezando por Inés, Celia y Elena que han estado ahí siempre para absolutamente todo desde que coincidimos aquí ya en 2008, os voy a estar siempre agradecida de todo corazón. Y por supuesto, gracias a los eazie al sol (Gaba, Carol, Jesús Hidalgo, Jesús, Ana, Jonathan y César) por todos esos eazie, comidas y cenas juntos, paseos en Panecuquen I y patxaranes. Esto sin vosotros no hubiera sido lo mismo. Gracias de corazón a mi coro, Singlarísimo, gracias a todos y cada uno de vosotros: David, Marta, Alicia, Ana Collado, Ana, Monika, Robert como adjunto, Álvaro, Xavi, Montse, Agustín, Eva, Víctor, Inés, Begoña, Suzanne, Ramón y Germán. Me habéis llenado de alegría en los momentos más bajos y habéis hecho de los sábados el día perfecto para compartirlo con vosotros con buena música y con un vino mejor. Quiero agradecer también a todas las chicas del fútbol de Lugdunum y Wonderbrains (Irene, Alicia, Nerea, Eli, Miri, Inés Alonso, Inés, Celia, Maria, Kim, Cristina, Ana y Ann-Marie). Gracias por todos los grandes momentos juntas, por todos partidos y derbies, especialmente aquellos contra Dream Team o ESOC. Quiero agradecer también a mi querido estudio de yoga, en especial a los profesores Santa, Nancy, Jerry y Robinson, por enseñarme a disfrutar tanto del yoga y mostrarme mi sitio seguro. Gracias también a Marieke y Yoga per tutti por tus maravillosas clases y transmitirme tanta paz. Gracias a Borja y Francis, por esas tardes de cena y cine. Gracias a Franchu y Tami por esas cenas geniales en vuestra casa. Gracias al grupo de la ESA como Pedro, Isa, Susana, Jonan, Judith, Berta, Xevi, Ana Laura, Laura, Gonzalo y Bernardo. Y finalmente quiero dar las gracias a Adriaan Goslinga, por hacernos las cosas más fáciles y ayudarnos en todo lo que ha podido.

Y que puedo decir de mis queridas kukis (Coro, Laura, Elena, Ester y Tina). Sois las mejores, habéis estado ahí siempre apoyándome y animándome a terminar el doctorado, sin dudar ni un momento de que lo conseguiría. Muchas gracias a todas. Habéis hecho que cada vez que volvía a casa, a Lasarte, sintiera como si el tiempo no hubiera pasado. Habéis conseguido que todas las navidades y fiestas sean memorables. Coro, ya sabes que para mi eres especial, mi amiga desde la infancia, has estado a mí lado a pesar de la distancia en todo momento, preocupándote todos los días de mandarme un "qué tal estás?" que me hacía sentirte tan cerca. No tengo palabras para expresar toda mi gratitud. Te quiero fea!

Muchas gracias también a todas las personas que han estado ahí a pesar de la distancia. Gracias a Ainara, Laura, Izas, Mertxe, Marta, Paula y Szil, un grupo de mujeres luchadoras que siempre me sirven de motivación, me dan fuerza y me siento tan orgullosa de que

seáis mis amigas. Gracias a las supernenas, Irenne y MC, siempre cerca a pesar de los años. Gracias a Nacho y Mario por seguir siendo tan auténticos como siempre. Gracias a los del barrio (Lore, David, Iñaki, Emi, Sanza, Marina, Lucía, Javi, Manoli y Carlos) por siempre rodearnos de ese buen rollo. Gracias a todos los de la ETSIA y Carlos (sois un montón), este año hace 20 años desde que nos conocimos, hemos pasado grandes momentos y espero que los sigamos disfrutando juntos. Gracias a Fernando, Ana, Claudia, Bea, Carmen, Celia, Rául, Óscar y Carlos. Para terminar, muchas gracias a Edurne, por acompañarme en este último año y medio. Gracias por enseñarme a pensar en el ahora, a priorizar y relativizar todas las situaciones. Sin tu ayuda esta tesis posiblemente no hubiera tenido un final. Gracias.

Finalmente quiero dar las gracias a toda mi familia por su apoyo incondicional. Empezando por mis padres, que han sido siempre un ejemplo de lucha y perseverancia. No lo han tenido fácil y a pesar de ello han hecho siempre todo los que estuviera en sus manos para darme un futuro mejor. A mí madre, ya sabe lo agradecida que estaré siempre, porque sin su apoyo y obstinación ante el resto de la familia nunca hubiera ido a Madrid a estudiar y no sería la persona que soy hoy. Mila esker ama! A mi hermano Martin, gracias por tu apoyo y comprensión, sé que en el fondo te sientes un poco orgulloso de tu hermana. A Marta, me alegro tanto de que hayas entrado en nuestras vidas y gracias por toda esa alegría y positividad que nos aportas. Gracias a mis cuñados y sobrinos, Juan Pablo, Bea, Sergio y Marta, por demostrarme día a día que puedo contar siempre con vosotros. Gracias a Mari Jose y a Txomin, goian bego, me alegro que volviéramos a retomar el contacto hace unos años y volvierais a formar parte de mi vida. Askenekoz, mila esker nire lengusuei (Asier, Garbiñe, Izarne, Gari, Amets eta Mikel). Momentu guztietatik alde polita ikusi egin behar da, eta zuek izan zineten oparirik bereziena Txominen aguarran. Asko pozten naiz kontaktua berritzeaz eta espero det hemendikan asko urtetarako mantenduko dugula.

Cover design by David San León
Concept by Igone Urdampilleta
Image credits: NASA/CXC